DAWG

Dedicated Autonomous Wildlife Guardian
Final Report

DSE Group 03

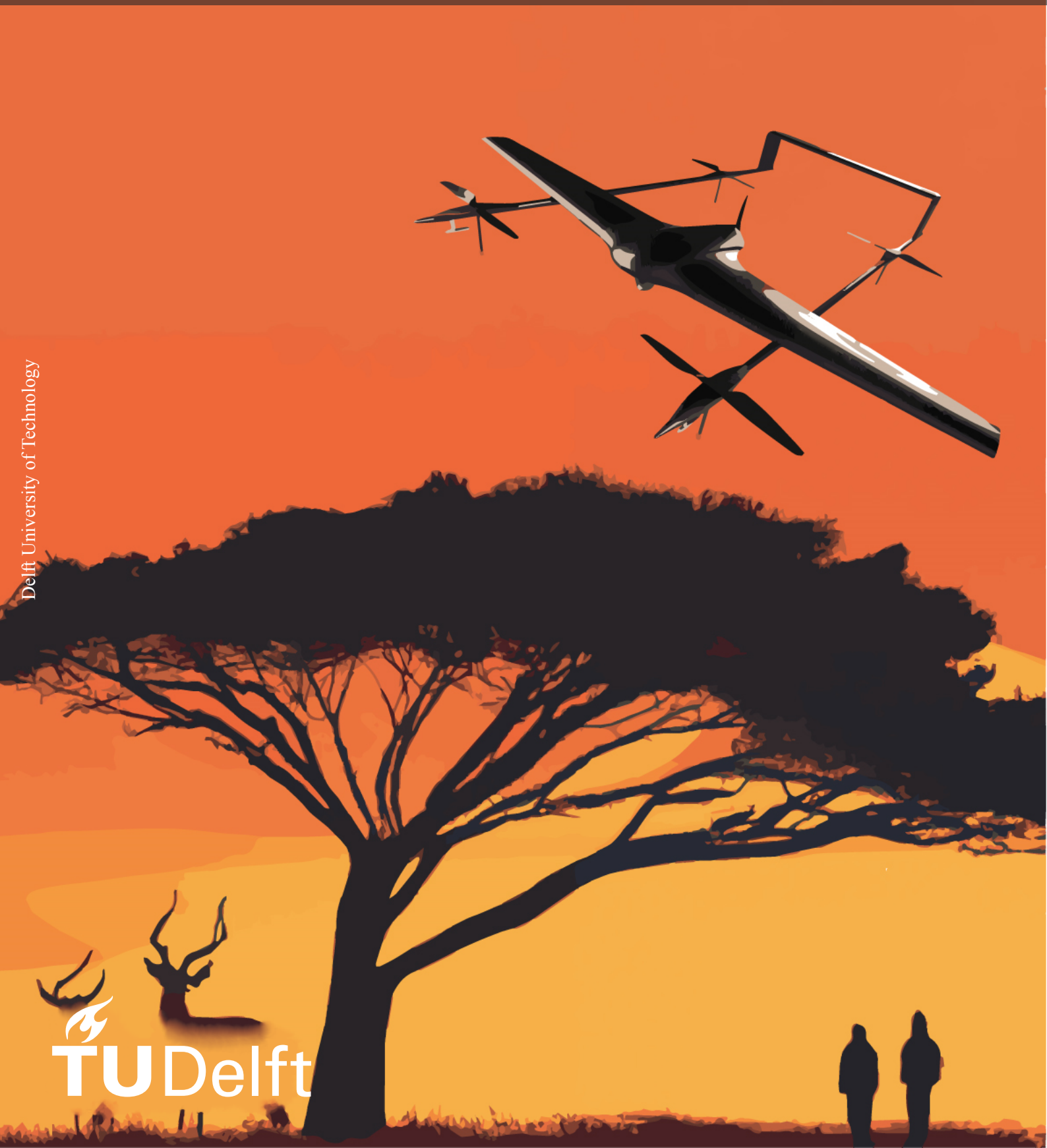

Delft University of Technology

TU Delft

DAWG

Dedicated Autonomous Wildlife Guardian
Final Report

by

DSE Group 03

Student Name	Student Number
Helena den Ouden	4859987
Philip Vaartjes	5075548
Job de Vries	5175879
Cindy Chen	5204941
Boris Van Praet	5218217
Vilius Valentukevičius	5237602
Jasper Barens	5268400
Dominik Špoljarić	5278627
Luc Thomas	5300010
Stijn van Teylingen	5304946

Principal Tutor: Roberto Merino-Martinez
Coaches: Siddharth Pantoji
Prashant Solanki
Faculty: Faculty of Aerospace Engineering, Delft

Style: TU Delft Report Style, with modifications by Daan Zwaneveld

TU Delft

Nomenclature

Acronyms

ABS Acrylonitrile butadiene styrene

AC Aircraft

C&DH Command & Data Handling

CFD Computational Fluid Dynamics

CFRP Carbon Fibre Reinforced Polymer

CG Center of Gravity

DAWG Dedicated Autonomous Wildlife Guardian

DEN Day, Evening, Night

DHI Diffuse Horizontal Irradiation

DNI Direct Normal Irradiation

DOD Depth of Discharge

DSE Design Synthesis Exercise

EOL End Of Life

ESC Electronic Speed Control

FC Fuel Cell

FOV Field Of View

GFRP Glass Fibre Reinforced Polymer

GHG Greenhouse Gas

GHI Global Horizontal Irradiation

GLONASS GLObal NAvigation Satellite System

GN Guidance & Navigation

GNSS Global Navigation Satellite System

GPS Global Positioning System

GS Ground Station

IMU Inertial Measurement Unit

ISA International Standard Atmosphere

LE Leading Edge

Li-air Lithium Air

Li-ion Lithium-ion

Li-Po Lithium Polymer

LiDAR Light Detection and Ranging

MAC Mean Aerodynamic Chord

MEMS Micro-electromechanical System

MTOW Maximum Take-Off Weight

PEM Proton Exchange Membrane

RAMS Reliability, Availability, Maintainability and Safety

RC Remote Control

ROC Rate of Climb

ROI Return On Investment

RPM Revolutions per Minute

SATCOM Satellite Communication

SDG Sustainable Development Goals

SEL Sound Exposure Level

SMR Small Modular Reactor

SPL Sound Pressure Level

TE Trailing Edge

UAV Unmanned Aerial Vehicle

USB Universal Serial Bus

V&V Verification and Validation

VL Vertical Landing

VLM Vortex Lattice Method

VTO Vertical Take-Off

VTOL Vertical Takeoff & Landing

XFLR An analysis tool for airfoils, wings and planes

Constants

ρ_0	Atmospheric density at sea lvl	$1.225\,\mathrm{kg\,m^{-3}}$
g	Gravitational Acceleration	$9.81\,\mathrm{m\,s^{-2}}$

Symbols

α	Angle of attack	$^\circ$
$\bar{c}$	Mean aerodynamic chord	m

$\frac{S_{proj}}{S}$	Projected area ratio	–
$\frac{W}{S}$	Wing loading	N m^{-2}
γ	Flight path angle	°
A_{sp}	Solar Panel Area	m^2
b	Wingspan	m
c_a	Chord length of the aileron	m
c_e	Chord length of the elevator	m
c_r	Chord length of the rudder	m
$C_{D_{cruise}}$	Drag coefficient in cruise	–
$C_{D_{to}}$	Drag coefficient during take-off	–
C_{dev}	Development costs	€
C_{EOL}	End-of-life costs	€
$C_{L_{max_a}}$	Maximum lift coefficient w.r.t changing aileron deflection	–
$C_{L_{max_e}}$	Maximum lift coefficient w.r.t changing elevator deflection	–
$C_{L_{max_r}}$	Maximum lift coefficient w.r.t changing rudder deflection	–
C_{nom}	Nominal capacity	A h
C_{oper}	Operational (maintenance) costs	€
$C_{prod/del}$	Production & Delivery costs	€
d	Distance	km
d_{fp}	Flight path distance	km
f	Frequency	Hz
$F_{y_{react}}$	Single attachment reaction force on the y direction	N
$FSPL$	Free space loss	dB
G_r	Receiver gain	dB
G_t	Transmitter gain	dB
I_{charge}	Charging current	A
L_m	Miscellaneous loss	dB
L_r	Receiver loss	dB
L_t	Transmitter loss	dB
L_a	Lift acting at aileron	N
L_e	Lift acting at elevator	N
L_r	Lift acting at rudder	N
M_a	Moment around hinge of the aileron	N m
M_e	Moment around hinge of the elevator	N m
M_r	Moment around hinge of the rudder	N m
M_{prop}	Propellant mass	kg
M_{tank}	Tank structural mass	kg
P	Power	W
P_r	Power of receiver	dB
P_t	Power of transmitter	dB
P_{GS}	Price per ground station	€
P_{UAV}	Price per UAV	€
Q_{GS}	Quantity of ground stations produced	–
Q_{UAV}	Quantity of UAV produced	–
r_{cent}	Maximum distance from centre of hexagon	km
ROC	Rate of climb	m s^{-1}
S	Wing surface area	m^2
S_a	Aileron surface area	m^2
S_e	Elevator surface area	m^2
S_r	Rudder surface area	m^2
S_w	Wing area	m^2
t_{charge}	Charging time	h
T_{cruise}	Thrust at cruise	N
t_{surv}	Time of surveillance	min
T_{VTOL}	Thrust in VTOL	N
V_{to}	Take-off velocity	m s^{-1}
W	Weight	N

Executive Overview

As the technical performance and application opportunities of modern-day UAVs are better than ever before, the preservation of wildlife is also one of the domains ready to benefit from these advances. Specifically, the surveillance UAV to monitor wildlife and their habitat has great potential in the modern market and thus is the basis of this design. In the following paragraphs, the essential aspects of such a design are highlighted and explained.

Mission Objectives & Requirements
The design team has been tasked with creating an aerial system design, consisting of a UAV and a ground station. To ensure the design goal is clear and consistent, the mission need statement has been defined:

Mission Need Statement:
Design an unmanned autonomous aerial surveillance system to monitor wildlife and orography, detect environmental threats, and identify the location of litter

The Project Objective Statement has also been identified:

Project Objective Statement:
Design an aerial surveillance system with integrated sensors and data processing capabilities capable of wildlife and orography monitoring, environmental threat, and litter detection, by ten students in ten weeks with a production budget of 150, 000 € per system

The system was designed to provide its services in a wide range of environments, with the majority of operations active in Africa, Australia and regions of the Middle East and South Asia.

The UAV design
The final UAV design consists of a fixed-wing, boom tail, and VTOL air vehicle. In Figure 1 a final render can be found. It can be seen that the horizontal booms, which are on either lateral side of the fuselage, provide support for both the tail and the VTOL motors and propellers. Next to that, The landing gears are also attached to the booms, which will give great stability and clearance from the ground. It has been decided to go for a blended wing-body to improve the aerodynamic characteristics of the UAV.

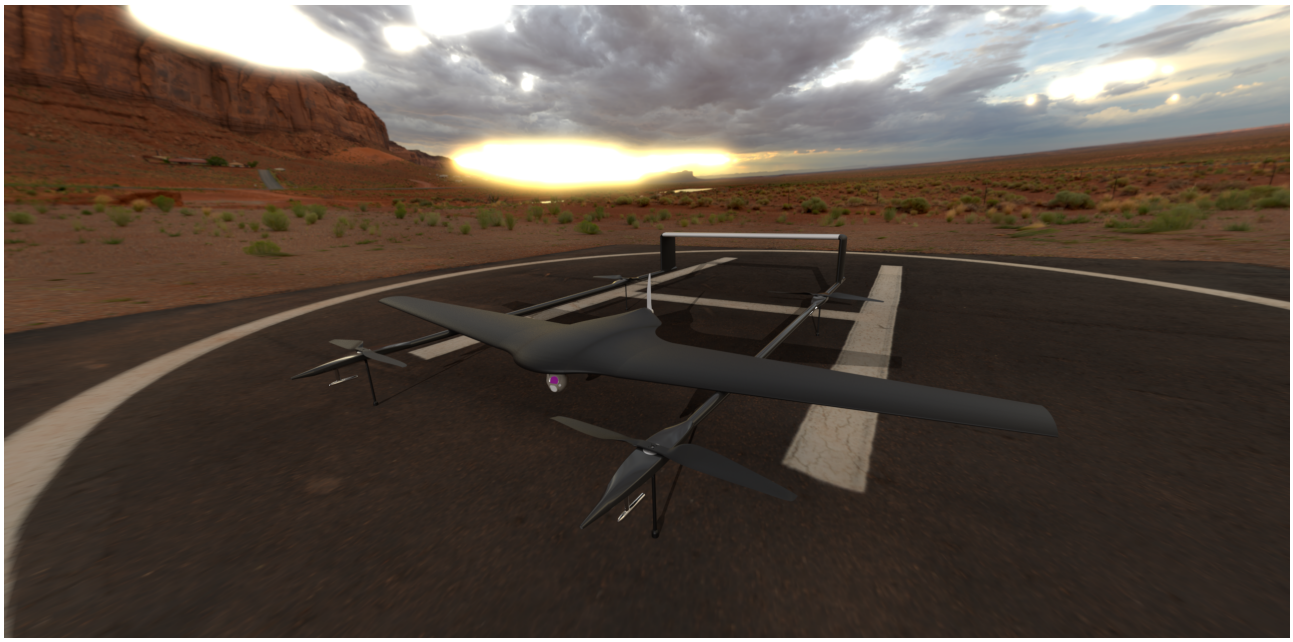

Figure 1: Render of the Final UAV Design

The payload and instrumentation layout can be found in Figure 2. The elements were put as much forward as possible to put the centre of gravity forward. This was necessary to improve the static stability of the UAV.

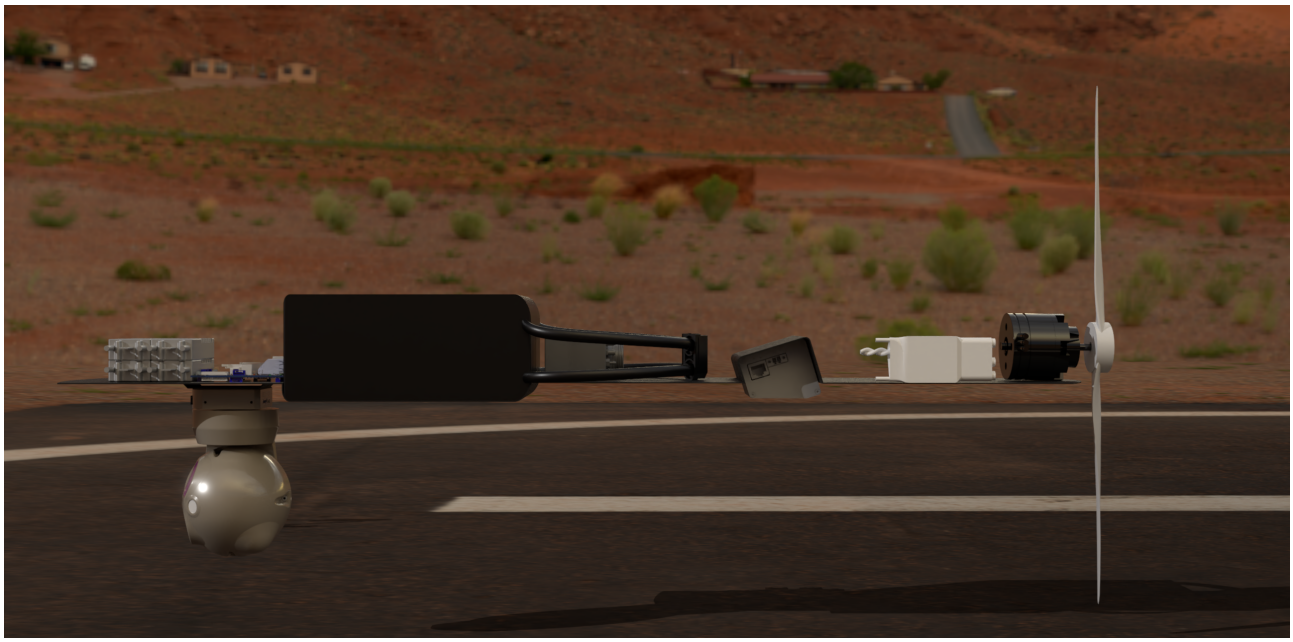

Figure 2: Internal view of the payload and instrumentation of the UAV.

Operations

Three potential options for the automatic charging system were evaluated: wireless charging, a docking station with a robot arm, and contact charging. After considering factors such as efficiency, reliability, and suitability, contact charging was determined to be the preferred method.

The positioning and landing procedure of the UAV during the charging process was detailed. This included steps such as notifying the ground station, initiating descent, correcting attitude, executing a precise vertical landing, and confirming a successful connection for charging.

The UAV's batteries, consisting of two lithium-ion cells, were discussed in terms of charging performance. The charge time was calculated based on nominal capacity and charging current and found to be 2 hrs for a full charge and less than 50 min after a nominal surveillance mission. Emphasis was placed on the batteries' estimated lifespan, highlighting the importance of durability and longevity. Proper battery management was emphasized for optimal performance, considering the expected number of charging cycles. At a depth of discharge of 30% for a nominal mission, the life cycle is over a year.

Design considerations for the charging surface were outlined, emphasizing the use of specialized tiles that enabled connection to positive, negative, or no power source as required. The landing legs of the UAV featured spring-loaded contact pins to establish a reliable electrical connection during charging, facilitating efficient power transfer and minimizing disruptions.

The operational region of the UAV system was evaluated. Considering factors such as maximum and minimum operating temperature, wind speed, forestation, and solar radiation an operational area was generated, see Figure 3.

The selection of a suitable grid system was explored, considering different grid patterns based on area coverage and the number of required ground stations. After evaluation, Grid 2 was chosen for its ability to reduce the number of ground stations while maintaining an acceptable response time for surveillance operations, see Figure 4. Grid 2 consists of 14 ground stations (for a 50 by 50 km area), each with two drones, with every tile covering $30\,\mathrm{km}^2$. Taking $4.0\,\mathrm{min}$ to reach the outer edge of the grid.

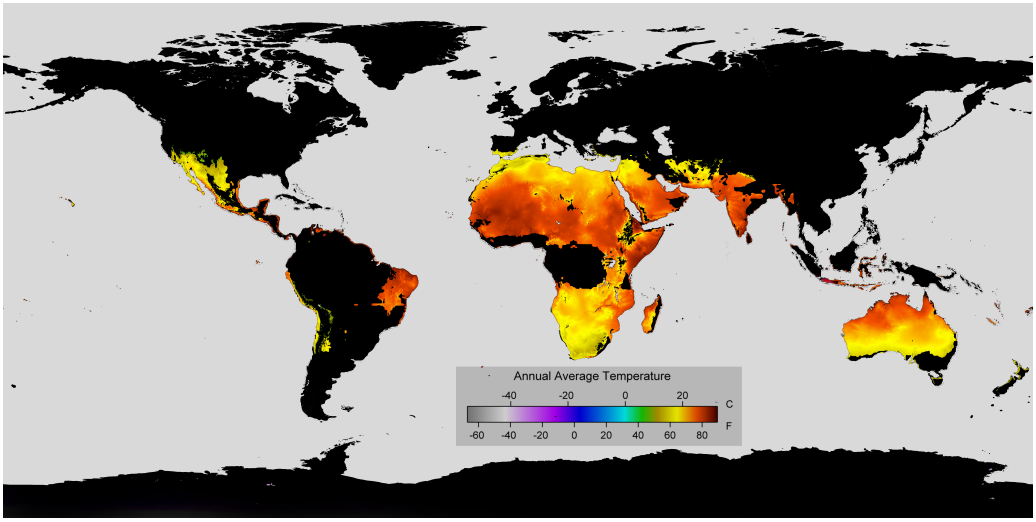

Figure 3: Map of Operating Regions on Earth. The black area represents the no-fly zones

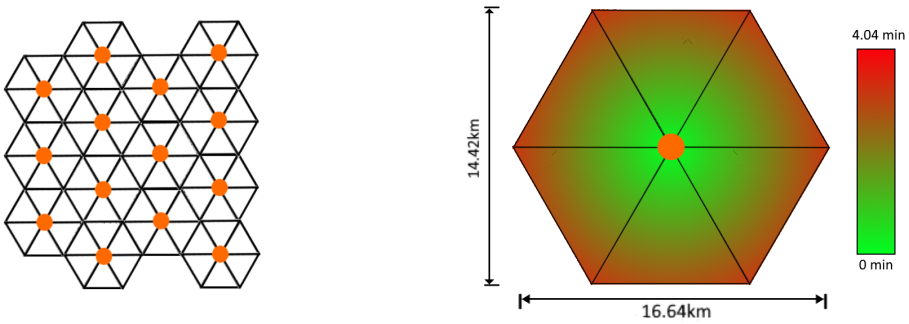

Figure 4: Grid selection (Left), Coverage percentage (right)

Power & Propulsion

As power & propulsion subsystems arguably drive the functionality of the UAV the most, it was important to analyse the power and thrust needs of the UAV and choose the components satisfying these needs.

The UAV is powered by two ARES 6s 30Ah batteries (see Figure 5), each providing 665.89 Wh of energy and making up 34.22 % of the total UAV weight. The propulsion system is comprised of five motors, four of which are used for VTOL purposes. Taking into account the necessary climb rate and unfavourable wind conditions (downdraft/side winds), the MN701S KV280 motor, equipped with G26*8.5 propellers and ALPHA 80A 6-12S ESC (Electronic Speed Controller), see Figure 6, was selected as the most optimal for VTOL application.

Figure 5: ARES 6s 30Ah battery.

(a) MN701-S KV280 produced by T-motor.

(b) G26*8.5 T-motor CFRP propeller for VTOL.

(c) ALPHA 80A 6-12S ESC.

Figure 6: Selected VTOL motor, propeller and ESC.

The remaining push motor is responsible for providing the UAV with thrust for climb and horizontal flight. For that reason, the motor selected is AT4130 Long Shaft KV450 that is used together with APC 18*8 propellers and AT 75A 6S ESC (see Figure 7).

(a) AT4130 Long Shaft KV450 produced by T-motor.

(b) 18*8 propeller produced by APC.

(c) AT 75A 6S ESC

Figure 7: Selected horizontal push motor, propeller and ESC.

Aerodynamic Design and Analysis

A large portion of the secondary lift surface analysis was dedicated to tail sizing. The tail sizing was performed using the method described in F. Oliviero (2022) where the tail is sized for controllability and stability[1]. As the UAV has VTOL capabilities the method deviated from F. Oliviero (2022) for the controllability of the UAV. Using a NACA0015 airfoil for the horizontal tail a tail area of $0.40\,\mathrm{m}^2$ is required with a boom length of $2.85\,\mathrm{m}$ measured from the centroid of the front VTOL propeller and the leading edge of the horizontal tail. The vertical tail sizing follows from reducing the downwash gradient over the horizontal tail by moving the horizontal tail out of the wake created by the main wing. The vertical stabilizer length is $0.30\,\mathrm{m}$. The vertical tail is therefore over-designed but the gain lowering the downwash gradient was considered more favourable.

Finally, the control surfaces and their geometries were identified and estimated. The UAV contains 3 main types of control surfaces, namely an elevator, ailerons and rudders. Starting with the elevator, its sizing is constrained by the take-off rotation performance and obstacle avoidance capabilities due to the VTOL presence. Only one elevator is used. Moreover, the UAV features a pair of ailerons. These were designed by considering the constraining turn when performing the orography mission. To conclude the control surface sizing, two coupled rudders were selected by analysing the empirical length fractions for rudder sizing.

The overview of control surface dimensions is shown in Table 1:

Table 1: Summary of control surface geometry

Control Surface	Length [m]	Chord [m]	Area [m^2]
Elevator	1.10	0.07	0.069
Aileron	0.50	0.10	0.047
Rudder	0.24	0.14	0.033

Aerodynamics

Estimating the aerodynamic performance of the UAV requires careful consideration of the main wing position and geometry as well as aerodynamic loads and flight configurations. To begin with, a trade-off with respect

to aerodynamic (drag, ground effects) and structural considerations (landing gear, structure) was performed comparing the low and high-wing configurations in addition to the blended mid-wing option. As a result, the latter was selected.

After this decision was made, a VLM analysis with OpenVSP was performed in order to perform 4 tasks: design the main wing, determine favourable flight configurations for different mission phases, obtain spanwise lift, drag and pitch moment distributions and acquire aerodynamic characteristics. Using the drag polar as depicted in Figure 9a the blended main wing was designed by defining 4 identical airfoils as cross-sections and the distances in between them. The final values can be read in Table 2 and visualised in Figure 8. Finally, a dihedral of 3° was introduced in the wing which does not affect flight performance but increases roll stability.

Afterwards, the angles of attack and velocities of different mission phases could be determined. It was found that nominal cruise is flown at a velocity of 80 km/h with an angle of attack of 1.55°. The lift distribution, drag distribution and pitch moment around the cg distribution were determined in order to design the DAWG UAV's structure. Figure 9b displays the half-spanwise lift distribution where the boom is located at 0.8 m. Furthermore, the aerodynamic coefficients are obtained in order to simulate the aerodynamic behaviour of the UAV in the flight model.

Finally, the results were verified by checking the convergence of the $\frac{L}{D}$, C_L and C_D residuals in nominal cruise conditions. The logarithmic residual is plotted as a function of the number of iterations in Figure 9cc.

Table 2: Geometry parameters of the main wing.

Parameter	Value	Parameter	Value
Chord_1	900 [mm]	Wing Surface	1.25 [m^2]
Chord_2	725 [mm]	L_12	150 [mm]
Chord_3	450 [mm]	L_23	200 [mm]
Chord_4	180 [mm]	L_34	1250 [mm]

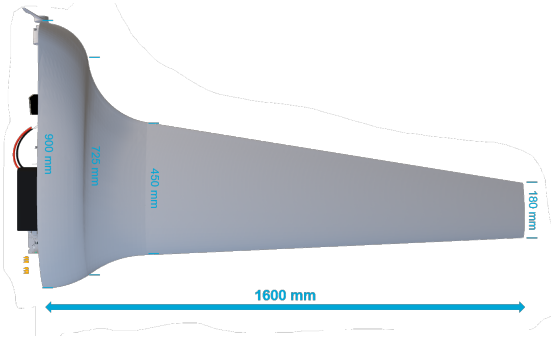

Figure 8: Visualisation of the wing geometry.

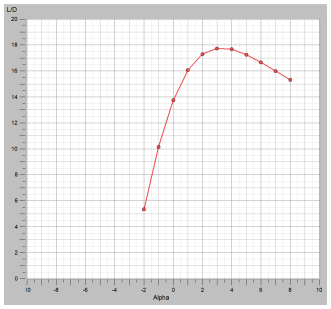

(a) Lift-drag polar in cruise conditions.

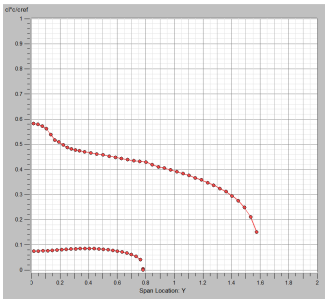

(b) Chord normalised lift coefficient distribution over half wingspan.

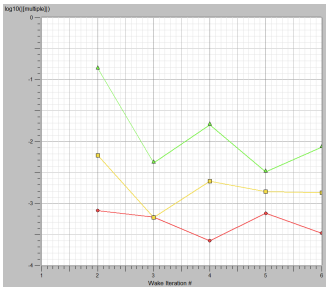

(c) Convergence of the aerodynamic parameters in nominal cruise conditions.

Figure 9: Aerodynamic parameters.

Structures & Materials

To ensure the construction of a robust and lightweight UAV, the selection of a material with high strength-to-weight ratio is crucial. In comparing the specific strength of Carbon Fiber, Aluminum, and Alloy Steel, it was determined that Carbon Fiber offers the most favorable characteristics. Among various Carbon Fiber options considered, two specific carbon fiber layups (CFRP TC380 Toray and CFRP TC250 Toray) emerged as top contenders due to their inherent quasi-isotropic nature, which streamlines the manufacturing process by reducing time requirements.

After careful evaluation, CFRP TC380 Toray was ultimately chosen, primarily due to its superior specific strength, particularly in the compression direction. This decision ensures that the UAV maintains optimal structural integrity while minimizing weight, making it an ideal choice for the intended application. Due to the harsh limitation on weight, only one layer of carbon fibre will be used. Therefore, in order to hold the structural integrity of the tail, a very lightweight material will have to be chosen. Rohacell is chosen for this. Lastly, brass will be chosen for the charging, due to the material not corroding and having great electrical conductivity.

For the structural design of the booms, flight at maximum velocity, maximum VTOL and stationary conditions are considered. The boom was designed to not exceed the yield strength of the material used. It was also required to not deflect the boom to a limit of 2%. The boom was designed for a safe deflection of 1.8 %, which appeared to be the limiting factor. The final parameters can be found in Table 3.

Table 3: The boom structural parameters.

Parameters	Section 1	Section 2	Section 3	Unit
Length	0-500	500-2005	2005-2857	[mm]
Diameter	15-20	20	20-16.5	[mm]
Thickness	0.5	0.5	0.5	[mm]

The wing structure was based on the loads experienced by the wing in forward flight, at maximum velocity, and at the ultimate load factor. The wing structure consists of a wing skin made of Toray TC380 CFRP, with internal stiffeners and ribs made out of Aluminum 7075-T6. The design is summarised by Table 4

Table 4: Summary of the internal wing structure

Structural Element	Value
Skin thickness $[mm]$	0.681
Rib locations along half-span $[m]$	[0.35, 0.35, 0.77, 1.18]
Rib thickness $[mm]$	1.5
Stiffener designs $(h \times w \times t \times L)$ $[mm]$	$[17 \times 17 \times 1.8 \times 350]$ $[10 \times 10 \times 1.5 \times 1250]$
Structural wing mass [kg]	3.36

The tail structural design was performed similarly, wherein the design loads were identified and designed for. The analysis resulted in two layers of Toray TC380 CFRP with a ROHACELL foam core.

The landing gear was designed to allow for adequate clearance between the camera and the ground, as well as sustaining a $5g$ landing load. This resulted in a hollow tube of two layers of Toray TC380 CFRP.

Flight Performance

The flight performance of the UAV was analyzed by conducting an analysis using a power and wing loading diagram. This analysis aimed to determine the design space for the UAV by considering various constraints such as cruise conditions, rate of climb, level turn, maximum service ceiling, and approach. The objective was to select the maximum wing loading at the lowest power-to-weight ratio to enhance flight performance and reduce power usage.

Load diagrams were generated to illustrate the load factors sustained by the UAV during different velocity conditions. These diagrams also incorporated the effects of gust loads on the UAV. The load factors ranged from -2 to 4.5 for speeds up to $29\,\mathrm{m\,s^{-1}}$, providing valuable information for the structural design of the UAV to ensure its ability to withstand these loads throughout its operational lifetime Figure 10.

A Doghouse Plot was used to comprehensively assess the combined effects of turning and climbing manoeuvres. Two distinct models were presented for each type of manoeuvre, taking into account climbing performance and aircraft turning capability Figure 11. The climb performance was analyzed using the conservation of energy principle, based on the work-energy theorem. This analysis derived the specific excess power and the rate of climb, considering factors such as altitude, weight, and gravitational acceleration. Turn performance was modelled based on a steady turn with a constant radius. The bank angle was determined using the aircraft's airspeed, turn radius, and gravitational acceleration. The load factor, representing the ratio of lifting force to the aircraft's weight, was calculated based on the balance of vertical forces. Additional parameters, such as the maximum instantaneous load factor and stall speed ratio, were defined to provide insights into the aircraft's load-carrying capability and stall characteristics. The doghouse plot provides the turn-climb performance and the maximum bank angle within the operating conditions.

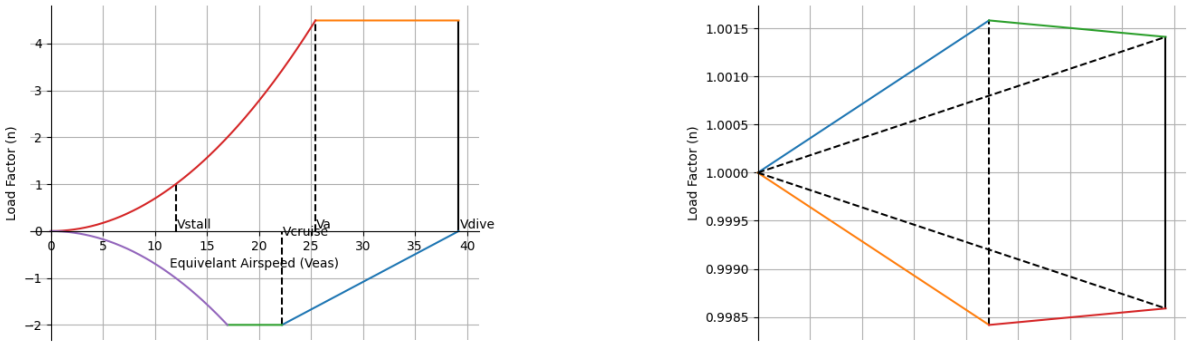

Figure 10: Load Diagrams

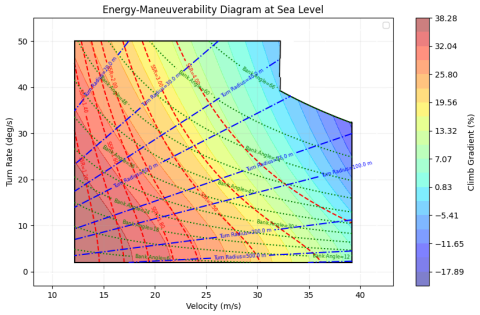

Figure 11: Doghouse Plot

Flight Simulation

Since building a physical prototype of the UAV is infeasible within the resources of the DSE, a flight simulation of the UAV was created. This is a non-linear six-degree of freedom simulation that has the ability to simulate the entire flight regime (including VTOL, transition and fixed-wing flight). This simulation uses the open-source and widely adopted JSBSim flight dynamics model.

To allow the aircraft to be commanded during flight, the open-source PX4 flight controller was used. This flight controller talks to the simulation, reading its environment through simulated sensors and controlling the system by providing actuator signals. While PX4 provides a robust platform for controlling the UAV's actuators and providing state estimations, the intelligence behind performing missions is not implemented on the flight controller but rather the NVIDIA Jetson AI computing module. To facilitate this external control, PX4's integration with ROS (Robot Operating System) 2 is used.

This ROS bridge allows acceleration, velocity and position setpoints to be sent from an external script and provides information about the current state of the UAV. While AI processing is outside of the scope of what can

be implemented in the DSE, the flight simulation demonstrated that it is indeed possible to interface with external control. It also demonstrates an easy-to-use testbed that can be used for further UAV software development - allowing for more safety and significantly faster development iterations than testing software on physical hardware.

Other than providing a proof-of-concept of the tooling and architecture used for the UAV's brains, the simulation was used to confirm various performance estimations. Firstly, it showed that the maximum achievable speed of the UAV is approximately $145\,\mathrm{km\,h^{-1}}$. Secondly, it showed that the take-off and transition procedure could be completed in less than a minute. Lastly, it showed that it was possible to cover a straight-line distance of almost $4\,\mathrm{km}$ in less than 4 minutes after the UAV takes off from the ground.

Extensive verification and validation took place for the propulsion system models used in the simulation (with other inputs having V&V procedures discussed elsewhere). Vehicle handling characteristics were also verified to ensure the vehicle responds in a manner that is to be expected. This process also ensured the UAV (with its controller) remained stable when subjected to various control inputs. All checks passed, though it identified a lack of performance for yaw control.

Noise

An essential requirement for the UAV system was that it must not disturb the wildlife/environment, therefore it had to be quiet. Therefore, the noise was extensively analyzed to investigate noise levels in different phases of a UAV's flight. The Hanson model was used to find a sound pressure level, and various transformations were used to obtain an accurate noise metric.

The main noise source of the system was the noise produced by the propellers as the airframe noise is negligible. The noise levels could be estimated using Hanson's model for propeller noise. This mathematical model allowed the decomposition of the sound, enabling the determination of the harmonics of the propeller noise. Several inputs were required to find these harmonic frequencies, including the number of blades per propeller, RPM, the velocity of the moving noise source, the location of the source with respect to the sound measurement location, and the propeller length.

Using the Hanson model, the sound pressure level (SPL) for each harmonic could also be found. The model made the approximation that the propeller's blades were thin and neglected radial source terms. Adaptations were made to implement the Hanson model for far-field noise by incorporating sound propagation.

The noise theory was based on Hanson's helicoidal surface theory, assuming that each noise source element travelled along a helical path. The pressure of the noise could be found using a Fourier Series, and the sound pressure level (SPL) for each harmonic was determined.

The harmonic frequencies of the propellers alone were not sufficient to assess the severity of their disturbance to the environment. Therefore, an additional method called A-Weighting was used. A-Weighting accounted for how humans perceive sound and calculated a factor that could be added to the base sound pressure level. A-weighted sound level, expressed in dBA, provided a metric for determining the influence of sound.

To account for the duration of a sound, the sound exposure level (SEL) was introduced. It incorporated the A-weighted sound level and added a time element to calculate a useful metric for sound influence.

The final noise metric applied was the Day-Evening-Night (DEN) average level. It took into account the number of times an event occurs per day and added a penalty factor for certain hours to account for varying background noise levels.

With the noise metrics established, a target value for the UAV system's noise level had to be determined. Regulations on noise limits/standards were consulted, particularly for African wildlife reserves. Tanzanian and South African standards for "rural" areas recommended equivalent noise levels, while European regulations for a National Park were also considered.

Using the inputs provided, the methods explained in the Hanson model were applied, and the results were obtained. The sound pressure level decreased as the harmonic increased for each phase, and the first harmonics were found to be the most dominant contribution. The system was found to comply with the requirement set by the stakeholder. The result is a final maximum mission DEN noise level of $37.79\,\mathrm{dBA}$.

Sensitivity Analysis
Sensitivity analysis on the control surface designed dimensions was performed. This was done by varying the moment arm from the control surface to the centre of gravity and determining a corresponding change in surface area and chord for the elevator and ailerons and documenting the corresponding change in yaw rate for the rudder. From this, it was concluded that the elevator and aileron design were robust, but that the rudder dimensions are fairly sensitive to changing moment arm. The latter is most probably due to the simple nature of the rudder design.

A sensitivity analysis on response times was also performed. This sensitivity analysis looked at the effect that changing the take-off mass by 20% had on the time it takes to respond to an incident 4.24 km out using the flight model. It found that the response time is mostly insensitive to the takeoff mass, showing a deviation of under 5 s (on a total of approx. 200 s). Recommendations are made for a more in-depth analysis that investigates the effect that mass has on the propulsion system power, especially during other flight plans such as loiter and the surveillance mission.

Finally, a sensitivity analysis was performed on noise levels. In particular noise during vertical takeoff was analysed as this turned out to be the most constraining phase for almost every noise metric. The distance between the observer and source, the event duration and the number of events per day were varied. The analysis rendered the design to be robust in terms of noise, however, the distance between the observer and source was found to have a significant influence on the noise level. Due to the high sound exposure level of climb during a response mission, the number of events for this parameter was also investigated due determine to what extent it would affect the DEN noise level, it was found to be insignificant.

Development, Manufacturing and Operations Strategy
In order to know how to improve the sustainability of the UAV, the Greenhouse Gas (GHG) emissions during its lifetime needed to be assessed. In order to produce a single UAV with a predicted lifespan of two years, 368.26 $kgCO_{2_{eq}}$ is emitted. As for the doghouse, it produces 14 634 $kgCO_{2_{eq}}$ for a fifteen-year timespan. The UAV, in combination with the ground station, is powered by solar panels, meaning that during an operation of two years, they emit 23.17$kgCO2_{eq}$. If both would use electricity from the Dutch net during their operation over a lifetime of two years, it would emit 3765.22 kgCO2eq. Installing in situ solar panels has a very large impact on the sustainability of the DAWG project. Furthermore, CFRP and Li-ion batteries will be used. Both of these are recyclable and together with the recyclable copper of the motors, the UAV becomes 76% recyclable. Finally, the UAV will contribute to the UN's 17 sustainability goals (SDG). Mainly SDG 9 states that innovation should be fostered and SDG 15 states that life on land should be protected.

Risk Assessment
Once the technical risks were identified and divided into operational, system, and manufacturing risks, they were evaluated based on the probability of occurrence and the impact they cause. To limit the likelihood and extent of the consequences of each risk, mitigation strategies were also presented. With mitigation applied, the significance of almost all risks becomes minimal. Nevertheless, two of the risks, namely laws prohibiting the use of UAVs and the onboard battery thermal runaway, were not sufficiently reduced post-mitigation. As for law changes, a contingency plan consists of altering the design or initiating a partial return procedure to implement the required design changes into the old design if possible. For the battery thermal runaway, the negative consequences (total failure of UAV due to explosion or fire) could be prevented by installing a fire-retardant foam reservoir onboard and fire-resistant coating to readily stop the spread of and extinguish the fire.

Finances
Assessing the success of this project can in part be achieved by evaluating its general financial performance and profits. The market for wildlife surveillance UAVs is still growing, thus resulting in the 10-year production forecast of 1450 UAVs and 730 GS with the selling price of 200 000 € and 50 000 € for a unit of each respectively.

During the design project, the UAV and GS expenses are split into the groups of development, production & delivery, operational and end-of-life costs. An extensive cost analysis from the perspective of the DAWG company is then performed to estimate the average costs each year. In addition to that, the Return On Investment (ROI), indicating the profit margins of the project, is also presented for a period of a year and a decade. The overview of the aforementioned figures is presented below:

Table 5: Return On Investment (ROI) of the project

Return On Investment	
P_{UAV}	200 000 €
Q_{UAV} (over 10 yr)	1450
P_{GS}	50 000 €
Q_{GS} (over 10 yr)	730
C_{dev}	276 819 €
$C_{\text{prod/del}}$ (over 10 yr)	105.6 mil €
C_{oper} (over 10 yr)	3.69 mil €
C_{EOL} (over 10 yr)	0
Return On Investment (10 years)	198%
Annualized Return On Investment	11.5%

Contents

Chapter 1: Introduction

Every week two rangers are killed while dedicating their life to protecting wildlife [1]. During the Australian bushfires of 2019-2020, almost 3 billion animals were killed or displaced[2], while the number of wildfires continues to increase globally due to climate change. In the US, 100 million pounds of litter is created per year in national parks[3]. Clearly, the adoption of more effective surveillance measures is imperative. In light of these challenges, unmanned aerial vehicles (UAVs) offer a compelling solution to this need due to their ability to efficiently and autonomously cover large areas mitigating the effect of natural wildfires and allowing for efficient monitoring of wildlife and litter.

This report represents the final design phase of the Unmanned Aerial Vehicle used for wildlife surveillance, named DAWG (Dedicated Autonomous Wildlife Guardian). In this final design phase, the report presents a comprehensive overview of the technical and non-technical aspects of the subsystems, the overall design, and the operational conditions and mission of the UAV.

This report starts off by analyzing the general compliance to the requirements outlined in Chapter 2 followed by an analysis of the UAV's functionality in Chapter 3. In Chapter 4 a summary of the trade-offs mentioned in the midterm report [2] is shown. Subsequently, the operations & logistics of the UAV including charging, operational region, flight path, ground station, the operative grid and instrumentation are discussed in Chapter 5. Chapter 6 discusses the design of the power & propulsion system which encompasses the motors, propellers, and batteries.

The payload and propulsion system determine the preliminary UAV configuration from which the secondary lifting surfaces such as the tail, and control surface sizing are designed. An aerodynamic analysis is then conducted in Chapter 7, generating a final wing design, aerodynamic coefficients, and control derivatives.

Structural analysis and selection of materials are performed in Chapter 8, providing structural values of the UAV. Using this structural design as well as the components selected in the preceding chapters, a final design layout is constructed using 3DEXPERIENCE. This has been shown in Chapter 9.

The performance of the entire design, supported by analytical analyses and a numerical flight simulation, is presented in Chapter 10. Additionally, the noise characteristics of this design are analyzed in Chapter 11. Verification and validation methods are discussed Chapter 12 to prove the validity of the design and the software used to create it. Lastly, to highlight the overall feasibility of the design a sensitivity analysis is performed in Chapter 13. Following this updated technical budgets are proposed in Chapter 14.

The manufacturing, production, testing, and certification aspects are important considerations for the final design and are presented in Chapter 15. This chapter also discusses sustainable development considerations including a life cycle GHG emissions analysis.

A risk assessment is performed in Chapter 16 ensuring potential negative consequences are addressed. Finally, a financial assessment is conducted in Chapter 17 showing an expected return on investment. This report concludes with Chapter 18 discussing recommendations for future iterations of the design.

[1] https://worldanimalfoundation.org/advocate/poaching-statistics/#:~:text=Statistics%20suggest%20that%20Africa's%20poaching,and%20critically%20endangered%20black%20rhinos., accessed on 22/06/2023

[2] https://www.theguardian.com/environment/2020/jul/28/almost-3-billion-animals-affected-by-australian-megafires-report-shows-aoe, accessed on 22/06/2023

[3] https://blog.nus.edu.sg/protectourparks/2020/10/10/littering-in-national-parks-how-it-leads-to-various-forms-of-pollution/, accessed on 22/06/2023

Chapter 2: Requirement Analysis

For a successful wildlife surveillance system design, a comprehensive list of requirements is needed before the design process begins. Once the needs of parties interested in the design (stakeholders) are well understood, the Mission Need Statement (MNS) and Project Objective Statement (POS) are established, Section 2.1. The requirements are then identified and derived from a Requirement Discovery Tree, Section 2.2, and a number of ”special” requirements are also introduced in Section 2.3. The summarized list of requirements for different subsystems is finally presented in Section 2.4.

2.1. Project Rationale and Objectives

Before defining the requirements and general objectives of the mission, it is important to define the Mission Need Statement (MNS) and Project Objective Statement (POS) for the project:

Mission Need Statement:
Design an unmanned autonomous aerial surveillance system to monitor wildlife and orography, detect environmental threats, and identify the location of litter

Project Objective Statement:
Design an aerial surveillance system with integrated sensors and data processing capabilities capable of wildlife and orography monitoring, environmental threat, and litter detection, by ten students in ten weeks with a budget of 150 000 € per system

2.2. Requirement Discovery Tree

The requirements are derived using the Requirement Discovery Tree, as shown in Figure 2.1.

2.3. Special Requirement Types

One important aspect to consider is the existence of three special types of requirements that are present in almost any engineering design in addition to the regular requirements. These are known as killer, driving, or key requirements, and are thus detailed in the table below:

Table 2.1: Special Requirements.

Type of Requirement	Description
Killer Requirement	A requirement that drives the design to an unacceptable extent. Satisfying such a requirement may be extremely difficult or costly and jeopardise the other requirements.
Driving Requirement	A requirement that drives the design more than average. Such requirement plays a significant role in the design and affects the success of the project the most.
Key Requirement	A requirement which is very important to the customer. This requirement shall be satisfied to meet the needs of users and stakeholders.

It shall be noted that key requirements are not necessarily driving the design whereas all driving requirements are automatically key requirements. Table 2.2 Depicts the killer and key requirements that are crucial in the design of the UAV. The remaining requirements are defined in Table 2.3.

Table 2.2: Killer, Key & Driving Requirements.

ID	Requirement	Category
REQ-DEP-4	The UAV shall be able to deploy and arrive at its required location in less than 2 minutes	Killer
REQ-NTC-NOI-1	The drone shall produce less than 40 dBA of DEN level noise	Killer
REQ-DEP-2	The UAV shall be unmanned (no passengers)	Key
REQ-GEN-1	The UAV shall follow surveillance path autonomously	Key
REQ-GEN-3	The UAV shall be able to cover an area of 20 km^2 in a single flight	Key
REQ-GEN-12	The UAV shall detect poachers	Key
REQ-GEN-13	The UAV shall detect litter	Key
REQ-GEN-14	The UAV shall surveil wildlife	Key
REQ-GEN-15	The UAV shall detect wildfires	Key
REQ-GEN-16	The UAV shall map the orography of the environment	Key
REQ-GEN-19	The surveillance area shall be surveilled twice a day	Key
REQ-NTC-COS-1	The UAV shall cost less than 100.000 EUR	Key
REQ-NTC-COS-2	The ground station shall cost less than 50.000 EUR	Key
REQ-NTC-SUS-1	At least 75% of the UAV shall be recyclable at EOL	Key
REQ-NTC-SUS-2	The UAV shall produce no harmful emissions	Key
REQ-PM-CS-5	The UAV shall be controllable autonomously	Key
REQ-PM-INS-7	The UAV shall be operable at night	Key
REQ-PM-SM-6	The UAV structure shall not be flammable	Key
REQ-REC-1	The UAV shall land autonomously at the GS	Key
REQ-GEN-7	The drone shall have a maximum endurance of at least 2 hrs	Driving
REQ-GEN-10	The drone shall be able to cruise at 80 km/h.	Driving
REQ-GEN-11	The UAV shall have a maximum range of at least 150 km.	Driving

2.4. Compliance Matrix

Table 2.3 shows an overview of all requirements and whether or not they have been met. Green indicates the requirement has been met or exceeded, orange that the requirement has been met partially, or it has yet to be determined and red suggests that the requirement has not been met.

Table 2.3: Compliance Matrix.

Identifier	Requirement	Actual Value/Rationale
REQ-DEP-1	The drone shall be able to lift off autonomously.	Veronte Autopilot 1X
REQ-DEP-2	The drone shall be unmanned (no passengers).	-
REQ-DEP-3	The drone shall not be deployed before performing self-checks on all systems.	-
REQ-DEP-4	The drone shall be able to deploy and arrive at its required location in less than 2 minutes in case of emergencies.	25% of surveillance area in 2 min, 100% in 4 min. See Chapter 5
REQ-EOL-1	The drone shall be able to make a safe emergency landing when a critical failure is detected.	Emergency landing system (parachute) is too heavy and drag-inducing to be added.
REQ-EOL-2	The drone shall be able to deploy its emergency landing systems in case critical failure is detected.	Emergency landing system (parachute) too heavy
REQ-EOL-3	The drone shall be able to activate its recovery beacon in case of an emergency landing.	tBeacon Onyx (onboard recovery beacon)
REQ-GEN-1	The drone shall follow the surveillance path autonomously.	Using onboard autopilot
REQ-GEN-2	The drone shall take off vertically.	VTOL propellers

REQ-GEN-3	The drone shall be able to cover a minimum area of 20 km^2 during a single flight.	30 km^2, see Chapter 5.
REQ-GEN-4	The system shall be scalable (to surveil larger zones).	See Chapter 5.
REQ-GEN-5	The drone shall reach cruise conditions within 1 min of deployment.	15 s (VTO) + 41.1 s (Climb) = 56.1 s, see subsection 6.1.1.
REQ-GEN-6	The drone shall have a cruise altitude of at least 120 m.	120m cruise altitude chosen
REQ-GEN-7	The drone shall have a maximum endurance of at least 2 hrs.	See section Power Budget section 13.2
REQ-GEN-8	The drone shall have a reliability of at least 90% for every 500 service hours.	In-depth testing/analysis required
REQ-GEN-9	The drone shall be able to determine its velocity.	Pitot tube
REQ-GEN-10	The drone shall be able to cruise at 80 km/h.	See section 6.1 pushing propeller
REQ-GEN-11	The drone shall have a maximum range of at least 150 km.	See Section 14.2
REQ-GEN-12	The drone shall detect poachers.	See section Camera Tradeoff 5.1 Midterm report
REQ-GEN-13	The drone shall detect litter.	See section Camera Tradeoff 5.1 Midterm report
REQ-GEN-14	The drone shall surveil wildlife.	See section Camera Tradeoff 5.1 Midterm report
REQ-GEN-15	The drone shall detect wildfires.	See section Camera Tradeoff 5.1 Midterm report
REQ-GEN-16	The drone shall map the orography of the environment.	See section LiDAR Midterm report
REQ-GEN-17	The drone shall be able to loiter for at least 90 min around a point of interest.	Endurance of more than 2hrs (Section 14.2)
REQ-GEN-18	The drone shall turn off automatically at the arrival of GS.	When starting to charge, the UAV automatically turns off
REQ-GEN-19	The surveillance area shall be surveilled twice a day.	See Chapter 5
REQ-GS-1	The drone shall be able to automatically recharge/refuel at a GS.	See section automatic recharging
REQ-GS-2	The GS shall accommodate automatic lift off of the drone from the GS.	
REQ-GS-3	The installation of GSs shall cause minimal disturbance to wildlife and the environment.	In-depth analysis required
REQ-GS-4	The design of the GS shall blend in with the environment in terms of colours.	Similar colour of GS compared to environment
REQ-GS-5	The GS shall have a maximum size of 10 m x 10 m x 3m.	Two charging boxes of 6x6 m, Solar Panels and one box in the middle for computer, microphone, antenna's
REQ-GS-6	The GS shall be able to instantly store data received from drones.	Live data stored from UAV
REQ-GS-7	The GS shall be able to store 1 TB of data or two weeks of data.	26 days of live footage requires 1TB of space on a drive.
REQ-NTC-COS-1	The drone shall cost less than 100.000 EUR.	See Section 17.2
REQ-NTC-COS-2	The ground station shall cost less than 50.000 EUR.	See Section 17.2
REQ-NTC-NOI-3	The drone shall not produce harmonic noise frequencies above 2000 Hz.	Chapter 11

REQ-NTC-NOI-4	The drone shall produce less than 40 dBA of DEN level noise.	Chapter 11
REQ-NTC-SUS-1	Drone shall be at least 75% recyclable/reprocessable at end of life.	See Section 15.3
REQ-NTC-SUS-2	The drone shall produce zero emissions during operation.	100% powered by electric batteries
REQ-NTC-SUS-3	Total environmental impact of the system shall be equal to or reduced relative to similar systems.	See Section 15.3 (all power is generated using solar panels)
REQ-NTC-SUS-4	The drone shall not harm the local wildlife during operations.	Using a camera for obstacle avoidance.
REQ-NTC-TIM-1	The design of the system shall be completed within 8 weeks.	Design duration given by DSE
REQ-PM-COM-1	The drone shall transfer data to the GS.	Swarmlink to AH-1726-16
REQ-PM-COM-2	The drone shall be able to transfer data on a 2.4 GHz bandwidth	2.2-2.5GHz (Swarmlink)
REQ-PM-COM-3	The drone shall send live footage to the ground station.	Swarmlink to AH-1726-16
REQ-PM-COM-4	The communication system shall be designed such that data breaches are prevented.	Secure communications system deemed too heavy.
REQ-PM-COM-5	The communication system shall have a range of at least 13.6 km.	
REQ-PM-COM-6	The drone shall have 4.5 GB of (temporary) storage.	Samsung Fit Plus 256GB Type-A 400MB/s USB 3.1 Flash Drive
REQ-PM-COM-7	The drone shall communicate with the ground station before landing.	Roof of GS has to open before landing, communication using SATCOM
REQ-PM-CS-1	The drone shall be controllable in three dimensions.	Ailerons, elevator, rudder (see section control and stability)
REQ-PM-CS-2	The drone shall be controllable in winds up to 50 km/h.	See Control and stability
REQ-PM-CS-3	The drone shall be able to determine its attitude.	IMU on autopilot
REQ-PM-CS-4	The drone shall be controllable in rainy conditions of at least 0.5 mm per hour (slight rain) [1].	Analysis outside of the scope of the project.
REQ-PM-CS-5	The drone shall be controllable autonomously.	Veronte Autopilot 1X
REQ-PM-CS-6	The drone shall be able to deviate from the flight path.	Veronte Autopilot 1X
REQ-PM-CS-7	The drone shall calculate the optimal response in case of an emergency.	Jetson Origin
REQ-PM-CS-8	The drone shall be able to accelerate to a ROC of 3 m/s.	4.57 m/s subsection 6.1.1
REQ-PM-CS-9	The drone shall avoid obstacles in its path.	LiDAR can detect objects underneath UAV but moving objects outside FOV cannot be detected
REQ-PM-GN-9	The GN system shall be accurate to 5 m.	GPS is accurate to 4.9m [2]
REQ-PM-INS-1	The drone shall detect litter with a surface area larger than 0.05 m^2.	See midterm report [2]. The camera can detect objects of 10 cm x 15 cm .

[1] https://water.usgs.gov/edu/activity-howmuchrain-metric.html, accessed on: 15/06/2023

[2] https://www.spatialpost.com/how-accurate-is-gps/, accessed on: 14/06/2023

REQ-PM-INS-2	The drone shall be able to map orography in three dimensions.	LiDAR is used to map orography.
REQ-PM-INS-3	The main camera shall have 720p resolution.	Trilium HD40-LV
REQ-PM-INS-4	The drone shall have (a) microphone(s)	Microphones are placed on the ground
REQ-PM-INS-4	The microphone(s) shall detect at least 60 dB of sound.	60 dB is the sound of a driving car
REQ-PM-INS-5	The microphone(s) shall be able to detect the direction of the sound by means of triangulation.	Omnidirectional MEMS microphone can detect the direction of the sound.
REQ-PM-INS-6	The microphone(s) shall be able to detect the distance to the sound.	Three microphones all detecting the direction and sound, calculate location using triangulation.
REQ-PM-INS-7	The drone shall be operable at night.	Thermal camera
REQ-PM-INS-8	The drone shall have a night camera that works below 0.01 lux.	Thermal camera
REQ-PM-INS-9	The thermal sensor shall be able to detect wildfires.	Thermal camera
REQ-PM-LIF-1	The VTOL propulsion system shall be able to produce a T/W ratio of 2.	Max T/W = 2.45
REQ-PM-LIF-2	The propulsion system shall require less than 6000 W of power.	For max throttle - VTOL: 4x1701 = 6804W, Cruise = 1540.06 W
REQ-PM-LIF-3	The propulsion system shall weigh less than 3 kg.	2.76 kg (5 ESCs, 5mot, 5props)
REQ-PM-PL-1	The payload shall require less than 200 W of power.	114 W, see Chapter 14
REQ-PM-PL-2	The payload shall weigh less than 2 kg.	1.4 kg, see Chapter 14.
REQ-PM-PL-3	The power source shall be able to generate at least 7000 W of power.	5760 (@cutoff voltage), 7560 (@max voltage)
REQ-PM-PL-4	The power system should be able to produce 200 W of redundant power.	P_max = 7560 W, P_max_req = 7028 W
REQ-PM-PP-1	The horizontal propulsion system shall be able to produce at least 10 N of force.	Section 6.1
REQ-PM-PP-2	The propulsion system shall have de-icing capability.	Drone is stored in a closed Ground Station but does not have onboard de-icing. Thus, if the air temperature is between 0 and $-5°$, UAV will not be operational, see Section 5.2.
REQ-PM-SM-1	Structure shall be large enough to fit all the payload.	Fit the camera, LiDAR, Batteries, Communication System,
REQ-PM-SM-2	Structure shall sustain vibrational amplitude of <TBD>mm	Requires further analysis
REQ-PM-SM-3	The wing structure shall sustain a minimum axial load of <TBD>N	No axial loads present on the wing during nominal flight conditions, further investigation required into potential axial loads
REQ-PM-SM-4	The wing structure of the drone shall sustain a minimum load of 300 N	Wing structure sized to meet the requirement
REQ-PM-SM-5	The wing structure shall sustain a minimum bending moment of 250 Nm.	Wing structure sized and designed to meet this requirement

REQ-PM-SM-6	Drone structure shall not be flammable.	Boric acid coating added fibres of CFRP Section 8.2
REQ-PM-SM-7	The material shall be chosen such that the structure is resistant to corrosion.	CFRP is resistant to corrosion Section 8.2
REQ-PM-SM-8	The material of the drone shall sustain the same amount of loads in temperatures range of -5 C°to 50 C°.	All chosen materials able to handle the temperature conditions
REQ-PM-SM-9	Structure shall sustain vibrations of <TBD>Hz.	Further investigation required
REQ-PM-SM-10	Structure shall sustain a maximum deflection of 2%.	The structure has been designed to have a maximum deflection of 1.8%
REQ-PM-SM-11	The drone shall be able to withstand dust of level IP6X.	Testing required
REQ-PM-SM-12	The drone shall be water resistant until IPX5.	Propellers and CFRP are water resistant and UAV is waterproof sealed
REQ-PM-SM-13	Structure shall be able to carry 5.6kg of payload.	Wing calculations assumed payload mass of 5.6 kg
REQ-PM-SM-15	The landing gear shall sustain a minimum axial load of 5g ($49\,\mathrm{m\,s^{-2}}$).	Landing gear sized to meet 5g requirement and can sustain at least that amount
REQ-PM-SM-16	The production shall be sustainable.	UAV structure production sustainable
REQ-PM-SM-17	The structure shall weigh less than 6 kg.	$5.78\,\mathrm{kg}$ see Chapter 14
REQ-REC-1	The drone shall land autonomously at the GS.	ArUco markers (subsection 5.7.4)
REQ-REC-2	The drone shall calculate its path to the GS.	Veronte Autopilot 1X
REQ-REC-3	The drone shall at all times know its own coordinates.	GPS onboard Veronte Autopilot 1X
REQ-REC-4	The drone shall be equipped with the required position recognition equipment.	LiDAR
REQ-REC-5	The drone shall return based on a GS signal or the amount of power left.	Veronte Autopilot 1X

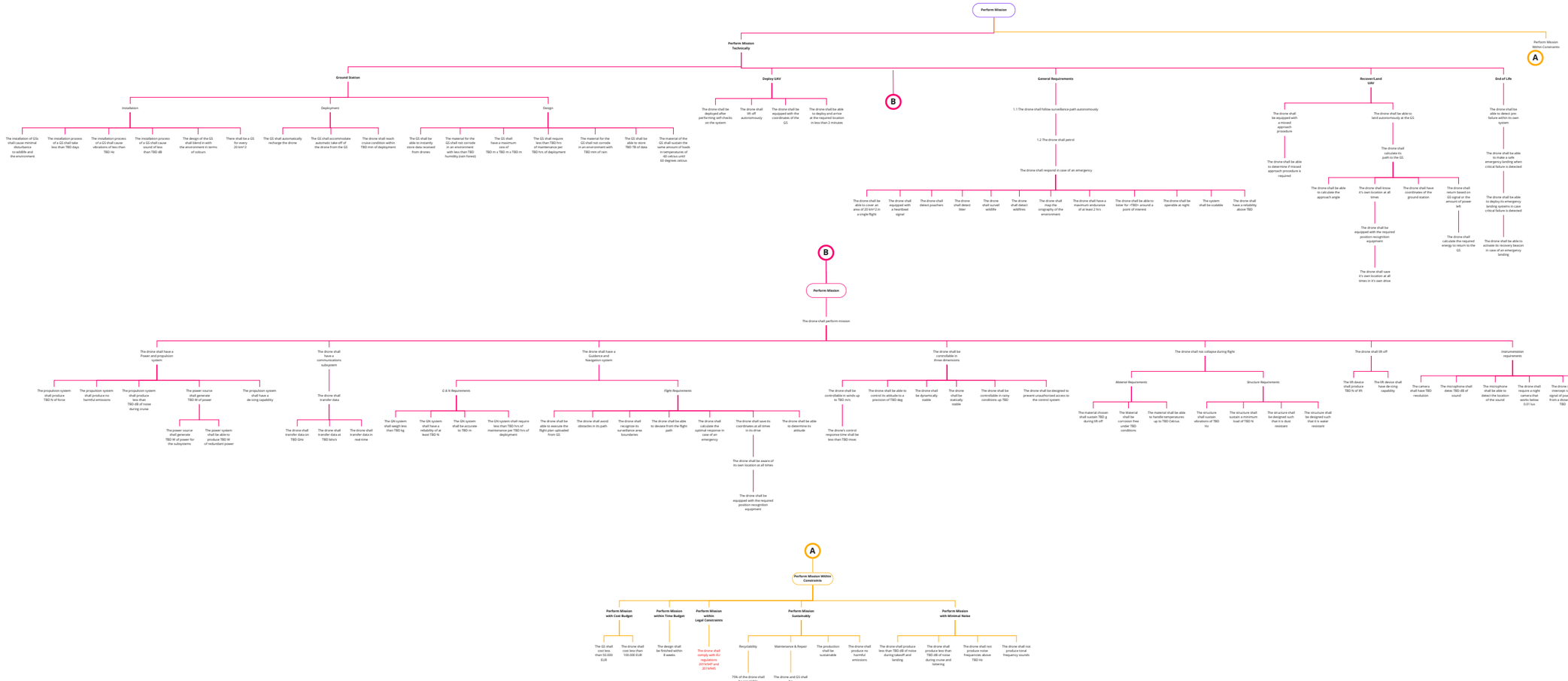

Figure 2.1: Requirements tree.

Chapter 3: Functional Analysis

To gain a better understanding of the functions and subsystems the system must provide, a functional flow diagram and functional breakdown structure can be created. Starting with the functional flow diagram, nine top-level tasks can be created. These top-level tasks will be elaborated on below.

The first step that must be taken to deploy a system, is manufacturing the parts required (*0.0: Manufacturing*) as well as deciding where to and installing the system (*1.0: Install System*). After installing the system, it must be initialized and tested to ensure the installation was a success (*2.0: Initialize Ground System (GS)*).

After the installation has been completed, the operational phase can begin. When an event is raised (such as an alert or the operator requesting the deployment), the first step is to deploy a new UAV (*3.0: Deploy UAV*). After the UAV is deployed, it will climb to cruise conditions and perform its mission (*4.0: Perform Mission*). This mission can have one of two types: a response mission, where it goes out to the point of interest and loiters there (*4.2A*), or a surveillance mission, where it follows a surveillance path (*4.2B*).

After completing its mission, the UAV will return to the ground station, where it will be captured by the ground station (*5.0: Recover/Land UAV*). After capture, the UAV is connected to the ground station to replenish its power source, transfer post-flight data, and run various other post-flight inspections and activities (*6.0: Post-Flight Servicing & Inspection*).

After operating the UAVs for a while there may, unfortunately, be some form of equipment failure that requires servicing by a maintenance crew (*7.0: Service UAV/Ground Station (Maintenance)*). Furthermore, after the system's usable lifespan has been completed, it should be decommissioned. This includes removing the system, restoring the installation site to its former glory, and evaluating the deployment (*8.0: System End of Life*).

All of these top-level tasks can now be subdivided into smaller tasks. This has been done for two additional levels and can be found in the Functional Flow Diagram in Figure A.1 (see Appendix A). In total, there are approximately 250 entries in this Functional Flow Diagram. As such, it is not feasible to provide a detailed description of all of them. Please refer to the diagram for the entries.

Each of these lowest-level tasks can be further subdivided into steps within a Functional Breakdown Structure such that each step can be assigned to a piece of hardware or software. The resulting functional breakdown structure has been shown in Figure A.2 (see Appendix A).

It is worth noting that some steps have not been split up. This is either because their assignment is obvious, or because any further division would be too vague in light of a large possible divergence in design. As an example of this last point: *3.7.4: Launch UAV* could be anything from a pressure cannon launching an object into the air, a quadcopter lifting off vertically to a small plane taking off from a runway; any further subdivision would depend on the mechanism chosen.

Chapter 4: Summary of Previous Trade-offs

In this chapter, a summary is given of all trade-offs that were done during the previous design stage. To understand the results of the tables, Figure 4.1 is included. Multiple options for different subsystems are considered and graded in these trade-off tables. To trade the concepts off effectively, some criteria were defined. Each concept will be judged by the criteria and will be given a score from Figure 4.1. These criteria are also given weights based on the relative importance of the criteria for the mission.

green	excellent, exceeds requirements	yellow	correctable deficiencies
blue	good, meets requirements	red	unacceptable

Figure 4.1: Legend of Trade-off Score Classes.

Following this method, there were trade-off tables made for the generation of the final concept and the instrumentation selection. The trade-off tables and their results are presented in the tables below. The first table shows the trade-off of preliminary concepts. These are distinguished by their different lift-providing subsystem.

Table 4.1: General Configurations Trade-Off.

CRITERION / CONCEPT	Noise	Control & Stability	Range & Endurance	V_{max} & Loading	Operational complexity	Design complexity	Instrumentation Adaptability	Weight	SCORE
Flying Wing Configuration	green Low required thrust means low propeller noise due to lower rpm. High service ceiling means that noise can be reduced by flying at higher altitudes.	yellow Heavy response to gusts, trimming with ailerons, complex control system.	green Flying wings have the highest lift to drag ratio. Range and cruise is maximized for maximimum CL/CD.	green Low drag means the flying wing has high excess power allowing a higher maximum velocity. The lack of a tail allows the aircraft to operate in higher gusts and loads.	blue Static stability can be achieved, and there are very few moving parts.	yellow Designing a stable, controlable, and efficient flying wing is hard to achieve.	yellow Fitting the payload in the flying wing will affect the available airfoil choices reducing the low drag advantages.	green structural weight is minimized by not needing any other structure than the wing.	2.87
Conventional Wing Configuration	blue Similar to Flying Wing Configuration, but slight loss in efficiency means slightly higher noise output.	green Easily designed to be statically stable, dynamic stability also viable. Trimmable with reliable well established control systems.	green High L/D ratio leading to great endurance and range performance.	green Convential aircraft UAV have been proven to have high operating speeds (>300km/h) and low operating speeds (<80km/h).	blue Incorporate more parts than flying wings but large amount of operational experience.	green Well proven technology and sizing methodology on both large and small scale.	blue Fuselage gives great amount of freedom in sizing and positioning payload. Usage of tail allows for large c.g. range.	blue High efficiency means carried power source can be smaller.	3.10
Multicopter	yellow Expected ground noise level of 55 dB when at 100m altitude; UAV needs to fly higher to reduce noise.	blue Great control and manoeuverability, great hovering and low-speed condition stability, but less stable in windgusts.	blue Meets requirements, but limited flying time compared to other options.	yellow Lower flight speeds than other options.	yellow Many moving parts, high risk of (partial) failure.	blue Proven technology.	yellow Small payload capabilities.	blue Comparable to other options.	1.80
Helicopter	yellow Expected drone noise levels are in the range of 70 - 80 dB, which will cause the UAV to fly higher.	yellow Difficult to control, a lot of effort should go into control systems.	blue Meets requirements, but limited flying time compared to other options.	yellow Generally low flying speed, but speed increase is possible at the cost of a large weight increase.	yellow Not fail-safe, as it only has one rotor.	blue Proven technology, attention needs to go to stability.	green Large fuselage that can incorporate instrumentation, easily scalable.	yellow Very heavy compared to other options, lighter options mean significantly less performance.	1.77

When a preliminary concept was chosen, the fixed-wing UAV, more detailed concepts were generated and analysed more thoroughly. This resulted in a second trade-off table that can be found in Table 4.2.

Table 4.2: Final Concept Configurations Trade-Off.

CRITERION / CONCEPT	Weight	Design Complexity	Scalability	Stability and Control	Take-off Performance	Operational Risk	Propulsion System Efficiency	Lift Efficiency	SCORE
Concept 1: Tilt rotor	red: Complex take-off mechanism is useful for specific cases but adds to much weight for this mission	yellow: UAV shape of conventional a/c. However, designing the tiltrotor mechanism is very complex.	green: Operations of UAV fully autonomous, great scalability	blue: Relatively good stability, due to horizontal tail	green: Vertical take-off	yellow: Complex tiltrotor mechanism which is prone te failure	yellow: Thrust matching complications (over-designed engines for cruise).	yellow: L/D = 9.6	5.11
Concept 2: Wing with boom via catapult	green: The simple design and lack of a full fuselage make this design very lightweight	blue: Simple UAV design, designing the launch system adds complexity	yellow: Difficult to make take-off and landing fully autonomous, will greatly increase design complexity and cost	green: Great stability, due to less downwash from wing	yellow: Plausible option, hard to automate and large ground station	yellow: One-engine failure	green: Single engine optimised for cruise	blue: L/D = 16.2	6.67
Concept 3: Wing with boom VTOL	blue: The design is very similar to concept two a slight weight penalty is payed for adding the 4 extra rotors to make the UAV VTOL	blue: Simple UAV design, VTOL device more complex	green: Operations of UAV fully autonomous, great scalability	blue: Center of gravity and aerodynamic center close together	green: Vertical take-off	blue: Many moving parts, but high redundancy.	blue: Lift and cruise engines separately optimised, but introduces additional weight and drag.	blue: L/D = 15.1	7.64
Concept 4: Canard with runway	yellow: According to reference data the canard conifguration seems to have a increased mass over the boomtail configuration	green: Simple UAV design, simple launch design	yellow: Multiple runways need to be installed, this has a large impact on the environment	yellow: Canard requires more development costs, due to complications	red: Requires 400% more power to operate on 25m runway	yellow: One-engine failure	blue: Engine must perform takeoff and thus is not optimised for both cruise and take-off.	yellow: L/D = 12.3	3.74

As can be seen in Table 4.2, Concept 3 (Wing with boom VTOL) is the concept with the highest score. The main reason is that this concept has superior scalability and take-off performance. It is also easier to upscale by adding ground stations due to the simplicity of the landing site. Besides, VTOL gives the advantage of fast deployment and recovery. This concept will be taken into further detail in this report.

The instrumentation selection was also done via trade-offs, which are presented in the tables below.

Table 4.3: Camera Trade-off.

Criterion / Cameras	Zoom	Weight [kg]	Size [mm]	Power [W]	Instrumentation for orography	FOV day [deg^2]	FOV night [deg^2]	SCORE
Trillium HD25-LV	3.00	0.36	76.00	10.00	0.00	63.02	580.81	2.80
Trillium HD40-XV	30.00	0.84	138.00	10.00	0.00	85.86	0.00	2.17
Trillium HD40-LV	10.00	0.67	138.00	10.00	0.00	85.86	331.24	2.90
Trillium HD45-LV-CZ	3.00	1.28	127.00	15.00	0.00	63.02	171.10	2.33
Trillium HD45-LV-CZ-GS	10.00	1.33	127.00	16.00	0.00	264.60	171.10	2.73
Trillium HD55-VV	36.00	1.29	152.00	20.00	0.00	104.04	0.00	2.47
Trillium HD55-LV-CZ-30x	30.00	1.56	152.00	20.00	0.00	85.86	171.10	2.50
Trillium HD55-MV	3.00	1.78	152.00	20.00	0.00	63.02	47.74	2.33
Trillium HD80-VV-510	30.00	4.27	245.00	25.00	3.00	85.86	0.00	1.20
Trillium HD80-LV-CZ-36X	36.00	3.85	245.00	25.00	3.00	103.86	171.10	2.27
Trillium HD80-MV-36X	36.00	4.67	245.00	25.00	3.00	103.86	33.00	2.07
Trillium HD80-MV-600	10.00	4.90	245.00	25.00	3.00	264.60	16.38	1.93
Trillium HD95	0.00	7.60	260.00	35.00	4.00	58.35	16.38	0.77
Octopus ISR E175	30.00	2.60	220.00	N.A.	3.00	49.27	34.40	1.63
TASE400 BLK II	29.00	3.67	267.00	10.00	0.00	85.50	55.10	1.53
FLIR Duo Pro R	0.00	0.33	85.00	10.00	0.00	2520.00	1665.00	3.20

Table 4.4: Positioning Trade-Off.

Criterion / Positioning	Update Frequency	Positioning Accuracy	Coverage Area	Complexity	Jamming Resistance	SCORE
GNSS Only	blue: ~50 Hz maximum	yellow: 10 meter accuracy	blue: Global Coverage	green: Mature technology	red: No resistance	1.47
GNSS + Dead Reckoning	green: >1,000 Hz possible	blue: 2.5m accuracy	blue: Global Coverage	green: Mature technology	blue: Dead reckoning gives short-term positioning solutions	2.47
GNSS + Dead Reckoning + Visual	green: >1,000 Hz possible	green: ~2.5m accuracy, O(cm) or better for close range with visual markers	green: GNSS coverage, visual for GNSS-denied areas	yellow: Components demonstrated, low adoption	green: Visual backup for absolute position solutions (providing regular references for dead reckoning)	2.77

Table 4.5: Navigation Trade-Off.

Navigation \ Criterion	Complexity	Predictability	Operational Guarantee	User Input	SCORE
Random Path	blue Well-researched topic	green Inherently random, so hard to predict	blue Less optimal, but coverage can be achieved	blue Point target input can be implemented	2.03
Pre-Determined Path	green Requires simple input, little to no path calculations	yellow Requires user intervention or additional integration of randomization systems	green Guaranteed by design	green User can directly input path selection or point to fly to or loiter around	2.23

Table 4.6: Re-Routing Strategy Trade-Off.

Re-Routing \ Criterion	Re-Routing Efficiency	Jamming Resistance	Complexity	Learning Capacity	SCORE
Ground Station Governed	green Can analyse full swarm	red Requires connection to the ground station, single point of failure	blue Orchestration algorithm required, Use of existing data link	blue All drones report back to the Ground Station, allowing for full (slightly outdated) knowledge	1.37
Autonomous	blue Only knowledge of self, periodic updates from the Ground Station	green No need for communication	green Local discision - simple Yes/No	yellow Only inputs from local UAV, needs its own memory system.	1.57
Cross-Linking	green Can analyse full swarm	blue System fails if no other nodes in range, local descision-making possible	yellow Need secondary P2P Data Link & distributed algorithm	green Direct communication between drones, live share of information	1.73

Table 4.7: Communication Architecture Trade-off.

Criterion / Communication Architecture	Infrastructure Costs	Reliability	Coverage Area	Complexity	Ease of Implementation	Security	Scalability	SCORE
Centralised	Green: Simplest option and therefore lowest costs	Yellow: Vulnerable to single point failure	Yellow: To allow more coverage, more ground stations necessary	Green: Simplest option	Green: Easily implemented in mission	Blue: Fewer points of access, resulting in high security	Yellow: Terrain may obstruct contact	2.333
Single-Layer Ad Hoc	Blue: Drones form the network with each other , so external network is not needed, resulting in lower relative costs	Yellow: Back up options, more random failure points	Blue: Multiple UAVs cover a greater area	Blue: Proven technology	Blue: Commonly used in drones	Yellow: Some access points, extra security system necessary	Yellow: Terrain should be taken into account	1.867
Multi-Group	Yellow: Generally higher costs than simple Ad Hoc system, but cheaper than Multi-Layer configuration	Blue: Expected failure can be handled effectively	Blue: Organized UAV communication allow greater coverage	Yellow: Detailed design for UAV communication structure	Yellow: Logistics of UAV deployement requires attention	Yellow: Similar to Single-Layer	Yellow: Similar to Single-Layer	1.767
Multi-Layer Ad Hoc	Yellow: Costs higher than Single-Layer Ad Hoc to account for interference and more intricate hardware/software onboard	Blue: Network as a back-up option	Blue: Additional network may allow UAVs to explore even greater areas	Red: Too complex for mission purpose	Yellow: Possible to implement with limited network	Yellow: Lot of access points, extra high quality security system necessary	Blue: Similar to Cellular Link	1.7
Direct Cellular Link	Yellow: High costs as cellular towers need to be built	Yellow: A lot of back-up towers	Yellow: Custom network would allow for a great coverage area	Yellow: Extra attention needed for network design	Red: Necessary to build entire network	Yellow: Anyone in the world can access data, a lot of security measures should be included	Blue: Good scalability due to network usage	1.733
Direct Satellite Link	Yellow: Higher costs as a result of groundstation and satellite maintenance	Yellow: Dependent on satellite performance	Green: Proven to have great coverage	Blue: Proven technology	Blue: Proven technology	Blue: Hard to breach link, higher level encription methods	Green: Access everywhere	2.433

Table 4.8: Power Source System Trade-Off.

CRITERION / POWER SOURCE	Mass Efficiency [Wh/kg]	Volume Efficiency [W/L]	Energy Specific Cost [US$/W]	GS Infrastructure	Environmental Safety	TRL	SCORE
Li-ion	yellow: 100-265	blue: 460.00	green: 0.94	green: Solar Panel or Windturbine at ground station	yellow: Fire and toxin hazard	green: Widely-available	5.86
Li-air	green: 5000-11000	green: 3436	green: 0.15	green: Solar Panel or Windturbine at ground station	blue: Very safe if electrolytes are solid state	red: Not market-ready	8.62
Li-Po	yellow: 245-430	green: 300-800	blue: 2.31	green: Solar Panel or Windturbine at ground station	blue: Safe Operation	green: Widely-available	6.78
Super Capacitor	red: 85.60	red: 15-60	yellow: 36.55	green: Solar Panel or Windturbine at ground station	green: Low Internal resistance makes them safe	green: Widely-available	4.71
Hydrogen Fuel Cell	green: 2400	blue: 114-209	blue: 8.64	yellow: Hydrogen production & transport is demanding	yellow: Fire hazard, requires extra reinforcement for crashworthiness	blue: Available, not fully mature	6.55

It can be seen that for the camera selection, the Trillium HD40-LV was chosen. This camera has one of the best FOVs during the night and is also not very heavy. A LiDAR was later also selected to complement the orography performances. This resulted in the Blickfeld Cube 1 Outdoor LiDAR. The positioning, navigation and re-routing architectures trade-offs resulted in a method that could be performed by the Veronte Autopilot 1x. The communication architecture selection makes it possible to design a functional antenna connection between the UAV and the ground station. The audio detection system will make use of simple MEMS microphones. There are required a lot of microphones to detect noise from poachers, which makes a cost-efficient option the best one. Finally, the power sources were traded off to select the most efficient green source of power. However, The communication and power selection did change between the previous design phase and the final design phase. The reasons for this are discussed in the following sections.

4.1. Airfoil selection

The airfoil of the wing has been decided by a trade-off as well. However, since this is a very technical subject and there are a lot of criteria to grade on, it was done in a slightly different manner. The trade-off table can be found in Table 4.9. It can be seen that the CAL2263m airfoil is the best airfoil for high-endurance missions. For that reason, it is the airfoil that will be used for the main wing of the UAV.

Table 4.9: Airfoil selection trade-off table.

Airfoil	C_{l_0}	$C_{l_{max}}$	α_{stall}	$C_{d_{min}}$	$C_l/C_{d_{max}}$	$C_l^{3/2}/C_{d_{max}}$	C_m	Final score
AG12	0.056	0.086	0.037	0.150	0.226	0.177	0.038	0.770
AG16	0.059	0.088	0.038	0.132	0.234	0.183	0.038	0.771
AG24	0.073	0.092	0.039	0.127	0.262	0.212	0.039	0.844
AG35-R	0.064	0.096	0.045	0.122	0.258	0.211	0.030	0.826
CAL1215j	0.059	0.086	0.042	0.112	0.267	0.219	0.043	0.827
CAL2263m	0.093	0.098	0.050	0.106	0.292	0.250	0.036	0.926
CAL4014L	0.007	0.092	0.046	0.116	0.238	0.193	0.039	0.730
E231	0.054	0.085	0.045	0.097	0.260	0.206	0.043	0.790
E374	0.048	0.075	0.038	0.108	0.296	0.234	0.050	0.850
E387	0.100	0.085	0.031	0.112	0.300	0.241	0.026	0.895
RG-14	0.048	0.077	0.035	0.132	0.240	0.175	0.033	0.741
RG-15	0.068	0.082	0.035	0.125	0.254	0.186	0.029	0.780
S7012	0.068	0.080	0.036	0.110	0.244	0.193	0.026	0.757
S8064	0.034	0.076	0.042	0.105	0.229	0.156	0.049	0.690
S9000	0.083	0.100	0.041	0.125	0.266	0.221	0.029	0.865
SA7035	0.074	0.093	0.039	0.127	0.274	0.227	0.027	0.860
SA7036	0.083	0.092	0.037	0.127	0.281	0.229	0.027	0.875
SD7037	0.093	0.092	0.038	0.127	0.284	0.236	0.027	0.898
SD7080	0.079	0.087	0.036	0.125	0.260	0.194	0.030	0.810

4.2. Communication restructuring

The communication architecture has changed since the previous design phase. From Table 4.7 it can be seen that previously, the direct satellite link was chosen as the best design option. Mainly due to the limited interference of mountains and other tall structures that would cross paths with the communication link. However, in the trade-off, the available data rate has not been considered. For smaller-sized satellite communication devices, this data rate is not close to the required data rate from the UAV payload. Therefore, a direct satellite link is not considered a viable option. Next to that, it is unclear how the UAV would directly connect to a satellite and then to the ground station, as it is not clear which satellites would be available above the wildlife reserves. Taking these matters into account, a centralised link is considered the best option. Hence, ground station and UAV antennas will be selected to establish a direct centralised link.

4.3. Hydrogen to Battery Pivot

Several problems were encountered with the operational side of using hydrogen as a power source. As the UAV will have to operate fully autonomously in remote locations it becomes a challenge to refuel each UAV. One two-hour flight would require 100 grams of hydrogen, calculated using the method explained in Section 14.2 which results in an energy requirement of 1315 W h per flight and H3dynamics datasheet about hydrogen tanks.[1] A single UAV will thus require 200 grams of hydrogen per day as it needs to fly two missions. This would mean that large cryogenic or high-pressure tanks would need to be installed at every ground station and they would need to be refuelled every month, making the UAV system less autonomous. Another solution would be to install hydrogen electrolysers at the ground stations. These could use solar power to turn water and oxygen from the air into hydrogen. This would require a natural water source which is not easy to come by in barren locations. River-, ground- and rainwater would also all need to be filtered as pure water is necessary for the electrolysers, this system would again require power and space. Such big installations would be very energy inefficient as you are generating electricity with solar panels to make hydrogen that is inserted into a UAV to again turn into electricity. Furthermore, it would result in large ground stations that disturb a nature reserve's

[1] https://www.h3dynamics.com/hydrogen-storage-and-accessories, accessed on 05-06-2023

peacefulness and overall purpose.

Carrying hydrogen on board a UAV comes with many risks. It is known that hydrogen is explosive and sensitive to environmental conditions as it needs to be stored at high-pressure or cryogenic temperatures. Safety systems would need to be installed on the UAV in case of a crash landing, these systems would add weight and complexity. Finally, hydrogen is a relatively new and untested power source in aviation. No clear international standards and regulations have been set to ensure safe usage. Getting a fully autonomous UAV certified is already a very tedious process, adding hydrogen will only make this harder and more complex.

Hydrogen is more energy dense than batteries and kerosene, which makes it a wanted renewable and zero-emission power source in the aerospace industry where weight is everything. It is however not often mentioned that the production of hydrogen is very inefficient. To obtain green hydrogen it must be produced through electrolytes by a renewable electric energy source. This means that electricity must be created by solar panels, windmills or hydropower to generate hydrogen through an electrolyser. This hydrogen is then compressed, cooled down or turned into a carrier gas such as ammonium for transportation to then be turned back into gaseous, room-temperature hydrogen so that it is usable for a fuel cell that can produce electricity. This whole process has an efficiency of around 30%. A sustainable battery needs a renewable power source to charge it and then it can be used to output electricity, this process has an efficiency of 90%. For the same amount of energy used, three battery-powered UAVs could fly for the same amount of energy required to fly a single hydrogen-power UAV. From a sustainability point of view, batteries are a better option.

It has been concluded that a hydrogen power source is mass efficient, but comes with a lot of operational challenges. These challenges can be overcome by enough resources and a well-trained ground team. The purpose of the wildlife surveillance UAV is to operate fully autonomously with minimal-sized ground stations. This was not taken into account in the previous power system trade-off, which resulted in a close win for hydrogen. Taking new arguments into account, the UAV's power source will pivot from a hydrogen fuel cell to a battery.

Chapter 5: Operations & Logistics

The UAV system is likely to be used in remote locations. On top of that, the system aims to be fully autonomous. It is therefore essential for the success of the mission to be logistically and operationally well-designed. This chapter aims to describe the operations and logistics of the entire system. Section 5.1 will first show the mission profiles of the system. Thereafter, Section 5.2 will investigate the areas across the globe in which the system can be operational. Section 5.3 and Section 5.4 will zoom into these operational areas and explain how they are set up, while Section 5.5 investigates the UAVs flight pattern. Following this, Section 5.6 will explain the ground station design. Section 5.7 and Section 5.8 will go into more detail about the automatic charging system and microphone selection. Lastly, Section 5.9 consists of an in-depth analysis of the instrument interface.

5.1. Mission Profile

Figure 5.2 presents the two mission profiles. The response- and nominal surveillance missions are represented by the red and blue lines respectively. The labels are associated with the blocks in Figure 5.2.

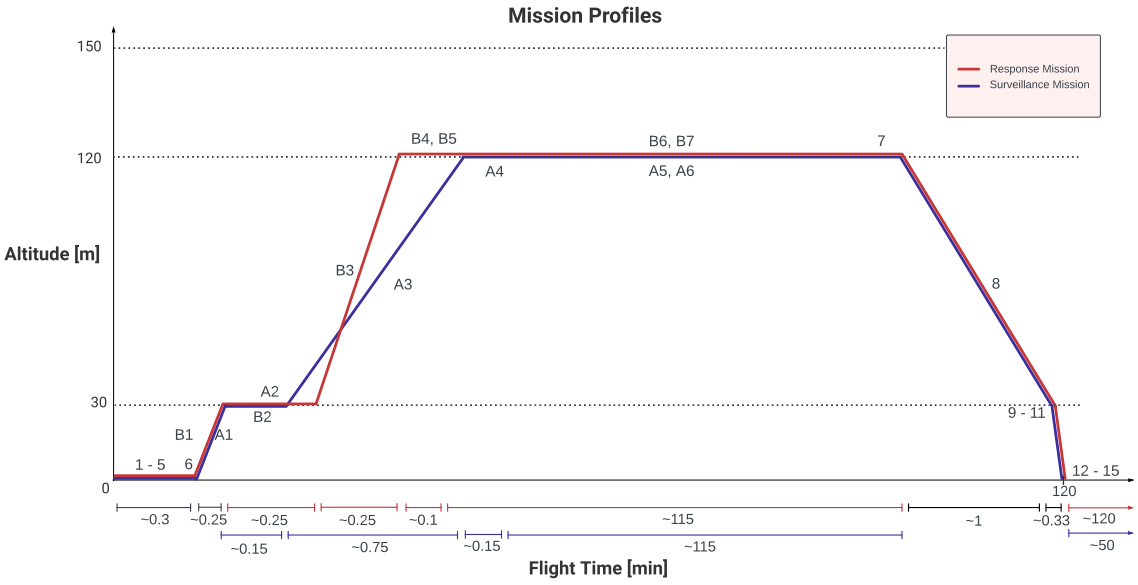

Figure 5.1: Mission profile for nominal surveillance mission (red) and response mission (blue).

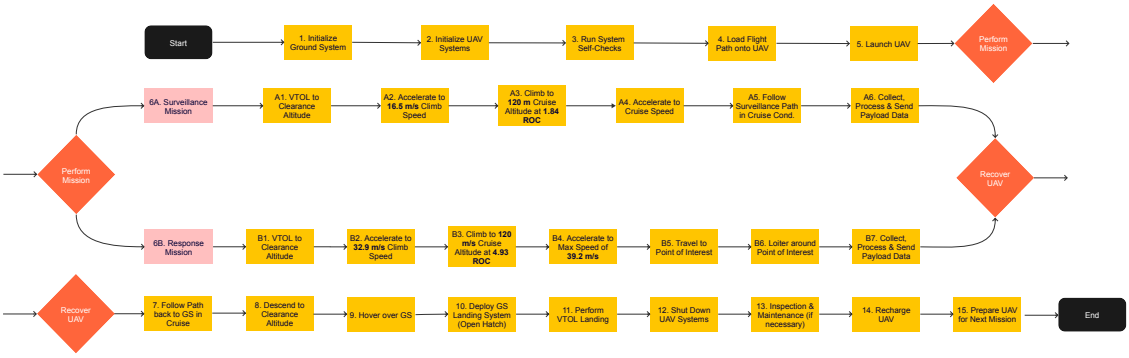

Figure 5.2: Operations Flow Diagram.

5.2. World Coverage

In Figure 5.3 a detailed map of the world coverage of the drone can be found. The black-coloured regions represent locations on earth incapable of operation. That is, the UAV cannot perform its operations in those regions. The operating area that was selected is based on annual average temperatures [1], on forestation [2], on elevation [3], normal solar irradiance and on mean wind speed [4]. The maximum and minimum temperatures are based on the operating condition of the drone. The hydrogen fuel cells are the most constrictive in terms of temperature; with an operating temperature of $-5°C$ to $40°C$. The elevation selected is based on the service ceiling of the design. The normal solar irradiance is described in subsection 5.6.1 The wind speed has been selected based on the minimum operating speed of the wind turbines for energy generation ($18\,km\,h^{-1}$ [5] and the maximum operating gust speed based on the gust loads: $32.76\,km\,h^{-1}$.

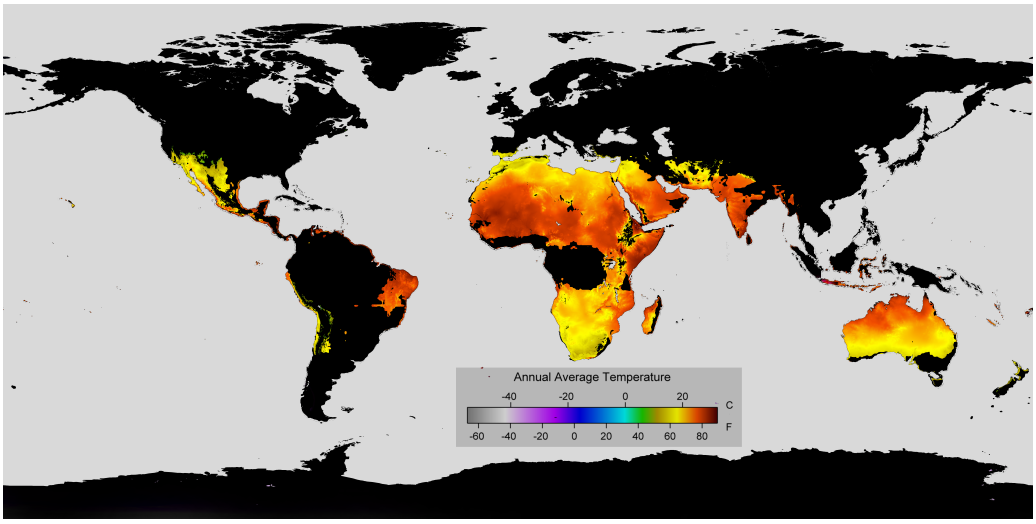

Figure 5.3: Map of Operating Regions on Earth. The black area represents the no-fly zones.

5.3. Grid Selection

In order to efficiently distribute the surveyed area it is important to select an area-efficient tiling system. Moreover, the grid selection also influences the response time in case of the detection of poachers as well as charging, communication and navigation considerations. There are three regular polygons suitable for the tiling of a grid. Namely, triangles, squares and hexagons. Assuming the GS is located at the centre of the tile squares result in large distances between the ground station and the outer points. Triangles suffer from the same problem. However, hexagons allow for the most area-efficient tiling of the surveillance area. Therefore, triangles conglomerated into a hexagonal shape and single hexagons are considered.

Each tile represents a surveillance area of $20\,km^2$, with the entire grid representing the total surveillance area of 50 km x 50 km. The grid options can be seen in Figure 5.4. It is essential to mention that in order to detect poachers the nearest drone will be deployed; that might be a drone already in operation, a drone on standby still at the ground station or a drone in an area of an adjacent GS; whichever drone is closer to the point of detection. Grid 1 uses a fully hexagonal setup with a ground station at the centre of each surveillance area and is optimized for limiting the deployment time to a maximum of two minutes (i.e. REQ-DEP-4). Using the time it takes for the drone to take off and land in addition to the maximum velocity and the distance to the outer edge of a tile, a response time of 1.86 min is estimated. This is considering the possibility of including a drone on standby as a way of ensuring surveillance and complying with the requirement to arrive at the location of poacher detection within 2 minutes. Grid 2 considers an operational setup of 6 triangles per ground station in the shape of a hexagon. In this setup, one GS covers 6 tiles of $20\,km^2$, significantly reducing the number of GS required from 132 to just 22. There will be two drones operative at each GS. They alternate in surveilling

[1] https://berkeleyearth.org/, accessed on 22-05-2023

[2] https://www.esa.int/Applications/Observing_the_Earth/Mapping_the_world_s_forests, accessed on 22-05-2023

[3] https://www.ncl.ucar.edu/Applications/topo.shtml, accessed on 24-05-2023

[4] Technical University of Denmark (DTU) - https://globalwindatlas.info, accessed on 24-05-2023

[5] https://www.daera-ni.gov.uk/articles/energy-wind, accessed on 24-05-2023

individual tiles and acting as a standby drone in case a poacher or wildfire alert is received. Finally, Grid 3 employs hexagon tiles just like Grid 1. However, instead of utilising a ground station in every tile, a ground station for every 3 tiles is considered. As described in the Midterm Report [2] this option was initially designed because Grid 2 couldn't comply with performing two surveillance missions on each tile per day. However, that has been resolved with the addition of an extra UAV to Grid 2 GSs. Thus the only reason to use Grid 3 is that the design is essentially a compromise between Grid 1 and 2 meet as it uses fewer resources than Grid 1 but more than Grid 2 and covers more area than Grid 1 and less than Grid 2. In case of maximum distance to the alert target location, the response time is calculated to be at 3.52 m.

All of these options allow for sufficient charging capacity for all drones and will be designed for accurate communication and navigation. In Table 5.1 more characteristics are mentioned. Solar panels are required to supply the ground station and drones with energy, although Grid 3 scores higher than both Grid 2 and Grid 1, it is important to note that although the ground station requires more power, it supplies power for up to 7 drones. Furthermore, the cost is estimated for the entire grid and the environmental impact is based on the number of ground stations needed, as more ground stations result in more disturbance of the local wildlife.

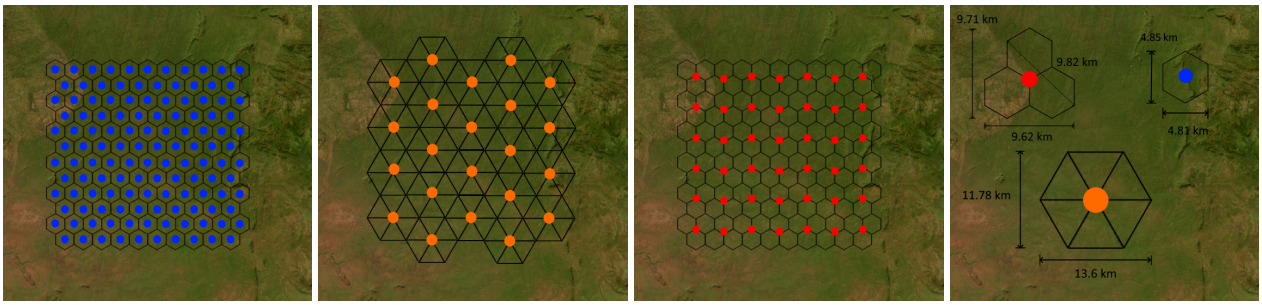

Figure 5.4: Honeycomb set-up with each ground station covering one area segment (1st fig., blue dots), 6 area segments (2nd fig., orange dots) and 3 area segments (3rd fig., blue dots). Each segment covers 30 km^2, and the total area covers 50 x 50 km. The right figure shows the dimensions of conglomerated areas for the three potential grid designs.

For the final design, the second grid has been chosen. As it reduces the number of ground stations to 22 while still providing sufficient response time, see Figure 5.5.

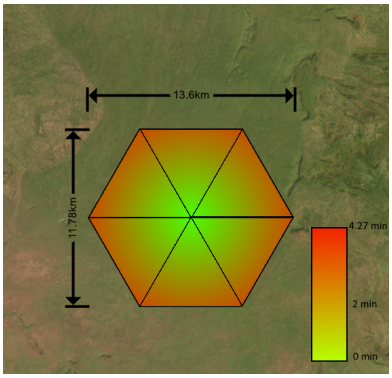

Figure 5.5: Compliance to REQ.DEP.4.

Table 5.1: Grid Characteristics.

Grid #	Response Time (Worst Case) [min]	Solar Panel Area Required [m2]	Environmental Impact (Number of GS needed to be installed)	Duty Cycle (2hr flights) %
Grid 1	1.86	13.53	132	5.54 (16.67)
Grid 2	4.27	17.08	22	33.24 (100)
Grid 3	3.52	22.4	49	16.62 (50)

5.4. Tile Area

REQ-GEN-2-1 states that each drone shall cover $20\,\text{km}^2$ of area per flight. Considering a camera field of view of $588\,\text{m}$ and assuming a perfect flight path, i.e. no area is covered more than once in the same flight, a total flight path of $34\,\text{km}$ needs to be traversed. The UAV must have an endurance of $150\,\text{km}$ according to REQ-GEN-11. Similarly, considering the cruise speed of $80\,\text{km}\,\text{h}^{-1}$ (REQ-GEN-10) surveillance time will amount to about $25.5\,\text{min}$ even though there is an endurance requirement of $2\,\text{h}$ (REQ-GEN-3). For a nominal mission where a UAV only has to cover one $20\,\text{km}^2$ area the UAV is significantly overdesigned in terms of endurance and range. However, these requirements are necessary for the case of a response mission where loitering around a target area for an extended period of time might be necessary. The seemingly low tile area of $20\,\text{km}^2$ is driven by the $2\,\text{min}$ deployment requirement (REQ-DEP-4), which is also needed for a response mission. Evidently, the two missions do not complement each other well regarding the UAV design. Although the aforementioned requirements do not prohibit the nominal mission from being performed, the mission is performed extremely inefficiently as much more energy than required is brought onboard. Also, considering that nominal missions will be performed much more frequently than response missions it seems sensible to adjust certain parameters to make the UAV perform more efficiently.

Essentially, the ranges and endurances required for the response and nominal missions need to be brought closer together. This can be done by decreasing the range and endurance of a response mission, however, this is undesirable as that would cause key requirements not to be met. Alternatively, the endurance and range of the nominal mission could be increased by increasing the area a UAV covers in a single flight. This would have two main implications for the mission. Firstly, an adverse effect would be the increase in deployment time. However, a beneficial consequence would be the further reduction in GSs necessary when a system needs to cover a large area. A balance between the two together with endurance/range must be struck to find an optimal configuration.

Table 5.2: Tile Surveillance Areas.

Area [km^2]	r_{cent} [km]	t_{req} [min]	No. of GS	d_{fp} [km]	t_{surv}[min]
20	6.50	3.36	21	34.01	25.51
25	7.30	3.70	17	42.52	31.89
30	8.03	4.00	14	51.02	38.27
35	8.70	4.29	12	59.52	44.64
50	10.45	5.04	9	85.03	63.78

Table 5.2 tabulates the results of an analysis performed to find an optimal area size. Note that Grid 3 is considered, i.e. a grid consisting of hexagonal conglomerated area, each consisting of 6 triangular tiles. The table shows r_{cent}, the maximum distance from the centre of a hexagon to the perimeter, t_{req}, the time it will take a UAV to arrive at a location located r_{cent} away from the centre, the No. of GSs per hexagonal area, the distance a UAV has to travel to cover a triangular tile (assuming a perfect flight path), and t_{surv}, the time to surveil a triangular tile. Based on the results, increasing the tile surveillance area to $30\,\text{km}^2$ was deemed to be the most balanced option. The number of ground stations decreases from 21 to only 14: using $20\,\text{km}^2$ tiles uses a staggering 50% more GSs. The range and endurance also increase by 50%, consequently, the energy and (battery) mass onboard are used much more efficiently. There is however an unwanted increase in max deployment time. This increases by $4.00 - 3.36 = 0.64$min or $38.4\,\text{sec}$, translating to an increase of 19%. However, considering the significant and desirable increase in area, range, endurance, and decrease in resources this was deemed to be acceptable. In Figure 5.6 an updated coverage area can be found. Relative to the using $20\,\text{km}^2$ tiles a loss of 11% is made in $2\,\text{min}$ coverage, a loss of 31% in $3\,\text{min}$ coverage but no loss in $4\,\text{min}$ coverage as the full area can be covered for both cases. The coverage of the revised grid can be found in Figure 5.7.

Table 5.3: Tile Surveillance Areas.

time	d [km]	$20\,\text{km}^2$	$25\,\text{km}^2$	$30\,\text{km}^2$	$35\,\text{km}^2$	$50\,\text{km}^2$
2 min	3.59	34%	27%	23%	19%	14%
3 min	5.95	93%	74%	62%	53%	37%

4 min	8.30	180%	144%	100%	92%	72%

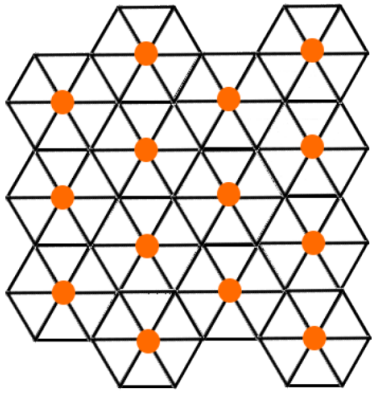

Figure 5.6: Revised Grid Design using a 30 km^2 Hexagon.

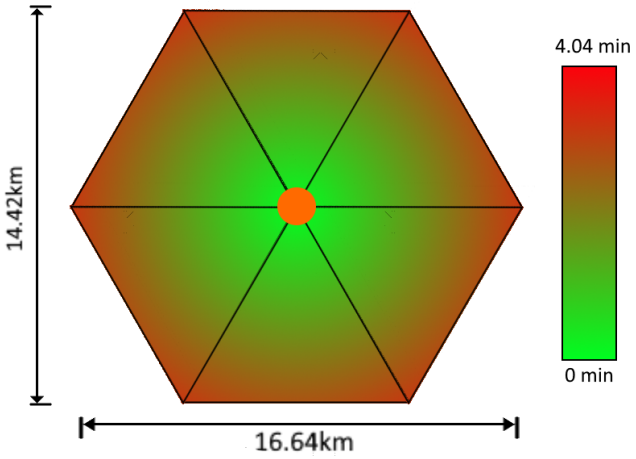

Figure 5.7: Coverage of Revised Grid.

5.5. Flight Pattern

The selection of an equilateral triangle leaves few options open for the flight path. A zigzag or spiral pattern is the most logical option. In the case where you need to return to the start location a zigzag makes more sense as it reduces the area that is covered twice. The zigzag pattern will leave one side of the equilateral triangle unscanned so that the UAV can scan that path on its way back to the ground station. Furthermore, the zigzag patterns were decided to start at the ground station so that the UAV spends most of its time near the far edge of the triangle. This makes the response to poacher detection faster as there are reserve UAVs at the ground station. The UAV in the air will handle the quick response on the far edge of the triangle and the UAV at the ground station will handle the quick response close to the ground station. The camera can identify faces at a maximum distance of 395 meters. Flying at this altitude means that the camera can only look straight down to identify poachers which is undesired. A more optimal approach would be to fly at the lowest altitude and use the camera gimbal to scan the ground more effectively. If the maximum camera range is used to determine the swath width of the ground track the scannable width equals 752 meters. The triangle however needs to be divided into an uneven amount of zigzag paths to ensure that the camera can make the return flight without rescanning an area. The optimum amount of zigzag passes in a single triangle is 9 passes which equals a swath width of 588.5 meters. The lower distance to the ground also allows for litter detection of objects smaller than

the human face which is preferable for detecting soda cans and such. Figure 5.8 shows six 20 km^2 areas, each area shall be scanned by one single aircraft in one single flight. The length of one flight path equals 35.6 km.

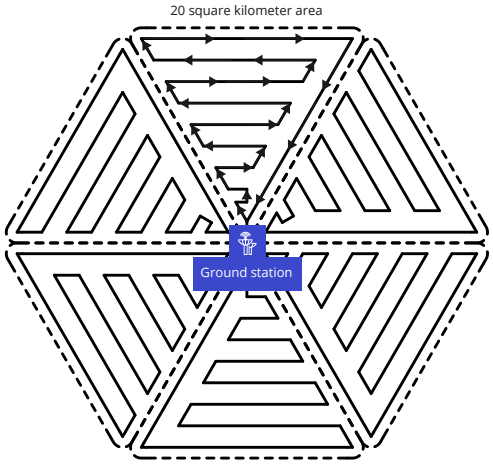

Figure 5.8: Surveillance flight path.

Orography will require a different flight path which will not meet the requirements. To perform orography a lower flight altitude of 60 m and a longer flight path of 239 km will be required. The orography of a single

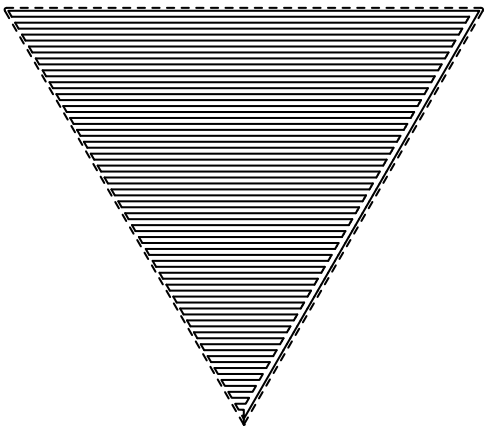

Figure 5.9: Orography flight path.

Finally, for response missions, the terrain's geometry should be considered when determining the fastest way to get to a destination. As an example, if the straight-line path has a large mountain in the way, but a small detour avoids climbing that large distance, it will be faster. Furthermore, (known) obstacles or terrain constraints may force the UAV to travel a path that is not a straight line. Literature for UAV path planning is often based on the R5DOS algorithm (an improved version of three-dimensional A-star) [3]. To the best of the author's knowledge, there is no open-source implementation of the R5DOS algorithm. As such, considering the limited time available for the design, the authors opted to perform a preliminary investigation into using the (very commonly used) a-star algorithm.

To generate a test environment, heightmap data was obtained from the European Union's Copernicus system[6]. From this, a patch of land showing interesting geometric features was selected, where the UAV starts in the top left corner - the case study (shown in Figure 5.10). The implementation of the algorithm starts by subdividing this height map into a discrete grid of 40 by 40 nodes, where each node is connected to its neighbour (there are no impassable objects in this example). This forms the graph to which the a-star algorithm will be applied.

[6] https://land.copernicus.eu/imagery-in-situ/eu-dem/eu-dem-v1.1, accessed on 15-06-2023

With the grid defined, a-star requires two functions to determine its best guess at the optimal path from the start to the destination. The first is a cost function that assigns a cost to move from a node to one of its neighbours. In this case study, it has been defined by Equation 5.1 (where HEIGHT_GAIN is a factor that penalizes gaining altitude). The second is the heuristic function, which estimates the cost from the current node to the destination. This function is simply defined as the distance between the current node and the targetted node.

$$g(a,b) = \sqrt{(a_x - b_x)^2 + (a_y - b_y)^2} + \begin{cases} (b_z - a_z) \times \text{HEIGHT\_GAIN} & b_z > a_z \\ 0 & \text{otherwise} \end{cases} \tag{5.1}$$

When this is all put together, the system can perform path planning as shown in Figure 5.10. It is worth noting that this algorithm is not yet optimal - it does not implement any form of smoothing or more advanced techniques, such as total energy optimization (where a gain in potential energy could be recuperated if the path eventually goes down). Nonetheless, this proof-of-concept shows that it is possible to perform path planning based on height maps which, for the proposed UAV would be originally obtained from satellites and then refined using LIDAR measurements taken during flight). Further development of the technique (or alternatively, implementing the aforementioned R5DOS algorithm) is strongly recommended for future iterations of the design that incorporate a more complete software suite.

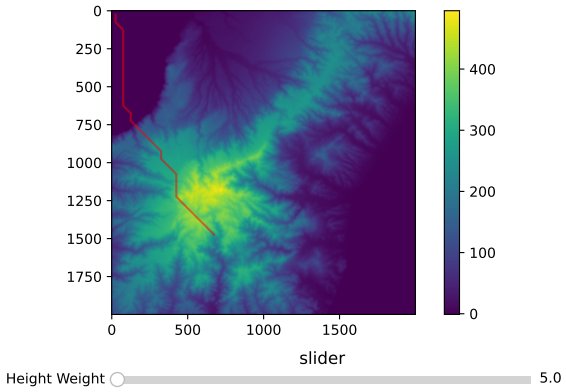

Figure 5.10: Case study with A-star being employed to avoid climbs.

5.6. Ground Station Design

The ground station of the UAV shall include several elements for the UAV to fulfil all its functions. All elements like the charging system, charging system protection, antennas, microphone and computer are discussed in this section.

The charging interface is discussed in subsection 5.7.2 and must be integrated into the ground station design. To do so effectively, the pads on which the UAV will land and charge will be slightly elevated to avoid the effect of rain and dust from the ground. For two UAVs per ground station, there must be two of these docking interfaces. These will be separated from each other so that one UAV will not damage the other in case of failure in landing.

To protect the charging dock and the UAV from animals and extreme weather circumstances, a shelter will be built around it with a roof cover that slides open during take-off and landing, called the DAWGhouse. There will be two of these placed for the two drones per ground station. In between, there will be a smaller structure that holds all relevant elements: the vehicle communication antenna, SATCOM, the battery, the microphone and the computer, as can be seen in Figure 5.11. The walls of the DAWGhouse will provide protection from surface gusts during the landing procedure and dust. Note that these walls will allow air to go through from the inside out to reduce the ground effect. In other words, there will be a one-way-in wall system in place for air ventilation. African elephants can reach heights up to 4 meters[7], which would require a wall height of 3

[7] https://www.elephantsforafrica.org/elephant-facts/

meters to keep these animals out, note that this also helps with shielding noise during VTOL. There will be 0.8 meters of clearance on each side of the UAV to avoid a clash with the walls. From the size of the UAV, stated in Section 7.4, it can be determined that the ground station would have the dimensions of 6 x 6 x 3 meters. Lastly, a fence will be placed around each ground station to protect the solar panels.

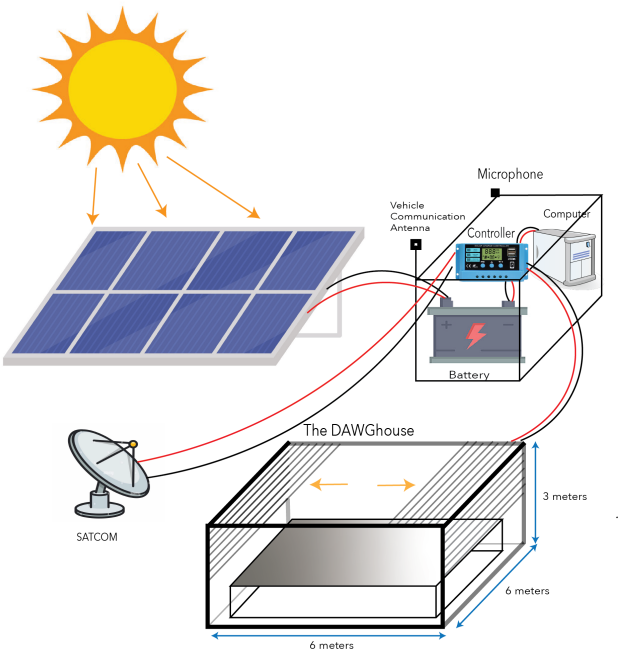

Figure 5.11: Ground Station Layout.

During take-off and landing, the roof of the ground station needs to open and close. Due to the response mission requirement, the door is required to open quickly. There is a limited amount of time for opening. The opening time is limited to 15 seconds as defined in subsection 5.7.2. The door should keep out any water, dust and animals. Next to that, the door should be made out of environmentally friendly material. This is achieved by installing a roller door, that can open fast.

As stated in Section 5.9 the antenna for the ground station is chosen. This element can be included in the ground station design to fulfil its communications functions. To achieve a good link between the antenna and the UAV, the ground station antenna should be elevated to avoid interference with nearby trees. This is done by mounting the antenna to a pole around which it can rotate. Next to the antenna, a microphone should also be mounted on a smaller pole so that poacher gunshots can be heard, as discussed in Section 5.8. It is important that the microphone will be mounted on top of the pole to again reduce interference. Finally, a satellite dish and antenna will be placed in this area to enable satellite communication between the ground station and the customer headquarters.

The raw data that comes in through the antenna should be converted to usable visual data and recorded. Therefore, a computer and data storage system should be in place on the ground station.

All these aspects combined together create the ground station as shown in Figure 5.12. This figure shows the central ground station with 11 solar panels and a Starlink internet connection.

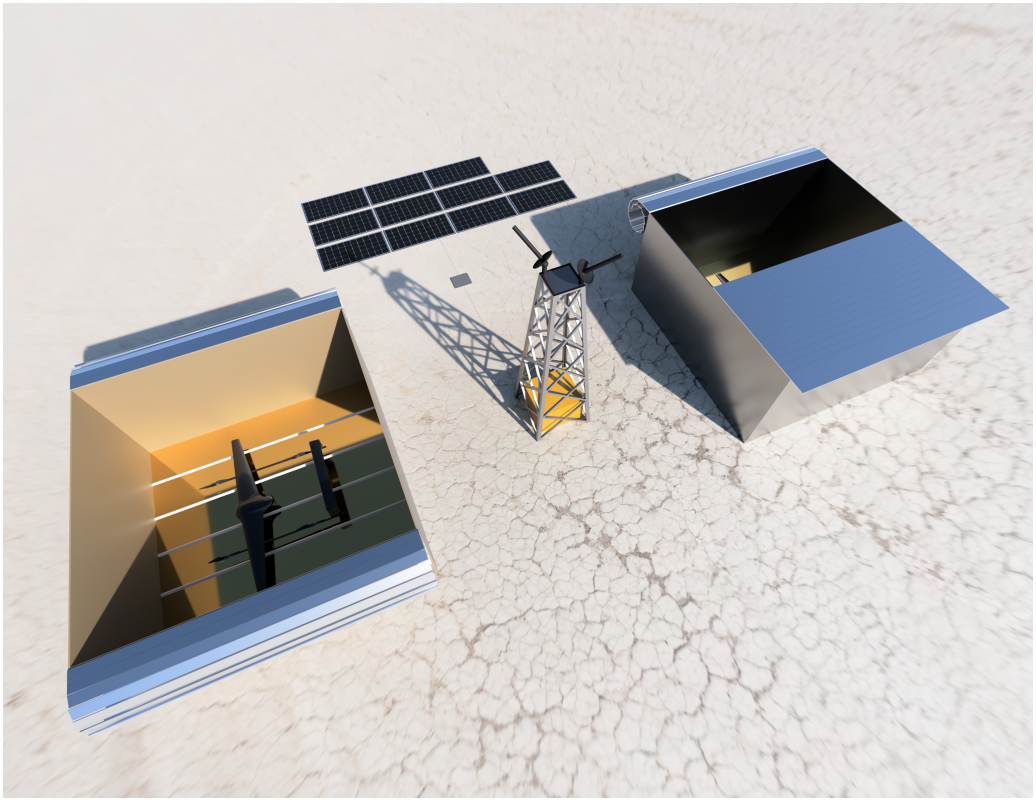

Figure 5.12: Ground Station.

5.6.1. Solar Panels

The entire ground station needs to be powered. This will be done by solar panels since this is the most effective emission-free method of power generation. Wind energy depends on the availability of wind and will introduce noise disturbances for the environment, while solar panels do not produce any noise. The method is also non-invasive, as there is no maintenance or control required for a long time. However, cleaning will be necessary on a regular basis. Fortunately, this is a process that could also be automated by using products such as Airtouch's AT 3.0 Robot[8]. It uses a combination of wind blowers and wipers to clean the solar panels, hence offering a water-free cleaning solution.

The required area for the solar panels and the required battery size is done below using the UAV and GS power budget of Section 14.2. For the UAV a total of 839.16 Wh is required per flight. For the GS a total of 664 W is needed and as the GS will be operational 24/7 this corresponds to a total energy of 15 936 Wh. There are two things to note however: firstly, only one central GS will have a Starlink and hence the remaining 13 will require 200 W less power. Secondly, although the GS will be operational 24/7 it will only be running at max power consumption during UAV flight missions which are only about 8 h per day, thus the solar panel estimation is very conservative. Furthermore, as mentioned in the Midterm Report [2], the solar panel sizing is done for a Global Horizontal Irradiation (GHI) level of $5\,\mathrm{kWh/m^2}$ per day[9]. The GHI is the amount of irradiation that hits a panel horizontal to the Earth's surface. It includes both Direct Normal Irradiation (DNI) and Diffuse Horizontal Irradiation (DHI), where DNI is the direct irradiation from the sun that hits a panel perpendicular and DHI is the diffuse irradiation that hits a panel that is horizontal to the Earth's surface[10]. GHI also takes into account the solar angle of incidence to adjust the DNI. Note that a GHI of $5\,\mathrm{kWh/m^2}$ is a relatively low average for Africa but high for regions far away from the equator. In practice, the solar panel area would need to be adjusted such that it is optimized for the system's local GHI. However, the $5\,\mathrm{kWh/m^2}$ covers most of Earth's land mass between 45 ° North and 45 ° South latitude[9] and hence suffices to make a global solar panel sizing estimation. Finally, solar panels have an efficiency of 22.7%. This leads to the following area of solar panels

[8] https://airtouchsolar.com/, accessed on 15/06/2023

[9] https://globalsolaratlas.info/map?c=-4.129477,32.252795,7&s=-2.15501,34.388073&m=site, accessed on 10/06/2023

[10] https://firstgreenconsulting.wordpress.com/2012/04/26/differentiate-between-the-dni-dhi-and-ghi/, accessed on 16/06/2023

required for the central GS:

$$A_{sp_1} = \frac{0.839kWh \cdot 12 + 0.664kW \cdot 24h}{5kWh/m^2 \cdot 22.7\%} = 27.47m^2$$

As such, 11 Jinko Solar Tiger Neo 565W solar panels (each having $2.58\,\mathrm{m}^2$ area) are required for the central GS. For the remaining 13 GS the following area is needed:

$$A_{sp_{13}} = \frac{0.839kWh \cdot 12 + (0.664 - 0.2)kW \cdot 24h}{5kWh/m^2 \cdot 22.7\%} = 22.40m^2$$

In this case, only 9 aforementioned solar panels are needed per GS.

The solar panels will charge the stationary GS battery which will power the rest of the GS and charge the UAVs. The battery will be placed in the middle section between the two charging stations underneath the antennas and the microphone. There will also be a controller element between the battery and solar panels that will cause the battery not to overcharge. This element is also placed in the middle structure. Finally, the solar panels are placed around the two stations.

5.7. Automatic Charging

Continuous use of the UAV requires it to be recharged. The charging system selection and general recharging strategy are thus detailed below.

5.7.1. Charging options

For the drone to operate entirely autonomously, it must charge on its own. This includes recognising when charging is needed, calculating how much energy is required to fly back with a margin, landing on the charging dock and initiating charging. Dependent on which charging method is chosen, the charging dock has to guide the drone to connect to the charging port in case there is one. The different methods looked at are wireless charging, docking station with a robot arm, and contact charging.

(a) Wireless UAV charging.[a].

[a] https://d1a2ot8agkqe8w.cloudfront.net/web/2019/05/global-energy-transmission-system_77305.jpg, accessed on 27-06-2023

(b) Robot arm for charging.[a].

[a] https://static.moniteurautomobile.be/clients/moniteur/content/medias/images/news/41000/600/50/638920.jpg, accessed on 27-06-2023

(c) Contact charging.[a].

[a] https://www.edronic.com/es/, accessed on 27-06-2023

Figure 5.13: Charging methods.

The optimal choice within these options is the method of contact charging due to several reasons. Wireless charging is the most inefficient way of energy transfer and a robot arm has many moving parts, making it less robust and reliable. As such, the batteries of the drone are charged through a cable inside the UAV that connects a small metal surface on the landing gear to the battery, shown in Figure 5.13c. However, in order to perform contact charging, the drone needs to be controllable with an accuracy equal to half the distance between the landing gear. If it is not possible to get such a high accuracy on control, a mechanical system on the docking station can be used to solve this problem as can be seen in Figure 5.14. This system can push the drone towards the charging strips by moving the outer blocks.

Figure 5.14: Mechanical Docking station.

5.7.2. Charging Operation & Strategy

The successful contact charging of the UAV is extremely dependent on the correct positioning of the UAV with respect to the contact pad. As such, a stepwise overview of the charging procedure, including the landing phase of the UAV, is developed:

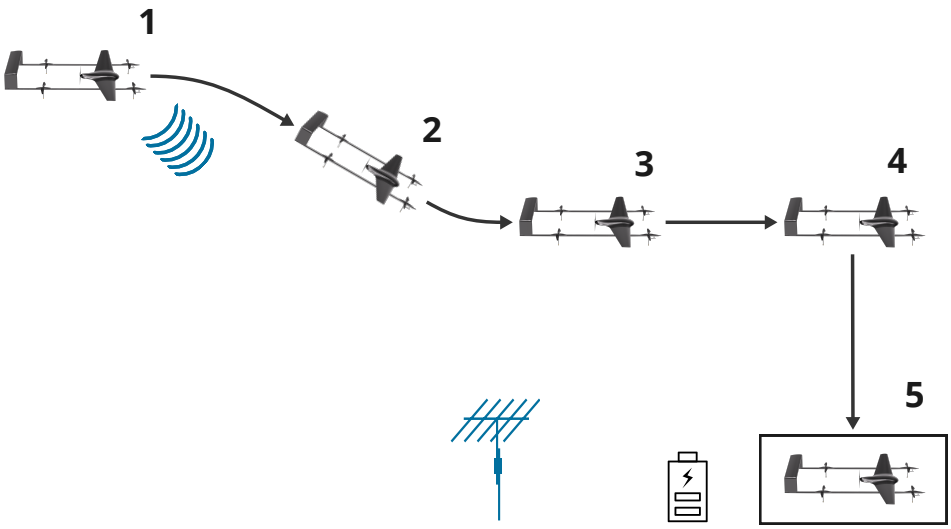

Figure 5.15: Charging Operation & Strategy.

1. **Alerting the ground station**
   When the UAV is within 500 meters of the ground station, a radio signal is sent out to the ground station, alerting it about the UAV's intention to land. This number is estimated based on the time it takes for the charging station covering to open. With an assumed opening time of 15 seconds and cruise speed of 22.22 m/s (80 km/h), this results in an alert distance of 330 m. To allow for contingency in case of unexpected events (e.g. sand is stuck in the motor-pulley system), an opening time of 25 seconds is assumed, resulting in 550 m. Note that this is just an estimate as the actual required alert distance is influenced by the contingency margin applied and decreasing velocity when descending.

2. **UAV descent**
   The VTOL motors on the UAV will take over the lift generation at an airspeed of roughly 10 m/s. At this airspeed, the angle of attack of the UAV equals 15 degrees. XFLR V5 could not give results for the lift coefficient past 15 degrees so unless more accurate estimates can be retrieved from a CFD analysis it is assumed that the wing experienced stall after this angle of attack, and it is deemed better to continue the descent procedure with the VTOL propellers.

3. **Initial attitude correction**
   To ensure better control of the landing, the UAV nose is then oriented in the direction of the wind. At this point, it is desired that the overall lift generated by the UAV is just enough to support its total weight, resulting

in the hovering of the UAV. The required decrease in the lift is then attained by altering the angle of attack of the wing by introducing a differential in the VTOL motor-generated thrust.

4. **Vertical landing**
   Once the UAV is hovering above the desired landing position, a vertical landing is initiated. As the entire UAV structure dips just below the top of the ground station house, at the height of 3 m, the UAV begins adjusting the UAV orientation around the vertical (landing) axis to ensure that each contact point of landing gear lands on the correct charging plate. This attitude adjustment is achieved by implementing a pattern of infrared LEDs, emitting electromagnetic waves of specified length, on the charging pad such that the UAV can lock on them and determine the needed orientation.

5. **Confirm landing**
   The landing of the drone can be confirmed using the LiDAR sensor. The distance between the bottom of the landing gear and the LiDAR sensor is known, the landing can therefore be verified if the expected distance to the ground is reached. Once the UAV has touched down it will send a small voltage to the brass plates to let the ground station know which pole is positive and which pole is negative. Once the ground station is aware of the negative and positive pole of the UAV battery charging system it will start the charging process.

5.7.3. Charging Performance

Each UAV is equipped with 2 lithium-ion ARES 6s 30Ah batteries as stated in Section 6.3. To assess the charging, it is important to estimate the relevant time metrics, namely the charge time of the battery. Firstly, the charge time calculation is straightforward and is found from the nominal capacity and safe charging current (30 Ah and 15 A respectively[11]):

$$t_{charge} = \frac{C_{nom}}{I_{charge}} = \frac{30}{15} = 2\,\text{h} \tag{5.2}$$

While the possible charging current goes up to 60 A, the maximum safe charging current as indicated by the manufacturer is 15 A. Nevertheless, the charging current can go above 15 A if urgently needed. One shall also note the battery will never need to be charged to full 100% capacity, so the charge time calculated is an upper limit rather than the exact requirement. It shall also be noted that the selected batteries have 300 charging cycles[12] (at 5C rate). In other words, each battery can go through 300 *complete* charge-discharge phases before its energy capacity decreases below 80%. Provided that the UAV will almost never need to perform the mission for the full duration, it can be estimated that the battery needs to be replaced roughly once per year.

5.7.4. Charging Surface Design

After considering many ground station charging pad designs (including two strips, similar to [4] and a grid array[13]) a combination of both was selected. It employs 4 tiles, as shown in Figure 5.16. These tiles can each be connected to nothing, the positive, or the negative terminal of the power source. The advantage of this approach over two strips is that it allows for more landing directions. At the same time, the limited number of panels (4) reduces the electronics and switching involved in the ground station. Finally, the large size of the tiles gives a fair bit of margin for slightly misaligned landings, both in terms of planar position and orientation.

Taking inspiration from [4], an ArUco marker[5] is placed in the centre of each ground station. Using the Jetson module and camera (carried as part of the payload), this marker allows for accurate positioning of the UAV relative to the ground station's centre. Centimetre-accuracy precision has been shown with these markers [6]. This makes them indispensable for reliable recharging performance.

[11] `https://www.t-drones.com/goods-1154-Ares+6S+30Ah.html`, accessed on 07-06-2023

[12] `https://www.t-drones.com/goods-1154-Ares+6S+30Ah.html`, accessed on 15-06-2023

[13] `https://www.skycharge.de/`, accessed on 14-06-2022

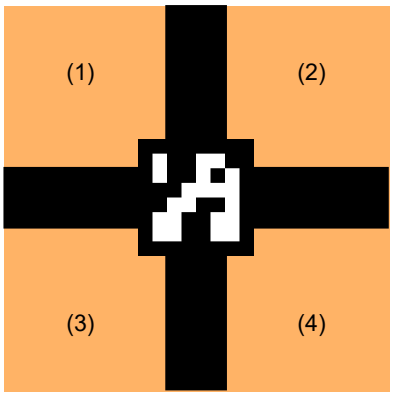

Figure 5.16: Sketch of charging pad (top view).

The UAV itself connects to the ground station using contacts in the landing legs. These contacts are spring-loaded pins to ensure a reliable connection even when small deformations pop up. This spring loading also allows for a better electrical connection, reducing the contact resistance (and thus waste heat produced). A more detailed design of the landing legs, containing these contact pins can be found later in this report.

5.8. Microphone selection

One of the main functions of the UAV is to detect poachers, which could also be done using microphones. By placing microphones in several locations, triangulation could be used to locate either a gunshot sound or the sound of the poacher's car. It is decided that the microphone will not be placed on the drone, as filtering out the noise from the propellers will be difficult. On the ground, there are several ways to place the microphones: they could be placed around the 50 km x 50 km perimeter to detect the sound coming from the car of the poacher, they could be placed within the whole perimeter at a distance and they could be placed only at the ground station.

There are several requirements for these microphones. According to **REQ-PM- INS-4-9**, the microphone shall be weatherproof, and according to **REQ-PM-INS- 4-3**, the microphone shall be able to detect where the gunshot is coming from. The microphones that are chosen are all omnidirectional so that sounds from every direction can be detected.

It is assumed that poachers usually use bigger rifles, that produce a sound of 153dB per shot from a 0.6m distance (148 dB from 1m)[14]. Furthermore, in order to get through the nature parks, it is likely that they utilize a car resembling a jeep, which produces 80 dB at a distance of 15 ft when driving 50 km/h (93 dB at 1 m distance), [15], with a frequency of 1600-4000 Hz. [16]. The background noise in the various locations that the drone will operate in, varies a lot depending on the different animal species, vegetation, and weather conditions. Assuming a background noise of 35 dB [17], it can be seen in Figure 5.17 that the sound of a car dies out at a distance of 794 m and the gunshot sound at $\sim$476 km. If a 10% margin is added for the microphone detection, a car can be detected by the microphone at a distance of 714.8646m whilst a gunshot can be detected at 428770.8 m.

Therefore, it is decided to place a round of MEMS microphones around the 50x50 km^2 perimeter in order to detect the car coming in from up close, whilst also placing microphones at the ground station to detect gunshots. MEMS microphones are chosen due to their low cost and small size. Furthermore, MEMS are omnidirectional and have low power usage. The VM1000 [18]is chosen, due to the weatherproof nature of this microphone. These microphones are placed at an interval of 714.86 m, resulting in 70 microphones per side, thus 280 microphones in total around the perimeter. Furthermore, each ground station will be equipped with a microphone. The distance between each ground station is 13.59 km and assuming that a gunshot can be detected from a 428.7 km distance, it should be more than sufficient. With 14 ground stations, there will be 301 microphones needed in

[14] http://recordinghacks.com/microphones/Telefunken-USA/AK47, accessed on 31/05/2023
[15] urlhttps://www.nonoise.org/resource/trans/highway/spnoise.htm
[16] https://www.scientific.net/AMM.307.196.pdf, accessed on 17-05-20223
[17] https://quietcommunities.org/nature-is-quiet/
[18] https://vespermems.com/products/vm1000/, accessed on 31/05/2023

total.

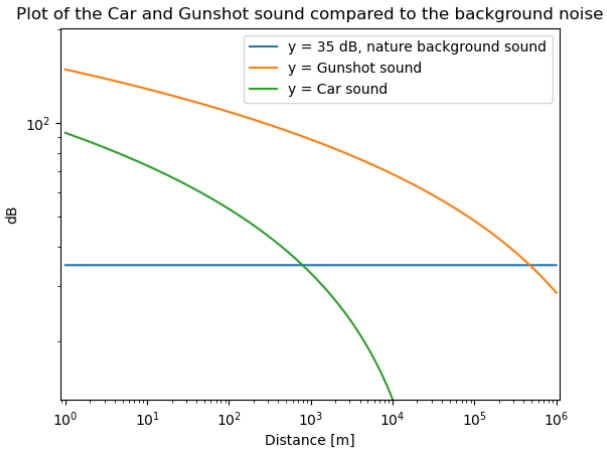

Figure 5.17: Car and Gunshot sound compared to the background noise, in a logarithmic scale.

5.9. Instrumentation Interface

To be successful in operations, the UAV should consist of several instruments that fulfil different functions. In the midterm report, the selection for the optical camera and LiDAR were already made by trade-off [2]. These resulted in the Trillium HD40-LV and the Velodyne Puck Hi-Res. However, this LiDAR product has a maximum range of 100 m. After some consideration, it was decided that the Velodyne Ultra Puck with a range of 200 m is much more compatible with the project UAV. Therefore, this LiDAR was chosen instead.

Next to that, other instrumentation elements should be selected. For example, a functional and commercially available guidance and navigation system can be selected. Note that in this report, a guidance, navigation and control system will be developed. The commercially available system is chosen such that it is able to do more than necessary as a worst-case estimation. The Veronte Autopilot 1x is a versatile system that can do positioning, navigation and control. It can also be used for, for example, camera control and obstacle avoidance. Therefore this system is considered more than capable for UAV purposes.

Another system is the computer and communication subsystems. The computer subsystem selection was based on computing and AI capabilities. The required computing rate depends on the data rate that the UAV instrumentation provides. The selected optical camera has a 720p HD resolution with H.264 encoding. If an ultra-high bit rate is used, this results in a data rate of $8\,\mathrm{MB\,s^{-1}}$ [19]. The used LiDAR outputs a data rate of $1.8\,\mathrm{MB\,s^{-1}}$, which follows from the frame rate and frame size [20]. With this value and the AI capabilities, the selected processor will be the NVIDIA Jetson Orin NX 16gb. This processor is more than capable of performing the necessary conversions and computations for control and navigation. The processor transfer rate, frequency band and maximum mission distance will define the required UAV antenna specifications. The maximum distance between the ground station and UAV is 6.27 km, as shown in Chapter 5. After some investigation, the SwarmLink MPSL2200 is seen as a great option for the UAV antenna. With the antenna being omnidirectional and having a bandwidth of 2200 MHz to 2500 MHz and a gain of 4 dBi it will be capable of transferring data to the ground system.

To prove the validity of the link between the ground system and the UAV, a link budget should be generated. This can be done via Equation 5.3[21].

$$P_r = P_t + G_t - L_t - FSPL - L_m + G_r - L_r \tag{5.3}$$

The loss due to the transmitter, receiver and miscellaneous losses are considered negligible. To account for this, the gain of the receiver is assumed to be equal to zero. The free space loss can be calculated by Equation 5.4[22]

[19] https://www.videoproc.com/media-converter/bitrate-setting-for-h264.htm

[20] https://autonomoustuff.com/lidar-chart

[21] https://en.wikipedia.org/wiki/Link_budget

[22] https://en.wikipedia.org/wiki/Link_budget

with the frequency and distance in MHz and km respectively.

$$FSPL = 32.45 + 20\log_{10}(f) + 20\log_{10}(d) \tag{5.4}$$

The biggest free space loss will occur at a frequency of 2500 MHz and a distance of 6.80 km. This results in a loss of 117 dB. Using the transmitter power and gain, available from the antenna specifications[23], which are 50 W or 47 dB and 4 dBi respectively, the received power can be computed. This results in a power received of -66 dB. To establish a useful link, the ground station antenna should have a receiver sensitivity which is lower in value. For direct cellular link, this is easily achievable, since the sensitivity can go up to -120 dB[24]. Therefore, this antenna is a use-able element for the project UAV.

From this conclusion, a ground station antenna can be selected as well. For this, a pointing antenna with a sufficient range should be chosen. The AH-1726-16 (EXTENDED RANGE CIRCULAR POLARIZED LHCP/RHCP HELICAL ANTENNA) from Antenna Experts is selected. This antenna complies with all mission requirements.

Having defined the operational and logistical workings of the surveillance system as explained in this chapter, diagrams can be generated summarizing the interrelations between and inside the UAV, the ground system, and other external factors.

5.9.1. Software Block Diagram

A software diagram is used to depict the main software components of the UAV and their interconnections. The software mainly ensures proper application of the designed system by handling data processing and generating flight paths. The software diagram can be found in Figure 5.18.

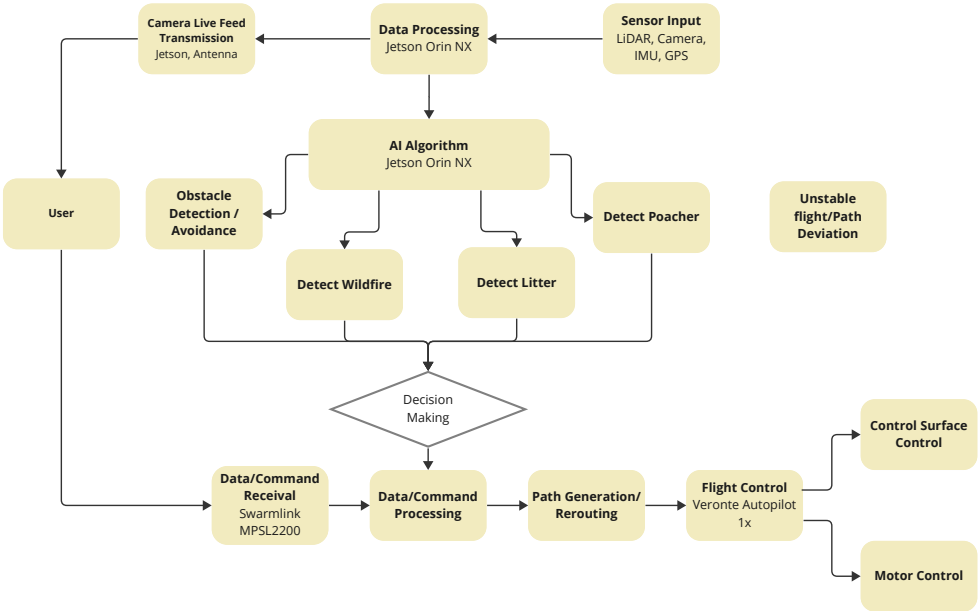

Figure 5.18: Software block diagram.

5.9.2. Hardware Block Diagram

The hardware block diagram from Figure 5.19 shows the interdependencies between all system hardware elements, where the off-the-shelf components are included where applicable. For clarification purposes, the hardware elements shown in the diagram are assigned different colours to indicate what main system components the elements relate to, as can be seen from the included legend. hardware elements can belong to data handling, battery, antenna, instrumentation and sensors, and flight control. Furthermore, the direct connections are shown as continuous-lined arrows, while wireless connections are displayed using dash-lined arrows.

[23] https://www.mpantenna.com/downloads/MPSL2200%20Model%20Data.pdf

[24] https://www.everythingrf.com/community/what-is-receiver-sensitivity

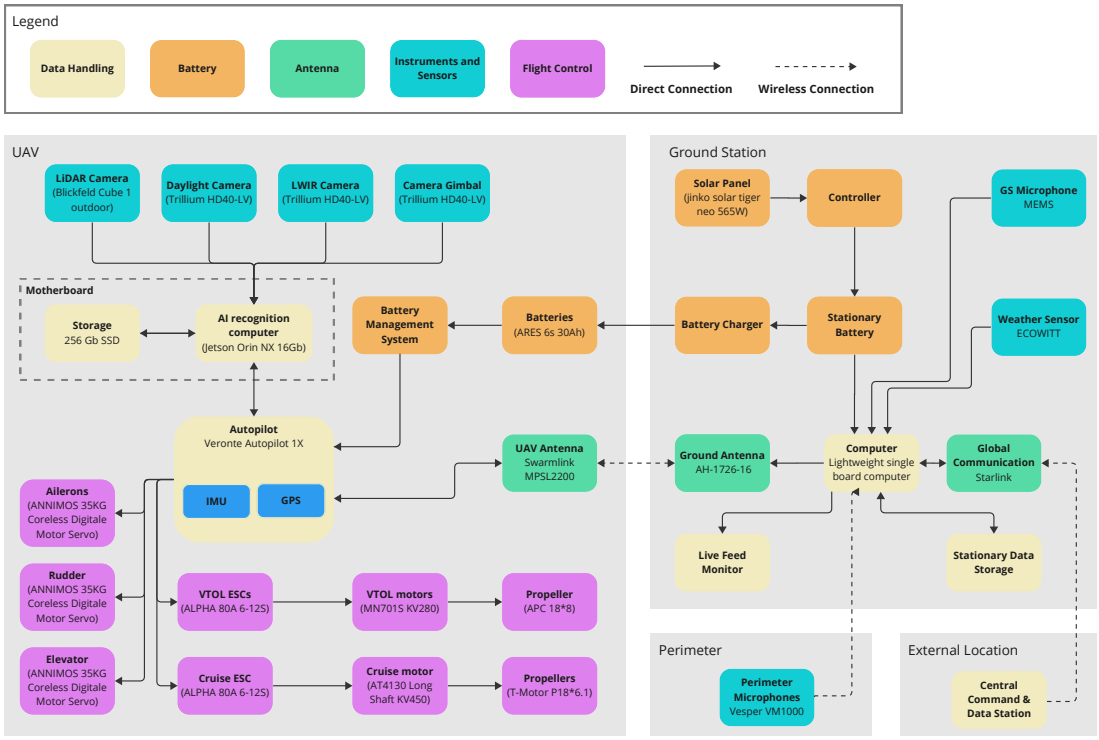

Figure 5.19: Hardware block diagram. Figure legend is included.

5.9.3. Communications Flow Diagram

The communication between subsystems can be presented in a flow diagram. This will give a clear overview of the data flow of the entire system. The diagram can be found in Figure 5.20. Note that the data rate output of every subsystem is given in the diagram as well. The data rate of the cameras, processor and antennas can be found or calculated. The remaining data rates are estimated by comparing them to similar operations. These are also considered insignificant compared to the data rate required for the visuals and processed data.

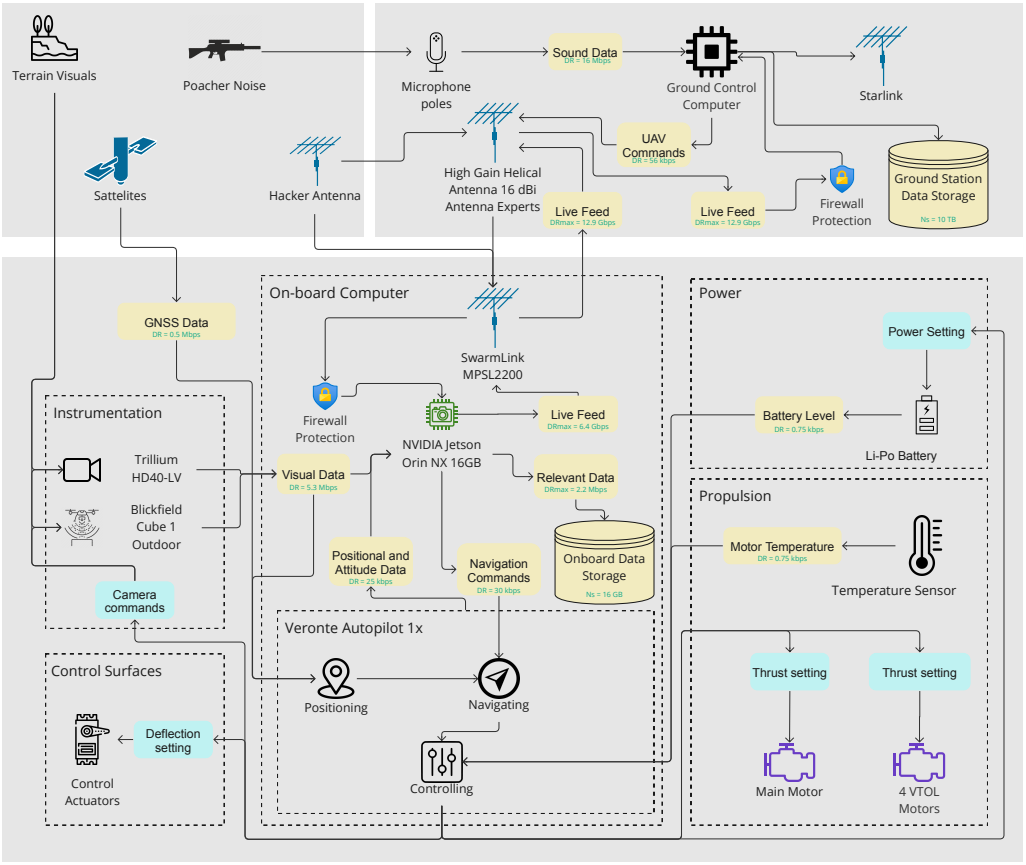

Figure 5.20: The communications flow/data handling diagram of the wildlife surveillance system.

5.9.4. Electrical Block Diagram

The components used onboard the UAV shall be clearly connected with each other to ensure the smooth operation of the UAV. The Veronte autopilot 1X is the brain of the UAV and will be the communication interface with the ground station. The Jetson Orin has the capability to analyze the footage and identify poachers during the day and at night. A live video will be streamed to the ground station but the footage analysis of the Trillium camera and Blickfeld LiDAR will be performed onboard the UAV. The footage is stored on internal storage in the case of a malfunctioning data link to be reviewed when the UAV has landed. The autopilot mentioned earlier is also responsible for controlling the VTOL ESCs during take-off, controlling the cruise ESC during horizontal flight and controlling the servos connected to the control surfaces. To perform these actions, inputs are required such as static and dynamic pressure from the pitot tube, ground station communications from the Swarmlink antenna, GPS data from the GPS antenna and visual input from the Jetson Orin. The connections between all electrical UAV components are shown in Figure 5.21. The colours of the connections differ to further clarify the type of data or power link between components and the autopilot.

The block diagram also contains servo motors to allow for control surfaces movement, namely elevator, ailerons and rudders. To begin with, the lift each control surface experiences is assumed to act at a quarter chord point (0.25c) and experiences a C_{L_max} of 1.2. With the relevant elevator, aileron and rudder areas and chord lengths provided in subsection 7.10.1, the lifts generated can be calculated. Starting with the elevator,

$$L_e = C_{L_{max_e}} \cdot \frac{1}{2}\rho V_{cruise}^2 \cdot S_e = 39.19\,\mathrm{N} \tag{5.5}$$

Following this, the hinge moment can be calculated:

$$M_e = L_e \cdot 0.25 c_e = 0.88\,\mathrm{Nm} \tag{5.6}$$

An analogous method can be used for aileron:

$$L_a = C_{L_{max_a}} \cdot \frac{1}{2}\rho V_{cruise}^2 \cdot S_a = 12.7\,\mathrm{N} \tag{5.7}$$

Again, the hinge moment can be calculated:

$$M_a = L_a \cdot 0.25c_a = 0.22\,\text{Nm} \tag{5.8}$$

Finally for the rudder,

$$L_r = C_{L_{max_r}} \cdot \frac{1}{2}\rho V_{cruise}^2 \cdot S_r = 12.34\,\text{N} \tag{5.9}$$

Again, the hinge moment (experienced by a single rudder) can be calculated:

$$M_r = L_r \cdot 0.25c_r = 0.43\,\text{Nm} \tag{5.10}$$

As such, the chosen servos shall be able to provide at least $0.88\,\text{Nm}$ or $8.97\,\text{kgcm}$ of torque while maintaining a relatively low weight and dimensions. One must note that the twin-boom UAV contains two rudders and two ailerons. While each of the ailerons requires an individual servo, both rudders can be controlled using a single one (this is a result of both rudders, contrary to ailerons, always moving in the same direction). Thus, a single DS Servo DS3235 servo, providing $35\,\text{kg cm}$ @ $5\,\text{V}$ and weighing $60\,\text{g}$ is selected[25]. Overall, 4 servo motors are used, resulting in an additional weight of 240g. In case of a slight moment increase, the servo motor should still be sufficient as it can provide up to $35\,\text{kgcm}$ of torque @ $7.4\,\text{V}$. On the electrical board, the servo is connected to the autopilot module (Veronte Autopilot 1X).

Provided all the information above, the electrical block diagram is presented:

[25] https://github.com/microrobotics/DS3235-270/blob/master/DS3235-270_datasheet.pdf, accessed on 20-06-2023

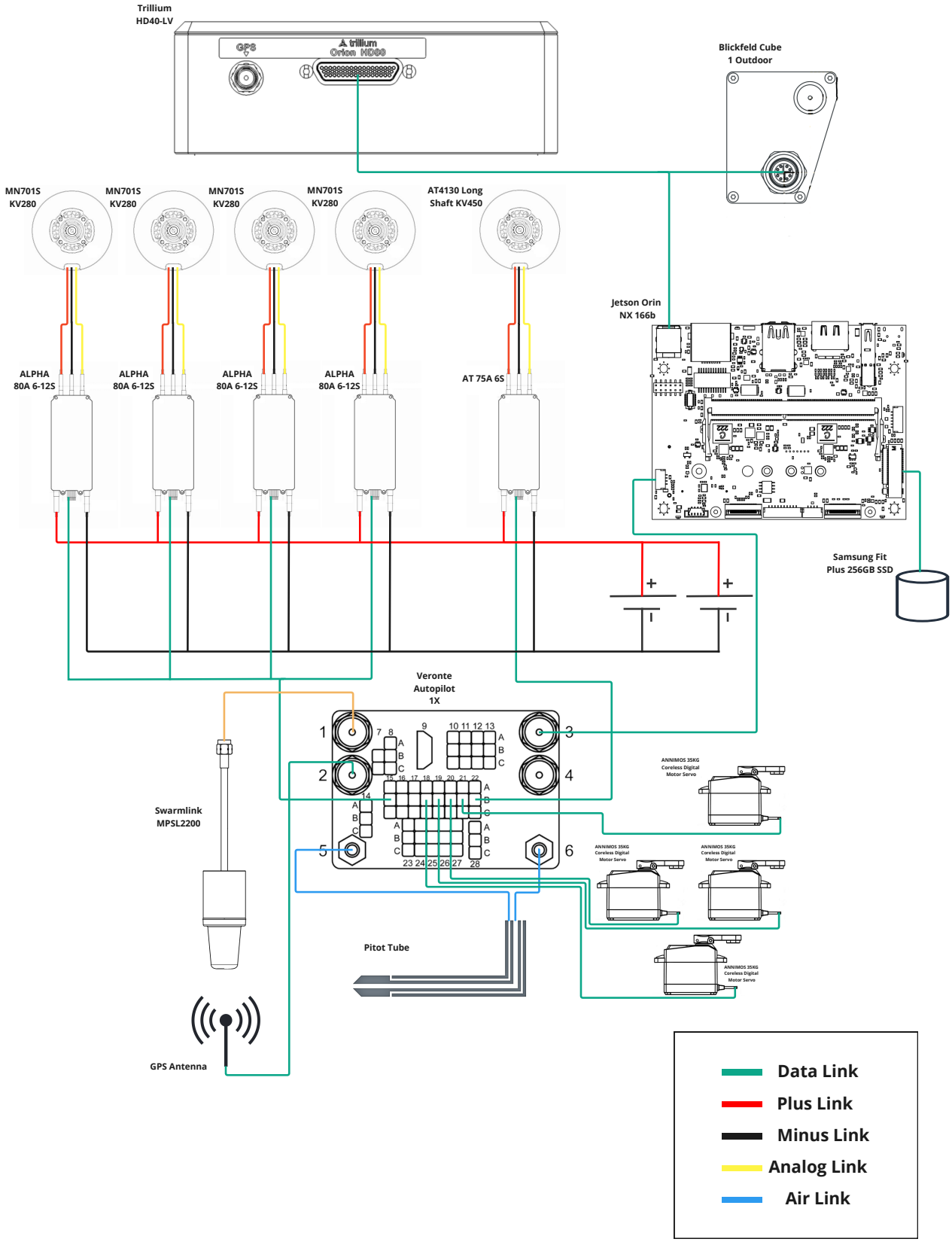

Figure 5.21: Electrical Block Diagram.

Chapter 6: Power & Propulsion System

The propulsion system comprises a single horizontal pushing propeller and four VTOL propellers. The required thrust is calculated for each propeller. Afterwards, off-the-shelve motors, propellers and ESCs are chosen to fulfil the thrust requirement. The power and energy requirements of the chosen motors and the onboard instrumentation are then used to determine the most optimal battery pack as a power supply. This process is iterated in order to find the most optimal solution.

6.1. Pushing Propeller

The pushing propeller will provide the UAV with thrust during climb and horizontal flight. As cruise flight is the most important part of the mission, the motor and propeller choice will be optimised for this situation. The cruise velocity is set at the minimum requirement of $80\ \frac{\text{km}}{\text{h}}$. The wing span is $3.2\ \text{m}^2$, as is described in Chapter 7. The drag coefficient for cruise, $C_{D_{\text{cruise}}}$, is determined to be 0.0267. The latter was found by performing a lattice vortex analysis of the UAV in OpenVSP as is described in Section 7.8. The required thrust during cruise can then be calculated by using Equation 6.1, where ISA sea level conditions are assumed.

$$T_{\text{cruise}} = C_{D_{\text{cruise}}} \frac{1}{2} \rho V^2 S \tag{6.1}$$

It is determined that $10.09\ \text{N}$ of thrust is required during cruise flight. From here, an iterative process started in which the most optimal off-the-shelf motors with propellers are identified. These have a datasheet that shows how much thrust is created for a specific supply of power. This thrust, however, is measured in static conditions. It is known that the thrust decreases with increasing velocity, therefore the selected motors and propellers are tested in JavaProp[1]. This software uses blade element theory in order to find the thrust output of a propeller and motor at cruise velocity. For most propellers, it was found that the lower the throttle level, the higher the propulsive efficiency. Thus the final propeller was chosen to operate at low throttle levels during cruise flight. This process contains a lot of trial-and-error with different motors and propellers. It was found that the most optimal motor is the *AT4130 Long Shaft KV450* by T-Motors combined with APC's *18*8 propeller*, the thrust vs velocity curve is displayed in Figure 6.1. The motor and propeller are depicted in Figure 6.3. Finally, the *AT 75A 6S* was chosen as ESC for the pushing propeller, this ESC is designed to work with a 6s battery and has an integrated UBEC for lower logic voltage.

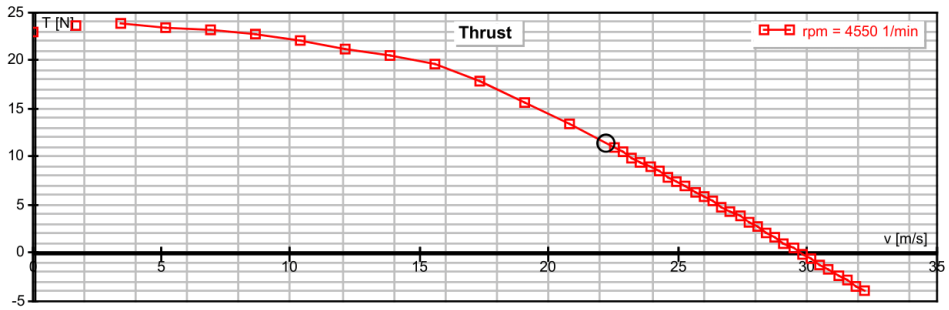

Figure 6.1: The thrust provided by the pushing propeller at 4550 rpm and 374 W as a function of the UAV's velocity.

[1] https://www.mh-aerotools.de/airfoils/javaprop.htm, accessed on 13-06-2023

(a) AT4130 Long Shaft KV450 produced by T-motor.[a]

[a] https://store.tmotor.com/goods-828-AT4130+Long+Shaft.html, accessed on 13-06-2023

(b) 18*8 propeller produced by APC.[a]

[a] https://www.apcprop.com/product/18x8/, accessed on 13-06-2023

(c) AT 75A 6S ESC.[a]

[a] https://store.tmotor.com/goods-904-AT+75A+6S.html, accessed on 21-06-2023

Figure 6.2: Selected push motor, propeller and ESC.

6.1.1. Rate of Climb

The rate of climb (ROC) is calculated and optimised for both the nominal and response mission. To simplify the climbing procedure (excluding VTOL), it was decided to split it up into three phases: acceleration to climb speed (at a constant 30 m clearance altitude, which is reached through VTOL), climbing to cruise altitude (at constant climb speed) and acceleration to cruise speed (at a constant 120 m cruise altitude). For the response mission, a climb condition has to be found such that the climb velocity is maximal (to minimise deployment time) while simultaneously maintaining a high ROC to minimise noise disturbance and to reach cruising altitude as quickly as possible so that the UAV can accelerate to max velocity. ROC can be calculated as follows

$$ROC = V \sin\gamma = \frac{(T - D)V}{W} \tag{6.2}$$

JavaProp was utilised to obtain data that relates velocity to thrust for a specific RPM and power/throttle (100%) setting which was obtained through motor data of the *AT4130 Long Shaft KV450*. For a certain input velocity, OpenVSP could then be used to find a lift and drag coefficient such that enough lift is produced. Combining this data lead to a ROC of $4.93\,\mathrm{m/s}$ at a total velocity of $32.9\,\mathrm{m/s}$. Note that the maximum ROC was actually $5.41\,\mathrm{m/s}$ but at a total velocity of $27.4\,\mathrm{m/s}$, which would cause the maximum deployment time to exceed 4 minutes. Increasing the total velocity to more than $32.9\,\mathrm{m/s}$ is also undesirable as the ROC decreases quickly due to drag increasing with the square of the velocity.

For climb during a nominal mission, a higher throttle setting is needed than during cruise as the excess power available is very low, even when flying at speeds lower than cruise velocity. The throttle of the push propeller is thus temporarily increased from 47% to 65%. At this throttle level a maximum ROC of $1.84\,\mathrm{m/s}$ can be obtained at a total velocity of $16.5\,\mathrm{m/s}$. Increasing the throttle even further will lead to a higher ROC but it was deemed unnecessary for a nominal mission as an efficient use of energy is desired. In Table 6.1 durations and horizontal distance travelled of the three phases of the climb procedure are tabulated for both the response and nominal mission. Table 6.2 shows several defining climb parameters for both missions. Note that the angle of attack for the response mission is negative, this is due to the high efficiency of the wing. As the lift increases with the square of velocity, the lift is very high during the response mission, hence requiring a slightly negative angle of attack.

Table 6.1: Response time and distances during transition, climb and acceleration.

	Acceleration to V_{climb}		Climb		Acceleration to V_{cruise}		Total		
	t [s]	d [m]	t [s]	d [m]	t [s]	d [m]	t [s]	d [m]	v_avg
Response	13.6	249.0	18.2	593.3	6.3	232.1	38.2	1074.4	28.1
Nominal	10.4	94.3	48.9	801.1	9.8	196.0	69.0	1091.4	15.8

Table 6.2: Flight parameters during climb.

	C_{L}	C_{D}	α [deg]	ROC [m/s]	γ [deg]	V_{climb} [m/s]
Response	0.18	0.020	-0.68	4.93	8.63	32.9
Nominal	0.71	0.046	4.9	1.84	6.41	16.5

6.2. VTOL Propellers

The four VTOL propellers will have to be capable of lifting up the UAV at a rate of climb of $3\,\frac{\mathrm{m}}{\mathrm{s}}$. There can also be a downwind during takeoff, and extra power is needed for controllability against side winds or when manoeuvring around obstacles. These extra thrust requirements are taken into account by having the UAV be able to resist downdrafts of $3.5\,\frac{\mathrm{m}}{\mathrm{s}}$, resulting in a total vertical velocity of $6.5\,\frac{\mathrm{m}}{\mathrm{s}}$ which is denoted as V_{to}. Flat plate theory can be used in order to calculate the drag during takeoff. The drag coefficient during takeoff, $C_{\mathrm{D_{to}}}$ is computed by using Equation 6.3 where the angle of attack, α, is $90°$. This results in a $\mathrm{C_D}$ value of 2.

$$C_{\mathrm{D_{to}}} = 2sin(\alpha)^2 \tag{6.3}$$

The total thrust that needs to be provided by the VTOL propellers needs to be higher than the addition of the UAV's weight and the drag during takeoff. The UAV's weight is $147.35\,\mathrm{N}$ and the drag is calculated using Equation 6.1. The only difference is the addition of a projected area ratio, denoted as $\frac{S_{\mathrm{proj}}}{S}$, which is multiplied by the wing area in order to estimate the total projected area. This ratio is equal to 1.46, which is the same area ratio as the Aerosonde HQ, a very similar UAV. This number is taken from the VTOL sizing by Arexy Monterroso.[7]

$$T_{\mathrm{VTOL}} = W + C_{\mathrm{D_{to}}} \frac{1}{2} \rho V_{\mathrm{to}}^2 S \frac{S_{\mathrm{proj}}}{S} \tag{6.4}$$

Equation 6.4 results in a thrust requirement of $230.635\,\mathrm{N}$. This thrust will be provided by 4 VTOL propellers, meaning that each propeller needs to provide $57.66\,\mathrm{N}$ at a velocity of $6.5\,\frac{\mathrm{m}}{\mathrm{s}}$. The same methodology for motor and propeller selection as in Section 6.1 is used. It was found that the most optimal motors for vertical takeoff are the *MN701S KV280* with *G26*8.5* CFRP propellers both produced by T-Motor. To operate the *ALPHA 80A 6-12s* was chosen as ESC. It works with 6s batteries and has the option to regenerate power when braking. The whole VTOL system is depicted in Figure 6.2.

(a) MN701-S KV280 produced by T-motor.[a]

(b) G26*8.5 T-motor CFRP propeller for VTOL.[a]

(c) ALPHA 80A 12S ESC.[a]

[a] https://store.tmotor.com/goods-473-MN701-S+KV280+-+2PCSSET.html, accessed on 21-06-2023

[a] https://store.tmotor.com/goods-407-G26%2A85+Prop-2PCSPAIR.html, accessed on 21-06-2023

[a] https://store.tmotor.com/goods-584-ALPHA+80A+12S.html, accessed on 13-06-2023

Figure 6.3: Selected VTOL motor, propeller and ESC.

6.3. Battery Selection

With the power required for VTOL and cruise a crude estimate can be made on the required battery size for a 2-hour mission. For the mission, a $1.33\,\mathrm{min}$ VTOL duration and a $1.97\,\mathrm{hour}$ cruise duration is assumed. The power required during these phases is $6267\,\mathrm{W}$ and $589\,\mathrm{W}$ respectively. Multiplying the duration with the power usage and adding the values up for VTOL and cruise suggests that a battery capacity of $1300\,\mathrm{Wh}$ is required.

Two ARES 6s 30Ah batteries, Figure 6.4 will provide sufficient current voltage and power for the mission duration of 2 hours.

(a) ARES 6s 30Ah battery

TECHNISCHE PARAMETER	
Name/Parameter	6S*30000mAh
Nominal Voltage	22.2V
Operating Voltage	25.2~16.8V
Capacity	30000mAh
Size	210*90*68mm(max)
Weight	2570g(max)
Energy Density	259.1Wh/kg
Charging Current	60A(max)
Continuous Discharge	150A(max)
Charging Temperature	0~45°C
Discharge Temperature(5C)	-20~45°C
Charging cycle(5C)	300

(b) Technical data of ARES 6s 30Ah[1]

Figure 6.4: Selected battery & its technical parameters

The battery has a relatively high energy density of 259.1 Wh/kg and mass of 2.57 kg[1], the energy provided by a single battery is 665.887 Wh. As this does not satisfy the energy requirement just yet, two batteries need to be implemented, resulting in an energy capacity of 1331.77Wh. As such, the batteries comprise $\frac{5.14}{15.02} = 34.22\%$ of total UAV weight.

[1] https://www.t-drones.com/goods-1154-Ares+6S+30Ah.html

Chapter 7: Aerodynamic Design and Analysis

The aerodynamic properties of the UAV are important to every stage of further design. Therefore the lifting and control surfaces need to be designed and sized. Finally, the aerodynamic properties are determined by performing a final vortex lattice method (VLM) analysis using OpenVSP. In Section 7.1 a trade-off for the wing configuration is performed and Section 7.3 shows the UAVs load diagrams. Section 7.4 describes the sizing of the main wing and the tail is sized in Section 7.5. Section 7.8 discusses the flight configurations for different mission phases and the force distributions are shown in Section 7.9. Finally, the control surfaces are sized in Section 7.10 and the aerodynamic coefficients used for stability are shown in Section 7.11.

7.1. Wing Configuration Trade-off

In order to decide the main wing position, a trade-off is performed between the low-wing, high-wing, and a wing-blended body with a mid-wing. The decision on the configuration of the wing will have an effect on many aspects of the aircraft like stability, drag, and more. The main criteria that the wing configuration is based on are shown in Table 7.1. Due to the high requirements on endurance and range, the focus is placed on finding the least drag possible whilst maintaining a light structure.

Table 7.1: Wing Configuration Trade-off Criteria

Criterion	Description	Weight
Skin Frictional Drag	Drag caused by the friction of air against the surface of the UAV.	6/10
Interference Drag	Drag generated when the airflow across one surface intersects with the airflow from another surface on the UAV.	6/10
Ground Effect	The extra lift that is created when a wing is close to the ground, due to the distortion of the air below the wing.	3/10
Roll Stability	Stability in the roll direction.	7/10
Landing Gear	The length of the shaft connected to the landing gear.	4/10
Structures	Consideration for the lightest structure.	5/10

CRITERION / CONCEPT	Skin Frictional Drag (6/10)	Interference Drag (6/10)	Ground Effect (3/10)	Roll Stability (7/10)	Landing Gear (4/10)	Structural Integrity (5/10)	SCORE
High Wing	blue Wetted surface area compared to BWB will be higher therefore the skin frictional is also higher	yellow Compared to the low wing, a higher interference drag	green Furthest away from the ground	green The center of gravity sits below the wing	yellow A longer structure is needed for the landing gear	blue There will be a stress concentration at the location where the fuselage and wing connect, thus thicker structure.	1,33
Low Wing	blue Wetted surface area compared to BWB will be higher therefore the skin frictional is also higher	blue Lower interference drag compared to the high wing, however not as streamlined as a blended mid wing	yellow Close proximity to the ground	yellow The center of gravity lies above the wing	green Wing close to the ground, therefore shaft for landing gear shorter	blue There will be a stress concentration at the location where the fuselage and wing connect, thus thicker structure.	1,87
Blended Mid Wing	green Due to the reduced wetted area, the skin frictional drag will be reduced as a consequence	green More streamlined surface thus less interference drag.	blue Not far from the ground but also not close	blue The center of gravity lies at the wing, roll stability neutral	blue Wing not far from the ground, medium length of landing gear shaft	green Uniform wing loading, because it is one structure	2,63333333

Figure 7.1: Wing Configuration Trade-off

As the focus is placed on minimizing drag, skin frictional drag and interference drag are first mentioned in the trade-off table. Even though there are more types of drag like pressure drag or lift-induced drag, it is acknowledged that the wing configuration does not have a huge influence on these drag effects. Due to the reduced amount of wetted area, the blended mid-wing has a lower frictional drag compared to the high and low wings. Interference drag is induced when different airflows on the UAV intersect due to sharp corners in the geometry. Due to the streamlined surface of the wing blended body, this effect is very minimal compared to the more traditional UAV shapes. For the high wing, there is a slightly higher interference drag compared to the

low wing [1].

Even though the ground effect may be crucial to consider for a conventional runway landing, it is only lightly considered in this trade-off because the UAV is designed to land vertically within a closed-off ground station. The further away the wing is from the ground, the less of a problem the ground effect imposes. On the other hand, stability is extremely important as it determines the control surfaces of the UAV. The roll stability is mainly considered, as the pitch and yaw stability are not significantly influenced by changing the vertical location of the wing. It is preferred that the aerodynamic centre is above the centre of gravity, as this implies that the UAV would be most stable. Therefore, the high wing is shown as the best option for roll stability.

The landing gear is also taken into account when performing the trade-off. Where the ranking is mainly based on the weight of the landing gear that each of the options would result in, as a strict weight limitation is imposed upon structures. The landing gears will be attached to the booms, which are attached to the wings. Hence, as the distance between the ground and the wings increases, the length of the landing gears will grow correspondingly. Lastly, the structures will have a significant influence on which configuration will be chosen. It is preferred to have little stress concentrations, as this will need a local stiffening in the structure, thus a heavier structure overall. Therefore, a more uniform structure, which is displayed in a blended wing body, is more favoured compared to a conventional structure.

7.2. Power and Wing Loading

A feasible design space for the to-be-designed UAV is generated by means of a power-over-weight (P/W) versus wing loading (W/S) diagram using constraining relations found in [8] and [9]. These constraints include cruise conditions, rate of climb, level turn, maximum service ceiling, and approach. The objective of these diagrams is to select the maximum (W/S) at the lowest (P/W) to increase flight performance and reduce power usage. The preliminary parameter values used for the generation of the diagrams in this section are shown in Table 7.2; these values should represent the final parameters accurately enough to perform a first-order performance analysis. The result of the first analysis is shown in Figure 7.2. From inspection of the graphs, it can be determined that a maximum wing loading of $16.3\,\mathrm{kg\,m^{-2}}$ can be obtained using a power of $5.6\,\mathrm{W\,N^{-1}}$ of the UAV design weight. When using the $32\,\mathrm{kg}$ first estimate design weight, this means that a power of $1.7\,\mathrm{kW}$ is needed to sustain the maximum wing loading. In the next stage of the UAV design, these results will be used primarily for the sizing of the wings and the power system.

Table 7.2: Preliminary parameter values for first-order flight performance analysis

Parameter	Value	Rationale/source
W_{design} [kg]	32	Preliminary weight estimation
AR [-]	7	From Baseline Report
c [m]	0.478	Airfoil analysis
$C_{l_{alpha}}$ [1/rad]	5.05	Airfoil analysis XFLR
$C_{L_{max}}$ [-]	1.3	Airfoil analysis XFLR
$C_{L_{max,hld}}$ [-]	1.46	[8]
$C_{D_{min}}$ [-]	0.0418	Airfoil analysis XFLR
C_{d_0} [-]	0.03	Airfoil analysis XFLR
e_0	0.839	$= 1.78 \cdot (1 - 0.045 \cdot AR^{0.68}) - 0.64$ [8]
η_{prop}	0.85	Propulsion analysis

Parameter	Value	Rationale/source
h_{cruise} [m]	120	Requirement
V_{cruise} [km/h]	80	Requirement
$h_{emergency}$ [m]	150	Operations and Logistics
$AMSL_{max}$ [h]	3150	From Baseline Report: areas up to 3 km + h_emergency
V_{max} [km/h]	104.4	Propulsion Analysis
$h_{approach}$ [m]	30	[8]
$V_{approach}$ [km/h]	54.6	[8]
stall margin [-]	1.1	[8]
$V_{stall,0}$ [km/h]	49.6	$V_{approach}$/stall margin [8]
ROC [m/s]	3	[8]
V_{climb} [km/h]	64	80% of V_{cruise} [8]
θ [deg]	45	[8]
n_{min} [-]	[8]	[8]
$n_{max,gust}$ [-]	[8]	[8]
$n_{max,dive}$ [-]	[8]	[8]

[1] https://pilotinstitute.com/high-wing-vs-low-wing/, accessed on 16/06/2023

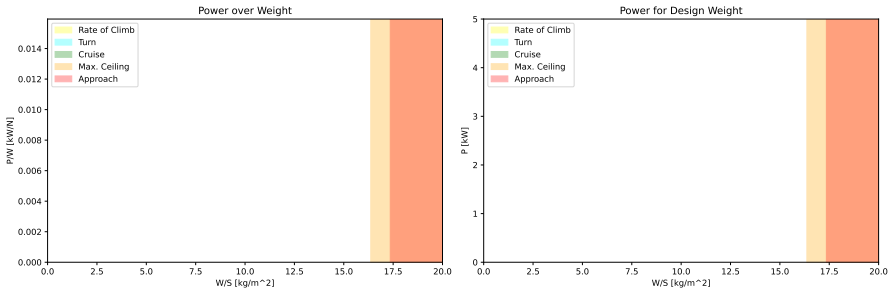

Figure 7.2: Power over Weight (P/W) versus Wing Loading (W/S) diagram.

7.3. Load Diagrams

A load diagram is a powerful tool showing the load factors that will be sustained by the vehicle during various velocity conditions. Moreover, the gust diagram shows the effects of gust loads on the UAV. The generation of the plots has been done in accordance to [8]. These diagrams, as can be seen in Figure 7.3, give an indication of the minimum and maximum load factors for each airspeed the UAV should be able to sustain when in operation. Constraints include load limits based on both UAV performance and regulations. From the graph, it was determined that the load factors the UAV will experience during its operational lifetime range from -2 to 4.5 for speeds varying up to 29 $\mathrm{m\,s^{-1}}$. These results are predominantly relevant to the structural design of the UAV that needs to sustain the loads during its full operation lifetime.

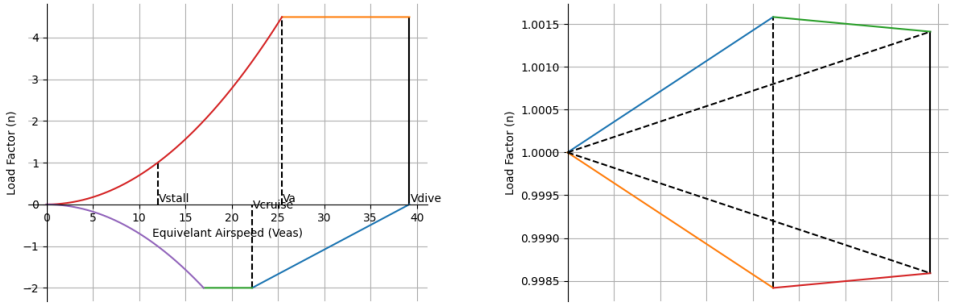

Figure 7.3: Manoeuvre loading diagram and gust loading diagram.

7.4. Main Wing Sizing

The main wing is sized to fly most optimal at nominal cruise conditions as well as meet the 2-hour endurance requirement at lower velocity. OpenVSP Figure 7.4a describes the lift-over-drag ratio of the whole UAV as a function of the angle of attack at a Reynolds number of 600000. The Reynolds number is calculated by using Equation 7.1 at ISA sea level conditions, where the velocity is set to the cruise velocity of 22.22 $\mathrm{m\,s^{-1}}$ and the $c_{\mathrm{ref}} = 0.381$ which is the length of MAC. It can be seen that the most optimal angle of attack is defined as α_{opt}, this can vary depending on the Reynolds number and extra drag that is added due to propellers that aren't included in the model. Importantly, during the nominal cruise, the UAV is most efficient when flying in between 2 ° and 5 ° angle of attack and thus $\alpha_{\mathrm{opt}} = 3°$.

$$Re = \frac{\rho V c_{\mathrm{ref}}}{\mu} \tag{7.1}$$

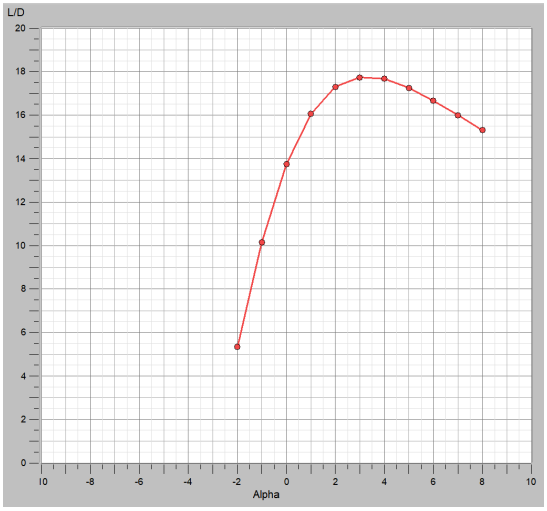

(a) Lift-over-drag ratio as a function of the angle of attack.

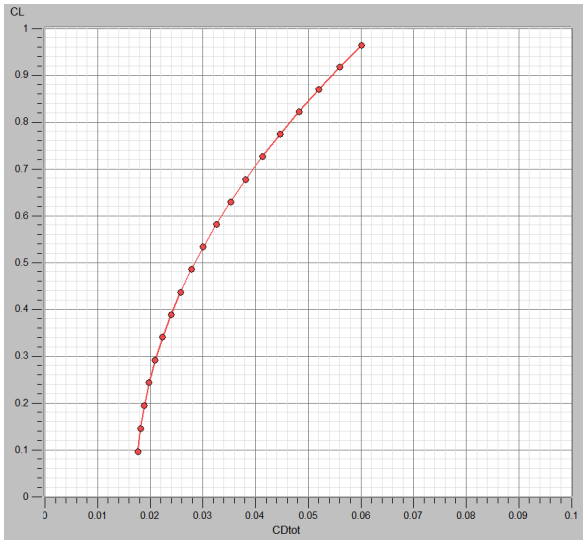

(b) Lift-drag polar in cruise conditions.

The $C_{L\text{req}}$ in order to cruise horizontally at $80\,\text{km}\,\text{h}^{-1}$ as is stated in REQ-GEN-10, is defined by Equation 7.2. The closer the angle of attack at which $C_{L\text{req}}$ is to α_{opt}, the more efficient the UAV will be during cruise. The velocity, density and weight are already defined for the nominal cruise condition, therefore the only parameter is S_{ref}. The reference surface area is defined as the main wing's surface area. Secondly, REQ-GEN-7 states that the UAV shall have at least 2 hours of endurance. It has been concluded in Section 14.2 that the push motor will have a maximum power of 275 W in order to achieve stay airborne for 2 hours. T-motor AT4130 has a power usage of 275 W at 47% throttle. JavaProp is used to compute the thrust at this throttle setting, the thrust varies with different velocities. Equation 7.3 defines the required $C_{D\text{req}}$ as a function of the reference surface area. The C_L and C_D per angle of attack of the UAV as a whole are described in Figure 7.4b. An iteration loop is performed over different angles of attack with different wing surface areas in order to find a solution that satisfies both REQ-GEN-10 and REQ-GEN-7.

$$C_{L\text{req}} = \frac{W}{0.5\rho V^2 S_{ref}} \tag{7.2}$$

$$C_{D\text{req}} = \frac{T}{0.5\rho V^2 S_{ref}} \tag{7.3}$$

Finally, as the design is a blended wing body, all instrumentation needs to be fitted into the wing. Therefore, the wing is split up into four identical airfoils as cross-sections with different chord lengths. The chord length of and distance between the middle two airfoils are determined by the size of the instrumentation that is fitted inside the wing. The chord length of the outer two airfoils as well as the distance between them are iteratively determined in order to satisfy the main wing surface area that has been found and a set taper ratio. The taper ratio for a non-swept wing should be 0.4[10]. After iterations were completed, the final main wing parameters are described in Table 7.3. As mentioned in the trade-off summary, the wing makes use of the CAL2236m airfoil.

Table 7.3: Geometry parameters of the main wing.

Parameter	Value	Parameter	Value
Chord_1	900 [mm]	Wing Surface	1.25 [m^2]
Chord_2	725 [mm]	L_12	150 [mm]
Chord_3	450 [mm]	L_23	200 [mm]
Chord_4	180 [mm]	L_34	1250 [mm]

7.5. Sizing of the tail

The lift generated by the main wing acts in front of the CG (centre of gravity). If no correction is implemented to counteract the moment caused by the lift, the aircraft will not be statically stable. The moment can be corrected in many ways, for this design a horizontal stabilizer attached to a boom-tail was chosen. The flight dynamics course [1] describes a horizontal tail sizing method derived from the lateral moment equilibrium. The controllability and stability of the aircraft drive the tail size. The tail size is preferably as small as possible to lower the aircraft's weight and improve efficiency.

7.5.1. Center of gravity

As moments are calculated around the CG it is very important to have an easy and iterative way of calculating the CG from a specified datum. The datum from which the CG is calculated is chosen as the centre of the front VTOL propeller. The placement of the batteries, cruise propeller and payload is determined by the shape of the blended wing body. The main wing is therefore treated as one single item. This leaves freedom in moving the CG by shifting the position of the rear VTOL propellers and elongating the boom length which in term will move the horizontal stabilizer backwards. The CG is preferably as far forwards as possible however a clearance for the propellers needs to be taken into account. Furthermore, attention needs to be paid to ensure that the centroid of the 4 VTOL propellers is as close as possible to the CoG otherwise stability during VTOL would be harder or impossible to achieve especially during wind gusts. The location of the CG can be calculated using Equation 7.4.

$$x_{cg} = \frac{x_{wing} \cdot m_{wing} + x_{rear\,VTOL} \cdot m_{rear\,VTOL} + x_{tail} \cdot m_{tail}}{m_{wing} + m_{rear\,VTOL} + m_{tail}} \tag{7.4}$$

7.5.2. Longitudinal Stability and controllability

With this in mind, a trade-off between boom length and tail area is made. Equation 7.5 and Equation 7.6, respectively static stability and controllability provide a ratio of the tail area compared to the main wing area. The equations use the values stated in Table 7.4, where the $\bar{x}_{cg}$ value is varied to determine the optimal CoG range to reduce the tail size. Note that x_{cg} divided by $\bar{c}$ equals $\bar{x}_{cg}$.

$$\frac{S_h}{S} = \frac{1}{\left[\frac{C_{L\alpha_h}}{C_{L\alpha_{A-h}}}\left(1-\frac{d\varepsilon}{d\alpha}\right)\frac{x_h - x_{cg} - SM}{\bar{c}}\left(\frac{V_h}{V}\right)^2\right]}\bar{x}_{cg} - \frac{\bar{x}_{ac} - SM}{\frac{C_{L\alpha_h}}{C_{L\alpha_{A-h}}}\left(1-\frac{d\varepsilon}{d\alpha}\right)\frac{x_h - x_{cg} - SM}{\bar{c}}\left(\frac{V_h}{V}\right)^2} \tag{7.5}$$

$$\frac{S_h}{S} = \frac{1}{\frac{C_{L_h}}{C_{L_{A-h}}}\frac{x_h - x_{cg} - SM}{\bar{c}}\left(\frac{V_h}{V}\right)^2}\bar{x}_{cg} + \frac{\frac{C_{m_{ac}}}{C_{L_{A-h}}} - \bar{x}_{ac}}{\frac{C_{L_h}}{C_{L_{A-h}}}\frac{x_h - x_{cg} - SM}{\bar{c}}\left(\frac{V_h}{V}\right)^2} \tag{7.6}$$

The downwash parameter $\frac{d\varepsilon}{d\alpha}$ is estimated using Equation 7.9 where m_{tv} is defined as "the distance between the horizontal tail and the vortex shed plane, which can be approximated with the plane from the wing root chord" according to [1] and is calculated using Equation 7.7 and Equation 7.8 where for the UAV a vertical distance of $0.30\,\text{m}$ and a wingspan of $3.2\,\text{m}$ are used. The vertical distance is chosen freely keeping in mind that a vertical stabilizer is needed either way and moving the horizontal tailplane up is preferable to mitigate downwash effects.

$$m_{tv} = \frac{2 \cdot \text{vertical distance}}{\text{b}_{\text{mainwing}}} \tag{7.7}$$

$$r = \frac{2(\text{x}_\text{h} - \text{x}_\text{cg} - \text{SM})}{\text{b}_{\text{mainwing}}} \tag{7.8}$$

$$\frac{d\varepsilon}{d\alpha} = \left(\frac{r}{r^2 + m_{tv}^2} \frac{0.4876}{\sqrt{r^2 + 0.6319 + m_{tv}^2}} + \left[1 + \left(\frac{r^2}{r^2 + 0.7915 + 5.0734\, m_{tv}^2} \right)^{0.3113} \right] \left\{ 1 - \sqrt{\frac{m_{tv}^2}{1 + m_{tv}^2}} \right\} \right) \frac{C_{L_{aw}}}{\pi A} \tag{7.9}$$

The values in Table 7.4 are either physical dimensions, assumptions or data retrieved from aerodynamic analyses. The values for $C_{L\alpha_h}$, $C_{L\alpha_{A-h}}$, $C_{L\alpha_h}$, and $C_{m_{ac}}$ are retrieved from XFLR using the CAL2263m airfoil [11] for the main wing and a NACA0015 airfoil for the horizontal tailplane. SM is a value that is chosen by the engineer as a stability margin. The mean aerodynamic chord $\bar{c}$ is determined using Equation 7.10 where the straight part of the wing is extrapolated until the centre of the fuselage to get a root chord estimate.

$$\bar{c} = \frac{2}{3} c_r \left(\frac{1 + TR + TR^2}{1 + TR} \right) \tag{7.10}$$

Table 7.4: Tail sizing parameters.

Parameter	Value	Unit
$C_{L\alpha_h}$	5.24	1/rad
$C_{L\alpha_{A-h}}$	5.93	1/rad
$\frac{d\varepsilon}{d\alpha}$	0.40	rad/m
SM	0.05	-
$\bar{c}$	0.403	m
x_h	2.86	m

Parameter	Value	Unit
$\bar{x}_{ac}$	0.25	-
C_{L_h}	0.15	1/rad
$C_{L_{A-h}}$	0.111	1/rad
$C_{m_{ac}}$	-0.0288	-
$\frac{V_h}{V}$	1	-

7.5.3. Horizontal tail planform

Figure 7.5 is the result from plotting Equation 7.5 and Equation 7.6. Usually, the slope of the controllability curve is negative as controllability is determined during landing conditions where the horizontal stabilizer will create a negative lift force. The UAV will have VTOL capabilities using the same concept as a quadcopter, therefore a conventional landing on a runway is not considered a situation that needs to be accounted for. The stability of the aircraft becomes the constraining factor for the UAV design, to meet this requirement with the CG location determined in subsection 7.5.1 a tail area of $0.40\,\mathrm{m}^2$ is required using a distance between the horizontal tail leading edge and the centroid of the front VTOL propeller of $2.85\,\mathrm{m}$. The horizontal tail wingspan and chord are free to be chosen at a later stage of the design as the distance between the booms will drive these values. The green area highlighted shows lower feasible tail sizes if the CG location can be moved more forward.

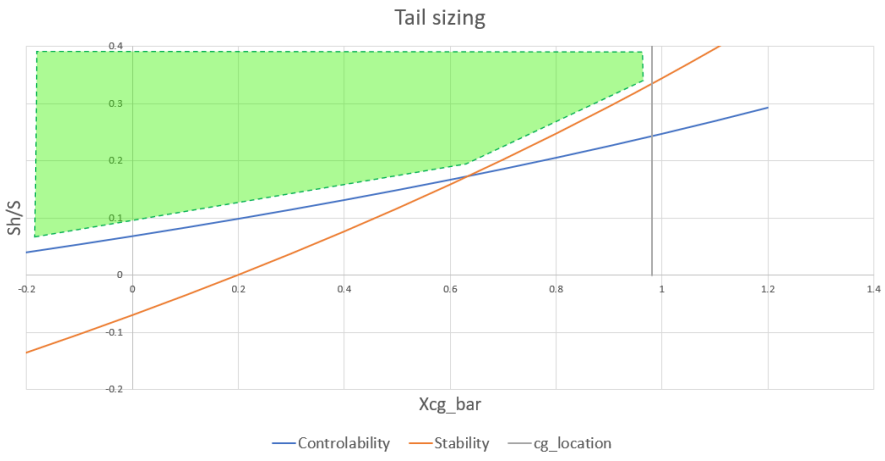

Figure 7.5: Tail sizing graph.

7.6. Analysis Setup

A model of the UAV was created in OpenVSP. The mesh of the model is depicted in Figure 7.6. The program is able to simulate the blended wing body as well as the inverse-U boom tail. The two booms are modelled as stretched-out ellipsoids. This represents the actual booms which will also have a sharp tip. The mesh of the blended wing body is finer around the curves of the blended-in fuselage in order to obtain a better convergence. LE and TE clustering is also introduced on both the wing and tail as well as clustering near the tips of the beam in order to increase accuracy. A more elaborate convergence study is described in Section 12.3. It can be seen that the propellers are not considered in this analysis. This complexity was determined to be beyond the scope of the DSE design and will be taken into account by adding an extra propeller drag factor. Finally, the control surfaces were added to the model. The orientations are shown with circular arrows. It can be seen that the left side of the elevator is indicated as upwards positive, this should not be the case and is thus correctly defined in the analysis but not visually. The effects of the control surfaces will be analysed to verify their sizing and provide stability and controllability derivatives for the flight simulation.

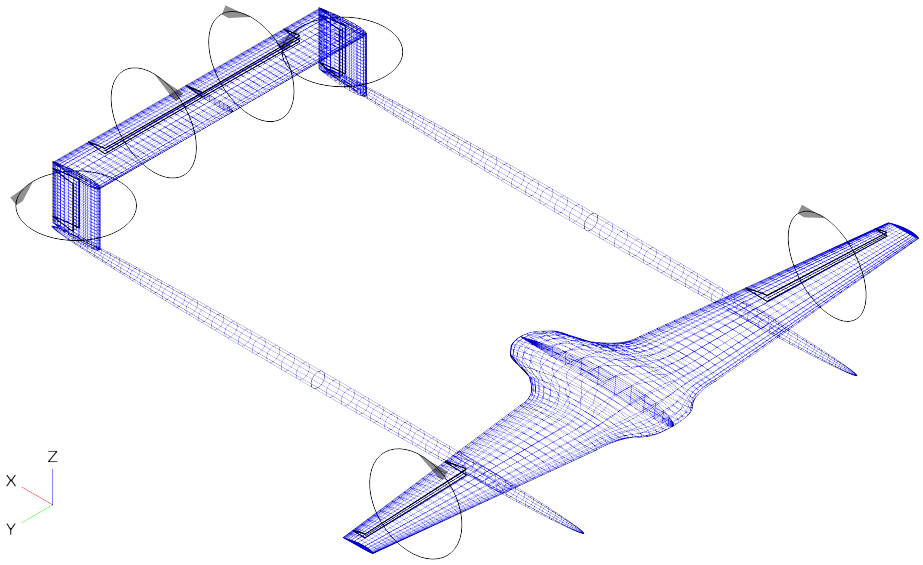

Figure 7.6: The mesh of the UAV model in OpenVSP.

Furthermore, the number of wake nodes is set to 128 as this significantly increased the convergence compared to 64 nodes. Increasing this value beyond 128 would require too much computational time. The number of wake iterations is varied depending on the required accuracy of the analysis versus the computational time it will take to perform the analysis. These settings are further discussed in Section 12.3.

7.7. Dihedral and Twist

In order to increase roll stability a dihedral of 3° is introduced as this is a common value for mid-wing aircraft.[2] After adding dihedral it was checked whether or not this change would have a large impact on the flight performance of the UAV. This was done by comparing the lift-drag polars during cruise conditions. The results are depicted in Figure 7.7 and it can clearly be seen that adding dihedral has a negligible effect on the lift-drag polar.

No twist is added to the wing. It has been considered, as wing twist can lower the angle of attack for optimal lift-over-drag ratio. This would be beneficial to reduce the wake created by the boom which sticks out in front of the main wing. It is seen from Figure 7.8b, where a positive tip twist is introduced, that the increase in C_L is minimal and it also comes with a slight increase in C_D. If the boom were positioned more to the root or the tip of the main wing, the twist would have a higher effect. It has been decided that due to manufacturability it is not worth the advantages to have a twist in the wing. This can be reconsidered in future designs.

[2] https://www.beyonddiscovery.org/aircraft-design/dihedral-angle.html, accessed on 15-06-2023

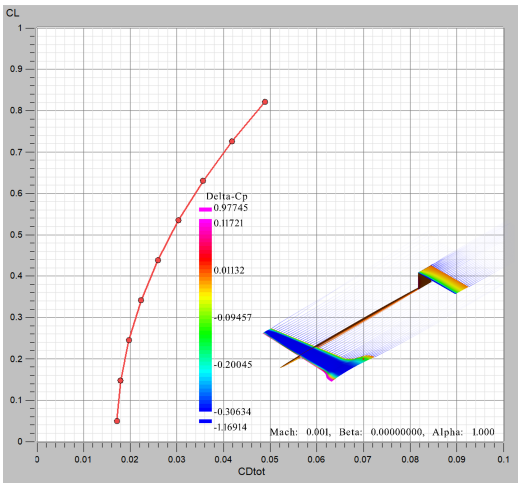

(a) The lift-drag polar without dihedral.

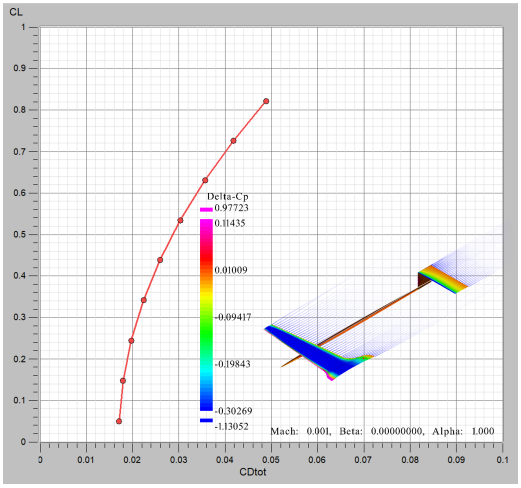

(b) The lift-drag polar with 3° of upwards dihedral.

Figure 7.7: Comparison of two lift-drag polars with and without dihedral.

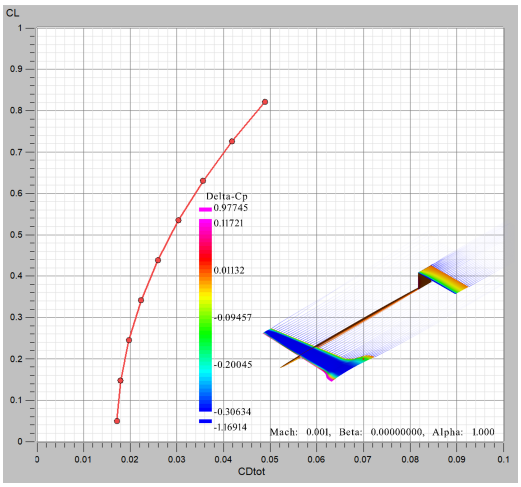

(a) The lift-drag polar without twist.

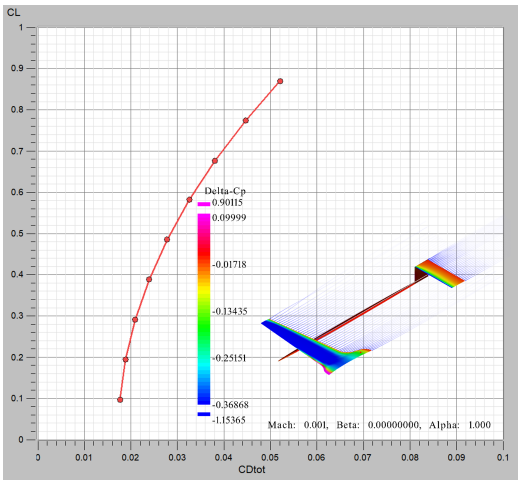

(b) The lift-drag polar with 3° of positive tip twist.

Figure 7.8: Comparison of two lift-drag polars without and with a twist.

7.8. Flight Configurations

The flight configurations of five flight phases are determined. Out of these five, there are three different cruise flight phases namely: nominal cruise at $80\,\mathrm{km\,h^{-1}}$, cruise in order to achieve maximum endurance of 2 hours and 14 minutes at a velocity of $64.8\,\mathrm{km\,h^{-1}}$ and cruise at the maximum velocity of $141\,\mathrm{km\,h^{-1}}$. Furthermore, the transition, climb and acceleration are defined as one aerodynamic configuration as they are flown at the same angle of attack. Finally, the descent phase will be flown at the minimum throttle. The vortex lattice method used in this aerodynamics analysis does not take the fixed propellers into account. In order to compensate for the extra drag that is not included in this assumption, the drag coefficient is increased by 10%.

The first flight phase includes a transition part from VTOL to straight flight at a favourable flying velocity. Then the UAV climbs at climbing velocity to the cruise altitude where it then accelerates again from climb velocity to nominal or Vmax velocity. These three parts are performed under the same angle of attack. For nominal cruise, the angle of attack is 1.55°. This is not the most optimal α for $\frac{\mathrm{L}}{\mathrm{D}}$, but it provides the aircraft with exactly 2 hours of endurance at a velocity of $80\,\mathrm{km\,h^{-1}}$. The wing area could be reduced more in order to obtain a lower C_L value at $80\,\mathrm{km\,h^{-1}}$ and thus fly at a higher $\frac{\mathrm{L}}{\mathrm{D}}$, but that would come at a cost of reducing the aspect ratio and thus increase drag again. This iteration is favourable and has been found to work for the mission

requirements. In future designs, several extra wing surface area iterations can be performed to be more efficient during the cruise phase. The driving constraint for maximum endurance is engine stall. The lowest throttle setting for the engine is 40%, in order to fly a horizontal flight where $L = D$, a velocity of $64.8\,\mathrm{km\,h^{-1}}$ must be flown at the optimal angle of attack. If the engine would be able to produce less thrust, the UAV could fly slower and thus experiencing less drag and creating thrust more efficiently. The maximum velocity is obtained when the push motor is throttled to 100%. Using JavaProp as well as Equation 7.3 and Equation 7.2 the angle of attack is found at which the UAV will fly a horizontal flight path. Finally, the descend phase has been defined to fly at the lowest thrust setting. The engine will stall before the aircraft stalls, thus in order to decelerate, the lowest thrust setting is used.

Table 7.5: The flight configurations for different mission phases.

Mission Phase	**Velocity [$\mathrm{km\,h^{-1}}$]**	**Angle of Attack [°]**	C_L **[-]**	C_D **[-]**
Transition, Climb and Acceleration to Nominal Cruise	22.68-80	4.9	0.71	0.046
Transition, Climb and Acceleration to Max Velocity Cruise	22.68-141.1	-0.65	0.18	0.019
Nominal Cruise Flight	80	1.55	0.393	0.0267
Cruise Flight for Max Endurance	64.8	3.66	0.595	0.0370
Cruise Flight for Max Velocity	141.1	-1.23	0.126	0.0174
Descent	64.8	3.66	0.595	0.0370

7.9. Force Distributions

The force distribution over the main wing and tail is used in the structural design. The lift-, drag- and pitch moment coefficient distributions are given in Figure 7.9, Figure 7.10 and Figure 7.11. The coefficients are also normalised for the reference chord of $0.381\,\mathrm{m}$ and they are calculated for the half-chord span.

Lift Coefficient

It can be seen that the most lift is created around the blended fuselage of the UAV. At a spanwise length of $0.8\,\mathrm{m}$ there is a slight impulse increase in lift. This makes sense as this is the position of the boom.

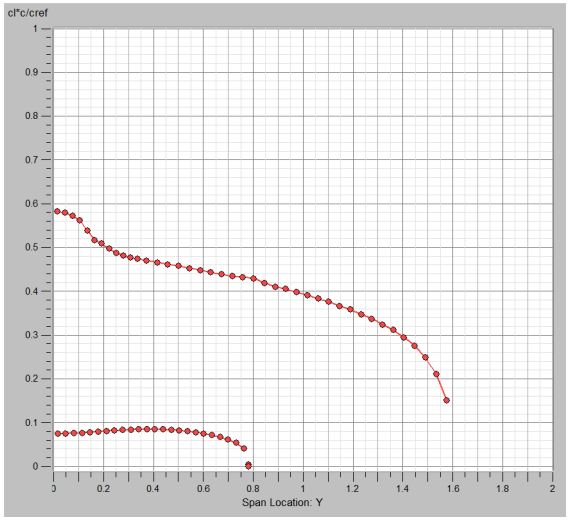

Figure 7.9: Chord normalised lift coefficient distribution over half the wingspan.

Drag Coefficient

The drag over the main wing is highest near the centre, where there is the most surface area on the UAV. There is also another drag increase near the wingtips due to vortices. The tail has a smoother drag distribution and fewer wingtip vortices because the vertical tails serve as winglets.

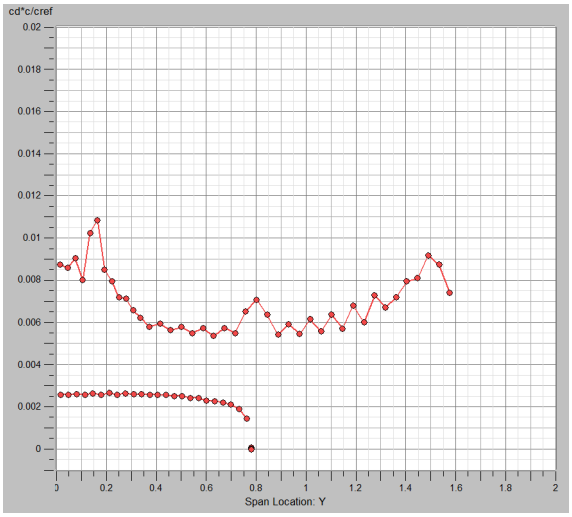

Figure 7.10: Chord normalised drag coefficient distribution over half the wingspan.

Pitch Moment Coefficient

The aerodynamic pitch moments are taken around the centre of gravity of the UAV as calculated in Section 8.2. The main wing produces a positive pitch-up moment with most of the moments being created around the wingtip and the tail will stabilise the UAV by creating a pitch-down moment. The highest moments due to the tail are created in its middle section.

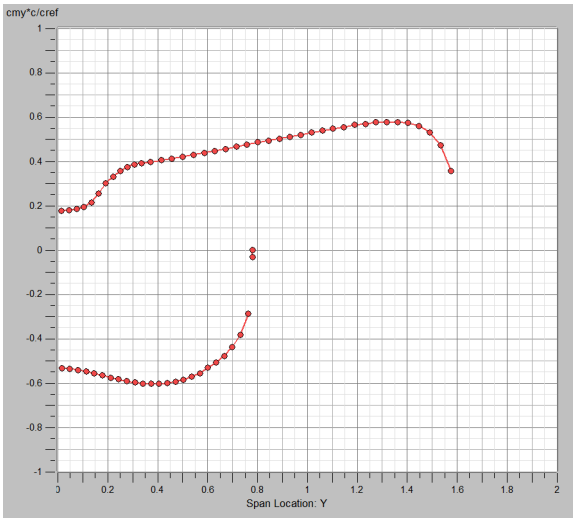

Figure 7.11: Chord normalised moment coefficient distribution over half the wingspan.

7.10. Control Surface Design and Sizing

Having defined the main wing and horizontal stabilizer, control surfaces can be designed, providing the UAV with longitudinal and lateral control. The aim of the section is to obtain the control surfaces' surface area, span and chord length, which will be done using the design logic as described in Sadraey and Colgren (2007) [12] and Sarker et al. (2017) [13] that is generally based on the change in moment about the axis of rotation the control surface needs to generate, see Equation 7.11. In this relation, it is assumed that the control surface is the only contributing factor to the change in the moment around the centre of gravity, i.e. the lift of the main wing and the horizontal tail do not change for changing angle of attack.

$$M = \ddot{\theta} I = \Delta L_{cs} l_{cp,cs} - \sum D_{rot} l_{cp} \tag{7.11}$$

Where M is the required moment about the axis of rotation of the corresponding manoeuvre in kg m. $\ddot{\theta}$ is the angular acceleration in $\mathrm{m\,s^{-2}}$ and is obtained from performance requirements, i.e. the change in angle of the

manoeuvre that needs to be obtained within a set time. The mass moments of inertia, I in $\mathrm{kg\,m^{-2}}$, for each rotational axis (x, y, and z) are derived from the currently defined UAV mass and geometry. The parameter of interest that needs to be determined from the relation as given in Equation 7.11 is ΔL_{cs}. This parameter addresses the change in lift the control surface (cs) is required to generate in N, with $l_{cp,cs}$ its the moment arm to the centre of gravity in m that was derived from the UAV geometry. D_{rot} in N is the drag induced by the rotational movement of the wing and horizontal tail surface at the instance the required change in angle is obtained (including contingencies); l_{cp} is their moment arm in m.

With the calculation of the required change in lift, the surface area needed for this change can then be determined using Equation 7.12.

$$\Delta L_{cs} \cdot \eta = (C_{l,max_{cs}} - C_{l,trim_{cs}}) \frac{1}{2} \rho_{ceiling} V_{cruise}^2 S_{cs} \tag{7.12}$$

Where $C_{l,max_{cs}} - C_{l,trim_{cs}}$ is the difference in lift coefficient (unitless) between trim conditions and maximum control surface deflection (the deflection is constraint by its effectiveness considering flow separation). As a preliminary reference airfoil shape, the NACA 0015 airfoil and its characteristic were used for this design process. $\rho_{ceiling}$ and V_{cruise} are used in Equation 7.12, as these are the constraining conditions[3] the UAV will fly in for which the control surface area needs to be defined. A contingency factor, $\eta = 2$, is included to account for the simplified nature of this method.

Then, when the required control surface area is calculated, the control surface chord (ratio) and span can be designed, taking into account the present UAV reference geometry.

The following subsections are dedicated to the documentation of the sizing and design process for the elevator, ailerons and rudders consecutively.

7.10.1. Elevator Design

In literature, the sizing of the elevator is primarily based on a conventional take-off run rotation performance for conventional aircraft [12]. Since the UAV of interest will use the VTOL system to take off, another performance constraint is used, namely obstacle avoidance capabilities; in Figure 7.12 a sketch of the reference situation is used.

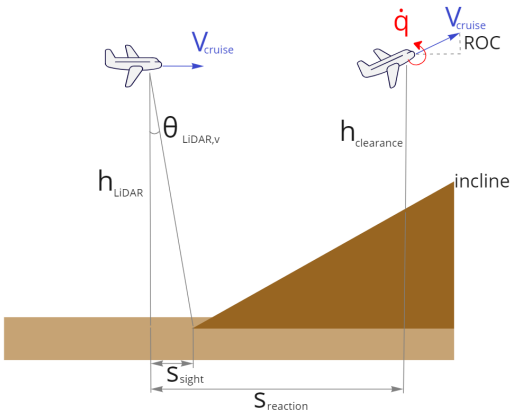

Figure 7.12: Obstacle avoidance constraining performance manoeuvre for elevator sizing and design.

Based on the sketched situation, the minimum performance requirements in pitch acceleration were calculated. The flow of this calculation, together with the used parameter values (including rationale) are summarized in Table 7.6. The first step of this calculation is to determine the distance the LiDAR can see ahead when the terrain surface first gets below the response height. Then, the time covered from obstacle detection to the smallest allowable distance to ground using cruise speed is calculated. From this, the required pitch acceleration is determined for the UAV to not have a distance to the ground of less than the critical response height.

[3] Technically, V_{stall} would be the constraining velocity condition, but having the VTOL system, it is assumed that this system will be used in case performance requirements cannot be met adequately at a lower airspeed.

Table 7.6: Obstacle avoidance required pitch rate calculation for elevator sizing and design.

	Input parameter(s)	Operations: $V_{cruise} = 22.22\,\text{m s}^{-1}$, $ROC = 3\,\text{m s}^{-1}$, $h_{min} = 30\,\text{m}$ LiDAR specifications: $h_{lidar} = 55\,\text{m}$, $\theta_{lidar,H} = 15°$ $incline = 100\%$ (set constraint) sf $= 2$ (set safety factor for performance margin)
1	**Relation(s)**	$s_{sight} = h_{lidar} \cdot \tan(\theta_{lidar,H})$
	Output parameter(s)	$s_{sight} = 14.7\,\text{m}$
2	**Relation(s)**	$\theta_{incline} = \arctan\left(\frac{incline}{100}\right)$ $s_{max} = s_{reaction} + (h_{lidar} - h_{min})\tan(\theta_{incline})$ $s_{max} = V_{cruise} t_{reaction}$
	Output parameter(s)	$s_{reaction} = 39.7\,\text{m}$, $t_{reaction} = 1.8\,\text{s}$
3	**Relation(s)**	$\Delta\alpha = \arcsin\left(\frac{ROC}{V_{cruise}}\right)$ sf$\Delta\alpha = \frac{1}{2}\dot{q}t^2$ $q = \dot{q}t_{reaction}$
	Output parameter(s)	$\dot{q} = 0.17\,\text{rad s}^{-2}$, $q = 0.30\,\text{rad s}^{-1}$

Having obtained a value for the required pitch rate, the lift the elevator needs to produce in order to acquire this pitch acceleration can be calculated, using Equation 7.11. A summarizing table of this calculation is given in Table 7.7. Firstly, a relation is given for the calculation of the rotational velocity of the lifting surfaces, i.e. the blended wing body and the horizontal stabilizer. Inputs for this calculation are the rotational velocity at the instance the desired change in angle, $\Delta\alpha$, is obtained and the moment arm of the lifting surface. Having calculated the rotational velocity of the wing and tail, the drag produced by these surfaces is then determined, from which the elevator required lift can be determined as per Equation 7.11. And then, using Equation 7.12, the elevator surface area can be determined.

Table 7.7: Elevator sizing calculations.

	Input parameter(s)	From operations: $\rho_{sl} = 1.225\,\text{kg m}^{-3}$, $\rho_{ceiling} = 0.8953\,\text{kg m}^{-3}$, $V_{cruise} = 22.22\,\text{m s}^{-1}$ From UAV design: $I_{yy} = 8.228\,\text{kg m}^{-2}$, $X_{cg} = 1.179\,\text{m}$, $S_{wing} = 1.25\,\text{m}^2$, $X_{cp,wing} = 0.773\,\text{m}$, $X_{cp,tail} = 2.924\,\text{m}$, $l_{tail} = X_{cp,tail} - X_{cg}$ $1.745\,\text{m}$, $b_{tail} = 1.5\,\text{m}$. From NACA 0015 airfoil data: $C_{l_{max,e}} = 1.2$, $C_{l_{trim,e}} = 0.4$. $C_{D_{flat}} = 2$ (Monterroso (2018) [7]), $V_{vert} = 2\,\text{m s}^{-1}$ (max estimated vertical velocity component) $\eta = 2$ (set to take into account unforeseen disturbances)
1	**Relation(s)**	$V_{rot} = q\lvert X_{cg} - X_{cp}\rvert + V_{vert}$
	Output parameter(s)	$V_{rot,wing} = 2.12\,\text{m s}^{-1}$, $V_{rot,tail} = 2.53\,\text{m s}^{-1}$
2	**Relation(s)**	$D_{rot} = C_{D_{flat}} \frac{1}{2} \rho_{ceiling} V_{cruise}^2 S$
	Output parameter(s)	$D_{rot,wing} = 6.90\,\text{N}$, $D_{rot,tail} = 3.27\,\text{N}$
3	**Relation(s)**	$\dot{q} I_{yy} = \Delta L_e l_{tail} - D_{rot,wing}\lvert X_{cg} - X_{cp,wing}\rvert - D_{rot,tail}\lvert X_{cg} - X_{cp,tail}\rvert$ $\Delta L_e \cdot \eta = (C_{l,max_e} - C_{l,trim_e}) \frac{1}{2} \rho_{ceiling} V_{cruise}^2 S_e$
	Output parameter(s)	$\Delta L_e = 12.20\,\text{N}$, $S_e = 0.069\,\text{m}^2$

Then, based on the elevator surface area, the elevator is sized. Using various span fractions of the horizontal tail span, the elevator span was varied and corresponding chords were calculated. From this set of elevator dimensions, one of the options was selected, keeping in mind that it is desired to minimize the hinge moment generated by the elevator (i.e. small chord is preferred) and clearances concerning the horizontal tail tips.

The chosen elevator dimensions are as follows: $b_e = 1.1$ m, $c_e = 0.07$ m, where the elevator is fully symmetrical in the UAVs' x-axis.

7.10.2. Aileron Design

Again, using the same logic as described before, the constraining performance requirements were determined for which the ailerons need to be designed. In the case of this particular UAV, the constraining turn to be performed is when performing the orography mission, as the LiDAR camera used to do this mission has the smallest swath width and thus the required turn radius. A sketch of this situation is shown in Figure 7.13. The top left sketch shows the situation as seen from behind or in front of the direction of flight, the lower left corner shows the situation from above and the right sketch indicates the forces acting on the UAV in a turn.

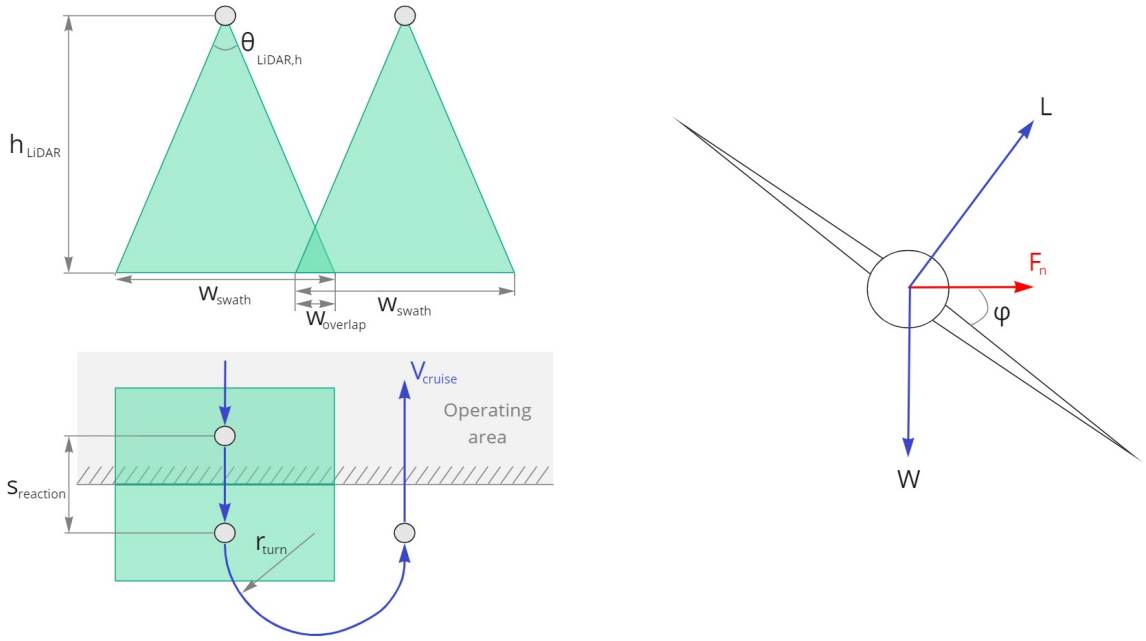

Figure 7.13: Turn performance constraining performance manoeuvre for aileron sizing and design.

With the situation as sketched in Figure 7.13, the required turn acceleration performance can be derived. This process is shown in Table 7.8 and is started by defining the turn radius based on swath width and the width the swath widths need to overlap for accurate terrain mapping. Then, the experienced force normal to the UAV turn curve can be calculated from which the required bank angle to make the turn is deduced. Since it is said that the UAV needs to have turned up to the determined bank angle in the time the LiDAR field of view is just outside of the area that needs to be scanned for orography, the reaction distance can be calculated as well as the time it takes to reach this distance. Lastly, the roll rate and roll velocity at the designated bank angle can be calculated.

Table 7.8: Turn performance required roll rate calculation for aileron sizing and design.

	Input parameter(s)	From LiDAR specifications: $h_{lidar} = 55\,\text{m}$, $\phi_{lidar,H} = 35°$, $\phi_{lidar,V} = 15°$, $s_{overlap} = 5\,\text{m}$ (set value) $m_{TO} = 15.02\,\text{kg}$ (UAV design), $V_{cruise} = 22.22\,\text{m s}^{-1}$ (operations)
1	**Relation(s)**	$r_{turn} = h_{lidar}\tan(\phi_{lidar,H}) - \frac{1}{2}s_{overlap}$ $F_n = V_{cruise}^2 r_{turn}$ $\phi = \arctan\left(\frac{F_n}{m_{TO}g_0}\right)$
	Output parameter(s)	$r_{turn} = 36.01\,\text{m}$, $F_n = 13.71\,\text{N}$, $\phi = 0.094\,\text{rad}$
2	**Relation(s)**	$s_{reaction} = 2h_{lidar}\tan(\phi_{lidar,V})$ $s_{reaction} = V_{cruise}t_{reaction}$
	Output parameter(s)	$s_{reaction} = 29.47\,\text{m}$, $t_{reaction} = 1.33\,\text{s}$
3	**Relation(s)**	$\phi = \frac{1}{2}\dot{p}t^2$ $p = \dot{p}t$
	Output parameter(s)	$\dot{p} = 0.11\,\text{rad s}^{-2}$, $p = 0.14\,\text{rad s}^{-1}$

Having obtained a value for the roll rate, the lift a single aileron needs to produce in order to acquire this acceleration can be calculated using Equation 7.11. A summarizing table of this calculation is given in Table 7.9. Firstly, a relation is given for the calculation of the rotational velocity of the lifting surfaces, i.e. the blended wing body and the horizontal stabilizer. Inputs for this calculation are the rotational velocity at the instance the desired change in angle, ϕ, is obtained and the moment arm of the lifting surface, i.e. the surfaces' half span. Having calculated the rotational velocity of the wing and tail, the drag produced by these surfaces is then determined, from which the aileron required lift can be determined as per Equation 7.11. And then, using Equation 7.12, the aileron control surface area can be determined.

Table 7.9: Aileron sizing calculations.

	Input parameter(s)	From operations: $\rho_{sl} = 1.225\,\text{kg m}^{-3}$, $\rho_{ceiling} = 0.8953\,\text{kg m}^{-3}$, $V_{cruise} = 22.22\,\text{m s}^{-1}$ From UAV design: $I_{xx} = 3.697\,\text{kg s}^{-2}$, $Y_{body} = 0.35\,\text{m}$, $S_{wing} = 1.25\,\text{m}^2$ $S_{tail} = 0.417\,\text{m}^2$, $b_{wing} = 3.2\,\text{m}$, $b_{tail} = 1.5\,\text{m}$ $C_{l_{max,a}} = 1.2$ (NACA 0015 data), $C_{D_{flat}} = 2$ (Monterroso (2018) [7]) $\eta = 2$ (set to take into account unforeseen disturbances)
1	**Relation(s)**	$V_{rot} = \frac{b}{2}q + V_{dist}$
	Output parameter(s)	$V_{rot,wing} = 2.22\,\text{m s}^{-1}$, $V_{rot,tail} = 2.10\,\text{m s}^{-1}$
2	**Relation(s)**	$D_{rot} = C_{D_{flat}}\frac{1}{2}\rho_{sl}V_{cruise}^2 S_a$
	Output parameter(s)	$D_{rot,wing} = 7.57\,\text{N}$, $D_{rot,tail} = 2.26\,\text{N}$
3	**Relation(s)**	$\dot{q}I_{xx} = 2 \cdot \Delta L_a Y_{cp} - D_{rot,wing}\frac{b_{wing}}{2} - D_{rot,tail}\frac{b_{tail}}{2}$ $\Delta L_a \cdot \eta = (C_{l,max_a} - C_{l,trim_a})\frac{1}{2}\rho_{ceiling}V_{cruise}^2 S_a$
	Output parameter(s)	$L_a = 12.47\,\text{N}$, $S_a = 0.047\,\text{m}^2$

Based on this surface area, the ailerons are sized. Using various span fractions of the blended wing body span, the aileron span was varied and corresponding chords were calculated. From this set of aileron dimensions, one of the options was selected, keeping in mind that it is desired to minimize the hinge moment generated by the elevator (i.e. small chord is preferred), clearances with respect to the wing tip and root, and placement of the VTOL boom structures.

The chosen aileron dimensions are as follows: $b_a = 0.5\,\text{m}$, $c_a = 0.10\,\text{m}$, where the aileron is perfectly centred between the wing tip and the VTOL boom structure with a centre of pressure location at $Y_{cp} = 1.18\,\text{m}$.

7.10.3. Rudder Design

Since the rudder is mainly used to correct for the lateral forces and moments acting on an aircraft due to airspeed under an angle of sideslip and for coordinated turns, there was no need to define a yaw rate requirement constraint. For the rudder design, a different design method is therefore applied. This method is used by Sarker et al. (2017) [13][14]. It takes a set vertical stabilizer fraction of $40\,\%$ and uses it to define the rudder area. Then, just as was done for the elevator and ailerons, the rudder span to vertical stabilizer span fraction was varied resulting in a set of rudder spans and corresponding chord lengths. From this set of dimensions, the most promising size was chosen.

Using this logic, the single vertical tail surface area of $0.0834\,\mathrm{m}^2$ results in a rudder surface area of $0.0334\,\mathrm{m}^2$. Having varied span and chord lengths of the rudder, the dimensions $b_r = 0.24\,\mathrm{m}$ and $c_r = 0.14\,\mathrm{m}$ were chosen. The corresponding acceleration in yaw from this rudder design is $\dot{r} = 0.493\,\mathrm{rad\,s^{-2}} = 28.3\,^\circ\,\mathrm{s^{-2}}$ (including a safety factor of 4, as was used in the elevator and aileron sizing). Note however that this method of sizing is vastly different from the elevator and aileron design and sizing process. When comparing the obtained yaw rate with pitch and yaw rates as shown in Table 7.7 and 7.9 respectively, it can be concluded that the rudder is vastly over-designed. Iteration of the rudder dimensions using a different method is therefore recommended.

7.10.4. Control Surface Design Conclusion

The dimensions of the control surfaces as designed in this section are summarized in Table 7.10. Furthermore, Figure 7.14 shows the dimensions of the control surfaces on the final UAV geometry.

Table 7.10: Summary of control surface geometry.

Control Surface	Length [m]	Chord [m]	Area [m^2]
Elevator	1.10	0.07	0.069
Aileron	0.50	0.10	0.047
Rudder	0.24	0.14	0.033

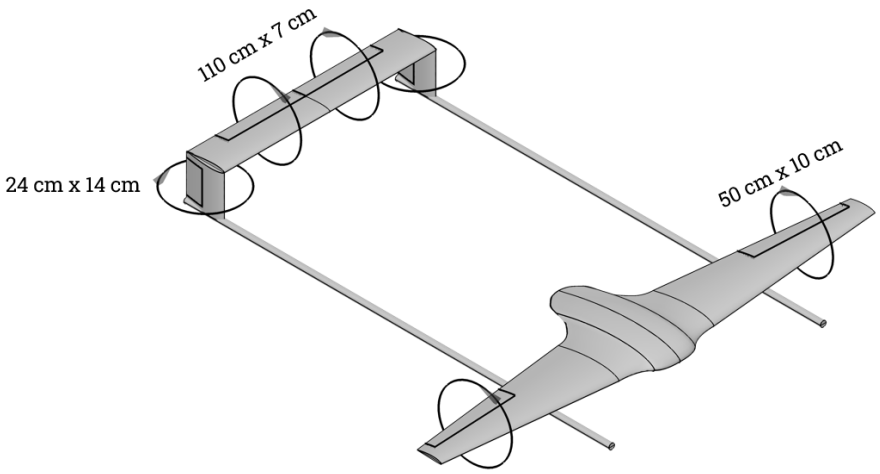

Figure 7.14: Final control surface dimensions as projected onto the UAV design geometry.

7.11. Aerodynamic Characteristics

In order to simulate the UAV in a flight model, the aerodynamic characteristics of the UAV need to be known. This is done by performing a stability analysis. This is performed by OpenVSP under nominal cruise conditions. In the stability analysis, several UAV parameters are varied in order to measure the aerodynamic coefficients of the UAV. These parameters are an increase in the angle of attack, an increase in the side slip angle, increasing the Mach number to 0.1 and applying a 1° positive deflection to both the ailerons, elevators and rudders. The lift distributions for this analysis are displayed in Figure 7.15.

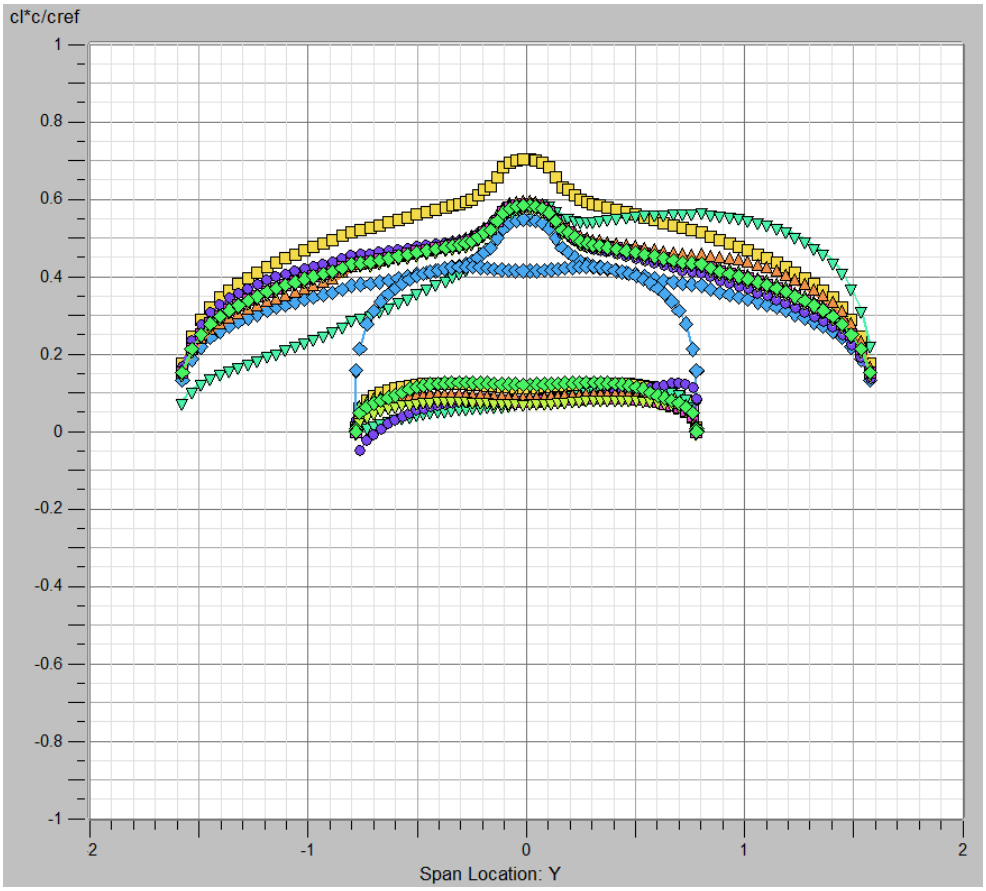

Figure 7.15: Chord normalised C_L distribution over the total wingspan for the analysis of the aerodynamic coefficients.

Chapter 8: Structures and Materials

The structure of the UAV is one of the integral parts of the UAV's shape and function. It should provide the attachment points for all other subsystems while being able to resist all loads that act upon its surface. The material used for the structure is also essential, as it is required to be sustainable, lightweight and stiff. The first section will cover the loads that can be expected to act upon the structure during operations. The second section will cover the material choice of the UAV structures. The final section will cover the structural design of the main load-carrying structures, namely the booms, wing and tail.

8.1. Expected Loads

The UAV is first divided into different sections when performing the material selection. Each group is expected to experience unique stresses, potentially necessitating other material choices accordingly. The UAV will be split up into the fuselage group, the wing group, the tail group and the landing gear. The main load to account for in the wing and tail group is bending, whilst axial loads are the main factor in the fuselage and landing gear. An in-depth analysis of the internal loads is performed in Section 8.3 which will determine the thickness and crosssection of the previously identified groups. For material selection, the type of load is more important than the actual load value and its distribution.

8.2. Materials Selection

Due to the high constraint on weight, lightweight material is needed, with high strength and stiffness properties. Therefore, even though the cost is high and the production is difficult, Carbon Fibre Reinforced Polymer (CFRP) is chosen as the main material for the UAV. The material is incredibly lightweight and has a high tensile strength and fracture resistance compared to Aluminium and Steel, as shown in Table 8.1. There are several different kinds of CFRP. A few examples of CFRP are Unidirectional CFRP, Fabric CFRP, Prepreg CFRP, Braided CFRP, Pultruded CFRP, and much more. Each type of CFRP and its respective production process can be advantageous in terms of manufacturability, strength, stiffness, impact resistance and strength directionality. As discussed before in Section 8.1 the loads for which the UAV shall be designed are bending and axial loads. These loads will appear in more than one direction limiting the CFRP choices when considering its directional strength characteristics. Furthermore, the design of the UAV is a non-continuous and complicated shape therefore not allowing a cheap mass production process such as pultrusion. The best option for the UAV would be a quasi-isotopic prepreg CFRP as this allows for precise control over fibre alignment and resin content, resulting in high-performance and lightweight parts.

CFRP TC380 Toray [1], CFRP TC250 Toray [2], Alloy Steel AISI5130 [3], and Aluminum 7075-T6 are analysed. The two CFRPs chosen are already quasi-isotropic layups so they are more easily comparable to the other two materials. The comparison shows the much higher specific strengths of the CFRP options making them favourable for a lightweight design. It is chosen to use a pre-impregnated fibre, whilst also choosing a thermoset composite that does not need an autoclave whilst curing, making the production of the UAV easier and cheaper. Some problems may arise using a composite material for the UAV structure. Common problems with CFRP are delamination, impact sensitivity, UV degradation, moisture absorption, manufacturing defects and buckling under compressive loads. These risks shall have to be mitigated and monitored, if a structural problem arises during the operation of the UAV a contingency plan shall be in place. UV degradation, moisture absorption, and manufacturing defects risks can be mitigated by sealing the CFRP from the environment with a weathertight coating and proper quality control. Risks such as delamination, and impact sensitivity will have to be monitored by a yearly inspection which will notify the maintenance team of any issues that need to be resolved. Buckling will have to be mitigated by making a proper structural design which may consist of locally increasing the plate

[1] https://www.toraytac.com/product-explorer/products/sbY3/TC380

[2] https://www.toraytac.com/product-explorer/products/sbY3/TC380

[3] https://www.quora.com/How-much-lighter-is-carbon-fiber-than-steel-and-aluminum-How-much-stronger-is-it

thickness, adding stiffeners where needed or tailoring the layup of carbon fibres to enhance the plate's resistance to buckling in specified directions.

Lastly, due to the risk of the UAV experiencing thermal runaway, fire-resisting carbon fibre was highly considered. The fire-resisting carbon could be either purchased off-the-shelf or a fire-resistant coating could be used over the chosen carbon fibre. Due to the limited options for off-the-shelf fire-resisting carbon, it was decided to use a Boric acid mixture as a coating. The boric acid mixture is sustainable, fire-resistant, and will not change the properties of the fibres significantly [4].

Table 8.1: Material Selection.

Material	E-Modulus [GPa]	Tensile Strength [MPa]	Density[gcm^{-3}]	Specific Strength[-]
CFRP TC380 Toray	61.8	1028	1.55	663.225
CFRP TC250 Toray	60.5	781	1.55	503.87
Alloy Steel AISI5130	205	1275	7.85	162.42
Aluminum 7075-T6	71.7	570	2.81	202.84

The charging system of the UAV system will consist of two metal pads that are integrated into the landing platform. These will be connected to the positive and negative sides of a power source. When the UAV lands, it will land on either side of the landing gear on a different pad, resulting in a closed loop as described in subsection 5.7.4. Underneath the landing gear, there will be two smaller metal rods integrated that will directly connect to the pads. These rods will be connected to the batteries. Hence, the batteries can be recharged when the electrical circuit is closed. It is important that the connection between the pads and the landing gear has a low electrical resistance, as this would otherwise significantly increase the voltage required for successful power transfer, resulting in a temperature increase at the contact point. A metal should be selected that has high electrical conductivity and a reasonable melting temperature to reduce the chance of suturing. Since the pads will be exposed to the atmosphere and rain, the material should be corrosion-resistant. Next to that, the material should also be non-toxic as toxicity should be avoided in nature reserves. In addition, the recyclability of the material is taken into account. If the part fails and it has to be replaced, the failed part can be melted and manufactured into a new part. Finally, the cost of the material should be as low as possible to reduce the production costs of the UAV. With these characteristics in mind, the material for the charging system can be selected.

Based on materials that are commonly used as electrical connectors, it was quickly found that brass was the best candidate for the purpose of the UAV charging system. Brass has a relatively high conductivity, due to the great amounts of copper in the alloy. Typically, brass alloys have a relatively low melting temperature when compared to other metals. However, the melting temperature is deemed sufficiently high to perform its function. Brass is also proven to be corrosion-resistant, so it is perfect for outside use. As for recyclability, most alloys are fully recyclable by melting and re-manufacture the part. The material is easily machinable and relatively inexpensive. Brass alloys can differ between nontoxic, toxic, and dezincification. The toxicity of brass is dependent on whether or not the alloy consists of lead. This element is included to improve machinability[5], however it is harsh on the environment. Dezincification is a form of indirect corrosion that selectively removes zinc from an alloy[6]. This will leave a porous material that is not fit as an electrical connector. For these reasons, the selected brass type should be free of lead and dezincification free. The latter is achieved when there is less than 15 % zinc or there is arsenic in the alloy. There are a few brass alloys available that satisfy all these requirements. The material CW511L DZR Brass was found to be the best brass type for the landing gear charging contacts.

The tail will require a foam core because of reasons that will be addressed in the tail design section. The Rohacell foam is selected, due to its resistance to high temperatures, that are required for carbon fibre laminations. It is also stiff enough to provide structural support, while also being lightweight.

[4] https://www.degruyter.com/document/doi/10.1515/epoly-2019-0010/html?lang=en

[5] https://journals.sagepub.com/doi/full/10.1177/0309324718796384#:~:text=Regarding%20machining%2C%20lead%20has%20been,chips%20and%20higher%20tool%20wear.

[6] https://www.corrosionpedia.com/definition/384/dezincification

8.3. Structural analysis

For structural analysis, the UAV components are split up into three different parts. These are the blended wing body, the tail structure and the booms that connect the two. Next to that, there are different critical load cases during the mission phases. Flying at maximum velocity will induce the highest amount of lift and drag, resulting in a critical compression case for the top surface of the wing and empennage. A second critical case for the boom is the maximum velocity in vertical take-off because the thrust of the propellers and the high drag of the tail and wing will exert forces on the boom that should be resisted. The final load case for the booms only is when the UAV is stationary during the charging phase of the mission. The weight of the motors and tail should not cause the booms of the UAV to fail. The combination of this yields nine cases that should be analysed separately. This process is documented in this section.

8.3.1. Boom Structure

The boom structure is analysed first. It is decided that the boom will have a hollow circular cross-section as this is the most efficient structure from an aerodynamic perspective. It is expected that the structure will induce a significant amount of drag, hence taking the most aerodynamic boom design is considered essential. This cross-section is also the strongest cross-section in torsion and is considered stiff enough under bending and shear loads. Due to many different point loads, the simplicity of this cross-section makes it possible to iterate and adapt easily.

To begin the analysis, the free-body diagrams for each load case. The side view of the boom with the applied external forces and reaction forces can be found in Figure 8.1. The left side of the boom is the position of the front VTOL propeller and the right side is the location of the tail structure. It is assumed that the wing is stiff compared to the boom and therefore the attachment point can be considered clamped. The quarter chord point of the wing is the thickest location of the wing, and therefore the clamped position is located at the quarter chord line of the airfoil at the span-wise location of the boom.

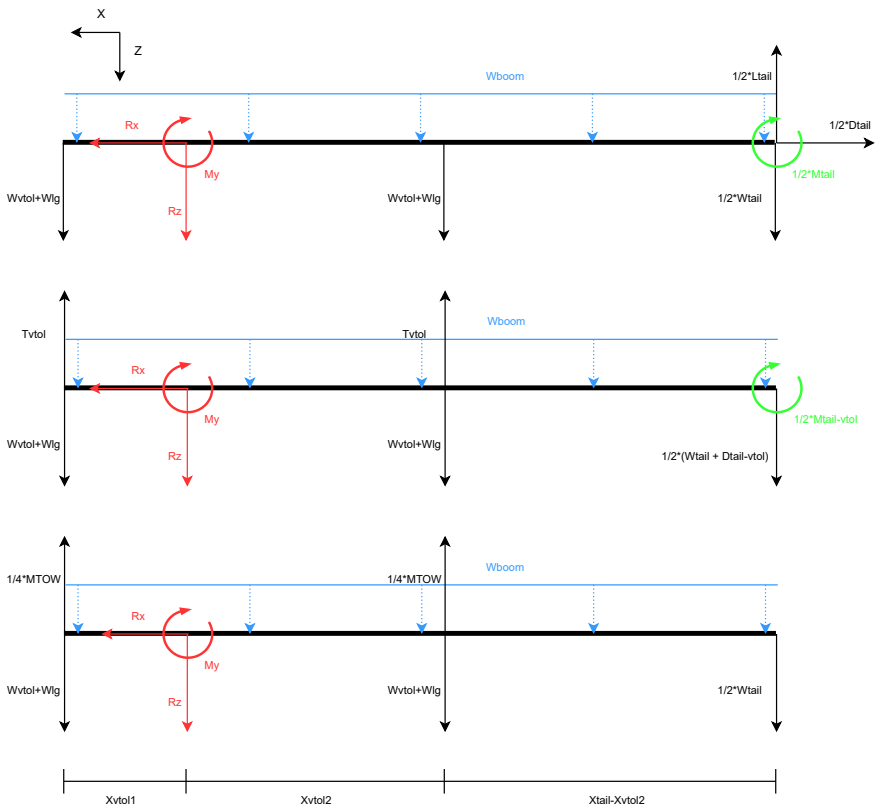

Figure 8.1: Free body diagrams of the boom under the different load cases. From top to bottom; Maximum velocity, Vertical take-off, Stationary.

In these diagrams, the applied forces are black, the distributed loads are blue, the applied moments are green

and the reaction forces are red. From these diagrams, the reaction forces can be calculated. These follow from the equations given below. The lengths x given are all with respect to the clamped location.

For maximum velocity:

$$\sum F_x+ : R_x = \frac{1}{2}D_{tail}$$

$$\sum F_z+ : R_z = \frac{1}{2}(L_{tail} - W_{tail}) - 2(W_{vtol} + W_{lg}) - \omega_{boom}l_{boom}$$

$$\sum M_R+ : M_y = -\frac{1}{2}M_{tail} - (W_{vtol}+W_{lg})(x_{vtol_2} - x_{vtol_1}) + \frac{1}{2}(L_{tail} - W_{tail})x_{tail} - \frac{1}{2}\omega_{boom}l_{boom}(x_{tail} - x_{vtol})$$

For vertical take-off:

$$\sum F_x+ : R_x = 0$$

$$\sum F_z+ : R_z = 2(T_{vtol} - W_{vtol} - W_{lg}) - \omega_{boom}l_{boom} - \frac{1}{2}(W_{tail} + D_{tail_{vtol}})$$

$$\sum M_R+ : M_y = -\frac{1}{2}M_{tail} + (T_{vtol} - W_{vtol} - W_{lg})(x_{vtol_2} - x_{vtol_1}) - \frac{1}{2}(W_{tail} + D_{tail_{vtol}})x_{tail} - \frac{1}{2}\omega_{boom}l_{boom}(x_{tail} - x_{vtol})$$

For vertical take-off:

$$\sum F_x+ : R_x = 0$$

$$\sum F_z+ : R_z = 2\left(\frac{1}{4}MTOW - W_{vtol} - W_{lg}\right) - \omega_{boom}l_{boom} - \frac{1}{2}W_{tail}$$

$$\sum M_R+ : M_y = -\frac{1}{2}M_{tail} + \left(\frac{1}{4}MTOW - W_{vtol} - W_{lg}\right)(x_{vtol_2} - x_{vtol_1}) - \frac{1}{2}W_{tail}x_{tail} - \frac{1}{2}\omega_{boom}l_{boom}(x_{tail} - x_{vtol})$$

With these reaction forces and all known applied external forces, the internal loads along the boom can be computed. The axial forces simply result from the equations above, while the shear force can be computed in a more complex way. This is done, using Macaulay's method [15]. The resultant shear force can be integrated to get the internal bending moments along the boom. The length-wise internal loads can be given with equations like the ones provided below. These take the maximum velocity case as an example.

$$N(\mathbf{x}) = 0 + R_x[\mathbf{x} - x_{vtol_1}]^0$$

$$V_z(\mathbf{x}) = -W_{vtol} - W_{lg} - \omega_{boom}\mathbf{x} - R_z[\mathbf{x} - x_{vtol_1}]^0 - (W_{vtol} + W_{lg})[\mathbf{x} - (x_{vtol_1} + x_{vtol_2})]^0$$

$$M_y(\mathbf{x}) = -(W_{vtol}+W_{lg})\mathbf{x} - \frac{1}{2}\omega_{boom}\mathbf{x}^2 - R_z[\mathbf{x} - x_{vtol_1}]^1 + M_y[\mathbf{x} - x_{vtol_1}]^0 - (W_{vtol}+W_{lg})[\mathbf{x} - (x_{vtol_1} + x_{vtol_2})]^1$$

These relations can be plotted in diagrams to give a better representation of the internal loads. These can be found below for every load case.

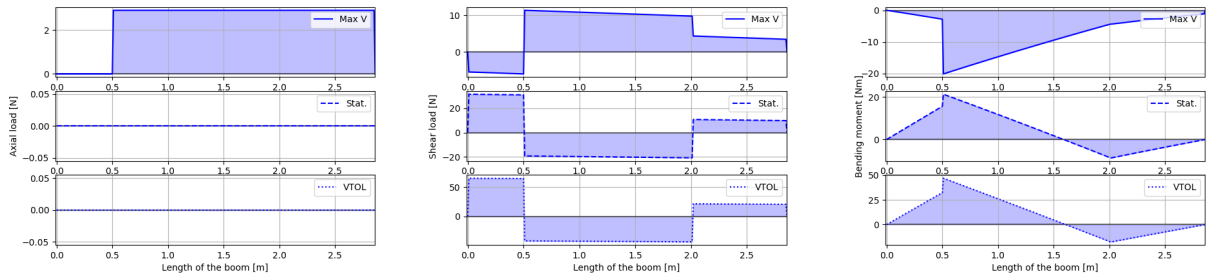

(a) Internal axial force against length.

(b) Internal shear force against length.

(c) Internal bending moment against length.

Figure 8.2: Internal axial force, shear force and bending moment diagrams of the boom under three different load cases.

According to the Euler-Bernoulli beam theory, the internal bending moment equation can be used to integrate and get the length-wise angular twist equation. A second integration step will yield the deflection of the boom. The equations for the maximum velocity example are given below.

$$\theta(\mathbf{x}) = \frac{1}{EI_{yy}}\left(-\frac{1}{2}(W_{vtol}+W_{lg})\mathbf{x}^2 - \frac{1}{6}\omega_{boom}\mathbf{x}^3 - \frac{1}{2}R_z[\mathbf{x}-x_{vtol_1}]^2 + M_y[\mathbf{x}-x_{vtol_1}]^1 - \frac{1}{2}(W_{vtol}+W_{lg})[\mathbf{x}-(x_{vtol_1}+x_{vtol_2})]^2 + C\right)$$

$$\delta(\mathbf{x}) = \frac{1}{EI_{yy}}\left(-\frac{1}{6}(W_{vtol}+W_{lg})\mathbf{x}^3 - \frac{1}{24}\omega_{boom}\mathbf{x}^4 - \frac{1}{6}R_z[\mathbf{x}-x_{vtol_1}]^3 + \frac{1}{2}M_y[\mathbf{x}-x_{vtol_1}]^2 - \frac{1}{6}(W_{vtol}+W_{lg})[\mathbf{x}-(x_{vtol_1}+x_{vtol_2})]^3 + C\mathbf{x} + D\right)$$

Using these formulas, the deflection at every point of the boom can be determined. This deflection should not exceed the set requirement. In Figure 8.3 these diagrams can be found. Note that the area under the graph is coloured if the parameter is constraining.

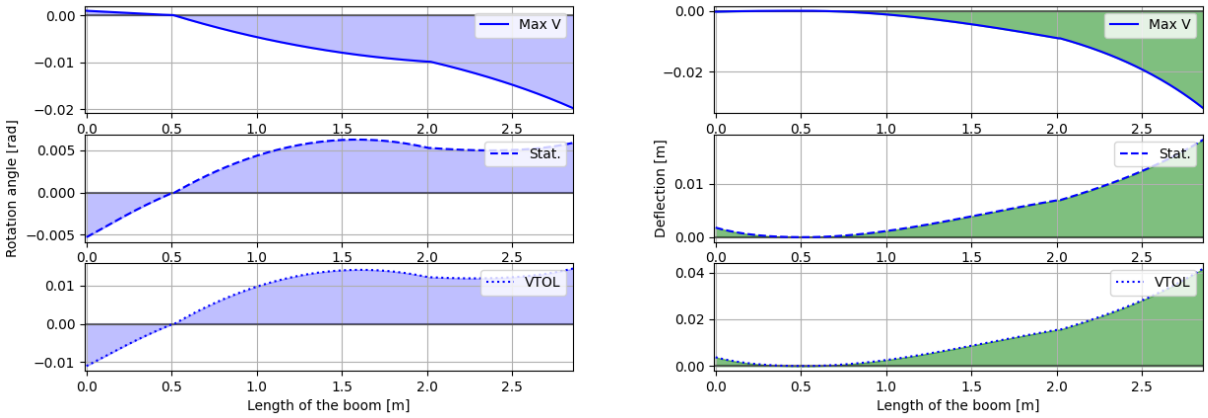

(a) Rotation angle of boom against length.

(b) Deflection of boom against length.

Figure 8.3: Rotation angle and deflection diagrams of the boom under three different load cases.

Finally, the structural performance with respect to the compression, tension and shear stresses should be analysed. The following equations can be used for a symmetric hollow thin-walled beam with a circular cross-section that is only loaded in two dimensions, axially and in shear [15].

$$\sigma_{max} = \pm\frac{M_r}{I_{yy}} + \frac{N}{A} \tag{8.1}$$

$$\tau_{max} = \frac{V_z Q_y}{I_{yy} t} = \frac{V_z A\bar{z}}{I_{yy} t} = \frac{8V_z rt}{3I_{yy}} \tag{8.2}$$

These equations can be used, together with the internal shear force and bending moment equations, to get the stress diagrams shown in Figure 8.4.

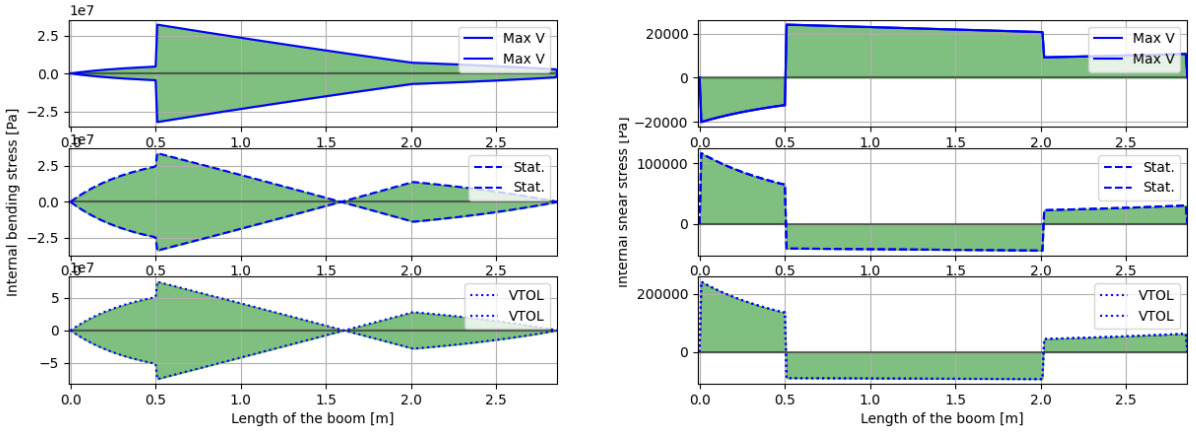

(a) Internal compression and tension stress against length.

(b) Internal shear stress against length.

Figure 8.4: Maximum stress diagrams of the boom under three different load cases.

The thickness and diameter of the boom are determined in an iterative process. The thickness and diameters are set to an initial value, after which the above diagrams are evaluated. When a structural characteristic exceeds the limits, the thickness and diameters are increased. After an acceptable structural design has been found, the design is optimised to reduce the overall weight. It was found that deflection is the limiting factor since T800S CFRP has a maximum strain of two percent. Finally, a boom design was found that is stiff enough and does not deflect too much. In Table 8.2 the dimensions of the boom structure can be found.

Table 8.2: The boom structural parameters.

Parameters	Section 1	Section 2	Section 3	Unit
Length	0-500	500-2005	2005-2857	[mm]
Diameter	15-20	20	20-16.5	[mm]
Thickness	0.5	0.5	0.5	[mm]

8.3.2. Wing structure

This section details the structural design of the main wing. The design loads upon which the structure is based are presented first. The analysed resulting stresses are then explained. The final design is presented in Table 8.3, alongside a discussion and review of the section's results.

Design Loads

Three potential design load cases are identified: VTOL flight during takeoff, forward flight at V_{max} with $+n_{ult}$, and forward flight at V_{cruise} with $-n_{ult}$. The most constraining case is determined by applying the corresponding external loads and identifying which results in the greatest internal loads. In order to calculate the internal loads, the half-span is modelled as a cantilever beam. This assumption does not perfectly reflect reality, since the portion of the wing containing the payload is not clamped in place. However, it still allows for a sufficiently accurate analysis of the wing upon which the internal structure can be based.

The generalised Free Body Diagrams of the external loads on the wing are shown in Figure 8.5. The magnitudes and directions of the forces and moments may vary for different flight conditions.

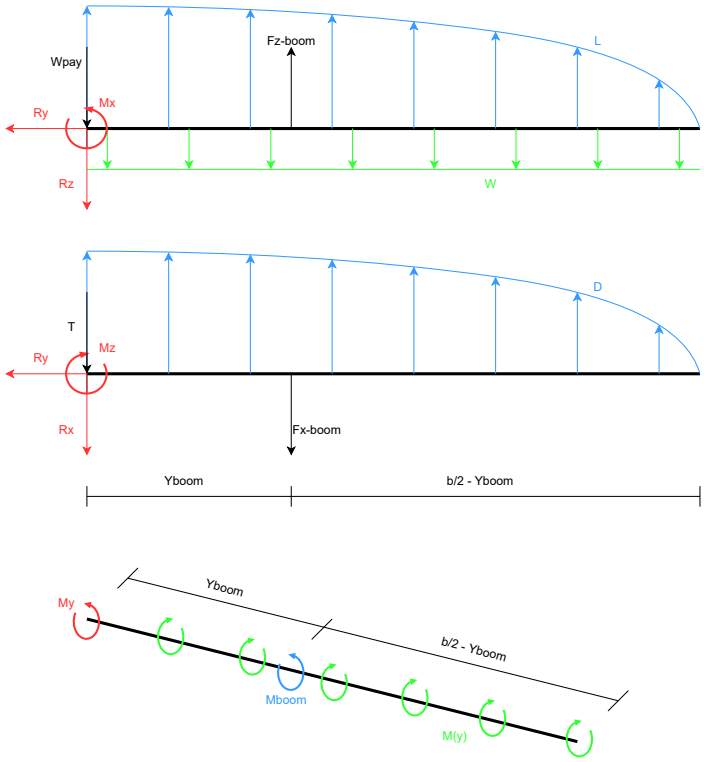

Figure 8.5: Generalised Free Body Diagrams of the external wing loads.

The most constraining load cases are forward flight at V_{max} and with a load factor $+n_{ult}$, and forward flight at V_{cruise} and with a load factor $-n_{ult}$. While the former case generates higher magnitude stresses in the wing, the negative load factor of the latter causes it to be constraining for the compression strength of the bottom wing skin. The resulting internal loads for the two design load cases are presented in diagrams Figure 8.6 and Figure 8.7, respectively.

The design loads presented in Figure 8.6 and Figure 8.7 are multiplied by 1.5 safety factors for all internal structural analyses. This allows for a sufficient margin in case the loads are greater than predicted or the material behaves worse than expected.

Wing Structure Design Procedure

A summary of the wing design process is described to provide an overview of the steps taken to arrive at a final design based on the previously discussed design loads.

Due to the relatively low loads experienced by the wing, it was determined that a wing box structure was not required. This is made possible by the high mechanical properties of TC380, allowing for a thin skin to large external loads. The thickness required to sustain the design loads was determined by analysing the normal and shear stresses resulting from said loads. This was performed by discretising the half-span and calculating the stresses at each section.

It was apparent that compression buckling was the most constraining failure mode for the wing skin. Therefore, an analysis was performed for the placement and sizing of ribs and stringers, respectively. Ribs reduce the effective sheet length and stiffeners both reduce the effective sheet width and increase cross-sectional critical buckling stress, both elements therefore increase the critical buckling stress. This design process was iterative, wherein stiffener analysis was performed based on a chosen arrangement of ribs. Then, based on the feasibility and optimality of the resulting structure, it was decided whether or not a new rib arrangement was required. This trade-off was based on weight, feasibility given the space inside the wing, and manufacturability.

Analysis of Stresses in Wing Skin

The stresses acting on the wing skin are determined throughout the half-span. The skin is assumed to be of a constant thickness to improve manufacturability, and therefore it is sized based on the maximum stress incurred at any point in the wing. The skin is sized to carry both the normal and shear stresses incurred from the design

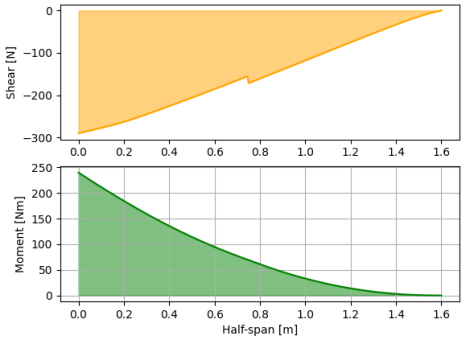

(a) yz-plane (lift plane).

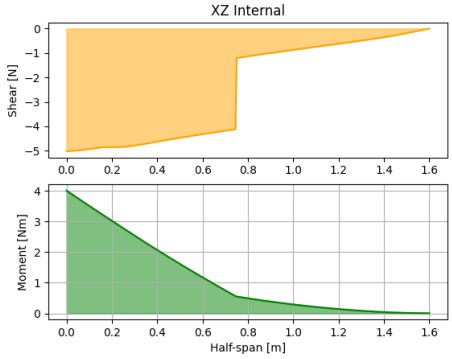

(b) xy-plane (drag plane).

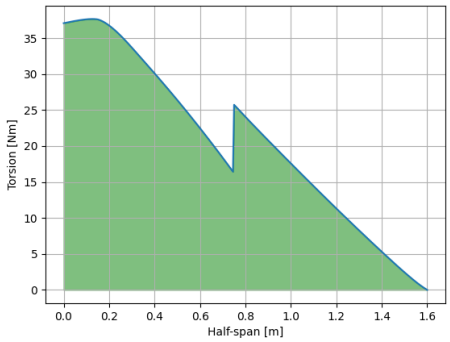

(c) Torsion

Figure 8.6: Wing internal loads at V_{max} and $n = n_{ult}$.

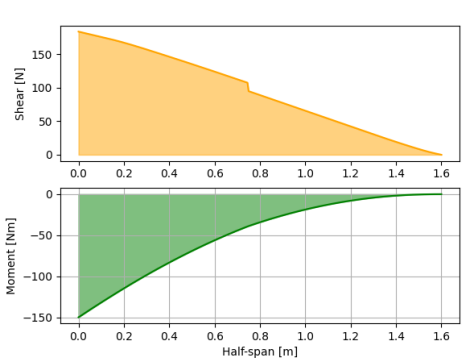

(a) yz-plane (lift plane).

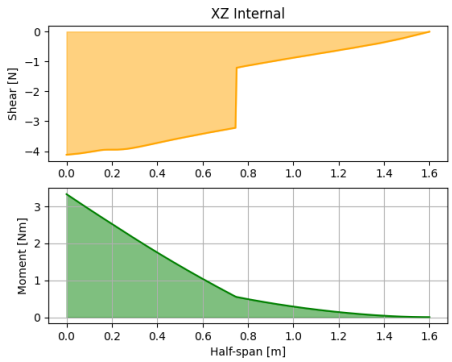

(b) xy-plane (drag plane).

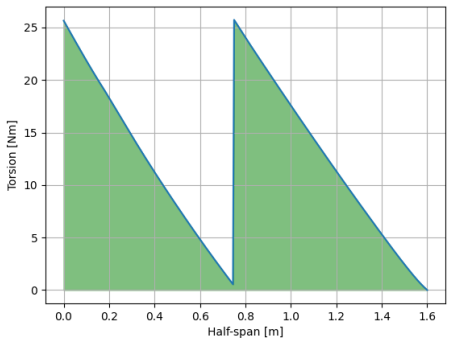

(c) Torsion

Figure 8.7: Wing internal loads at V_{cruise} and $n = -n_{ult}$.

loads. The stresses are analysed by discretising the wing into cross-sections and analysing the stresses based on the local cross-sectional geometry and loading.

The normal stresses in the wing skin are calculated according to Equation 8.3 [16].

$$\sigma_z = \frac{(M_x I_{yy} - M_y I_{xy})y + (M_y I_{xx} - M_x I_{xy})x}{I_{xx} I_{yy} - I_{xy}^2} \tag{8.3}$$

The wing is modelled as a thin-walled beam, which holds because the skin thickness is significantly smaller than either the chord length or airfoil thickness. Therefore, the shear stresses in the wing are analysed by calculating shear flows in each distressed section. The shear flow due to pure shear is determined using Equation 8.4 [16].

$$q_s = q_b + q_{s0} = \frac{V_y I_{yy} - V_x I_{xy}}{I_{xx} I_{yy} - I_{xy}^2} \int_0^s t y ds - \frac{V_x I_{xx} - V_y I_{xy}}{I_{xx} I_{yy} - I_{xy}^2} \int_0^s t x ds + q_{s0} \tag{8.4}$$

The basic shear flow q_b is determined by making a "cut" at the leading edge of the local airfoil and subsequently analysing it as an open section beam. The additional constant shear flow q_{s0} is calculated using Equation 8.5, which presents the moment equivalence between the shear forces and internal shear flow, about the shear centre [16].

$$V_x \eta - V_y \xi = M_b + 2A q_{s0} \tag{8.5}$$

Where η and ξ represent the position of the shear centre with respect to the location of the internal shear forces, in the vertical and chordwise directions, respectively. The value M_b is the moment about the shear centre due to the calculated basic shear flow.

Since the shear forces are assumed to act at the shear centre, Equation 8.5 simplifies to Equation 8.6

$$q_{s_0} = -\frac{M_b}{2A} \tag{8.6}$$

Since the pure shear forces are assumed to act as the shear centre of each airfoil, the shear flow due to the internal torque load must be added. This is determined using Equation 8.7 [16].

$$q_t = \frac{T}{2A} \tag{8.7}$$

The resultant shear flow is $q_{\text{resultant}} = q_b + q_{s0} + q_t$, and therefore the maximum shear stress in the section is $\tau_{\text{max}} = \frac{\max(q_{\text{resultant}})}{t}$.

Based on the material properties of TC380 and the discussed stress calculations, only a single layer of the CFRP weave is required to carry all design loads. However, using only a single layer presents risks when considering delamination, because there is no safety factor as there are no subsequent layers to carry the loads. Typically odd numbers of layers are preferred, to ensure symmetric fibre orientations, and therefore three layers of TC380 are chosen for the wing skin. The resulting stresses along the wing half-span are shown in Figure 8.8, for both design load cases.

The resulting stresses in Figure 8.8 show that the wing skin can carry all the required design loads, based on the strength properties of TC380 [17].

Stiffener and Rib Design

In order to mitigate buckling, ribs and stiffeners are introduced into the internal wing structure. Two unique stiffeners are designed, one for the fuselage and one that runs along the length of the wing. An arrangement of ribs is first chosen, sectioning off the wing, and then a single stiffener is placed along both the top and bottom wing skin. Note that a mandatory rib is placed on either side of the connection point between the fuselage and the wing. The required stiffener geometry is then calculated, and interaction in the process is performed based on the design's manufacturability, weight, and feasibility. To ease manufacturing, the stiffener is sized for the top skin, since it experiences the greatest compressive stresses, and is then mirrored on the bottom skin.

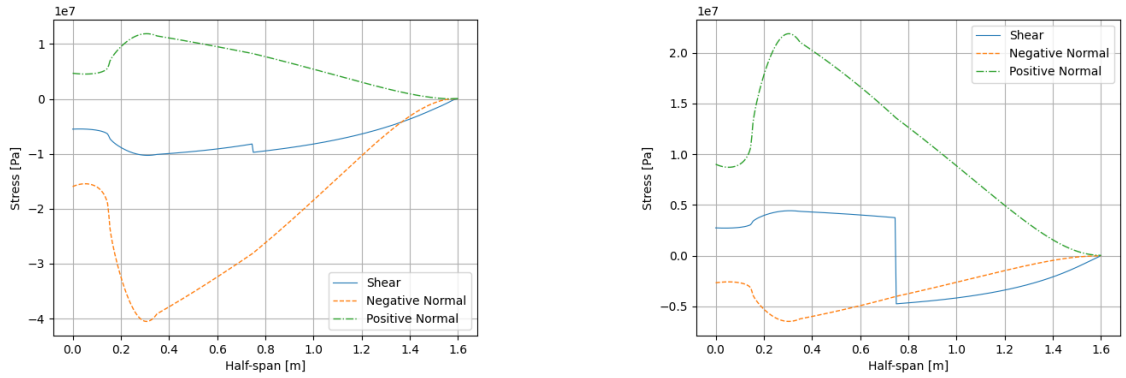

(a) V_{max} and $+n_{ult}$ **(b)** V_{cruise} and $-n_{ult}$

Figure 8.8: Shear and positive/negative normal stress distributions along the half-span for three layers of TC380, for both design loads.

Designing the stiffener requires consideration of both its own column buckling/crippling as well as its stiffening effect on the wing skin. The stiffener is first designed to meet the column buckling requirement. The column buckling stress is defined by Equation 8.8, where C is the end fixity coefficient and is dependent on the boundary conditions of the column. The stiffener in the wing is assumed to be pinned at each rib, resulting in $C = 1$, and in the fuselage it is fixed at the rib and free on the other end, resulting in $C = 0.25$ [18]. An L-beam stiffener because its height is not constrained by the mirrored stiffener as well as its simple manufacturing. The area and area moments of inertia of the stiffener are presented in Equation 8.9 and Equation 8.10, respectively. Where t_{stiff}, w_{stiff}, and h_{stiff} are the thickness, width, and height, respectively, and x_c and y_c are the local coordinates of the centroid. Note that h_{stiff} is constrained to 90% of the smallest airfoil thickness, to allow margin for both stiffeners to be placed inside the wing.

$$\sigma_{cr} = \frac{C\pi^2 EI}{AL^2} \tag{8.8}$$

$$A_{stiff} = w_{\text{stiff}} t_{\text{stiff}} + (h_{\text{stiff}} - t_{\text{stiff}})\, t_{\text{stiff}} \tag{8.9}$$

$$I_{xx_{\text{stiff}}} = \frac{th^3}{12} + ht\left(\frac{h}{2} - y_c\right)^2 + \frac{(w-t)t^3}{12} + (w-t)t\left(\frac{t}{2} - y_c\right)^2 \tag{8.10}$$

$$I_{yy_{\text{stiff}}} = \frac{(h-t)t^3}{12} + (h-t)t\left(\frac{t}{2} - x_c\right)^2 + \frac{tw^3}{12} + wt\left(\frac{w}{2} - x_c\right)^2 \tag{8.11}$$

After sizing the stiffener for column buckling, its effect on the buckling of skin is studied. In the following analysis, the top and bottom half of the wing are each modelled as a thin plate. Since the moments causing compression on the top and bottom half of the wing (e.g. lift and weight) are significantly larger than those that induce stresses at the leading and trailing edge (e.g. drag), the simplification is made that the wing can be separated into a top and bottom panel. In the design loads discussed above, it will be the case that compression almost exclusively occurs on either the top or bottom half of the panel, allowing for the separation of the two. The analysis relies upon thin plate buckling theory, which assumes a constant width plate. The skins throughout the entire wing are not constant in width, however, the sections created by placing ribs do not have a large variation in width. Since one continuous stringer is used throughout the wing, its design is based on the most constraining section of the wing, while assuring that it fits throughout the wing. Finally, the CFRP wing skins are analysed using the same equations as the Aluminium stiffeners. While more applicable to Aluminium, the theory still provides a basic understanding of the CFRP wing skins, especially due to the quasi-isotropic nature of TC380.

The ratio of crippling stress to yield stress of a thin plate is described by Equation 8.12 [18]. The stiffener is modelled as two thin plates, joined at the corner. For each thin plate in stiffener, $\alpha = 0.8$ and $n = 0.6$. If

$\sigma_{cc}/\sigma_y > 1$ then σ_y is considered in subsequent calculations, not crippling stress. The crippling stress of the stiffener is then defined by the weighted average of the crippling stresses of the two thin plates, as defined in Equation 8.13. The factor K is chosen based on Figure 8.9, wherein each thin plate is assumed to be simply supported at the corner and at each end of the stiffener, and free on the free edge, namely the SSFS boundary condition. Conservatively, it is assumed that $K = 0.425$ for both thin plates of the stiffener. The crippling stress of the wing skin is calculated according to Equation 8.12, where it is assumed $\alpha = 1$ and $n = 0$. As with the stiffener, the plate is assumed to have SSFS boundary conditions, resulting in $K = 2$ in the fuselage and $K = 0.425$ in the wing. The width of the plate is half the original width due to the presence of a stiffener. The crippling stress of the stiffened wing skin is defined by Equation 8.13, where the elements considered are the wing skin and stiffener. The stiffener design resulting from the column buckling analysis is subsequently altered if it is insufficient in preventing thin plate buckling, therefore arriving at a final design.

$$\frac{\sigma_{cc}}{\sigma_y} = \alpha \left(\frac{K}{\sigma_y} \frac{\pi^2 E}{12(1-\nu^2)} \left(\frac{t}{b} \right)^2 \right)^{1-n} \tag{8.12}$$

$$\sigma_{cc} = \frac{\Sigma \sigma_{cc}^{(i)} A_i}{\Sigma A_i} \tag{8.13}$$

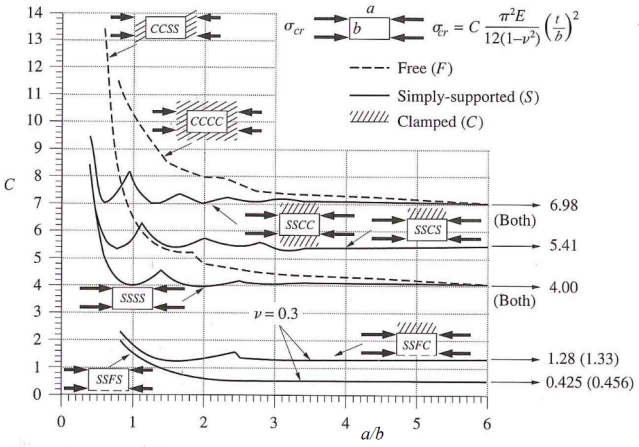

Figure 8.9: Coefficient C for various boundary conditions [19].

Wing Structural Design and Discussion

The structural design resulting from the previously described analyses is presented in Table 8.3.

Table 8.3: Summary of the internal wing structure

Structural Element	**Value**
Skin Thickness [mm]	0.681
Rib locations along half-span [m]	[0.35, 0.35, 0.77, 1.18]
Rib thickness $[mm]$	1.5
Stiffener designs (h × w × t × L) [mm]	[17 × 17 × 1.8 × 350] [10 × 10 × 1.5 × 1250]
Wing mass [kg]	3.36

While the previously discussed calculations show that the designed wing box can sustain all required loads, there are some aspects that must be discussed which relate to the efficiency and feasibility of the design. Implementing a wingbox may have been a more lightweight solution, however, a full analysis would be required to confirm that. The simplification that splits the top and bottom half of the wing in two, although not far removed from the real loading case, may not fully represent the real-life situation. The ribs were not thoroughly designed. They are assumed to be made of AL 7075-T6, and their thickness was estimated based on the other wing structure

geometries. Further analysis is required to determine their structural integrity and feasibility. Another concern revolves around space in the fuselage. While there is space for the stiffener to be attached to the top skin, there is a lack of space at the bottom skin. This issue was recognized at a late stage of the design and therefore was not enough time to consider iterating/changing the design. However, two solutions are presented and would be explored given additional time. The first solution is to redesign the fuselage section of the wing. Either by reorganising the components inside or simply increasing the airfoil thickness, enough space could be generated to fit manufacturable stiffeners. A second solution is to add more layers of CFRP to the bottom of the fuselage section. It would require an additional 15 layers of TC380, increasing the UAV weight by 1 kg. However, while feasible, there was not enough time to implement this change by the time the issue was discovered. As aforementioned, a further iteration would be performed to account for this change. Additionally, the calculations presented do not take into account the effects of hatches/holes in the fuselage or the bonding/fastening of different structural elements. A further investigation would be required to confirm the structural properties in these areas. A final suggestion is to perform the following analyses: vibrational analysis, tip deflection, and angle of twist. It is important for the eigenfrequencies of the wing to be outside of the frequencies generated by the spinning of the propellers. Furthermore, analysing the tip deflection and angle of twist would ensure the proper functioning of the wing while in operation.

8.3.3. Tail Structure

The process for tail structural design is similar to that of the main wing. However, the tail is smaller than the wing, which makes it considerably unnecessary to add stiffeners to the tail to recuse buckling. Besides, the tail is not required to provide room for wiring. Therefore it was decided to fill the tail with foam. Adding a foam core also eliminates the effect of sheet buckling, as the foam core will resist this type of failure mode [20]. Therefore a sheet buckling analysis is not required for the tail structure. However, this method does introduce new failure modes, which should be analysed in order to generate a strong design. These failure modes are not included in this report, yet it is highly advised to analyse these in further design iterations. To design the tail thickness, the stress distributions were analysed. These can be found in Figure 8.10. It can be seen that with a thickness of 0.5 mm, the stresses are not close to the failure modes.

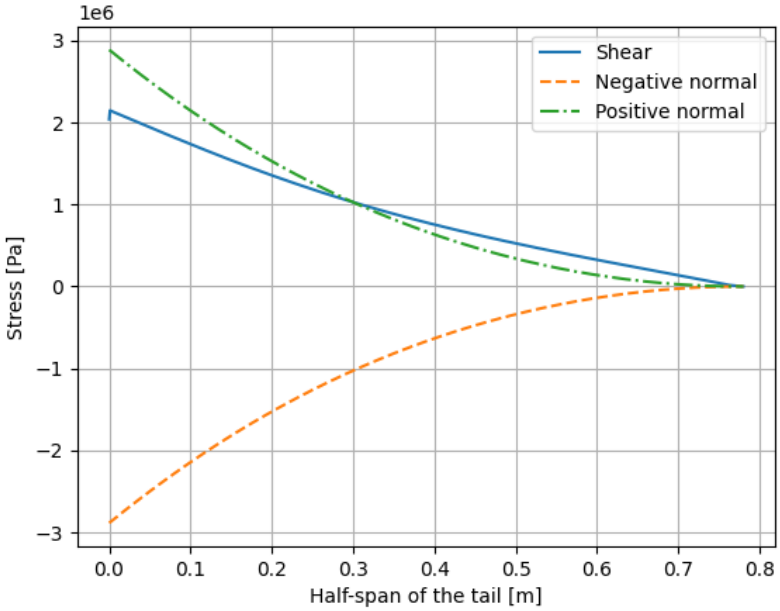

Figure 8.10: Internal stresses of the tail structure with a thickness of 0.5 mm.

The resulting design is two layers of TC380 wrapped around a foam core of ROHACELL foam[7]. While only two layers of CFRP may present the delamination and insufficient safety factors risk, the presence of foam provides additional structural integrity and is thus not as risky as hollow layers.

[7] https://performance-foams.evonik.com/en/products-and-solutions/rohacell/rohacell-rima-170039.html, accessed on 10-06-2023

Chapter 9: Layout

The final design configuration and layout have been designed using the CATIA environment on 3DExperience. In Figure 9.1 several views of the UAV can be seen, showing the location of the VTOL and cruise propellers. Furthermore, the positioning of the booms and the tail can also be seen with respect to the wings and each other. Lastly, at the front of the booms the antenna protrudes together with a pitot tube at the bottom. The landing gear below each VTOL propeller is also visible note the brass contact points on the landing gear, these will be used to automate the charging. A schematic drawing showing the top, front and side view has also been provided in Figure 9.2.

(a) Front View

(b) Top View

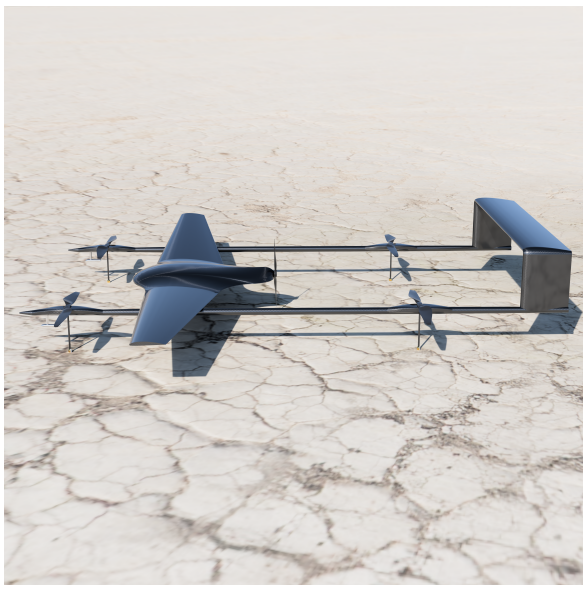

(c) Side View

Figure 9.1: several exterior views of the UAV.

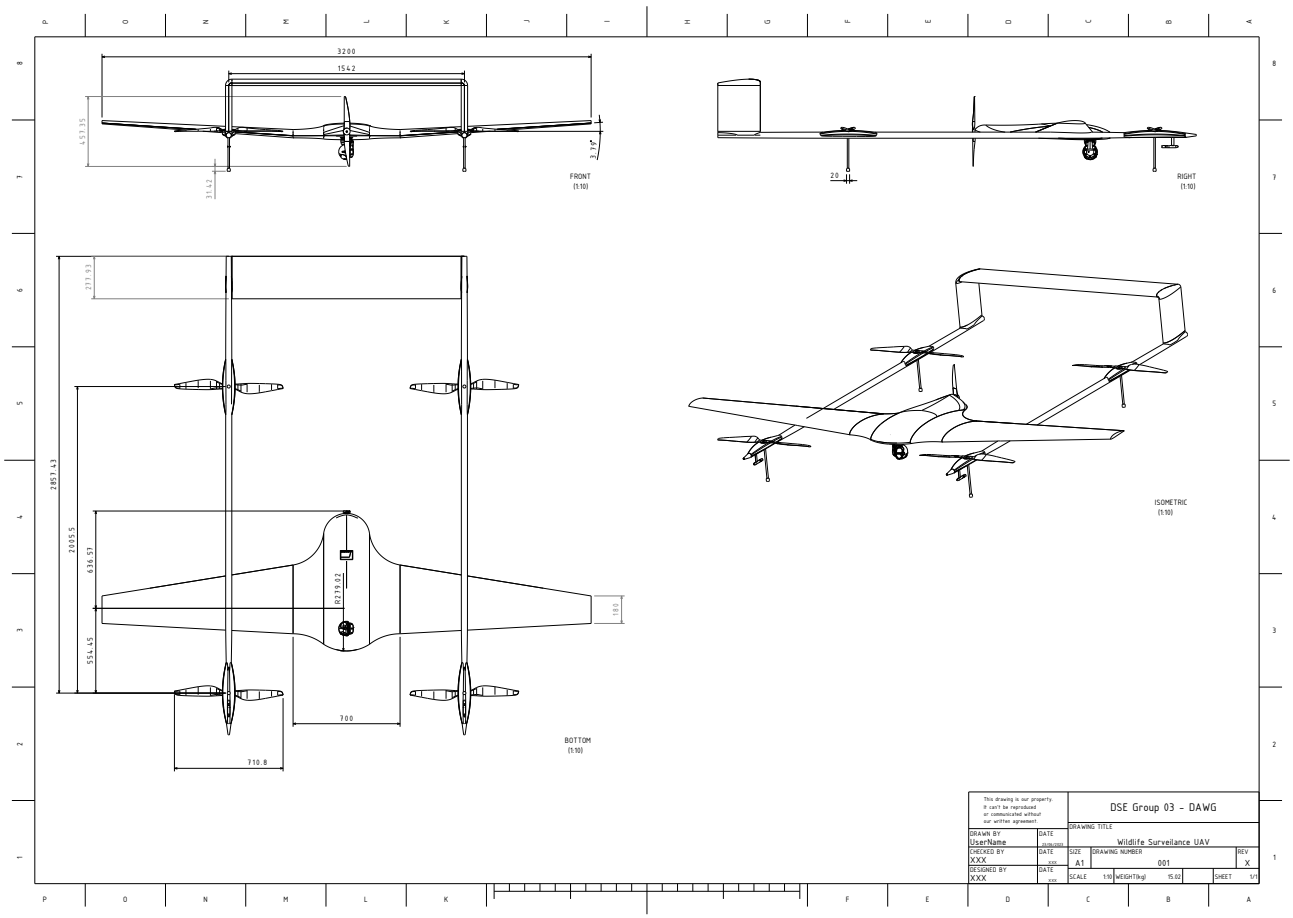

Figure 9.2: Engineering Drawing of the UAV

In Figure 9.3 the internals of the UAV have been modelled. In the left image, from left to right, the VTOL ESCs, camera (bottom), the motherboard with its corresponding chips (top), batteries, flight computer, LiDAR, cruise ESC, cruise motor, and cruise propeller can be seen. The right image shows the electrical power connections between the ESCs, motors, and batteries. The cable portrayed on the right continues outwards into the boom flowing into the VTOL motors.

Figure 9.3: Internal View of the UAV. The left image shows the overall view, while the right image focuses on the electrical wiring.

Lastly, a final render can be found in Figure 9.4. Showing the blended wing body and the connection between all parts of the design.

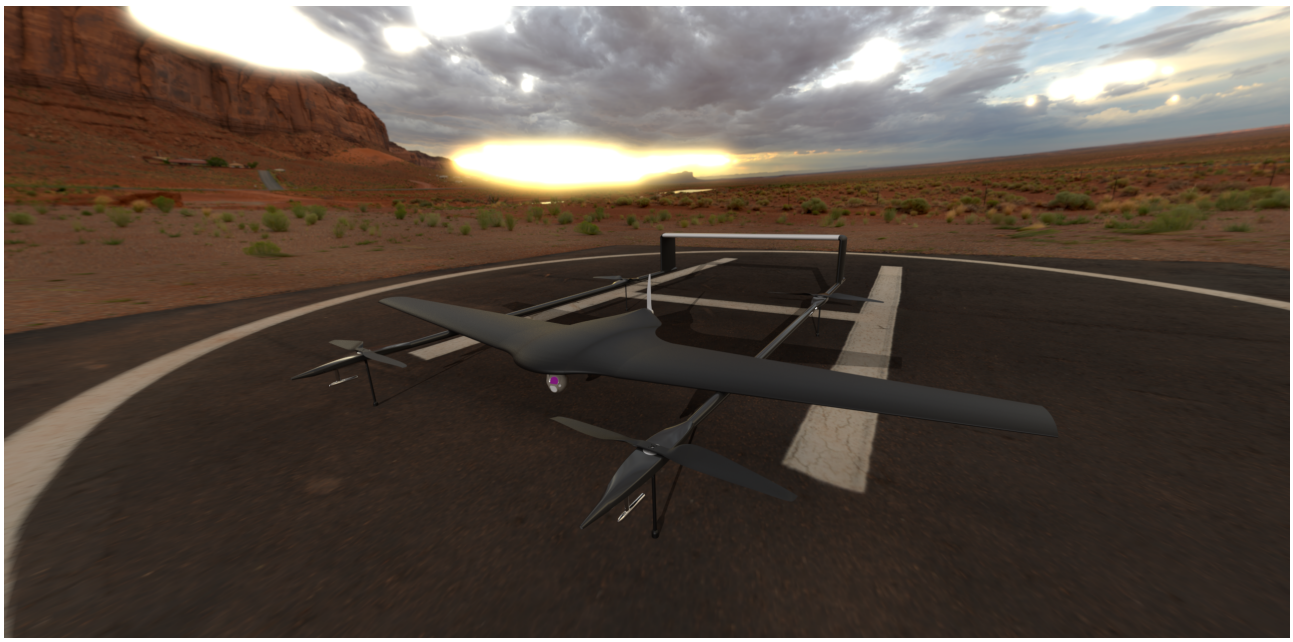

Figure 9.4: Render of the Final UAV Design

Chapter 10: Flight Performance

This chapter discusses the flight performance of the UAV. It starts off with an analysis of the climbing and turning performance of the aircraft. It then combines this information into a doghouse plot that shows the aircraft's turning performance for various flight speeds and climb gradients. In addition to an analytical analysis of aircraft climbing and turning performance, a non-linear three-dimensional simulation of the aircraft was created to confirm performance during all phases of flight, including VTOL, transition and fixed-wing stages of flight.

10.1. Climb Performance

The conservation of energy principle is used to model the aircraft, based on the work-energy theorem. By taking the time derivative of the energy equation, an expression in terms of power can be derived. According to this equation, the excess power (T - D) multiplied by the velocity (V) is equal to the rate of change of energy. This equation (10.1) demonstrates that the excess power is associated with the change in potential and kinetic energy:

$$(T - D)V = \frac{dE}{dt} = \frac{d(mgh + \frac{1}{2}mv^2)}{dt} \tag{10.1}$$

Here, h represents altitude, W is the weight of the aircraft, and g is the acceleration due to gravity.

It should be noted that the small angle approximation is a reasonable simplification for this model. By assuming a small flight path angle, the thrust is modelled to directly counteract drag. However, for steep flight paths, where the effects of thrust offset become significant, a more nuanced model is required. Additionally, this model assumes that weight is constant and does not vary with time. This assumption is valid for a battery-powered UAV.

By dividing Equation (10.1) by the weight of the aircraft, we can define the specific excess power (P_s) as:

$$P_s = \frac{(T - D)V}{W} \tag{10.2}$$

Assuming a climb at constant kinetic energy, we can neglect the last term in Equation (10.2). Therefore, the specific excess power (P_s) can be approximated as the unaccelerated rate of climb (ROC):

$$ROC \approx P_s = \frac{d(h)}{dt} \tag{10.3}$$

Equation (10.3) reveals that the ROC is approximately equal to the specific excess power since it represents the change in altitude over time. This relationship is a powerful variant of the E-M theory. By assuming a constant or nearly constant velocity throughout a turn, the specific excess power becomes directly related to the change in altitude. The amount of excess power an aircraft possesses in a certain configuration completely determines its ability to climb. However, this version of the ROC is not entirely accurate. A linear correction factor, denoted as K_{acel}, is applied to compensate for the acceleration induced by climbing at a constant velocity. The true ROC, taking into account this correction factor, is expressed in Equation (10.4):

$$ROC(V) = K_{acel} \times ROC_{unaccelerated}(V) \tag{10.4}$$

The correction factor K_{acel} accounts for the changes in velocity during the climb manoeuvre. It quantifies the ratio of the true ROC to the unaccelerated ROC at a given altitude and velocity.

10.1.1. Turn Performance

In this model, a steady turn is considered an arc with a constant radius. The bank angle is determined based on the instantaneous airspeed, turn radius, and gravitational acceleration using the following equation:

$$\phi = \arctan\left(\frac{g \times R}{V^2}\right) \tag{10.5}$$

Where ϕ represents the bank angle, V is the velocity, and R denotes the turn radius.

The load factor (n) is defined as the ratio of the lifting force to the weight of the aircraft. It can be derived from the balance of vertical forces as follows:

$$n = \frac{W}{L} = \frac{g \times R}{V^2} \tag{10.6}$$

Where L represents the lifting force.

By manipulating Equation (10.5) and using trigonometric identities, we can express the turn radius (R) in terms of the bank angle (ϕ) and velocity (V):

$$R = \frac{g \times \tan(\phi)}{V^2} \tag{10.7}$$

Equations (10.5) and (10.7) enable us to calculate the bank angle and turn radius, respectively, for a given velocity.

10.1.2. Load Factor and Stall Speed Ratio

The maximum instantaneous load factor (N_z) can be defined as the ratio between the maximum lift coefficient ($C_{L_{\max}}$) and the instantaneous lift coefficient (C_L) of the aircraft. The maximum lift coefficient is determined by the maximum angle of attack that the aircraft can achieve before encountering buffeting or stall. Buffeting occurs when the flow is disturbed by a shockwave, leading to vibrations and oscillatory changes in lift. The maximum load factor is given in Equation 10.8.

$$N_{z_{\max}}(V) = \frac{C_{L_{\max}}(V)}{C_L(V)} \tag{10.8}$$

The stall speed ratio (SSR) represents the ratio of the stall speed to the incident flight speed. It is expressed in Equation 10.9.

$$\text{SSR}(V) = \sqrt{\frac{C_{L_{\max}}(V)}{C_L(V)}} \tag{10.9}$$

These parameters provide insights into the aircraft's load-carrying capability and stall characteristics.

10.1.3. Models for Ground Reference Frame

While the previous models discussed are aircraft-centric, for obstacle clearance purposes, the ground reference frame becomes relevant. Wind velocities must be taken into account to relate ground speed to airspeed. Wind affects the operating conditions of the aircraft, such as lift and drag. In the ground reference frame, an oncoming headwind increases the speed of the airflow but does not change the speed of the aircraft relative to the ground. This means that a headwind would increase the rate of climb (ROC), resulting in a steeper ground reference frame climb gradient. The conversion from true airspeed (TAS) to ground speed (V_G) can be found in Equation 10.10.

$$V_G = V_{TAS} - V_W \cos(\theta) \tag{10.10}$$

Similarly, while rates of climb are aircraft-centric, climb gradient is not. The conversion from ROC to climb gradient (ClimbGrd) is given by Equation 10.11.

$$\text{ClimbGrd} = \frac{\text{ROC}(V)}{V_G} \tag{10.11}$$

These models allow for the consideration of wind velocities and the conversion between different reference frames.

10.2. Doghouse Plot

The doghouse plot is a comprehensive assessment of the combined effects of turning and climbing manoeuvres. In this section, two distinct models for each type of manoeuvre are presented, incorporating E-M theory for climbing performance and simple geometry for modelling the aircraft's turning capability [1]. The radius of turn, which is used for lateral separation from obstacles, can be easily calculated from the aircraft's speed and bank angle. However, the decrement in climb gradient is specific to each aircraft, especially for bank angles up to 15 degrees. Higher bank angles can also be covered if relevant to the expected operation of the aircraft.

10.2.1. Results

In Figure 10.1 the doghouse plot for the design has been generated. It has been plotted from the stall speed to the maximum velocity achievable by the UAV. The maximum bank angle possible is 66 °. In the diagram, it can be seen how the UAV will perform during certain turn rates.

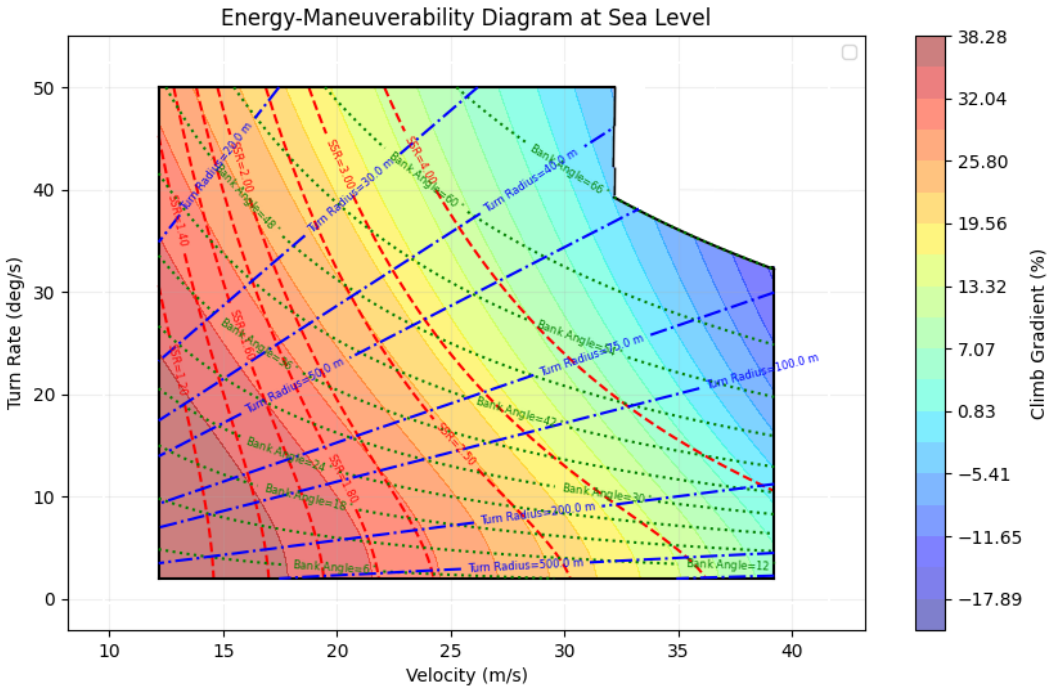

Figure 10.1: The Doghouse Plot.

10.2.2. Discussion

The doghouse plot incorporates models for the climb and turn performance, as well as additional parameters such as load factor and stall speed ratio. It uses the conservation of energy principle to describe climb performance, considering the excess power and the change in altitude over time. Correction factors are applied to account for changes in airspeed and temperature during climbs at a constant velocity. For turn performance, a steady turn model is used, deriving the bank angle and turn radius based on velocity and gravitational acceleration. The additional models for load factor and stall speed ratio provide insights into the aircraft's load-carrying capability and stall characteristics. Furthermore, the inclusion of ground reference frame models allows for the consideration of wind velocities and the conversion between different reference frames. These comprehensive models and parameters enable a thorough assessment of the combined effects of turning and climbing manoeuvres on the aircraft's performance.

[1] https://keep.lib.asu.edu/_flysystem/fedora/c7/187407/Wilson_asu_0010N_17391.pdf Accessed on: 10-06-2023

The Doghouse plot is used in aviation for assessing the performance of larger aircraft, including commercial airliners and military fighters. However, it can also provide valuable insights when applied to smaller fixed-wing unmanned aerial vehicles (UAVs). While there may be some differences in scale and operating conditions, the fundamental principles underlying the Doghouse plot remain applicable to UAVs.

For small fixed-wing UAVs, the Doghouse plot can help evaluate their manoeuvrability, climb capability, and turning performance. By analyzing the climb and turn models discussed earlier, UAV operators can assess the UAV's ability to ascend rapidly, execute sharp turns, and maintain stability during these manoeuvres.

The load factor and stall speed ratio parameters are particularly important for UAVs. UAVs operate at lower altitudes and lower speeds compared to larger aircraft. Understanding the maximum load factor and stall speed characteristics is crucial for ensuring safe and efficient flight operations. By studying the Doghouse plot, the limits of the UAV can be identified and the stall speed conditions to avoid can be recognized.

Finally, the models for the ground reference frame become significant for small UAVs as they are more susceptible to wind effects due to their lower mass and size. Wind variations can significantly impact UAV performance, altering airspeed, climb rates, and turning behaviour. By considering the ground reference frame models, the influence of wind velocities on the UAV's flight characteristics can be better understood.

10.3. Flight Dynamics Model

As mentioned previously, the simulation uses a non-linear flight dynamics model. The authors opted to use the open-source JSBSim flight dynamics framework [21]. JSBSim takes in the aerodynamic, structural and propulsive properties of the aircraft and performs a non-linear 6-degree-of-freedom simulation of the aircraft's motion in time. It has been used by numerous publications, receives active development and has been subjected by V&V by third parties (see e.g. [22]). Some key drivers behind its selection are its open-source and extendable nature, wide adoption and existing integration with third-party tools (such as PX4, discussed later).

JSBSim itself is simply a 6-degree-of-freedom dynamics simulation package, with various tools and components that make it easy to use it for aircraft simulation. It does not force an aircraft type upon the user - as a matter of fact, it can be used for anything from conventional aircraft to helicopters, rockets and balloons. This freedom is what makes it possible to use the tool, even for slightly less conventional designs such as V-tailed aircraft (where a control surface deflection can cause a moment around multiple axes) and hybrid VTOL aircraft like the one designed in this report.

While there are many ways to go about setting up a model in JSBSim (incorporating various levels of fidelity), the first iteration of the aircraft model will be based on an existing small UAV model. Specifically, the Rascal aircraft developed by ThunderFly Aerospace[2] was used because of its comparable size. Furthermore, inspiration was taken from the DJI F450 drone that comes packaged with FlightGear[3]. These two models were combined into a combined system which consisted of a conventional aircraft with four VTOL motors and propellers attached to it. Modifications were made to enforce the flat plate drag assumption while flying up vertically [2].

The flight dynamics model still required numerous inputs such as mass and aerodynamic coefficients. This data was obtained from the 3D CAD model Chapter 9 as well as stability and aerodynamic analyses performed in OpenVSP Chapter 7. An overview (omitting tabulated data because of its size) has been shown in Table 10.1. Aerodynamic properties are multiplied by the freestream dynamic pressure as well as any appropriate reference dimensions (S,b,c) to turn them into forces and moments within the simulation framework. For more information about the various coefficients, please refer to the structural and aerodynamic analysis chapters.

With the model configured, the simulation can be performed. This was done using a timestep of $4\,\text{ms}$, or a simulation rate of $250\,\text{Hz}$. This rate was chosen because of the highly accurate discrete time integrators (that reduce the effect of taking large time steps) JSBSim employs. It is also slightly higher than typical control loop rates used for UAVs - avoiding instabilities associated with a sluggish controller.

While the flight controller will be discussed in more detail in Section 10.4, but it is worth discussing sensor emulation. A flight controller will not be able to obtain a completely accurate picture of its state and the world around it. Instead, it must rely on sensors which incorporate various error sources (such as a bias, gain and

[2] `https://github.com/ThunderFly-aerospace/FlightGear-Rascal`, accessed on 21-06-2023

[3] `https://github.com/JSBSim-Team/jsbsim/tree/master/aircraft/F450`, accessed on 21-06-2023

random noise) and might not always be available (e.g. GPS or airspeed at low velocities). To model this in the simulation, JSBSim's sensor class[4] can be used. This class makes it possible to add noise, drift, gain, bias and delay to virtual sensor readings made on the aircraft. The SITL simulation bridge (discussed later) also has the ability to expand upon this with more advanced noise models or even packet drops.

Table 10.1: Key constants used in the flight simulation model.

(a) System physical properties

Property	Value
m [kg]	14.01
I_{xx} [kg m^2]	8.228
I_{yy} [kg m^2]	3.697
I_{zz} [kg m^2]	11.69
S [m^2]	1.25
b [m]	3.2
c [m]	0.44

(b) Aerodynamic force coefficients. Table values are at $\alpha = 0$. L=LIFT, D=DRAG, S=SIDE.

Name	Value	Axis
$C_L(\alpha)$ [-]	TABLE (0.244)	L
$C_{L_{\delta a}}$ [rad^{-1}]	0.874858	L
$C_{D_0}(\alpha)$ [-]	TABLE (0.0172)	D
k [-]	0.042	D
C_{D_β} [rad^{-1}]	0.000699	D
$C_{D_{\delta e}}$ [rad^{-1}]	0.052745	D
$C_{D_{\delta a}}$ [rad^{-1}]	0.002774	D
$C_{D_{\delta r}}$ [rad^{-1}]	0.001267	D
C_{Y_β} [rad^{-1}]	-0.26192	S

(c) Aerodynamic moment coefficients. P=PITCH, Y=YAW, R=ROLL.

Property	Value	Axis
C_{m_α} [rad^{-1}]	0.736492[5]	P
$C_{m_{\delta e}}$ [rad^{-1}]	-4.55576	P
C_{m_q} [s rad^{-1}]	-99.6782[6]	P
C_{n_β} [rad^{-1}]	0.161881	Y
C_{n_r} [s rad^{-1}]	-0.22906	Y
$C_{n_{\delta r}}$ [rad^{-1}]	0.128221	Y
$C_{n_{\delta a}}$ [rad^{-1}]	-0.0152	Y
C_{l_β} [rad^{-1}]	0.006985	R
C_{l_p} [s rad^{-1}]	-0.47259	R
C_{l_r} [s rad^{-1}]	0.052634	R
$C_{l_{\delta a}}$ [rad^{-1}]	-0.30843	R
$C_{l_{\delta r}}$ [rad^{-1}]	-0.01365	R

10.4. Flight Controller

There are numerous flight controllers with support for VTOL planes (also referred to as a QuadPlane). These ready-to-use flight controllers often include mature drivers for physical hardware, as well as software-in-the-loop simulation. This means software can be developed using the simulation and then deployed to a real-world UAV with a minimum of changes required, should the project ever get to that stage. It also avoids the complexities associated with implementing controllers for the VTOL takeoff, transition and fixed-wing parts from scratch - all of which would take a significant time investment.

While there are numerous flight controllers, the lack of budget limits the selection of open-source options[7]. There are two popular open-source flight controllers that are known for their ability to support fully autonomous UAV applications where an off-board, or secondary, computer controls the UAV. These are PX4[8] and ArduPilot[9]. Because the team had more prior experience with PX4, it was selected as the flight controller for flight simulation.

To tie the flight controller to the simulation environment, the PX4 JSBSim Bridge[10] was used. Various code modifications took place to ensure compatibility with the bridge and the latest main/v1.14 release of PX4. Source code modifications were also made to enable compilation and integration of PX4 and ROS 2 Humble[11] under Ubuntu 22.04 LTS. The ROS framework is used to write the autonomous systems of the UAV that respond to events and follow the pre-determined surveillance path. The vast majority of custom code for analyses and mock missions was written in Python, with small parts prototyped or written in C++ (where its strong typing and more robust toolset made reverse-engineering some of the PX4 internals easier). A screenshot of the development environment simulating a response mission can be found in Figure 10.2.

The source code (modifications) made to set up the flight simulation can be provided on request by reaching out to the team.

[4] `https://jsbsim-team.github.io/jsbsim/classJSBSim_1_1FGSensor.html`, accessed on 21-06-2023

[5] The positive value of C_{m_α} (across the range of angle-of-attacks) would suggest static instability of the aircraft. This has been addressed in subsequent iterations of the design, but time did not allow the flight simulation model to be updated to reflect this change.

[6] The large magnitude of this number in comparison to others warrants further investigation, e.g. into the aerodynamic convergence for this property.

[7] The Veronte 1x autopilot selected for cost analysis does have simulation software available, but is not freely accessible

[8] `https://px4.io/`, accessed on 06-06-2023

[9] `https://ardupilot.org/`, accessed on 06-06-2023

[10] `https://docs.px4.io/main/en/simulation/jsbsim.html`, accessed on 06/06/2023

[11] `https://docs.ros.org/en/humble/index.html`, accessed on 23-06-2023

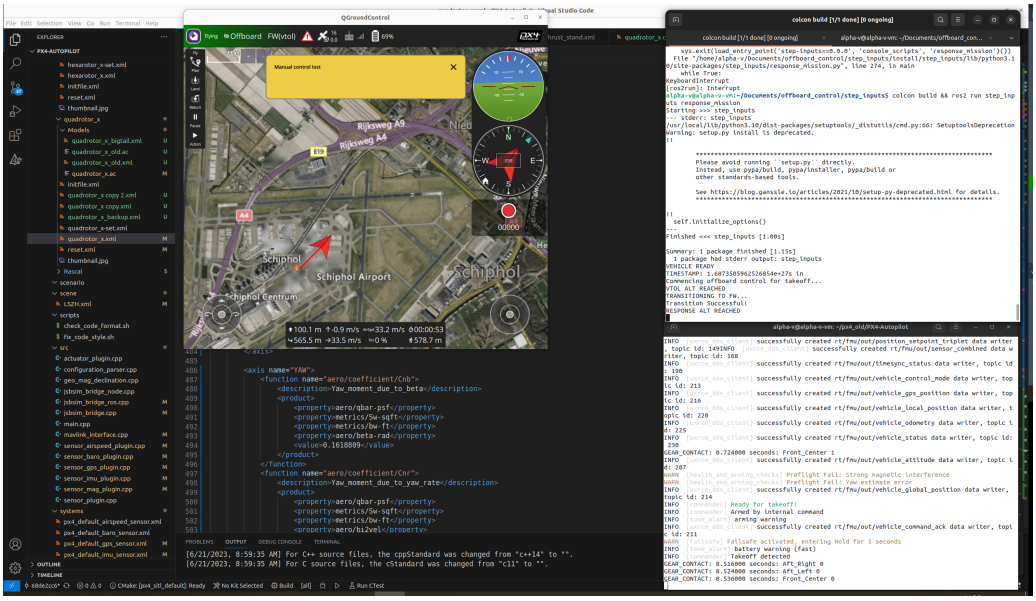

Figure 10.2: Screenshot of UAV Simulation Development Environment.

10.5. Plant & Controller Response

To confirm the controllability of the UAV system (the vehicle dynamics together with its controller), two stability studies took place. The first focuses on the VTOL aspects of flight. After taking off to a height of 30 m AGL and stabilizing, unit step inputs were given to the four dimensions of control: x, y, z and ψ. The inputs and responses have been shown in Figure 10.3.

Before generating this diagram, tuning of the various rate, attitude and position controllers used in multirotor mode had to take place. While px4's autotuning functionality could be used for some of the prototypes, it quickly became apparent that yawing performance for the final design was sub-optimal to the point where the autotuning functionality consistently failed[12]. Because of this, manual tuning was needed to improve the performance. In addition to this manual tuning, the yawing rate was restricted to a maximum of $\pm 2\,^\circ\,\mathrm{s}^{-1}$. This avoids the significant overshoots that were plaguing the system.

The reduced yawing performance can be seen in Figure 10.3 by its large settling time. The yawing motion also shows little damping, apparent by the large number of oscillations that can be seen after a manoeuvre. In spite of this low damping, the oscillations appear to die out so it is reasonable to conclude that yawing motion is stable. Step inputs in the other, positional, axes show stable (damped) behaviour. Step inputs in both horizontal planes appear slightly underdamped (apparent by the oscillations following the steps), while step inputs in the z-axis appear to be either critically or overdamped, showing little to no oscillating behaviour after reaching its setpoint.

The reduced yawing performance of the system in VTOL mode is an area of concern, as it makes it difficult to perform a rapid response in a direction that opposes the UAV's stored direction. It is worth investigating the possibility of landing UAVs facing in opposing directions and selecting the UAV that has the smallest yaw angle with respect to the target direction. In addition to this, further effort should be spent on tuning the yaw controllers, potentially extending them with additional terms and/or incorporating gain scheduling to reduce the overshoots. Should this still not provide sufficient performance, physical modifications such as propellers with more inertia or motors able to provide more torque should be considered for the next iteration of the design.

It is also worth noting that the rise times and oscillations for horizontal plane motion can likely be reduced by further tuning the controllers responsible for these dimensions. Furthermore, the constant small yawing oscillation with an amplitude up to about 6 ° can likely be reduced by increasing the damping of the yaw controller. While it is not possible to perform this tuning iteration within the scope of this report, it is most certainly worth investigating for a potential future iteration of the design (potentially after flight test data has been collected to help further validate the flight simulation model).

[12] The vehicle's high inertia around the z axis coupled with limited differential torque meant the autotuning system did not create enough of a response to perform its tuning. The authors later discovered that it is possible to give a larger input (to help with the signal-to-noise issue that is currently blamed for the failure), but time did not allow this to be used.

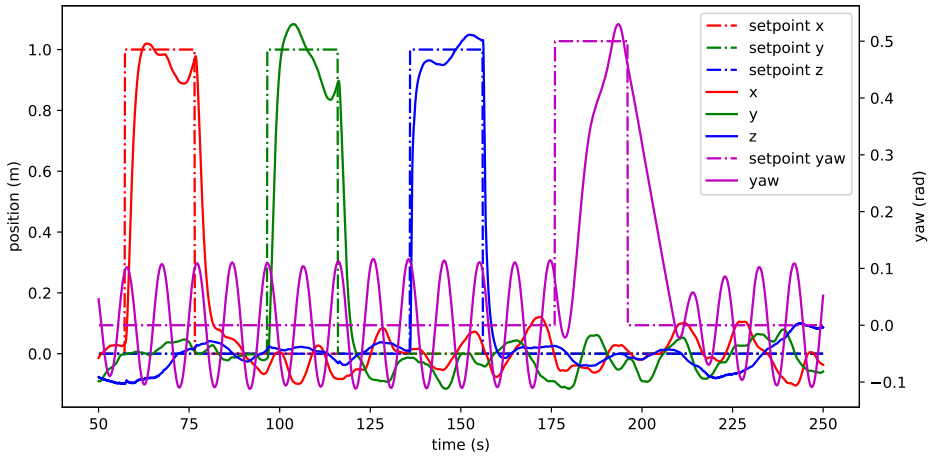

Figure 10.3: Response of Vehicle & Controller in Multi-Rotor Mode.

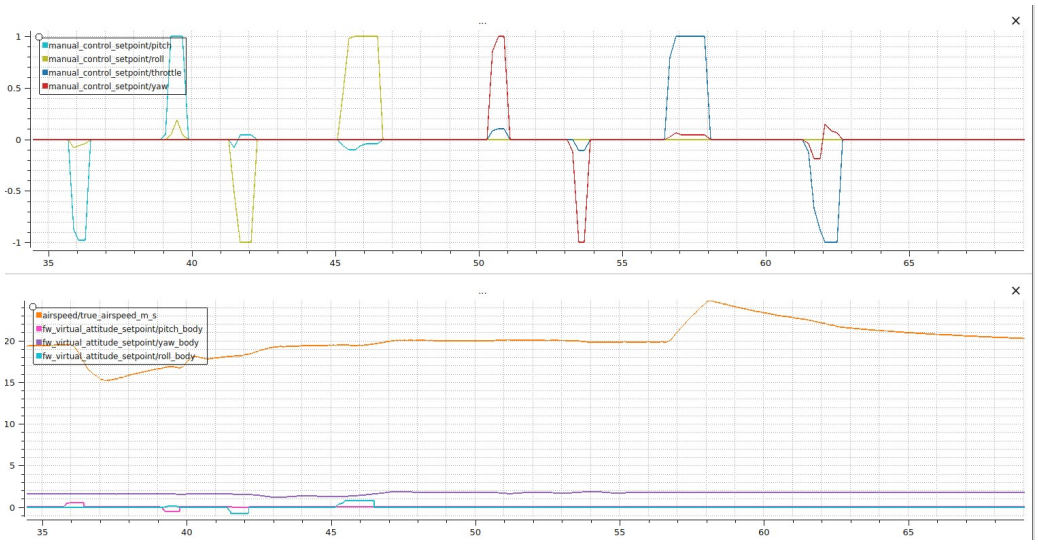

Figure 10.4: Response of Vehicle & Controller in Wixed-Wing Mode.

In a similar fashion, a stability study took place for the fixed-wing phase of flight. In light of the continual forward motion of the aircraft, taking step inputs in the positional axes is not possible (barring the perfect headwind, there will always be some motion to sustain the lift). Instead, the authors chose to analyze the response to inputs to the pitch (θ), yaw (ϕ) and roll (ψ) axes as well as throttle (causing an increase in the speed of the aircraft). This has been shown in Figure 10.4.

From Figure 10.4 it is apparent that all step inputs are stable, with minimal oscillation. The airspeed response is a little more complicated, as both pitch and throttle have a large influence on it. This is expected, and overall the results are deemed acceptable for use in the design. It is worth noting that in spite of the negative C_{m_α} coefficient (meaning static instability), the aircraft is able to trim itself for level flight and execute pitching manoeuvres without getting stuck in an unstable flight regime.

During later stages of the design, the characterisation of the fixed wing's ability to follow waypoints should be investigated. This was not considered feasible within the limited resources available for this final report.

10.6. Simulation Results

Two simulation studies were performed as part of this project. The first is a surveillance mission - from take-off till it landed back at the ground station. The second simulation run focused on response missions. By simulating a response mission to randomized points within the coverage area, metrics such as average response time can

be estimated. The methodology taken for both approaches, as well the results. These are used to confirm the vehicle's performance and operational performance (in the absence of a physical prototype).

10.6.1. Surveillance Mission Simulation

Using the surveillance pattern described in Chapter 5, a scenario where the UAV takes off in VTOL mode, transitions to fixed-wing flight, follows the surveillance path and finally returns to the ground station where it transitions back to VTOL mode and lands can be created. The results of this simulation were not yet available at the time of handing in the draft report and will be provided during the final review. Key data collected during this study will include the resources (in terms of time, energy, etc.) used for the surveillance path, as well as an average time to detection of an event given the camera's field-of-view as well as UAV height.

10.6.2. Response Mission Simulation

Before discussing a case study of a response mission, some important aspects of the commanding logic for this phase of flight will be discussed. Because speed is of the essence for a response mission, the set point for many of the control laws is set to a value higher than what is needed resulting in a faster overall operation. This avoids the usual "slow down" near the targeted value (where e.g. the P-term of a PID controller is smaller), meant to avoid overshooting it. Instead, the offboard controller will detect cases where it is close to the target and let it overshoot, setting a new setpoint so it can recover the excess (vertical) energy gained by the overshoot.

To make the above a little more clear, consider the vertical take-off procedure. One way to perform this is by setting a target altitude of $30\,\mathrm{m}$, and then executing a transition command after the UAV has approached this altitude. This is undesirable in a response mission, as the final part of the approach will be slow. Instead, the UAV is commanded to maintain (x, y) position and to try to reach a vertical speed of $15\,\mathrm{m\,s^{-1}}$ (not quite achievable by the UAV, at not least within the $30\,\mathrm{m}$ available). Once the offboard controller detects $30\,\mathrm{m}$ has been passed, it will switch to a stabilized approach (that will essentially maintain a hover, very slowly losing vertical speed) while starting up the pusher propeller at maximum speed - allowing the UAV to keep some of its vertical momentum going while transitioning.

A similar system is in place for the fixed wing climb phase, where a setpoint $50\,\mathrm{m}$ above the target altitude is provided (specifying vertical speeds in FW mode is not possible), and then immediately starts accelerating when it gets close to the target altitude. Because, in an aircraft, it is easy to turn potential energy into kinetic energy (by simply pitching down) any height that the aircraft overshoots by can simply be used for its acceleration to maximum speed.

While more advanced trajectory analysis can be used to optimize this response path further, the rough idea behind this over-setting of targets is to operate the motors at near full power the vast majority of the time, maximizing the amount of energy that is added to the system. In addition to performance optimizations of the trajectory, the authors would like to acknowledge potential heating or wear concerns associated with rapid spin-ups and prolonged operation at the maximum power of the various components. Because of this, future optimization should also take these effects into account and attempt to mitigate them where possible.

A response mission to a faraway point, $10\,\mathrm{km}$ away in each axis (for a total distance of approx. $14.1\,\mathrm{km}$ from the ground station) has been shown in Figure 10.5. The system is assumed to have a continuous voltage of approximately $25\,\mathrm{V}$. This voltage is on the high end of the charge percentage but is needed to squeeze every last bit of performance out of the propulsion system (resulting in a faster response). The fact that this voltage is constant was deemed acceptable in light of the low energy drain from the battery during the response mission when compared to the full battery, which can sustain an endurance of $2\,\mathrm{h}$ or a range of $150\,\mathrm{km}$.

The system starts off with a vertical takeoff procedure that lasts approximately $8\,\mathrm{s}$ seconds after release from the ground. After this, the aircraft transitions from VTOL mode to fixed wing mode - a process that takes approximately $6.5\,\mathrm{s}$. It is worth noting that the system does not stop its horizontal velocity before transitioning - instead, it simply accelerates while maintaining hover throttle. The result is that it slows down somewhat, but can still climb a little over $30\,\mathrm{m}$ during the transition procedure.

After transitioning, the aircraft climbs to the response target altitude of $100\,\mathrm{m}$ after which it accelerates to the maximum speed achievable given wind conditions (this speed is limited by maximum thrust). In the current version, PX4 its built-in Total Energy Control System (TECS) will sacrifice some altitude for additional speed.

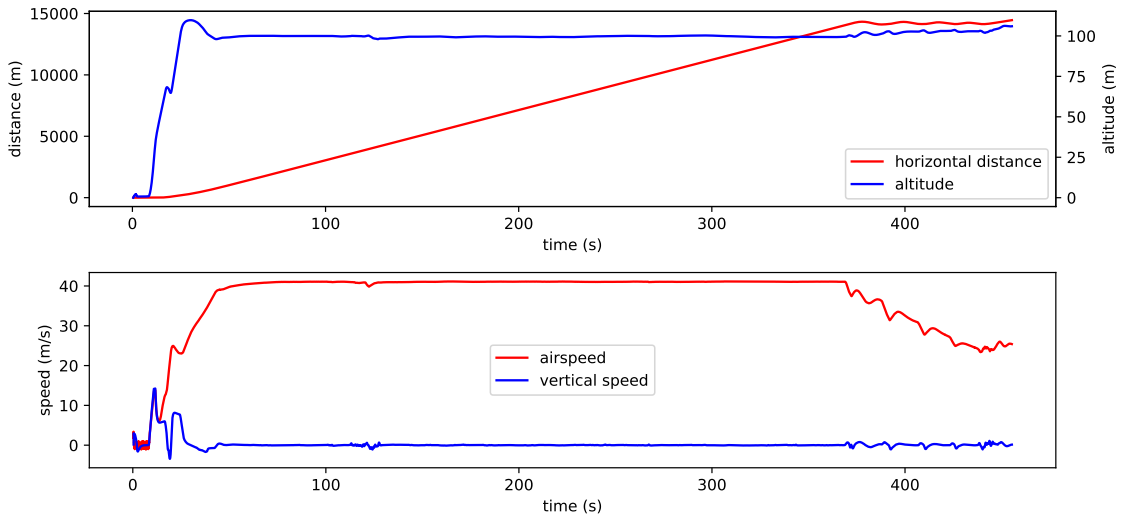

Figure 10.5: Response mission to $(10,000; 10,000)$

This means that the aircraft will glide down slowly till its settling altitude of $80\,\mathrm{m}$ to gain additional speed. This would need to be addressed in the final iteration of the design but was unfortunately not possible within the timeline of this report. The result would likely involve a custom lower-level flight controller that fixes the thrust at 100% (thus adding the maximum amount of energy to the system per second) while maintaining (at least) that target altitude, with safeguards to ensure maximum safe speeds are not exceeded.

Unfortunately, time did not allow the (a-star) path-finding algorithm to be implemented into the simulation software. Because of this, the aircraft will simply maintain its maximum speed and head towards its target in a straight line after reaching its cruising altitude. After encountering the point of interest, the system will slow down to its cruising speed (approximately $22.2\,\mathrm{m\,s^{-1}}$) and loiter around the point of interest. This is the final "oscillatory" distance phase that can be seen in Figure 10.5.

Overall, it appears the simulation reaches a maximum speed of approximately $41\,\mathrm{m\,s^{-1}}$ (or $148\,\mathrm{km\,h^{-1}}$). It takes approximately $60\,\mathrm{s}$ after leaving the ground to perform the transition, climb and accelerate to this maximum speed. The total distance covered within this time span is around $1.8\,\mathrm{km}$. During VTOL operation and transition, approximately $8700\,\mathrm{J}$ (approximately $2.4\,\mathrm{W\,h}$) of energy are used, following which fixed-wing propulsion system continues consuming approximately $1.86\,\mathrm{kW}$. After reaching the response target, the (slower, $22.2\,\mathrm{m\,s^{-1}}$) cruise propulsion system uses approximately $600\,\mathrm{W}$.

Power consumption can be lowered by reducing the airspeed to that for maximum endurance, but this was not simulated for the response scenario given here. It is worth noting that these estimations only consider the propulsion system. The actual UAV would also incorporate various other power sinks, such as the payload and flight controller not modelled here. Please refer to Figure 10.6 for a time-series representation of the instantaneous power of each propulsion system, as well as the overall energy consumed by the propulsion systems.

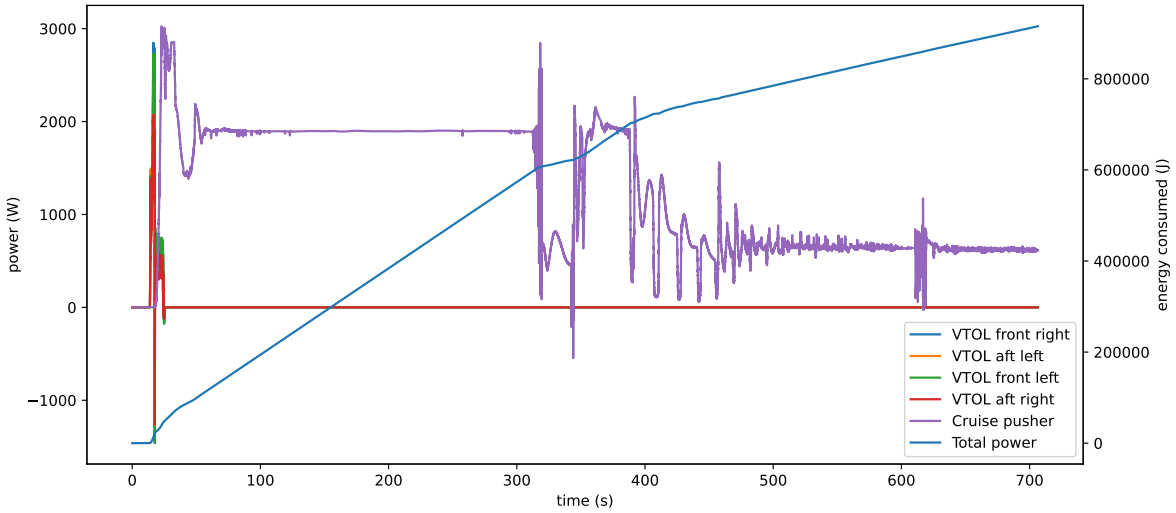

Figure 10.6: Response mission instant. power and cumulative energy used

Chapter 11: Noise Emissions

An essential requirement for the UAV system is that it must not disturb the wildlife/environment, therefore it must be quiet. In this chapter, the noise is extensively analysed to investigate noise levels in different phases of a UAV's flight. The Hanson model is used to find a sound pressure level and various transformations are used to obtain an accurate noise metric.

11.1. Hanson Model

The main noise source of the system will be the noise produced by the propellers. The noise levels can be estimated using the Hanson model [23] for propeller noise. This is a mathematical model which can be used to decompose the sound allowing the harmonics of the propeller noise to be determined. As the harmonics drive the sound, it is imperative to analyse their characteristics. To find these harmonic frequencies, several inputs are required: the number of blades per propeller, RPM, the velocity of the moving noise source, the location of the source with respect to the sound measurement location, and the propeller length. Using the Hanson model the sound pressure level (SPL) for each harmonic can also be found. The only approximation that the model makes is that the propeller's blades are thin and that radial source terms are neglected. Furthermore, in order to implement the Hanson model a few adaptations were made:

- The Hanson model is generally used for near-field noise (although it is still very similar to far-field noise theory) but can be adapted for far-field noise by implementing sound propagation into the model.
- Decomposition of the noise results in decreasing amplitudes of the harmonics, with the first harmonic being the most important, (i.e. it has the highest sound pressure level) as is typical for propellers. Thus, only the first three harmonics were analysed.

The noise theory is based on Hanson's helicoidal surface theory, where each noise source element is assumed to travel along a helical path. Hanson found that the pressure of the noise can be found using a Fourier Series as follows

$$p = \sum_{m=-\infty}^{\infty} P_{mB}\, e^{i\, m\, B(\phi - \Omega t)} \tag{11.1}$$

where P_{mB} is the Fourier coefficient, m is the harmonic number, B is the number of blades, ϕ is the phase lag, Ω is the rotational velocity of the propeller shaft.

P_{mB} consists of four different pressure contributions: P_{Dm} and P_{Lm} take into account the propellers' lift and drag contributions, P_{Vm} represents the noise created due to volume displacement, i.e. the displacement of air due to the volume of the propeller blades. It is also referred to as thickness noise. Finally, P_{Qm} accounts for the noise due to quadrupole sources, their contribution is most prominent when blade tip speeds reach transonic regions. This is applicable to the drone as for example during cruise the local flow velocity at the tips is around Mach 1.2. The contributions can be added up to find P_{mB} as can be seen below:

$$P_{mB} = P_{Vm} + P_{Dm} + P_{Lm} + P_{Qm} \tag{11.2}$$

Using integration by parts each contribution can be found individually as follows

$$\begin{Bmatrix} P_{Vm} \\ P_{Dm} \\ P_{Lm} \\ P_{Qm} \end{Bmatrix} = \frac{-i\,\rho_\circ\, c_\circ^2\, m\, B^2 M_T}{8\pi M_x} \int_{z_{\text{root}}}^{z_{tip}} M_r^2 \int_{-\infty}^{\infty} e^{i(\phi_\circ + \phi_s + \phi_x)} J_{mB}\left[\frac{m\, B\, z\, M_r}{M_x}\sqrt{M_x^2\, k^2 - (k-1)^2}\right] \cdot H_{mB}^1\left[\frac{2m\, B\, M_T}{M_x}\frac{y}{D}\sqrt{M_x^2\, k^2 - (k-1)^2}\right] \begin{Bmatrix} k_x^2 t_b \Psi_V\left(k_x\right) \\ i\, k_x \frac{C_D}{2} \Psi_D\left(k_x\right) \\ -i\, k_y \frac{C_L}{2} \Psi_L\left(k_x\right) \\ \Psi_Q\left(k_x, k_y\right) \end{Bmatrix} dk\, dz \tag{11.3}$$

Equation 11.3 contains a multitude of unknowns, which will all be explained. First of all, to each of the contributions a normalised transform term Ψ must be applied, these can be found according to

$$\begin{Bmatrix} \Psi_V(k_x) \\ \Psi_D(k_x) \\ \Psi_L(k_x) \end{Bmatrix} = \int_{-\frac{1}{2}}^{\frac{1}{2}} \begin{Bmatrix} H(x) \\ f_D(x) \\ f_L(x) \end{Bmatrix} e^{i\,k_x\,x} dx \tag{11.4}$$

Here $H(x)$ is the airfoil thickness distribution and f_D and f_L integrate to be equal to 1. The transform term for the quadrupole is found differently according to

$$\Psi_Q = k_x^2 \Psi_{11} + 2k_x k_y \Psi_{12} + k_y^2 \Psi_{22} \tag{11.5}$$

where

$$\Psi_{ij}(k_x, k_y) = \iint \frac{T_{ij}}{\rho_o U_o^2} e^{i\,k_X\,X} e^{i\,k_y\,Y} dX\,dY \tag{11.6}$$

k_x and k_y represent the chordwise and normal wavenumber variables and can be found using

$$k_x = \frac{2m\,B\,B_D\,M_T\,k}{M_r} \tag{11.7}$$

$$k_y = \frac{2m\,B\,B_D}{z\,M_x\,M_r}\left(k\,z^2 M_T^2 - M_r^2\right) \tag{11.8}$$

Here B_D is the chord-to-diameter ratio, M_T the rotational Mach number at the tip and M_r is the section relative Mach number ($M_r = \sqrt{M_x^2 + z^2 M_T^2}$, where M_x is the flight Mach number and $z = \frac{r}{r_{tip}}$ is the normalised radial coordinate). Finally, there are phase lags present. $\phi_\circ$, ϕ_S and ϕ_X are related to the face alignment (FA) offset, mid-chord alignment or sweep (MCA) and the observer's axial position (x_1), respectively. They are found as follows:

$$\varphi_\circ = \frac{2m\,B}{z}\frac{kz^2M_T^2 - M_r^2}{M_x\,M_r}\frac{FA}{D} \tag{11.9}$$

$$\phi_s = \frac{2m\,B_T\,k}{M_r}\frac{MCA}{D} \tag{11.10}$$

$$\phi_x = \frac{2m\,B\,M_T(k-1)}{M_x}\frac{x_1}{D} \tag{11.11}$$

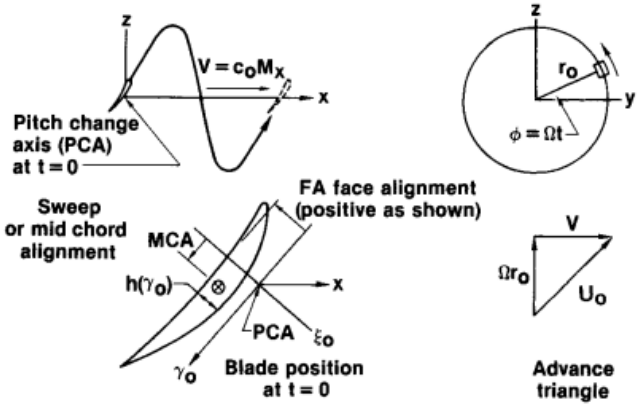

Figure 11.1: Blade element in helical coordinates [23].

Using this set of equations Equation 11.3 can be implemented which allows one to find the pressure with Equation 11.1. With this pressure, the SPL can be found as follows after first transforming the pressure into the root mean squared (rms) pressure:

$$p_{rms} = \left|\frac{p}{\sqrt{2}}\right| \tag{11.12}$$

$$SPL = 20\log_{10}\left(\frac{p_{rms}}{p_{ref}}\right) \tag{11.13}$$

where p_{ref} is the reference pressure of air, which is equal to 20 µPa[1].

[1] https://svantek.com/academy/sound-pressure-level-spl/, accessed on 18/06/2023.

11.2. A-Weighting

Solely determining the harmonic frequencies and SPLs of the propellers is not sufficient to assess the severity of their disturbance to the environment. Certain frequencies may for instance affect the environment more than others. Thus, the harmonic frequencies must account for this using an additional method. One such method is A-Weighting. It specifically accounts for how humans perceive sound [2]. Note that in the environment the UAV will be operational mainly wildlife will be affected by the noise. Unfortunately, methods analogous to A-weighting are not available for animals. Thus the assumption is made that animals perceive noise in a similar way to humans.

The A-Weighting method calculates a factor in dB (as a function of the noise frequency) that can be added to the base sound pressure level, the A-weighting curve[3] can be seen below in Figure 11.2. After the A-Weighting is applied the noise metric is expressed in dBA, which simply indicates the noise has been A-Weighted but the unit has the same scale as dB. Their meanings are different however, two sounds with the same sound pressure level values but with different frequencies will have identical values in dB but different values in dBA. The A-weighting factor, ΔL_A, can be calculated as follows [24]:

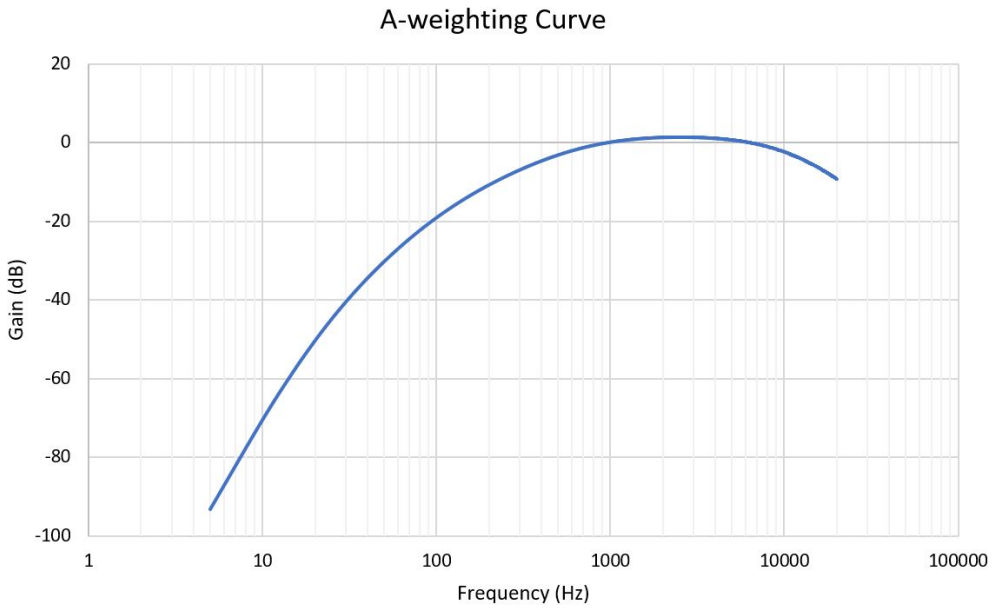

Figure 11.2: A-Weighting Curve.

$$\Delta L_A(f) = -145.528 + 98.262 \log_{10} f - 19.509(\log_{10} f)^2 + 0.975(\log_{10} f)^3 \tag{11.14}$$

ΔL_A can then be superimposed on L_p to find the A-weighted sound level, L_A:

$$L_A = L_p + \Delta L_A \tag{11.15}$$

11.3. Sound Exposure Level

Sound exposure level (SEL) builds on A-weighting to obtain a useful metric for determining the influence of sound. It takes into account the duration of a sound by adding a time element. The following equation can be applied to the A-weighted sound level [24]:

$$L_{SEL} = 10 \log_{10} \left(\frac{1}{T} \int_{t1}^{t2} 10^{L_A/10} dt \right) \tag{11.16}$$

[2] https://www.ansys.com/blog/what-is-a-weighting, accessed on 08/06/2023

[3] https://acousticalengineer.com/the-abcs-of-frequency-weighting/, accessed on 21/06/2023

Here $t1$ and $t2$ are the start and end times of the period, T is a reference time value taken to be equal to 1 sec and L_A is the A-weighted sound measurement.

11.4. Day-Evening-Night Average Level

The final noise metric that is applied is the Day-Evening-Night (DEN) average level. This takes into account the number of times an event occurs per day. If a noise has a slightly lower SEL than another noise (e.g. 60 vs 65 dBA) but occurs much more frequently (e.g. 20 vs 1), then naturally the noise with the lower SEL should be classified as more disturbing. The DEN noise level, L_{DEN}, can be found using [24]:

$$L_{DEN} = 10\log_{10}\left(\frac{1}{86400}\sum_{i=1}^{N} 10^{(L_{SEL_i}+W_i)/10}\right) \tag{11.17}$$

Usually, a penalty factor, W_i, is added to the SEL for certain hours of the day to account for the impact of varying background noise levels during the day. However, due to the fact that the UAV system will predominantly be operating in desolate areas in terms of human activity, the background noise is also assumed to be more or less constant throughout the day and thus no penalty values were added in the calculation. N is the number of events per day.

11.5. Noise Requirement

Now that an adequate metric to determine the sound level has been established, a target value for this metric must be determined. Regulations on noise limits/standards should be consulted to do this, preferably regulations from various institutions/countries should be consulted to obtain a value such that the system is as universally operable as possible.
As African wildlife reserves would be very suitable for the UAV system, regulations in these areas were researched. The most applicable regulations that were found were for Tanzanian and South African standards for "rural" areas. The standards recommend an equivalent noise level, L_{Aeq} of 35 dBA at night, 45 dBA during the day and 45 dBA for an entire day[25, 26]. L_{Aeq} is an A-weighted equivalent continuous noise metric and is identical to L_{DEN} except for the fact that it ignores penalty factors[4]. However, as mentioned before L_{DEN} is analysed without penalty factors by the team, hence the two metrics can be compared without discrepancies. European regulations were also researched: for National Park the Hoge Veluwe, an equivalent noise level of 40 dBA is strived for [27]. In order to produce a market-competitive product it was decided to require the noise levels to be below 40 dBA.

11.6. Results & Discussion

Using the inputs in Table 11.1, the methods explained in the Hanson model could first be applied to find the results listed in Table 11.2. For each phase, the sound pressure level decreases as the harmonic increases, which is to be expected as the frequency increases. Comparing the value of the SPL of the first harmonics to the total SPL confirms that it is indeed the most dominant contribution and that adding higher harmonics would cause negligible changes. Note that superimposing sound levels that are expressed in the logarithmically scaled decibels must be done according to

$$L_{tot} = 10\log_{10}(10^{L_1/10} + 10^{L_2/10} + ... + 10^{L_n/10}) \tag{11.18}$$

where L_i is a sound pressure in dB. Furthermore, it is important to mention that the SPL is relative to a certain reference distance. This explains why the SPL of V_{max}, which has a reference distance of 120 m, is lower than the SPL of VTO, which has a reference distance of 10 m even though the RPM is much higher. The reference distances can be found in Table 11.1 in the 'Distance' column. Finally, note that a Doppler effect was also added to account for the source moving, where the adjusted frequency is equal to

$$f_{doppler} = f \cdot \frac{343}{343 \pm v} \tag{11.19}$$

[4] https://www.acoustic-glossary.co.uk/definitions-l.htm, accessed on 09/06/2023

where 343 corresponds to the speed of sound (sea level conditions at 20 °C) and v is the velocity of the source. The Doppler-adjusted frequencies are used when converting the SPL to the A-weighting, SEL and DEN metrics.

Table 11.1: Hanson Model Inputs.

Phase	RPM	No. events	Blades	V [m/s]	D_{blade} [m]	Distance [m]	Event duration [s]
VTO	4048	12	2	6.5	0.6604	10	15
Resp. Climn	7201	1	2	32.9	0.4572	30	69
Nom. Climb	5413	12	2	16.5	0.4752	30	69
Cruise	4086	12	2	22.22	0.4572	120	2316
V_{max}	7201	1	2	39.2	0.4572	120	158.4
VL	3055	12	2	-2	0.6604	10	20

Table 11.2: Hanson model outputs for all mission phases: vertical takeoff (VTO), response mission climb (Resp. Climb), nominal climb, nominal cruise, cruising at V_{max} during a response mission (V_{max}) and vertical landing (VL)

Phase	Harmonic	Frequency [Hz]	Doppler [Hz]		Sound Pressure Lvl [dB]
			Min	Max	
VTO	1	134.9	132.5	137.5	71.1
	2	269.9	265.0	274.9	58.5
	3	404.8	397.5	412.4	45.9
	Total				71.4
Resp. Climb	1	240.0	219.0	265.5	66.7
	2	480.1	438.1	531.0	57.2
	3	720.1	657.1	796.5	47.7
	Total				67.2
Nom. Climb	1	180.4	172.2	189.6	56.2
	2	344.3	344.3	379.1	42.3
	3	541.3	516.5	568.7	28.2
	Total				56.4
Cruise	1	136.2	127.9	145.6	35.8
	2	272.4	255.8	291.2	16.9
	3	408.6	383.7	436.9	2.0
	Total				35.9
V_{max}	1	240.0	215.9	270.2	55.2
	2	480.1	431.8	540.5	45.7
	3	720.1	647.7	810.7	36.1
	Total				55.8
VL	1	101.8	101.2	102.4	61.4
	2	203.7	202.5	204.9	44.1
	3	305.5	303.7	307.3	26.8
	Total				61.5

In Table 11.3 the final results of the sound levels with metrics applied for all phase missions can be found. As mentioned, the Doppler effect has been accounted for, resulting in each metric being split up into a minimum and maximum value column. Naturally, the difference between these two values becomes larger as the velocity of the mission phase increases as the Doppler effect aggravates, for example, compare the difference in the V_{max} and VL phase. Analysing the A-weighting next, it is evident that as expected the sound levels are tempered with respect to the SPL as the noise frequencies for all mission phases are between 127-811 Hz, which correspond to a negative gain according to Figure 11.2. For the following SEL metric, the time duration is taken into account for a reference time of 1 s, As all event durations range between 15-2316 s it can be seen that the sound levels increase, with longer durations resulting in larger increases in SEL. The final metric, DEN, takes into account the number of events during a day. Due to the relatively low number of events all noise levels get attenuated,

leading to a maximum DEN level of 34.70 dB for vertical takeoff. Combining all the DEN levels from all the mission phases according to Equation 11.18 results in a final maximum noise level of 37.79 dB. This is lower than the required 40 dB, indicating that the requirement is met.

Table 11.3: Hanson model outputs with A-weighting, sound exposure level (SEL), and day-evening-night (DEN) noise level applied.

Phase	Harmonic	A-Weighted [dBA]		SEL [dBA]		DEN [dBA]	
		Min	Max	Min	Max	Min	Max
VTO	1	55.6	56.1	74.7	75.1	36	36.5
	2	50.4	50.8				
	3	41.1	41.3				
	Total	62.9	63.3				
Resp. Climb	1	56.8	58.6	77	78.6	27.6	29.2
	2	53.1	54.4				
	3	46	46.9				
	Total	58.6	60.2				
Nom. Climb	1	43.8	44.8	62.9	63.9	24.3	25.3
	2	36.4	37.1				
	3	25.2	25.7				
	Total	44.6	45.6				
Cruise	1	19.8	21.4	53.8	55.4	15.2	16.8
	2	8.5	9.6				
	3	-3.1	-2.2				
	Total	20.2	21.7				
V_{max}	1	45.2	47.3	69	70.9	19.6	21.5
	2	41.5	42.9				
	3	34.3	35.3				
	Total	47	48.9				
VL	1	42.4	42.5	61.9	62.1	23.3	23.5
	2	33.4	33.6				
	3	19.9	20				
	Total	48.9	49.1				
Combined Tot.						37.2	37.8

Chapter 12: Verification & Validation

This chapter discusses the verification and validation (V&V) approaches taken in the project.

12.1. Code Verification & Validation

12.1.1. Structural Analysis

The internal load calculations were first partially verified by performing smaller unit tests. Such tests include

- Hand calculations on implemented equations (e.g. reaction forces)
- Verifying that loads are zero at free edges
- The shapes of internal loads match the external loads
- Checking the order of magnitude of the results
- Printing and verifying that input values are correct
- Plotting and confirming the inputted external loads

Such unit tests ensure that the smaller parts of the code are performed correctly. They do not verify the code at large, however, instil confidence in the results of specific parts of the program.

Larger system tests are then performed to verify the overall output of the code. The larger-scale tests performed are

- Verifying expected relations between inputs and outputs
- Analysing a simpler problem

These tests confirm the behaviour of the program as a whole. Verifying the relations between inputs and outputs confirms that the model generally behaves as expected, however, it does not confirm that the specific results are correct. For example, increasing the lift should increase the reaction force at the clamped edge. A final system-level test involves running the program on a simpler loading cases, for which analytical solutions exist. An example of such a problem is shown in Figure 12.1.

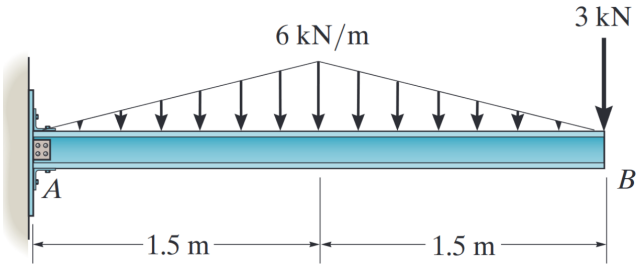

Figure 12.1: Sample problem for structures V&V [28]

The model outputs the same internal loading as the analytical solutions. While this verifies the program for only these particular load cases and geometries, it does suggest that the code is correct.

The process of verifying the stress calculations is similar to that of the internal loading calculations. Unit tests are performed on formulas relating to the geometric aspect of a cross-section:

- Plotting problem geometry
- Hand calculate the centroid
- Hand calculate the shear centre
- Hand calculate area moment of inertia
- Ensure that basic shear flow starts and ends at zero

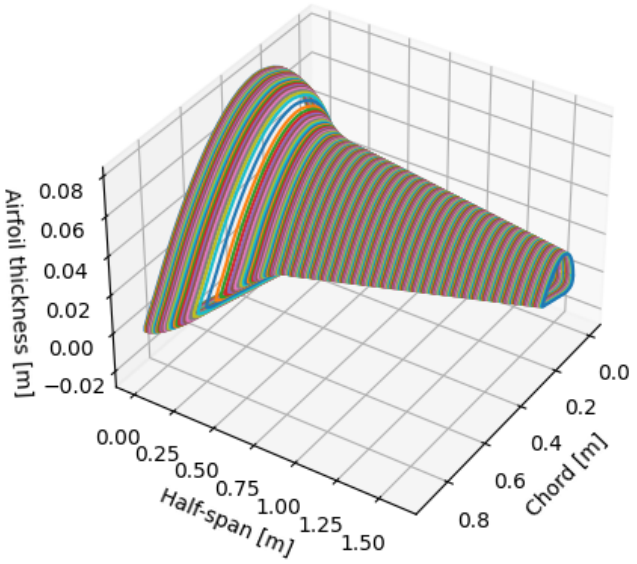

Figure 12.2: Plot of discretised wing

Plotting the problem geometry confirms that the code correctly converts the inputs. An example of such a plot is presented in Figure 12.2.

A plot such as Figure 12.2 helps visually confirm that the wing is correctly discretised. Many obvious mistakes can be caught at this stage.

The system-level tests are similar to those of the internal loading calculations.

- Verifying expected relations between inputs and outputs
- Analysing a simpler problem

12.1.2. Flight Performance

The power-over-weight versus wing loading diagram, the manoeuvre loading diagram, and the gust loading diagram was generated using the handbook for designing small UAVs [8], in which the full Python code was given. This code was adopted, using only the relevant constraints for the DAWG system, i.e. the take-off and landing performance constraints were not considered when generating the plots. Verification was done using the parameters stated in Keane et al. (2019) [8], and comparing the obtained graphs to the graphs as shown in the handbook. The generated plots were considered verified as the used constraints resulted in the same graphs for these constraints as in the handbook. Furthermore, the design logic as followed in Keane et al. (2019) [8] was compared to the methodology as taught by Vos et al. (2021). Since both methodologies use the same underlying theory, the method was considered validated.

For the verification and validation of the doghouse plot, verification was performed visually by cross-checking the generated plots with achievable values. Furthermore, individual calculations of the code were verified by generating the singular output of those calculations and confirming its feasibility by examining units and order of magnitude. Next, validation was performed by cross-examining the generated output with the values of similar UAVs.

12.1.3. Control Surface Design

Since computational relations used for the control surface design and sizing were considered to be automated calculations for a fairly simple calculation process, verification and validation of the control surface design calculations were done by comparing each intermediate parameter value with hand-calculated values.

12.2. Flight Simulation V&V

The flight simulation developed as part of this project is based on JSBSim, an open-source flight dynamics model. Because of the limited time available, and the large number of papers that use this FDM (including ones that validate its performance such as [22]), V&V will proceed under the assumption that the FDM has been implemented correctly. Instead, the focus will be shifted to ensuring the inputs are correct. As an example - a motor/propeller combination produces the thrust quoted in a datasheet. A visual inspection of handling characteristics will also take place, as well as positive and negative step inputs for all control surfaces to ensure their effect is as expected.

12.2.1. Propulsion Validation

To ensure the simulated propulsion system closely matches real-world performance, a virtual thrust stand is constructed. This thrust stand consists of a large mass ($W \gg T$) and supports that ensure the stand cannot rotate. The simulation outputs for *RPM*, *thrust* and *power* are recorded for the battery voltages and throttle settings shown in the datasheet of the motor that is under investigation.

For the initial versions of the system, large discrepancies could be found mainly in the thrust and power outputs. This difference varied significantly by PWM input, hinting at non-linearities in the C_p and C_t coefficients of the engine. To address this, performance information for the propeller at different RPM levels was fed into the simulation. This necessitated minor modifications to JSBSim that were verified by running the original case with the modified 3D table format to ensure the same results were achieved. In addition to using multiple sets of performance parameters, motor parameters (such as internal resistance) were tweaked iteratively until all parameters fell well within a 15% error margin. Special attention was paid to the values critical to the mission, such as cruise performance and maximum VTOL thrust.

The resulting validation plots for the cruise propulsion system (T-MOTOR AT4130 Long Shaft KV450 motor & APC 18*8 propeller) can be found in Figure 12.3. It is worth noting that thrust produces a conservative estimate, and that power is conservative for the medium power settings (where the aircraft will spend the vast majority of its time/power). As such, these deficiencies are considered acceptable.

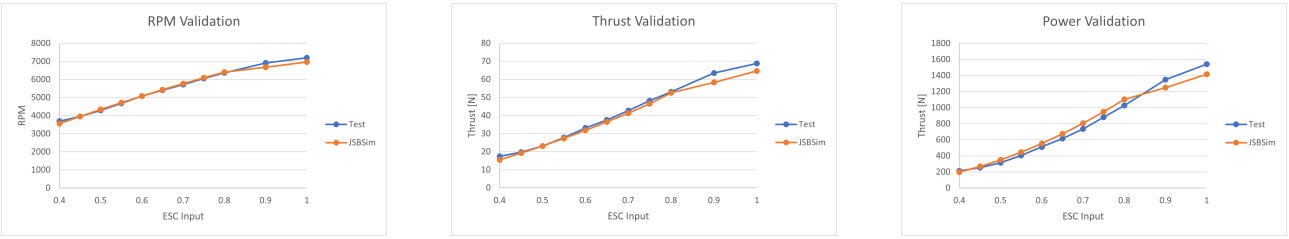

(a) RPM validation **(b)** Thrust validation **(c)** Power validation

Figure 12.3: Validation of cruise propulsion

Similarly, the validation plots for the VTOL propulsion system (T-MOTOR MN701S KV280 motor & T-MOTOR G26*8.5 propeller) can be found in Figure 12.4. Average deviations are 1.5% for RPM, 3.9% for thrust and 4.0% for power. Power estimations are conservative for all data points. Thrust estimations are non-conservative for low thrust levels, but conservative for the middle and high levels - this means that any manoeuvre predicted is likely possible, but might require a slightly higher thrust setting than predicted. Because of this conservativeness, the results are considered acceptable.

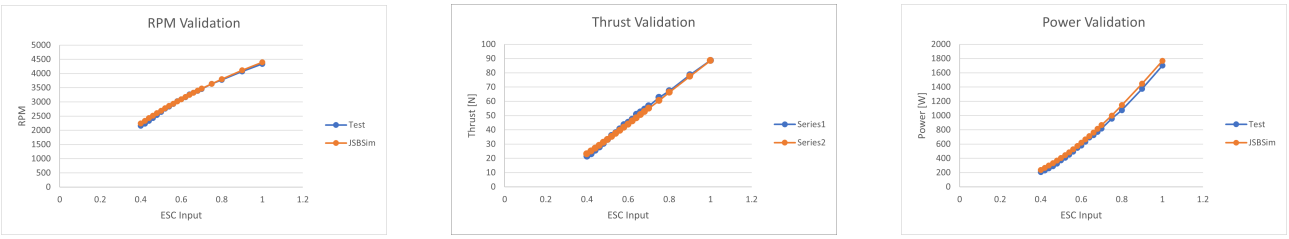

(a) RPM validation **(b)** Thrust validation **(c)** Power validation

Figure 12.4: Validation of VTOL propulsion

It is worth noting that data is only available for stationary thrust measurements. This means that simulation predictions might differ as the UAV's speed increases. While the incorporation of JavaProp results with different advance ratios does mean that the simulation will predict lower-thrust performance at higher velocities, this is not a guarantee that they accurately model reality. Furthermore, some model fitting took place to ensure results matched static thrust levels. These adjustments were linearly applied to the higher advance ratios (justified by the fact that C_T, C_P are linear in thrust and power respectively), but this might not accurately model real-world performance. In any case, with the lack of more time or available test data, the authors consider this level of V&V for the propulsion system acceptable to use in the final simulation results.

12.2.2. Handling Response Analysis

As described in Section 10.5, step inputs were given to the UAV's controlled variables. Section 10.5 showed that the system was stable under these inputs, and had the correct outputs/control deflections. Based on this, as well as a visual inspection of the coefficients that make up the flight simulation model it was concluded that they made sense.

In addition to these step responses, the authors created a testing setup where a joystick was attached to the simulation. This way a human can give control inputs and visually observe (through the FlightGear visualization) how the UAV responds. This was first done for various ready-to-use models of quadcopters and RC aircraft to gain a better understanding of how they respond. After this, similar manoeuvres were performed for the flight model proposed here.

In the authors' view, the flight dynamics model felt *realistic* the vast majority of the time. The main exception to this is when the UAV (crash) lands and tips over during the landing procedure. This can result in an uncontrolled spinning motion that does not look like it would be physically possible. At present, this is not a situation in which the flight dynamics model will be used. Furthermore, it is easy to detect either programmatically (by setting up a watch that looks for a sustained high angular rate) or by visual inspection. Because of these two facts, it is not considered problematic for the flight simulation's use.

Ideally, the simulation's performance would be evaluated against a prototype of the UAV. However, because of the limited time and budget associated with this project, this was not deemed feasible. Because of this, the analysis performed here is considered all that was possible to validate the performance of the flight model. Further information on how coefficients were obtained (with any relevant V&V procedures) can be found in other sections and is used as supporting evidence that the flight simulation can be trusted to produce accurate results.

12.3. Aerodynamic Convergence

In order to determine the correctness of the values gathered from the vortex lattice method aerodynamics analysis, the results' convergence needs to be assessed. Figure 12.5 shows the convergence of the $\frac{L}{D}$, C_L and the C_D in green, yellow and red, respectively. The x-axis indicates the number of iterations that have been performed and the y-axis indicates the residual on a logarithmic scale. This convergence is for an analysis performed with 6 wake iterations per point and 64 wake nodes. The lift-over-drag ratio converges around 0.01 residual, this accuracy is robust as $\frac{L}{D}$ values have always been rounded off to the first decimal. The C_L and C_d values converge to a residual of 0.002 and 0.0003, respectively. As only the first two and three decimals are used respectively, this convergence is deemed accurate. The accuracy of convergence can still be improved by increasing the wake nodes to 128. This requires twice the amount of computational time and is thus not used. Increasing the number of wake iterations has little effect on a relatively simple model that is being analysed. Figure 12.6 displays the convergence of the aerodynamic coefficients used for the flight model. It can be seen that all coefficients converge to a residual of 0.01 or lower.

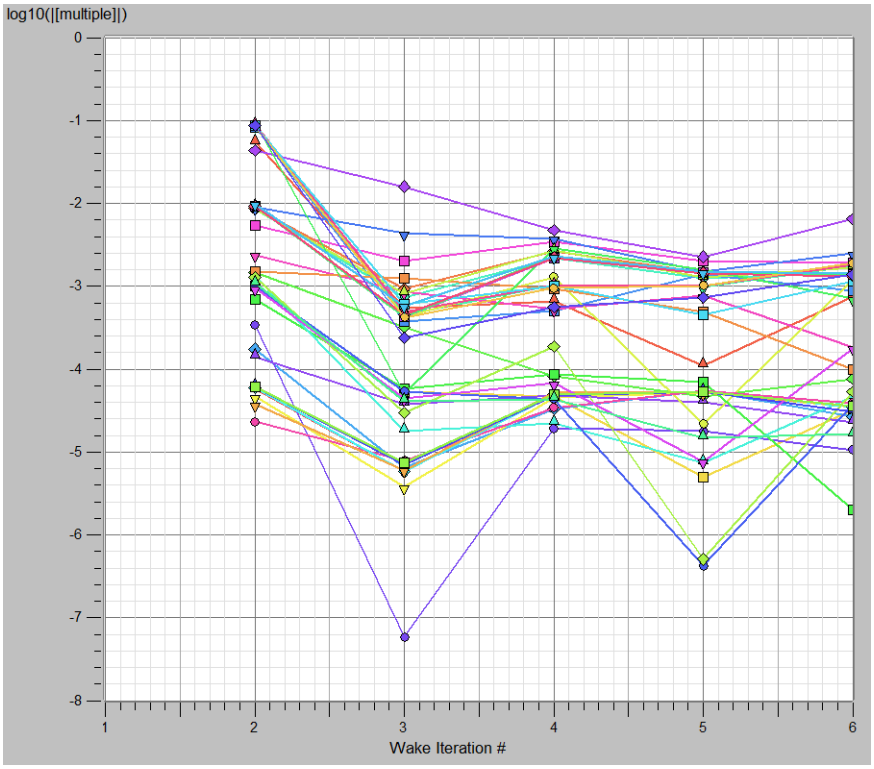

Figure 12.6: Convergence of aerodynamic coefficients in the OpenVSP VLM analysis.

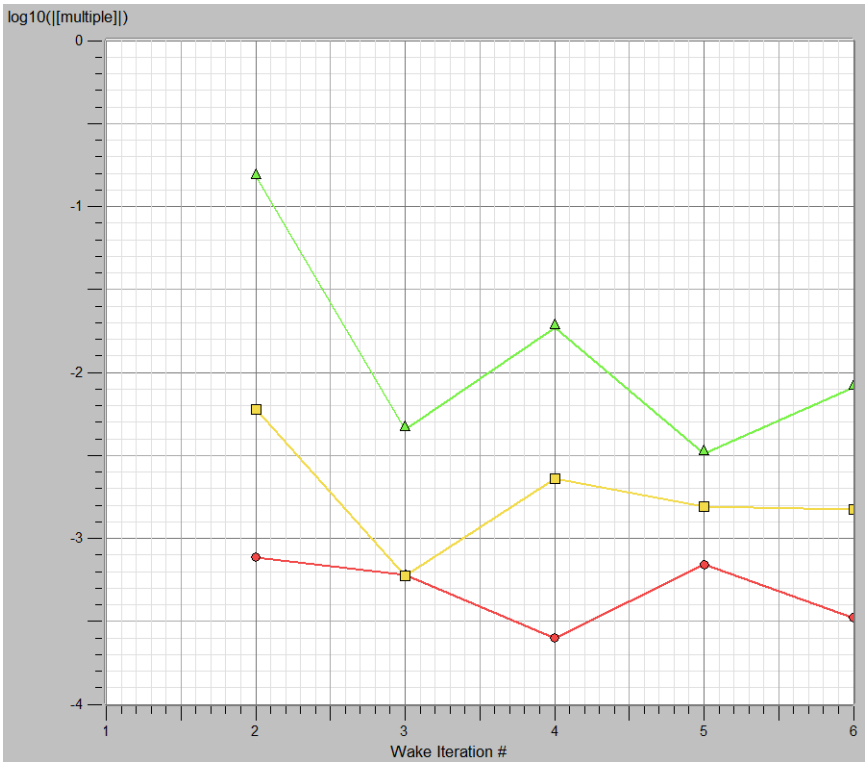

Figure 12.5: Convergence of $\frac{L}{D}$, C_L and the C_D in the OpenVSP VLM analysis.

It was also considered to model the booms as wing structures instead of simple geometry. This would then take into account the flow disturbance over the main wing and vertical stabilisers caused by the booms. The accuracy drop due to this assumption change was very large and all other calculations would become unverified. Therefore, it was decided not to include this effect.

12.4. Noise Model Validation

Metrics applied after the Hanson Model do not require further validation as they are simple equations for very commonly used sound metrics and thus have already been extensively validated. The calculations were verified using hand calculations. The Hanson model itself has to be validated. Fortunately, this has been done in earlier research by J. Barens et al. [29]. For this research experimental wind-tunnel data was used to specifically validate the Hanson model for both turbulent and clean flow. A minor deviation in how the noise was analysed compared to this report was that the research was performed in a near-field noise setup. A correction for noise propagation was thus added according to

$$L_{r_2} = L_{r_1} - 20\log_{10}(\frac{r_2}{r_1}) \tag{12.1}$$

where L is the sound intensity and r_1 and r_2 are the original and new distance respectively. This was verified in the model by means of a simple hand calculation.

Chapter 13: Sensitivity Analysis

In this chapter, the robustness of the design is addressed. By changing input parameters, it is tested whether the design is still able to operate. It is also discussed what needs to be adapted if a requirement is not met, due to a change in input parameters. The most sensitive subfields are the control surfaces, noise and the weight of the UAV. Hence, these will be discussed in the following sections.

13.1. Control Surface Design

Sensitivity analysis on the control surface design was performed by varying the distance of the control surfaces' centre of pressure to the UAVs' centre of gravity location. The elevator and the ailerons were sized by defining a constraining manoeuvre rate and calculating the required surface area needed to obtain such a manoeuvre rate, i.e. pitch and roll acceleration. Therefore, the varying parameter investigated for these control surfaces is the surface area needed for different locations of centre or pressure; S_e and S_a in m for elevator and ailerons respectively. The rudder on the other hand was sized using a typical value for area percentage of the vertical tail and based on that, the yaw rate the rudders are able to generate was found. For this reason, the parameter investigated for the rudder design is the yaw rate, $\dot{r}$ in rad s^{-2}.

For the elevator, the location of the centre of gravity was varied, from which the change in surface area and chord length were determined (assuming constant elevator span of 1.2 m). The results of this sensitivity analysis are shown in Table 13.1. Values for the centre of gravity were taken to be the reference location plus/minus 10% of UAVs' length, $\pm 0.1 l_{UAV}$. From this, it can be concluded that the elevator design is fairly robust in terms of changing centre of gravity location, as a change of 0.08 m results in a changing chord length of 0.01 m or less.

Table 13.1: Sensitivity analysis on elevator dimensions for the varying centre of gravity location.

ΔX_{cg} [m]	S_e [m^2]	b_e [m]	c_e [m]
-0.32	0.1284	1.20	0.11
-0.24	0.1187	1.20	0.10
-0.16	0.1104	1.20	0.09
-0.08	0.1032	1.20	0.09
0.00	0.0969	1.20	0.08
+0.08	0.0913	1.20	0.08
+0.16	0.0863	1.20	0.07
+0.24	0.0818	1.20	0.07
+0.32	0.0778	1.20	0.06

For the aileron, the centre of pressure of the aileron was varied, i.e. lateral placing of the aileron on the wing, from which the change in surface area and chord length were determined (assuming constant aileron span of 0.5 m). The results of this sensitivity analysis are shown in Table 13.2. Values for the centre of pressure were taken to be reference location plus/minus 10% of the wings' half span, $\pm 0.1 \frac{b_{wing}}{2}$. From this, it can be concluded that the aileron design is fairly robust in terms of changing the centre of pressure locations, since a change of 0.04 m results in a changing chord length of 0.01 m or less.

Table 13.2: Sensitivity analysis on aileron dimensions for varying aileron centre of pressure locations.

$\Delta Y_{cp,ail}$ [m]	S_a [m^2]	b_a [m]	c_a [m]
-0.16	0.0659	0.5	0.14
-0.12	0.0629	0.5	0.14
-0.08	0.06	0.5	0.13
-0.04	0.0575	0.5	0.13
0.00	0.0551	0.5	0.12
0.04	0.0529	0.5	0.12
0.08	0.0509	0.5	0.11
0.12	0.0491	0.5	0.11
0.16	0.0473	0.5	0.10

For the rudder, the moment arm to the centre of gravity was varied, from which the change in yaw acceleration was determined. The results of this sensitivity analysis are shown in Table 13.3. Values for the centre of gravity were taken to be the reference location plus/minus 10% of the horizontal tail length, $\pm 0.1 \frac{b_{tail}}{2}$. From this, it can be concluded that the rudder design is sensitive to changing moment arm, since an increase in moment arm of $0.05\,\text{m}$, results in a change in yaw rate of more than $1°$. This is probably because of the used design methodology, causing the rudder to be somewhat overdesigned and has therefore a large effect on changing the moment arm, at maximum rudder deflection that is.

Table 13.3: Sensitivity analysis on rudder performance for the varying centre of gravity location.

ΔY_{cp} [m]	$\dot{r}$ [° s^{-2}]
-0.15	24.99528
-0.10	26.06958
-0.05	27.1582
0.00	28.24682
0.05	29.32112
0.10	30.40973
0.15	31.49835

13.2. Noise

Reevaluating Table 11.3 and Table 11.2, it is evident that for nearly all metrics the VTO phase is the most constraining. Thus, a sensitivity analysis will be performed on the inputs of the VTO phase. First, a more elaborate explanation of the inputs for the current results is necessary. RPM, Blades, V and D_{blade} are derived directly from power/motor and propeller requirements.

A few input parameters have been determined with less certainty than others due to simplifications made. These are event duration, distance and velocity. Input parameters RPM, Blades, V and D_{blade} are dependent on motor and propeller requirements and are thus not likely to change, so were excluded from the analysis. For the distance, the minimum distance to an observer on the ground must be taken. During VTO the closest an observer could get would be along the fence of the GS parameter. Considering the dimensions of the GS this would be about $4.6/2 = 2.3$m (as the UAV station is 4.6 m wide) plus another 2 m of distance between the fence and the GS, this would amount to 4.3 m of horizontal distance between the UAV and the observer. As the UAV must also clear the 3 m height of the GS there is also a vertical distance of 3 m between the UAV and the observer. The minimum distance is thus equal to $\sqrt{4.3^2 + 3^2} = 5.5$m. However, it is important to realise that the distance increases during the event as the UAV is climbing to 30 m. The model can only account for a constant distance, thus a conservative average of 10 m was taken. Note that a similar procedure was done for the climb phases, where a distance of 30 m was used (which is where the climb altitude starts) even though at the end of the climb phase the UAV is at an altitude of 120 m. With this in mind, a sensitivity analysis can be done for the extreme case where the distance is taken to be the minimum distance of 5.5 m. Furthermore, the time duration of VTO is difficult to estimate as it is very dependent on the vertical downwind during VTO. Considering the UAV has a maximum VTO velocity of $6.5\,\text{m/s}$ for a 30 m climb, the max velocity might seem excessive. However,

the duration of 15 s was taken as a conservative estimate in case there is a downwind of around 3 m/s. For a sensitivity analysis, the duration could be increased even more to discover where the limit is w.r.t the noise requirement of 40 dBA. Finally, the number of events is based on operational requirements and is not likely to change but it can still be investigated where the limit lies.

Another interesting case to note is the SEL of the climb during a response mission. At 78.6 dBA it is even higher than VTO SEL (75.07 dBA) but for DEN it is much lower. This is due to the fact that the number of events is very low for a response mission, but due to the remarkably high SEL it should be included in the sensitivity analysis. In Table 13.4 the results of the sensitivity analysis can be found.

Table 13.4: Noise Sensitivity Analysis.

Phase	Parameter	Old Value	New Value	DEN (phase)	DEN (tot)
VTO	Distance [m]	10	5.49	42.07	43.53
	Duration [s]	15	26	38.85	40.1
	No. of events	12	21	38.9	40.1
Response mission	No. of events	1	6	36.98[1] (29.23[2])	40.36

V_max For all but one of the parameters analysed, a substantial increase is needed to exceed the 40 dBA DEN level. The VTO duration would need to be increased to 26 sec which would amount to a very low average velocity of just above 1 m/s. This would only occur at very high downwind. It was however decided the UAV will not take off in conditions where downwind is higher than 3.5 m/s, rendering the case of a 26 sec VTO irrelevant. The number of VTO events needs to be increased to 21. Besides there being little reason to increase it to this number it is most likely also not possible due to battery limitations. Furthermore, the number of response missions would need to increase to 6 per day, meaning 6 poacher or wildlife alerts per GS, which is also extremely unlikely to happen. The only parameter that could potentially cause issues is the distance of the UAV during VTO. Assuming the absolute minimum distance from the UAV to an observer the DEN increases to a considerable exceedance of 43.53 dBA, also note that this is considering a fence offset of 2 m from the GS which is quite large. However, as previously mentioned a constant distance is still assumed even though the source moves but as the sound intensity decreases by the square of the distance according to the inverse square law, the minimum distance is still very important. All in all, it is evident that distance plays a significant role in influencing the sound level.

13.3. Influence of mass on response time

While a fair amount of detailed design work has gone into UAV proposed in this report, a potential final prototype will no doubt have differences from what was discussed within this report. One of the most important aspects, or budgets, that must be accounted for is the mass budget of the UAV. If the UAV is heavier, it will need to generate more lift, use more energy and be harder to accelerate. To gain a better understanding of how changes in the UAV's take-off mass affect its performance during the response mission, a sensitivity analysis has been performed.

To perform the sensitivity analysis, it will be assumed that the mass moments of inertia around all axis scale linearly with mass. Furthermore, it is assumed that the design's outer shape remains constant, even as the mass changes resulting in constant aerodynamic properties. Under these assumptions, the response time to reach a target at 4.24 km out can be recorded for three different mass cases. The first is the unchanged case (mass: 14.01 kg), a 20% decrease in mass (mass: 11.208 kg) and a 20% increase in mass (mass: 16.812 kg). Three responses are analysed per mass case using the flight simulation model and averaged to reduce random effects, the results of which have been shown in Table 13.5.

[4] Response Climb
[5]

Table 13.5: Response time mass sensitivity.

Mass [kg]	Response time [s]
11.21	198.5
14.01	203.0
16.81	205.7

While small differences can be observed in the response times (as expected, the response time is higher for the higher-mass UAVs), the effect appears to be rather small, but the increase yields a slightly more significant difference than the decrease in mass. Overall, the response time appears largely insensitive to the UAV's take-off mass. Due to resource constraints, this was the only mode that could be analyzed during the timeframe of the DSE, but further investigations into power usage and the effect on the endurance requirement are highly recommended, as the authors expect the influence of mass to be larger in those areas.

[1] Response Climb

[2] V_{max}

Chapter 14: Technical Budgets

With the selection of various parts and analyses performed as part of the detailed design phase, updated technical budgets can be constructed. The updated UAV mass budget has been described in Section 14.1. The updated power budget for both the UAV and ground station has been described in Section 14.2. This chapter concludes by verifying that the previously selected battery is capable of providing the power derived from this budget for the entire duration of the mission.

14.1. Weight Budget

Weight estimation and distribution between key components that make up the UAV can be derived from the data sheets for individual parts as well as the analyses performed in the previous chapters. This process has been performed for each of the 5 key subsystem groups: structures, batteries, VTOL propulsion, payload and push propulsion. The components that make up the latter three groups have been shown in Table 14.1, Table 14.2, Table 14.3 respectively. Structural weight estimation follows from Chapter 8 and battery weight follows from Section 6.3. The subsystem mass estimates have been aggregated in Table 14.4 and visually shown in a pie chart in Figure 14.1.

Table 14.1: VTOL Propulsion weight budget.

Component	Weight per unit [kg]
Motor MN701S KV280	0.355
ESC ALPHA 80A 6-12S	0.11
Propeller T-Motor P26*8.5	0.07
Total (4 VTOL motors)	**2.14**

Table 14.2: Push Propulsion weight budget.

Component	Weight per unit [kg]
Motor AT4130 Long Shaft KV450	0.408
ESC AT 75A 6S	0.082
Propeller APC 18*8	0.132
Total (1 push motor)	**0.62**

Table 14.3: Payload weight budget.

Component	Weight per unit [kg]
Veronte Autopilot 1X (Remote ID V4.8)	0.201
Swarmlink MPSL2200	0.031
Jetson Orin NX 16Gb	0.028
Trillium HD40-LV	0.645
Blickfeld Cube 1 Outdoor	0.33
reComputer J202	0.075
GPS antenna AS-ANT2B-HEL-L1L2-SMA-00	0.018
tBeacon Onyx	0.01
Samsung Fit Plus 256GB	0.003
Total	**1.341**

Table 14.4: Subsystem weight budget.

Subsystem	Weight [kg]
Structures	5.78
Batteries	5.14
VTOL Propulsion	2.14
Payload	1.34
Push Propulsion	0.62
Total	**15.02**

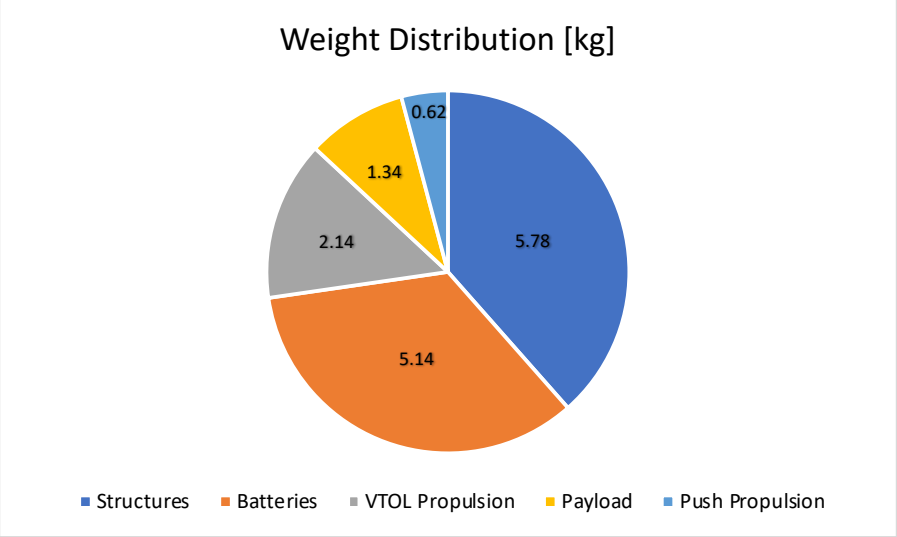

Figure 14.1: Weight distribution.

14.2. Power Budget

To evaluate the required power of the UAV, it is necessary to assess how the power requirements for the UAV subsystems shift at different stages of the mission. This is a result of differing speeds during each phase, thus necessitating varying levels of thrust and power accordingly. In addition, power requirements for ground stations also play a role.

14.2.1. UAV Power Budget

The power budget considers three distinct mission profiles, namely varying in the cruise phase objective. The first two mission profiles deal with satisfying the cruise speed and maximum possible endurance requirements respectively as meeting both of these in the same mission would lead the design to an unacceptable extent. The remaining cruise configuration refers to flying at a maximum operative speed. The other phases considered in each mission profile are take-off, climb, descent and landing. Table 14.5 shows the budgets of the mission phases.

Table 14.5: Subsystem power budget for different mission phases.

Mission Phase	Instrumentation Power [W]	GNC & Comms Power [W]	Total Propulsion Power [W]	Total Power [W]	Duration [s]	Velocity [m/s]	Energy Consumption [Wh]
Take-Off	-	90	6154.11	6245	15	0-6.3	26.02
Transition	24	90	3739	3853	10	6.3-16.5	10.70
Climb	24	90	617	731	33	59	11.98
Acceleration	24	90	617	731	10	16.5-22.22	2.03
Cruise (speed @80 km/h)	24	90	386	389	7109	22.22	768.2
Cruise (max endurance @64.8 km/h)	24	90	213	327	8509	18.0	772.9
Cruise (V_{max} @141.12 km/h)	24	90	1540	1655	1637	35.43	752.1
Descent	24	90	212	326	30	22.22-18.33	2.72
Landing	24	90	2188	2302	20	18.33-0	12.79

There are some important considerations regarding the budget above:

- Instrumentation Power refers to the power required by the camera and LiDAR sensor. Moreover, the power for GNC & Communications and propulsion encapsulates the power needs of the autopilot, computational/data processing modules, antenna and motors respectively.
- The propulsion during the cruise is assumed to be entirely driven by the main motor. In other words, VTOL motors are not used at this stage. Furthermore, the payload/instrumentation is not activated during the take-off phase. Finally, the UAV is assumed to descend by gliding, resulting in no power required for propulsion.
- The maximum Depth of Discharge (DoD) of the battery has been set at 70%. Such range allows for a higher cycle life of the battery compared to an undesirable 0-100% depth. This can be seen in Figure 14.2: for a DOD of 70% the Cycle Life more than doubles compared to 100%. To prevent self-discharge it is desirable for the battery state of charge (SoC) to be as close as possible to 40-50%[1]. Taking into account the DOD of 70% the selected battery's SoC ranges between 15% and 85%. In addition, the typical discharge efficiency for Li-ion batteries is 80-90% [30], so for calculations, the upper limit (90%) is arbitrarily assumed.

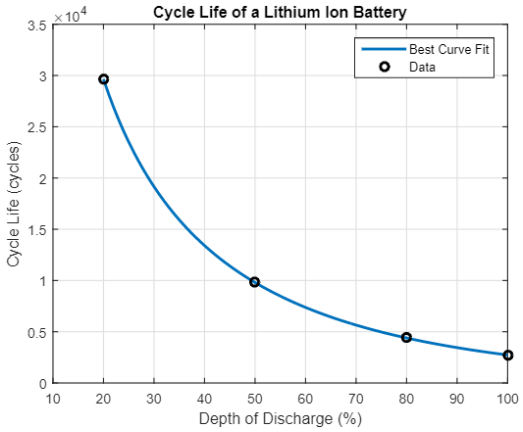

Figure 14.2: Depth of Discharge (DOD) plotted as a function of Life Cycle for a Li-ion battery [31]

- To simplify the analysis of power requirements, the thrust level/throttle is assumed to remain constant throughout each phase. These levels are shown in Table 14.6 where V and P stand for VTOL and horizontal push motor(s) accordingly.

Table 14.6: Throttle Levels.

Mission Type	Throttle Level [%]
Take-Off	95 (V)
Transition	95-0 (V) and 54-85 (P)
Climb	85 (P)
Cruising @ 80 km/h	47 (P)
Cruising @ Max Velocity	100 (P)
Cruising @ Max Endurance	40 (P)
Descent	40
Landing	58 (V)

The battery size decided upon in Section 6.3, needs to be verified now that the mission phases are identified more precisely. Using Equation 14.1, the battery percentage used in each step of the mission can be determined, taking into account the aforementioned considerations.

$$DoD = \frac{P_{\text{load}} \cdot t_{op}}{\eta_{\text{tot}} \cdot V_{\text{load}} \cdot C_{\text{actual}}} \tag{14.1}$$

During the initial sizing, the DoD and discharge efficiency are not taken into account. It is possible to fly at a cruise speed of $80\,\text{km/h}$ for $2\,\text{h}$ and $27\,\text{s}$. At this velocity, the maximum range requirement of $150\,\text{km}$ (REQ-GEN-11) is also met as $88 \cdot 2.007 = 160.56$ km. Alternatively, it is possible to fly at an airspeed of $64.8\,\text{km/h}$

[1] https://batteryuniversity.com/article/bu-702-how-to-store-batteries, accessed on: 13-06-2023

for 2 h and 24 min, which is useful for performing the orography measurements as this will be done at a lower altitude due to limitations of the LiDAR. For the quick response time, it is most interesting to consider the maximum airspeed. At an airspeed of 141.12 km/h, a flight time of 29 min and 15 s is feasible. Note that during each of these 4 missions, the total energy consumed is the same and results in approximately 858 Wh.

To facilitate the possible adjustments or improvement of UAV subsystems during the design, the power consumption of the individual subsystem components is crucial to consider. Such data is thus in Table 14.7:

Table 14.7: Power consumption of instrumentation instrumentation & GNC/communication subsystems.

Subsystem	Component	#	Total Power Consumption [W]
Instrumentation	Trillium HD40-LV camera[2]	1	15
	Blickfeld Cube 1 Outdoor[3]	1	9
GNC & Communications	Veronte Autopilot 1X[4]	1	15
	Swarmlink MPSL2200 antenna[5]	1	50
	Jetson Orin NX 16Gb system-on-module[6]	1	25

14.2.2. Ground Station Power Budget

To accommodate the charging of the UAV and data processing, a number of components need to be present in the ground station to make it fully functional. These components draw power, which necessitates consideration of a power budget which is needed for solar panel sizing. The budget is presented in Table 14.8:

Table 14.8: Ground Station Power Budget.

Component	Power Consumption [W]
AH-1726-16 Polarized Helical Antenna[7]	150
VM1000 Microphone [8]	≈ 0
Starlink High Performance Kit [9] [10]	200
ThinkStation P358 Tower Workstation [11]	300
Beetronics 15VG7M Live Feed Monitor [12]	14
Weather Station ECOWITT (sol. pan. incl.)[13]	-
Total	**664**

All components, except for the Starlink High-Performance Kit, are present in every ground station, meaning that a regular GS has a power budget of 464 W. Within an entire system, Starlink is only present in one central GS. Furthermore, there is a weather station that operates independently as it is powered by its own solar panel thus it does not contribute to the overall power usage of the ground station.

14.3. UAV Battery Choice Verification

To verify the choice of a battery suitable for achieving the designated mission purpose, one shall consider the energy consumption as estimated earlier. With the UAV intended to be capable of performing 4 separate missions, it is important to look into the energy capacity of two batteries combined together (the design uses two batteries) and compare it to the total energy used per mission. To find the former, the following relation holds:

$$E = Q \cdot V \cdot \eta_{disch} \cdot DoD = 60 \cdot 22.2 \cdot 0.9 \cdot 0.7 = 839.16\,\text{Wh} \tag{14.2}$$

[2] https://www.trilliumeng.com/gimbals/hd40, accessed on 21-06-2023

[3] https://www.blickfeld.com/lidar-sensor-products/cube-1/, accessed on 21-06-2023

[4] https://www.embention.com/product/veronte-autopilot-1x/, accessed on 21-06-2023

[5] https://www.mpantenna.com/mp-sl-series-antennas/, accessed on 21-06-2023

[6] https://www.nvidia.com/en-us/autonomous-machines/embedded-systems/jetson-orin/, accessed on 21-06-2023

[7] https://www.antennaexperts.in/docs/AH-1726-16-Datasheet.pdf, accessed on 16-06-2023

[8] https://vespermems.com/products/vm1000/, accessed on 09-06-2023

[9] https://www.starlink.com/specifications?spec=2, accessed on 09-06-2023

[10] https://www.makeuseof.com/how-much-power-does-starlink-use/, accessed on 09-06-2023

[11] https://www.lenovo.com/nl/nl/workstations/p-series/ThinkStation-P358-Tower-AMD/p/LEN102S0008, accessed on 09-06-2023

[12] https://shorturl.at/dknrz, accessed on 09-06-2023

[13] https://www.ecowitt.com/shop/homePage, accessed on 09-06-2023

where Q[Ah], V[V], η_{disch} [-] and DoD [%] refer to charge capacity, nominal voltage, discharge efficiency and depth of discharge respectively. As mentioned earlier, the total energy consumed per mission is 858 Wh, thus indicating seemingly insufficient batteries. While the exact cause of such discrepancy is unclear, it is suspected to be caused by determining the DoD at the beginning of the phases of the mission while *de facto* it should be updated each second. This means that the assumed actual battery capacity is a bit lower in reality.

Chapter 15: Development, Manufacturing and Operations Strategy.

In this chapter, the post-development processes and strategies are discussed. The chapter starts with the manufacturing plan, which will give insight into the way the UAV will be manufactured according to a step-by-step plan. After that, the project logic is discussed. A diagram is included that gives an overview of all upcoming phases and what can be expected. Lastly, the strategy with respect to sustainability is discussed.

15.1. Manufacturing, Assembly & Integration Plan

The manufacturing of the UAV is an essential part of the post-design phase. To do so successfully, a coherent plan should be set up that allows workers and mechanics to manufacture and assemble the parts. The manufacturing of these parts is discussed first. Secondly, the assembly processes are listed and given in the second section. An overview of the production plan is given in Figure 15.1.

15.1.1. Manufacturing

To manufacture the parts, there are several steps that should be taken. First, a list of parts is given in Table 15.1.

Table 15.1: List of parts that require manufacturing with corresponding material and manufacturing method.

Subsystem	Component	Number of parts	Material	Manufacturing method	Comments
Blended Body	Base Plate	1	Aluminium 7075	Die Forming and Punching	Using female rubber dies
	Fuselage Bottom Shell	1	TC380 CFRP	Laminating and Curing	Making use of a MDF mould
	Fuselage Top Shell	1	TC380 CFRP	Laminating and Curing	Making use of a MDF mould
Wing	Shell	2	TC380 CFRP	Laminating and Curing	Making use of a MDF mould
	Stringers	8	Aluminium 7075	Cutting and Rubber Forming	
	Ribs	8	Aluminium 7075	Water Jetting and Rubber Forming	Using male rubber dies
	Aileron Shell	2	TC380 CFRP	Laminating and Curing	Making use of a MDF mould
Boom	Boom Strut	2	TC380 CFRP	Laminating and Curing	Making use of a circular mould
	Landing Gear Strut	4	TC380 CFRP	Laminating and Curing	Making use of a circular mould
	Landing Gear Brass Core	4	CW511L DZR Brass	Casting	
Tail	Vertical Tail Foam Core	2	Rohacell Foam	Hot Wire Cutting	
	Vertical Tail Shell	2	TC380 CFRP	Laminating and Curing	Laminate upon foam core
	Rudder Shell	2	TC380 CFRP	Laminating and Curing	Making use of a MDF mould
	Horizontal Tail Foam Core	1	Rohacell Foam	Hot Wire Cutting	
	Horizontal Tail Shell	1	TC380 CFRP	Laminating and Curing	Laminate upon foam core
	Elevator Shell	1	TC380 CFRP	Laminating and Curing	Making use of a MDF mould

To manufacture these parts, the steps proposed in Table 15.2 should be followed.

Table 15.2: Production Plan for Parts

Identifier	Instruction
1	**Base Plate**
1.1	Use an aluminium-7075 1 mm thick sheet with minimum dimensions of 1 by 1 meter.
1.2	Make female rubber dies with the shape of the batteries and LiDAR.
1.3	Perform die forming to add buckets to the sheet on the location where the instruments should be placed.
1.4	Mark the shape of the base plate around the buckets.
1.5	Punch the base plate shape out of the aluminium sheet, using a punching machine.
2	**Bottom shell fuselage**
2.1	Create an MDF (Medium Density Fibreboard) negative split mould (cut through the horizontal axis) with a horizontal edge at the end of both sides.
2.2	Put a release agent chemical over the MDF mould so the carbon fibre can be released easily after curing.

2.3	Laminate over the MDF mould to create a positive split mould out of carbon fibre TC380. A carbon fibre mould is created because MDF has a different expansion coefficient from carbon fibre. If the part is directly made from the MDF mould, it will induce stress concentrations into the carbon fibre part.
2.4	Heat up the curing oven to 180 degrees Celsius.
2.5	Put the mould in a vacuum bag at full vacuum.
2.6	Cure the mould in the curing oven at 180 degrees Celsius.
2.7	Remove the carbon fibre mould from the MDF mould.
2.8	Put a release agent chemical over the carbon fibre mould so the carbon fibre can be released easily after curing.
2.9	Laminate 3 layers of carbon fibre TC380 prepreg over the negative carbon fibre mould.
2.10	Vacuum bag the part twice (Double Vacuum).
2.11	Heat up the curing oven to 180 degrees Celsius.
2.12	Cure the part in the curing oven.
2.13	Remove the carbon fibre part from the mould.
2.14	Post-process the part if needed (for example: sanding the edges).
3	**Top shell fuselage**
3.1	Repeat steps 2.1-2.14 for the upper shell of the fuselage
4	**Stringers**
4.1	Use aluminium 7075 I-beam stringers with a minimum length of 3 meters.
4.2	Cut the aluminium stringers with a metal cutting saw to the required stringer lengths.
4.3	Bend the aluminium stringers to fit the wing and fuselage shape, using a metal beam roller.
4.4	Bend the outer flanges of the stringers to allow a better fit to the airfoil shape.
5	**Ribs**
5.1	Use an aluminium 7075 2-mm thick sheet with minimum dimensions of 1 by 1 meter.
5.2	Mark the shapes of the required ribs on the sheet.
5.3	Cut the aluminium ribs out the sheet, using water jetting.
5.4	Make male rubber dies with the correct shape of the ribs.
5.5	Perform die forming to add flanges to the ribs.
6	**Wing Shells**
6.1	Create a MDF (Medium Density Fibreboard) mould in the wing shape, however, (2x0.681mm) smaller in thickness on all sides compared to the wing shape.
6.2	Put a release agent chemical over the MDF mould so the carbon fibre can be released easily after curing.
6.3	Laminate one layer of carbon fibre TC380 over the MDF mould for a carbon fibre mould.
6.4	Heat up the curing oven to 180 degrees Celsius.
6.5	Put the mould in a vacuum bag at full vacuum.
6.6	Cure the mould in the curing oven at 180 degrees Celcius.
6.7	Remove the carbon fibre mould from the MDF mould.
6.8	Put a release agent chemical over the carbon fibre mould so the carbon fibre can be released easily after curing.
6.9	Laminate three layers (0.681mm) of pre-preg carbon fibre TC380.
6.10	Heat up the curing oven to 180 degrees Celsius.
6.11	Vacuum bag the part twice (Double Bagging).
6.12	Cure the part in the curing oven.
6.13	Remove the carbon fibre part from the mould.
6.14	Post process the part if needed (for example: sanding the edges).
6.15	Follow steps 6.1-6.14 for the right wing.

7	**Aileron Shells**
7.1	Use a block of 0.07 x 0.05 x 0.5 m (chord x thickness x span) MDF and cut a NACA0015 airfoil shape (0.681 mm smaller circumference) out of the plane with 0.1 x 0.05 m.
7.2	Put a release agent chemical over the MDF mould so the carbon fibre can be released easily after curing.
7.3	Laminate one layer of TC380 carbon fibre prepreg over the MDF mould.
7.4	Heat up the curing oven to 180 degrees Celsius.
7.5	Put the mould in a vacuum bag at full vacuum.
7.6	Cure the mould in the curing oven at 180 degrees Celsius.
7.7	Remove the carbon fibre mould from the MDF mould.
7.8	Put a release agent chemical over the carbon fibre mould so the carbon fibre can be released easily after curing.
7.9	Laminate three layers (0.681 mm) of pre-preg carbon fibre TC380 over the mould.
7.10	Heat up the curing oven to 180 degrees Celsius.
7.11	Vacuum bag the part twice (Double Bagging).
7.12	Cure the part in the curing oven.
7.13	Remove the carbon fibre part from the mould.
7.14	Post-process the part if needed (for example: sanding the edges).
7.15	Repeat steps 7.1-7.14 for the second aileron shell.
8	**Horizontal Tail**
8.1	Create mould and horizontal stabilizer core out of Rohacell foam block.
8.2	Hotwire cut a block 300 x 150 x 1500 mm (chord x thickness x span) of Rohacell foam, start at the trailing edge and cut in the shape of a NACA0015 with a length of 1500 mm.
8.3	Put a layer of adhesive film over the inner piece of the Rohacell cutout.
8.4	Laminate one layer of TC380 carbon fibre prepreg over the adhesive film.
8.5	Vacuum bag this under full vacuum.
8.6	Put the laminated wing (with the vacuum bag over it) back into the outer piece of the Rohacell cutout. (To secure the shape during curing).
8.7	Vacuum bag the mould with the wing inside under half vacuum. Double vacuum bagging is done so that the fibre-over-resin ratio will be better and it optimized the quality of the composite. As no autoclave is used in this process, double vacuum bagging is used.
8.8	Heat up the curing oven to 180 degrees Celsius.
8.9	Cure the part in the curing oven.
8.10	Take the part out of the mould and both vacuum bags.
8.11	Post-process the part if needed.
9	**Vertical Tail**
9.1	Create mould and vertical stabilizers core out of Rohacell foam blocks.
9.2	Hot wire cut a block 300 x 150 x 300 mm, (chord x thickness x span) of Rohacell foam, start at the trailing edge and cut in the shape of a NACA0015.
9.3	Follow steps 8.2-8.11 twice for each vertical stabilizer.
10	**Elevator Shell**
10.1	Use a block of 0.09 x 0.045 x 1.2 m (chord x thickness x span) MDF and cut a NACA0015 airfoil shape (0.681 mm smaller circumference) out of the plane with 0.1 x 0.05 m.
10.2	Follow steps 7.2-7.14.
11	**Rudder Shells**
11.1	Use a block of 0.09 x 0.045 x 1.2 m (chord x thickness x span) MDF and cut a NACA0015 airfoil shape (0.681 mm smaller circumference) out of the plane with 0.1 x 0.05 m.
11.2	Follow steps 7.2-7.14.

12	**Boom Shells**
12.1	Make MDF mould of the boom shells by having a solid rod of MDF with flatter parts where the propeller engines are attached.
12.2	Follow steps 7.2-7.14.
13	**Landing Struts**
13.1	Use a block of 0.25 x 0.05 x 0.05 m MDF and cut the landing struts shape out with 0.681 mm smaller on all sides.
13.2	Follow steps 7.2-7.14.
14	**Charging Core**
14.1	Create a graphite mould with the charging core shape.
14.2	Heat up brass to 930 degrees Celsius.
14.3	Pour the liquid brass into the mould.
14.4	Let the brass cool down in the mould.
14.5	Remove brass part from mould
14.6	Polish the brass part

15.1.2. Assembly

Together with the off-the-shelf products, the manufactured part can be assembled to finalise the UAV. The steps required for assembly are found in Table 15.3.

Table 15.3: Production Plan for Assembly

Identifier	Instruction
1	**Fuselage**
1.1	Mark the attachment points for every instrumentation on the base plate.
1.2	Attach the camera and LiDAR to the bottom side of the bottom of the base plate, using screws.
1.3	Clamp the base plate from the ground top up with enough clearance for the camera.
1.4	Attach the motherboard, processor and data handling instrumentation to the base plate, using screws.
1.5	Bolt the motor and ESC to the base plate.
1.6	Attach the power supply to the base plate, using screws.
1.7	Connect all instrumentation to each other.
1.8	Fix the fuselage bottom shell to the bottom of the base plate.
1.9	Attach the opening mechanism to the base plate.
1.10	Attach the fuselage top shell to the opening mechanism.
1.11	Test the closing and opening of the opening mechanism.
2	**Wing**
2.1	Use adhesive to attach both the top and bottom, outer stringers to the inside of the left wing shell and let dry.
2.2	Use adhesive to attach the outer rib to the inside of the left wing shell and let dry.
2.3	Repeat steps 2,1 and 2,2 until all stringers and ribs are attached to the left wing shell.
2.4	Attach servo and left aileron shell to the left wing shell.
2.5	Repeat steps 2.1 to 2.4 for the right-wing shell.
3	**Wing-Body**
3.1	Place the wings next to the fuselage
3.2	Connect wiring to the instruments through the sides of the fuselage.
3.3	Connect wiring to the servos of the ailerons
3.4	Lead wiring through the wings to the place where the booms will be attached.
3.5	Use a fast clamp mechanism to clamp the wings to the fuselage shells.

4	**Empennage**
4.1	Attach the servo and rudder shell to the left vertical tail.
4.2	Repeat step 4.1 for the right wing.
4.3	Attach the servo and elevator shell to the horizontal tail.
4.4	Connect wiring to the servos of the elevators and horizontal tail.
4.5	Lead the wiring from step 4.4 to the bottom of the vertical tails.
4.6	Connect the vertical tails to the horizontal tail.
5	**Booms**
5.1	Use insulating adhesive to fix the brass core to the landing strut.
5.2	Repeat step 5.1 for all four of the landing struts.
5.3	Lead wiring through the left boom to the location of the instrumentation, VTOL motors, landing gear and left vertical tail.
5.4	Connect and fix the pitot tube and antenna to the front of the left boom.
5.5	Connect and fix the VTOL motors in the two holes in the left boom.
5.6	Connect and screw two landing struts to the left boom underneath the VTOL motors.
5.7	Repeat steps 5.3 to 5.6 for the right boom.
6	**UAV**
6.1	Place the wing-body, booms and empennage in the right layout on the ground.
6.2	Connect the wiring from the left boom to that of the left wing to each other.
6.3	Fix the left boom to the bottom of the left wing shell.
6.4	Repeat steps 6.2 and 6.3 for the right side of the UAV.
6.5	Connect the wiring from the left boom to that of the left vertical tail.
6.6	Fix the left vertical tail to the end of the left boom.
6.7	Repeat steps 6.5 and 6.6 for the right side of the UAV.
6.8	Screw the four VTOL and single pushing propellers to the corresponding motors.

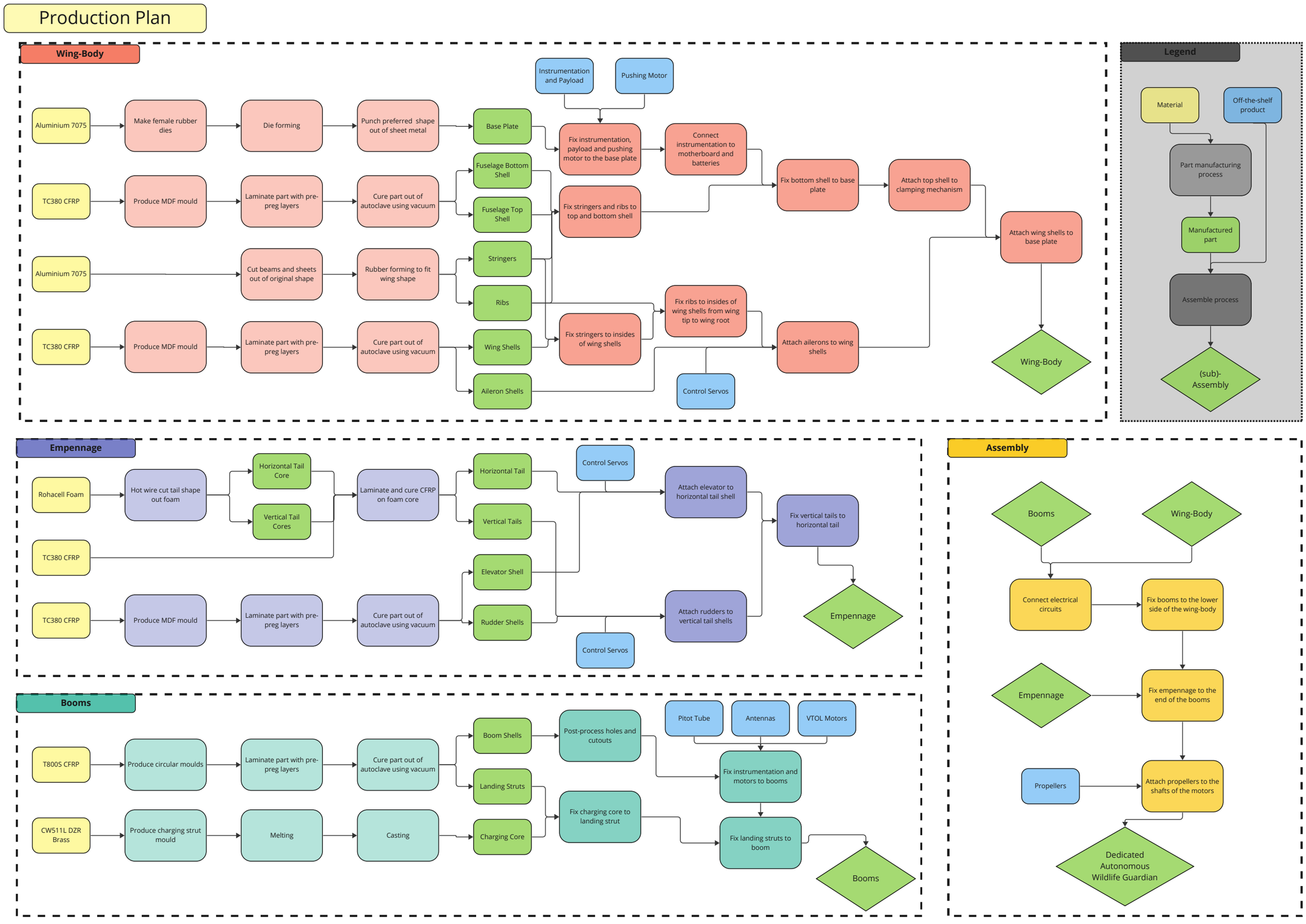

Figure 15.1: A diagram of the production plan with logically ordered steps.

15.2. Project Design and Development Logic

The result of this research and design process is not the final stage of the development process. The design should be manufactured, tested and validated. Afterwards, a flight certification should be attained to allow the UAV and ground station to become commercially available. A detailed description of the steps required is included in this chapter.

The design generated in the making of this report is yet to be finalised. Although the wiring is included, an electrical engineering process should be done to establish a working interface between all subsystems. The mechanism to control the control surfaces' deflection should also be designed. This would require a more elaborate evaluation of the required forces that act upon these surfaces. Next to that, the computer software should be developed to ensure the correct functioning and communication of the instrumentation. Finally, the design will be iterated multiple times until a convergent design is established. Once the design is finalised, the prototyping phase can commence.

With carefully selected preliminary tooling, a prototype can be made, following the production plan. This or multiple prototypes can be tested extensively and validated to fit the requirements. It might be necessary to make adaptations to the design to comply with a requirement. Once this is done, the UAV will be required to get a flight certificate. For the construction of the ground stations in nature and wildlife reserves, building permits should be attained. This will go hand in hand with exploring market opportunities.

A thorough market analysis will be performed to establish an updated market share and return on investment. This would give the most accurate estimate for probable costs and revenues. Contracts can be set up with investors and customers to ensure future endeavours. During this phase, a marketing plan should be put in place. Socials will be set up and advertisements will be put up in appropriate places.

When there is gathered a sufficient budget to launch the company, the manufacturing process can start. The company will need a headquarter and a factory to manufacture the drones. Workers will be hired to produce both the UAV and the ground station. Next to that, connections with external part manufacturers will be established to successfully gather the required parts. After that, it is a matter of selling and transporting the UAVs and building the ground stations.

During the operation phase, the company will be available for potential support and maintenance instances. This phase will last at least ten years, as stated in the return on investment section. Software should be kept up to date to ensure the promised security to the customers. All phases and processes can be found in Figure 15.3 below. Furthermore, an overview of costs can be found in Figure 15.2.

The Gantt chart for the future design stages can be found in Figure 15.4.

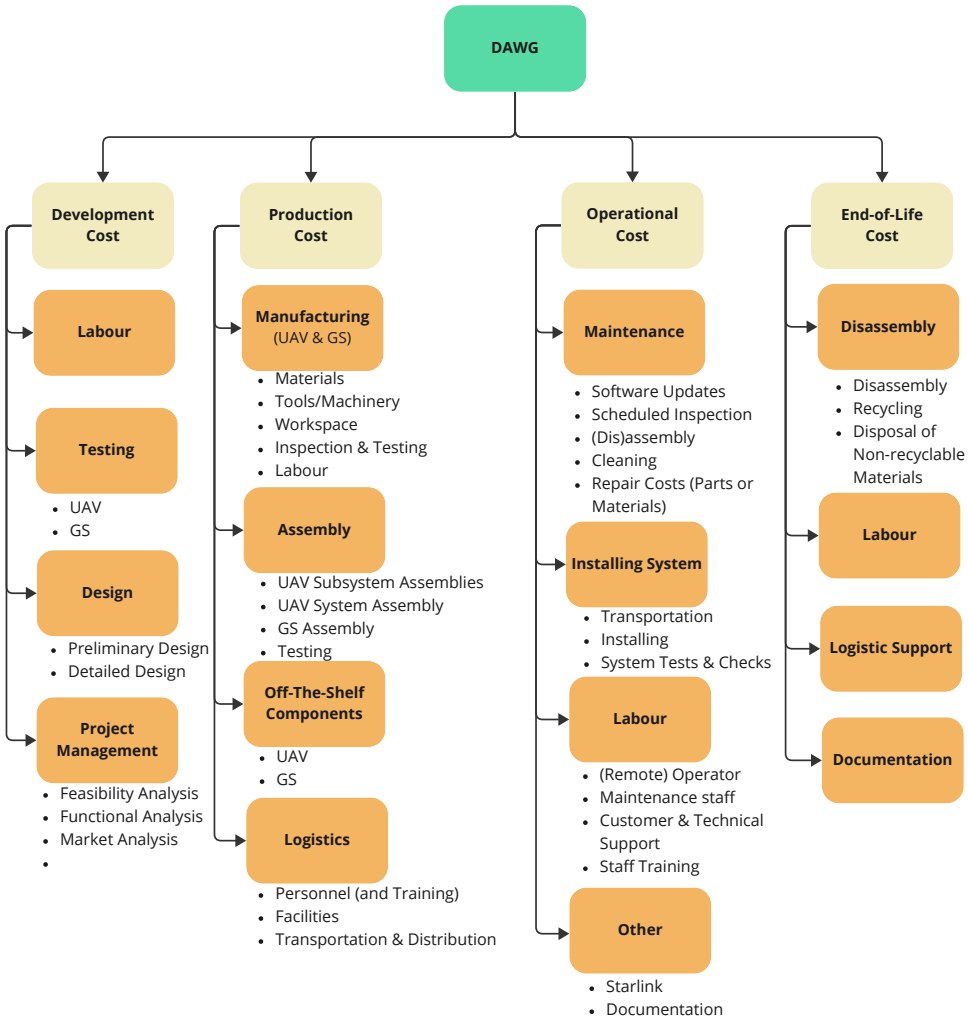

Figure 15.2: Cost Breakdown Structure

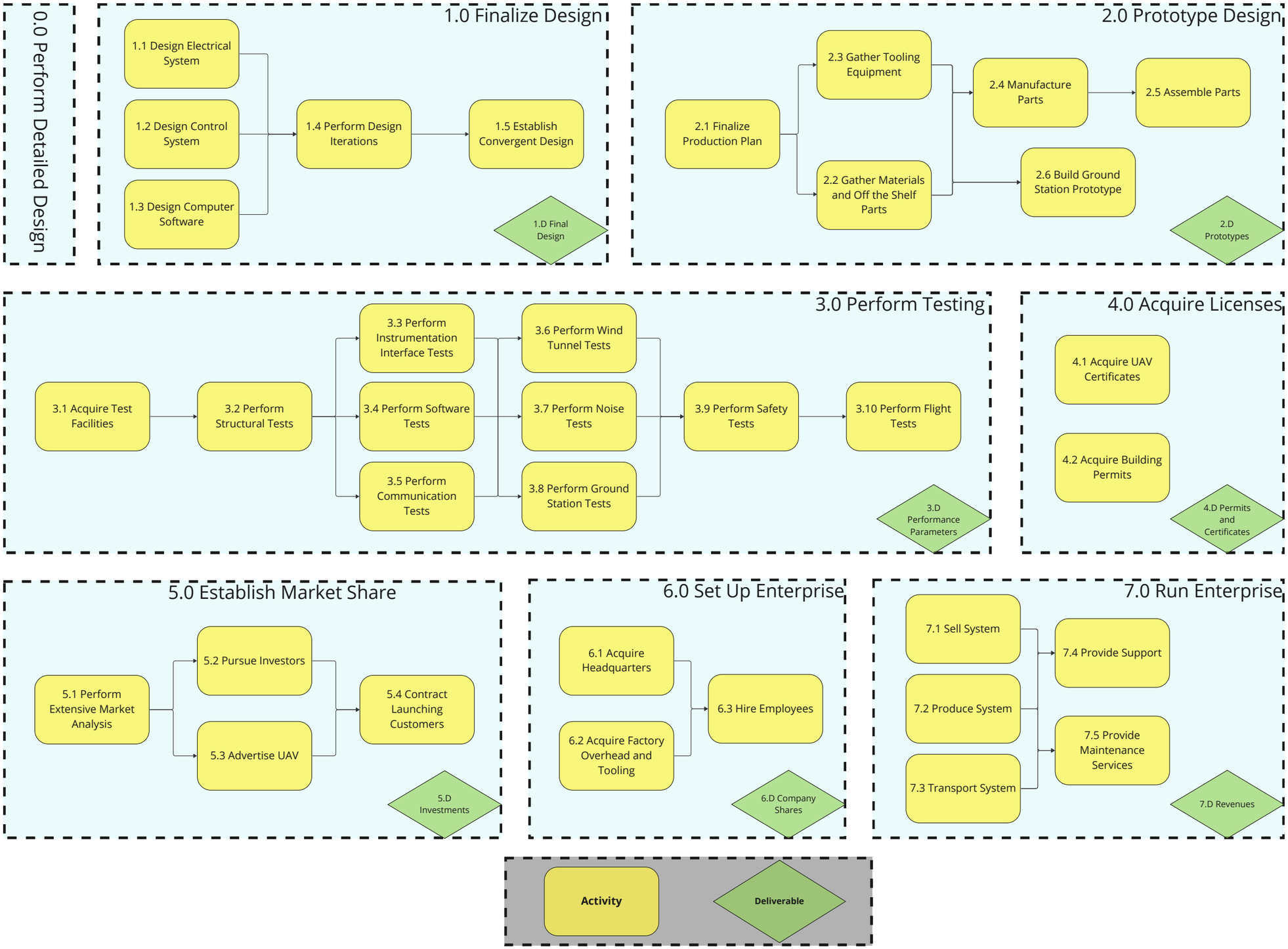

Figure 15.3: The post-design project design and development logic diagram.

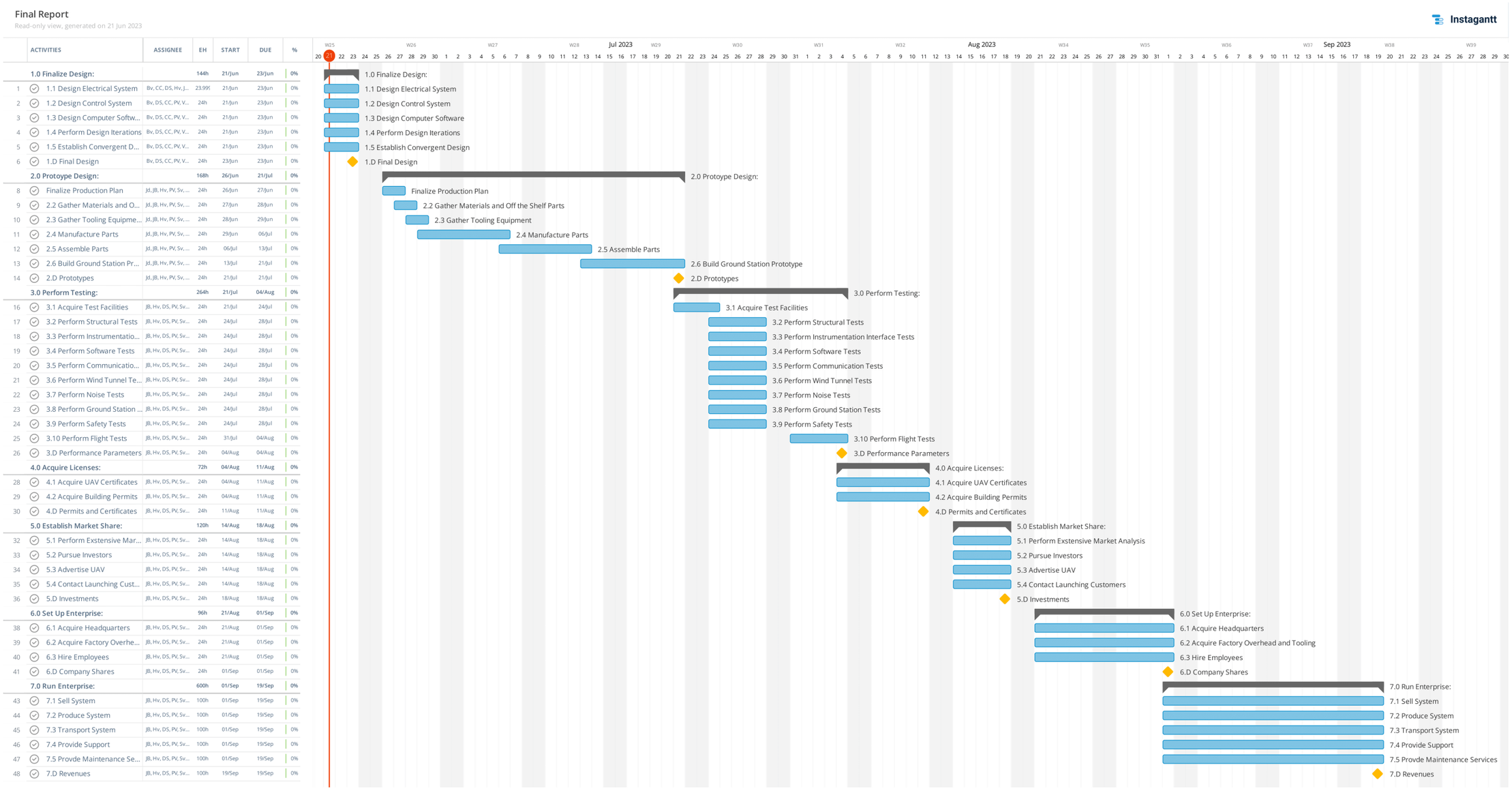

Figure 15.4: Gant Chart.

15.3. Sustainable Development Strategy

As the depletion of energy resources and environmental issues are becoming prevalent topics in modern society, sustainability considerations when designing aerial surveillance systems or any other engineering projects play a crucial role in ensuring the successful and long-term operation of the design. As such, the life cycle of the drone and power sources are discussed and compared with respect to greenhouse gas (GHG) emissions in subsection 15.3.1. Finally, the contribution towards sustainability by the UAV is described in subsection 15.3.2.

15.3.1. Life Cycle GHG Emissions

The UAV emits GHG throughout its entire lifespan, namely production, operation and end-of-life. It is important to assess the relative GHG emissions for said 3 parts of the UAV's life. During production, the GHG emissions of the raw materials need to be taken into account. CFRP, consisting of carbon fibre and epoxy resin, is used as the main material for the UAV. Virgin PAN carbon fibre requires approximately 24 $\mathrm{kgCO2_{eq}} \cdot \mathrm{kg_{CF}^{-1}}$ to be produced and epoxy resin emits approximately 6.7 $\mathrm{kgCO2_{eq}} \cdot \mathrm{kg_{ER}^{-1}}$.[32][33] This means that the production of CFRP emits a total of 30.7 $\mathrm{kgCO2_{eq}} \cdot \mathrm{kg_{CFRP}^{-1}}$. It has been determined that the UAV's structure has a mass of $5.48\,\mathrm{kg}$ resulting in a production emission of 168.26 $\mathrm{kgCO2_{eq}}$ for the UAV structure. Furthermore, the UAV is powered by two Li-ion batteries, which emit 150 $\mathrm{kgCO2_{eq}} \cdot \mathrm{kWh}^{-1}$.[1] One Li-ion battery has a capacity of 666 Wh, meaning that the UAV requires 1.33 kWh from Li-ion batteries. Thus, the production of the two Li-ion batteries emits 200 $\mathrm{kgCO2_{eq}}$. These are the most polluting factors during production, therefore other production emissions due to the communication system and the instrumentation are negligible. This results in a total UAV production emission of $368.26\mathrm{kgCO2_{eq}}$. The Doghouse ground station will also emit GHG during production, mostly coming from the concrete structure that the UAV will be parked in. The shelter consists of 4 recycled aluminium walls that are 6m wide and 3m tall and one foundation of 6 m by 6 m. Each wall is assumed to have a thickness of $0.05\,\mathrm{m}$. Recycled aluminium panels are chosen because of their low GHG emissions. If concrete was used to make the same structure, the GHG emissions would be approximately $63000\mathrm{kgCO2_{eq}}$. Assuming that the woven bends of the aluminium plate increase the volume by 50%, $10.8\,\mathrm{m}^3$ of aluminium is required in order to build two shelters. Recycled aluminium has a density of $2710\,\frac{\mathrm{kg}}{\mathrm{m}^3}$ and emits 0.5 $\mathrm{kgCO2_{eq}} \cdot \mathrm{kg}^{-1}$.[2][3] This results in a total production emission of $14634\mathrm{kgCO2_{eq}}$. The solar panel's production emissions will already be taken into account in the scope three carbon footprint analysis. The GHG emissions due to the production of the doghouse ground station are rather high compared to the UAV. It is important to note that the UAV will have a lifetime of 2 years, while the doghouse is estimated to operate for 15 years. Therefore, the GHG emissions are normalized to a lifespan of two years for this analysis, resulting in $1951.2\mathrm{kgCO2_{eq}}$ emissions for the production of the doghouse.

The operational area for this GHG emission analysis is defined as one gridded hexagon of $16.64\,\mathrm{km}$ by $14.42\,\mathrm{km}$, as is defined in Chapter 5. This hexagon is built up of six triangles with an area of $30\,\mathrm{km}^2$ which is surveilled twice a day. One hexagon requires two drones in order to surveil the area twice a day. It has been calculated in Chapter 14 that 398.2 Wh is required per surveillance mission. Twelve surveillance missions are flown per day and the expected lifetime of a single UAV is two years. This results in a lifetime energy requirement of 3478.3 kWh in order to nominally operate two DAWG UAVs. Besides the UAVs, the ground station requires $11.136\,\mathrm{kWh}$ per day in order to operate. Meaning that over the time span of two years, the ground station requires $8107\,\mathrm{kWh}$. This energy will be produced in situ by solar panels. A scope three carbon footprint study by TNO (2011) states that solar panels emit 0.002 $\mathrm{kgCO2_{eq}} \cdot \mathrm{KWh}^{-1}$. This results in operational GHG emission of $6.9\mathrm{kgCO2_{eq}}$ for the DAWG UAV and 16.2 $\mathrm{kgCO2_{eq}}$ for the doghouse ground station.[4] If this same operation is performed by using electricity from the Dutch net which emits $0.325\ \mathrm{kgCO2_{eq}} \cdot \mathrm{KWh}^{-1}$, the UAV and ground station combined would emit 3765.22 $\mathrm{kgCO2_{eq}}$. [5] Supplying the energy through solar panels makes a large impact. The results of these GHG emissions are plotted in Figure 15.5. It can be seen that the GHG emitted

[1] https://8billiontrees.com/carbon-offsets-credits/carbon-footprint-of-lithium-ion-battery-production/, accessed on 19-06-2023

[2] https://www.thyssenkrupp-materials.co.uk/density-of-aluminium.html, accessed on 20-06-2023

[3] https://www.climateaction.org/news/carbon-footprint-of-recycled-aluminium, accessed on 20-06-2023

[4] https://pubs.rsc.org/en/content/articlehtml/2022/se/d2se00444e, accessed on 04-05-2023

[5] https://www.statista.com/statistics/1290441/carbon-intensity-power-sector-netherlands/, accessed on 03-05-2023

during operations has been successfully reduced. The biggest impact is now coming from the production of the ground station. This is an acceptable level and new materials can always be used in the future in order to reduce the emissions even more.

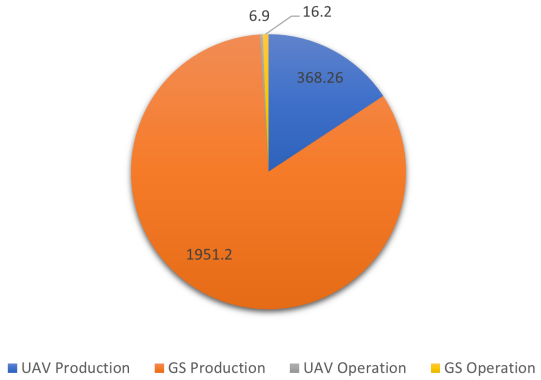

Figure 15.5: A comparison of the GHG emissions for production and operations of the DAWG project.

The UAV's structure will be made out of CFRP. This CFRP can be recycled into carbon fibres that are then used in other applications. Using recycled carbon fibre can also be considered. This would reduce the GHG emissions of CF from 24 $kgCO2_{eq}$ to 1.1 $kgCO2_{eq}$, a seemingly significant change [34]. However, one shall consider that tensile strength is 10-20% lower than virgin CF, which results in more weight to the drone and thus requires more power during operations. The CFRP and the Li-ion batteries make up 70% of the UAV's weight and are both partially recyclable. The motors contain 50% copper which can be recycled too, making the drone minimally 76% recyclable. It has been seen before that efficient operation is much more impactful than production, therefore the UAV will be made out of virgin CF. Due to the large size of the doghouse, it requires a lot of material and thus has high GHG emissions during production.

15.3.2. Impact of Application

The application of wildlife surveillance UAVs has a large impact on sustainability. As the main goal is to monitor wildlife and detect poachers, forest fires and litter. The UAVs are designed to help fulfil the UN's 17 sustainable development goals (SDG). The data about animals and wildfires will then be used to fulfil SDG 4: quality education. Understanding wildlife and having real-time monitoring data allow educators around the world to teach the new generation in an accurate and informative way. Knowledge about forest fires can be shared with the communities who live in arid areas and will have to handle these problems. A lot of nature reserves are located in developing countries, meaning that the wildlife surveillance project would increase sustainable economic growth and promote education to prepare new specialists. This contributes to SDG 8: decent work and economic growth. SDG 9: industry, innovation, and infrastructure indicate that innovation should be fostered. Creating a drone that is emission-free and quiet requires technology that can be applied in other fields of aviation. In this project, innovations are not a luxury but a necessity. SDG 12, responsible consumption and production, ensure sustainable consumption and production. As the UAV is designed to detect poachers, it will put control on the trade of ivory and other luxury products coming from endangered animals. Surveilling wildfires aids to prevent them, which helps combat climate change and thus contributes to SDG 13: climate action. Lastly, SDG 15: life on land aims to protect the fauna and flora on land. In general, the UAV is driven by the goal of preserving wildlife.

Chapter 16: Technical Risk Assessment & RAMS

In this chapter, the technical risk management for the final design is addressed. Firstly, the technical risks and their possible mitigation strategies are identified and assessed in Section 16.1. As these are presented, the results are then depicted in the form of risk maps, shown in Section 16.2. The contingency plans for the most critical risks are also created in Section 16.3 to minimize their impact.

16.1. Risk Identification & Mitigation

To ensure the successful performance of the surveillance system, it is necessary to identify the risks that the final system might be subjected to as early as possible and evaluate them in a way that would allow for a straightforward analysis of the possible mitigation strategies. As such, the identified risks were first split into three major categories, namely operational, system, and manufacturing/production risks. Each of the risks is then documented by providing the label and name of the risk, its description and effects as well as the proposed mitigation strategy for each. The evaluation of risks, both before and after the applied mitigation strategy, is also provided in terms of their likelihood and impact.

The influence of each risk shall be quantified to allow for deeper analysis, so the risks were assigned two key metrics to capture their importance, namely likelihood, and impact. The likelihood refers to the probability that a risk occurs whereas the impact of risk captures the severity of consequences. See Table 16.1 for a detailed description of the different degrees of impact and likelihood and their assigned weights.

Table 16.1: Impact and likelihood description and weights.

Impact	Impact Description	Likelihood	Likelihood Description	Assigned Weight
Negligible	Little to no effect system functionality; resolved by standard/minor operation procedures	Very Low	<15% probability	1
Marginal	Considerable, but acceptable decrease in system performance; resolved by minor design/operation modifications	Low	15-35% probability	2
Significant	Significant threat system operations; requires significant modification practices	Moderate	35-60% probability	3
Critical	Major malfunction or decrease in performance; requires partial redesign of the system	High	60-80% probability	4
Catastrophic	Total system failure/destruction; require total redesign of the system	Very High	>80% probability	5

Operational risks can be interpreted as the risks that threaten the day-to-day operation of the aerial surveillance system. These risks are often affected by environmental conditions and unlikely/unpredictable events. Such risks are identified and presented in Table 16.2. Manufacturing risks are the risks related to the production and manufacturing of the design (Table 16.3). System risks, shown in Table 16.4, are related to the technical aspects of the design, such as malfunctioning subsystems and individual components, flawed design decisions, or inadequate integration of the overall system.

16.2. Risk Maps

To visualize the benefits of mitigation strategies, the risk maps for each type of technical risk are developed, both before and after the mitigation strategy is applied. As visible from the maps in Figure 16.1 and Figure 16.2 the critical risks that are most probable and pose the highest threat to the successful aerial vehicle design are situated towards the top right corner of the maps, indicated by deep red cells. On the contrary, risks that are unlikely to occur and have a generally low impact on the final design are all gathered at the bottom left area of the map in darker green. One can also observe that none of the 39 risks is considered critical (red region). Before applying the mitigation procedures, the majority of risks are observed to lie in between the aforementioned dark green and red regions, validating the need for a number of mitigation strategies. The benefit of these is clear as their implementation leads to the risks shifting to the green region of the map, with only two risks remaining in the yellow diagonal, requiring a contingency plan to respond effectively in case they actually happen.

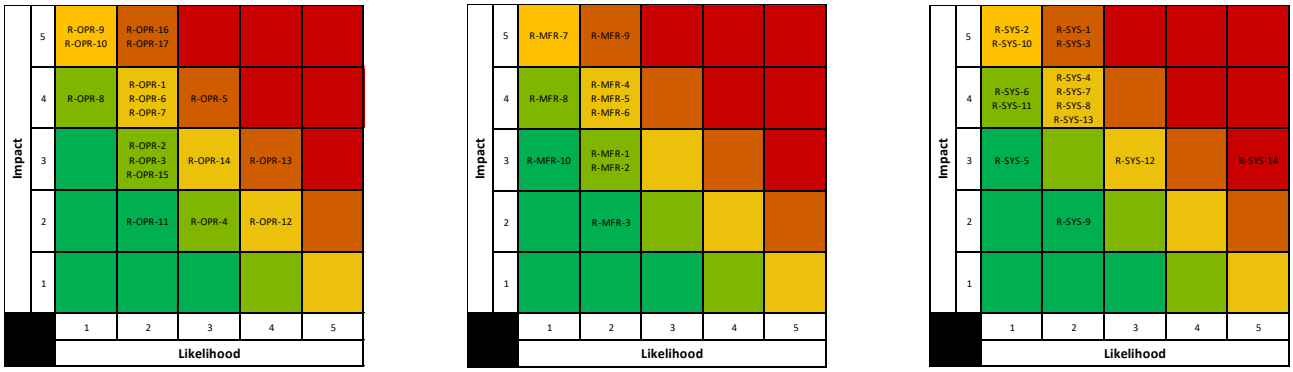

(a) Operational risk map (pre-mitigation).

(b) Manufacturing risk map (pre-mitigation).

(c) System risk map (pre-mitigation).

Figure 16.1: Pre-mitigation risk maps.

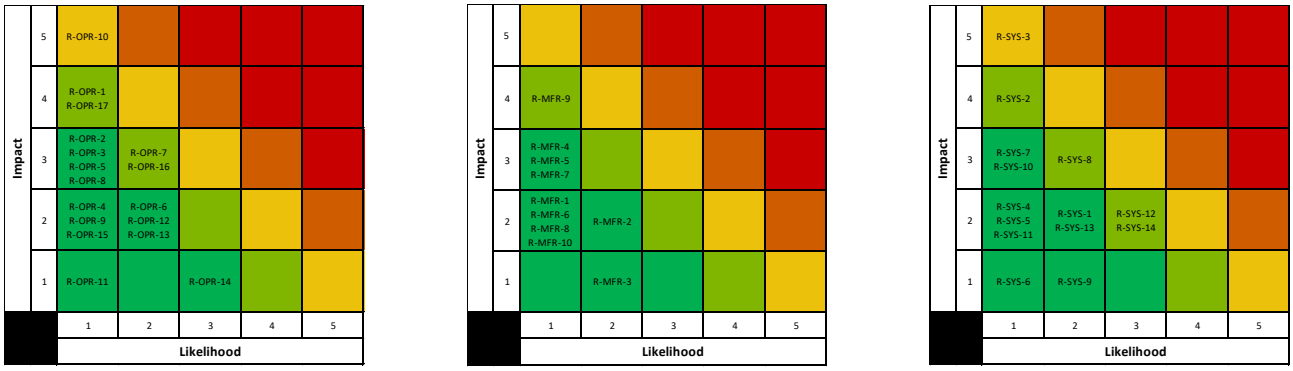

(a) Operational risk map (post-mitigation).

(b) Manufacturing risk map (post-mitigation).

(c) System risk map (post-mitigation).

Figure 16.2: Post-mitigation risk maps.

16.3. Contingency Plans

Risk mitigation is an important aspect of managing the identified risks and aims to lower the probability and/or impact. Some risks, however, are not sufficiently reduced by mitigation and therefore need a contingency plan. A contingency plan is made for the risks in the yellow blocks shown in Figure 16.1, and Figure 16.2. Since there are no risks in the yellow blocks for manufacturing in Figure 16.2b, no contingency strategies are presented for risks of this kind. Post-mitigation operational risks have only one risk that cannot be sufficiently reduced by mitigation. R-OPR-10 deals with the changing laws. There is no mitigation possible as this is out of the design team's control. However, if the laws prohibiting the production, selling or operation of the UAV are passed during UAV manufacturing, the design shall be altered to meet the new regulations (if possible). For UAVs that have been sold recently, a partial return procedure can be implemented to install the design changes into the old design. If a considerable amount of time has passed since the UAV purchase, the contract should state that the company responsible for the design of the UAV is not held accountable for the legality of its use.

As for system risks, one system risk can not be sufficiently reduced by mitigation. R-SYS-3 refers to the thermal runaway of the onboard battery. While the probability of such an incident is lowered by mitigation, an onboard fire will most likely still cause the UAV to crash. Therefore, the contingency plan focuses on making the impact of the crash on the environment as low as possible. More precisely, the contingency plan considers extinguishing the fire onboard the UAV before it crashes. This can be achieved by equipping the UAV with a fire-retardant foam reservoir and fire-resistant coating around the battery, which would drastically slow down or completely extinguish the fire onboard. The crashed UAV can then be retrieved and any remaining debris is to be disposed of from the crash site.

Table 16.2: Operational risks.

ID	Name	Description	Effect	Likelihood	Impact	Risk Mitigation	Likelihood After Mitigation	Impact After Mitigation
R-OPR-1	The UAV is hit	The UAV is shot (e.g. by the poachers) or hit by small debris	The UAV is damaged	2	4	Paint the UAV in camouflage colors (e.g. forest or skyline shades)	1	4
R-OPR-2	Overheating	The UAV electronics overheat	The electronics may start malfunctioning	2	3	Actively cool the electronics	1	3
R-OPR-3	Low temperatures	The UAV electronics experience very low temperatures	The electronics may become dormant/malfunction	2	3	Actively heat the electronics	1	3
R-OPR-4	Icing	The UAV surface experiences build up of ice	Lift is reduced, aircraft weight increases, sensors can get stuck and their view hindered	3	2	Fly at lower altitude and/or higher temperatures or actively heat up or break ice on moving parts of the UAV	1	2
R-OPR-5	Extreme weather conditions	The aerial vehicle experiences extreme weather conditions, e.g. high windspeeds, high gusts, heavy rain, lightning strikes, blizzard	The UAV crashes	3	4	Ensure access to accurate weather forecasts and ground the UAV during storms. Build a booth around the charging pad.	1	3
R-OPR-6	Connection loss	The UAV is unable to communicate with the ground station	The UAV directional/functional control is lost, so the UAV can not come back to the station or crashes	2	4	The UAV is equipped with systems that would allow it to temporarily fly without information from the ground station	2	2
R-OPR-7	Collision with objects	The aerial vehicle hits a flying animal during operations or another aerial object/vehicle	The UAV propulsive/structural system is damaged, leading to crash	2	4	Fly at different altitude levels and perform extensive testing in controlled environment to adapt drone stabilisation mechanism	2	3
R-OPR-8	Solar flares	The aerial vehicle experiences high exposure to electromagnetic radiation (e.g. solar flares)	Solar flares could disrupt the electronics onboard the UAV affection	1	4	Electronics inside are insulated with good resistance properties. Also, ensure possibility of gliding with all electronics turned off.	1	3
R-OPR-9	Cybersecurity	The UAV is accessed by a hacker	The UAV is used for malicious purposes (e.g. self-destruction or crashing into animals/people, etc.)	1	5	Implement good cybersecurity to keep hackers out of the system	1	2
R-OPR-10	Changing laws	The government decides that UAVs are no longer allowed to be used by commercial companies	The UAV may not be used anymore	1	5	–	1	5
R-OPR-11	Air polution	When flying over a wildfire the smoke negatively affects the camera vision of UAV	UAV can get damaged, or crash	2	2	Implement smoke particle detection systems in the UAV to readily adjust the flight path	1	1
R-OPR-12	Humid conditions	The aerial vehicle internal parts experience rain or humid conditions in general	The UAV electronics can experience short circuits	4	2	Use watertight joints, water-insulated electronic parts and/or hydrophobic coating	2	2
R-OPR-13	Dust/Sand	The aerial vehicle components are covered in small particles such as dust or sand	The sensors cannot function properly	4	3	Use omniphobic coating/materials, implement aerial vehicle washing procedures in the ground station	2	2
R-OPR-14	Terrain irregularities	Uneven or rugged terrain complicates the take-off and landing procedures	The drone can not take-off/land in time, leading to possible UAV damage or delays	3	3	UAV takes-off vertically	3	1
R-OPR-15	Undesired vibrations	UAV internal components experience significant vibrations	UAV instrumentation is damaged, leading to inaccurate data measurements	2	3	Install coating materials to damp the vibrations	1	2
R-OPR-16	Fire onboard	UAV starts burning	UAV experiences partial/full failure as components burn down	2	5	Use fire-retardant foams that quickly extinguishe the fire	2	3
R-OPR-17	Failed charging	The UAV does not charge or charges extremely slow	UAV cannot perform the mission or is forced to begin mission with low battery level. Might lead to crash or subsystems shutting down.	2	5	Perform regular charging pad checkups.Stop the UAV take-off if battery is not charged properly. Implement redundant wiring for charging pad.	1	4

Table 16.3: Manufacturing risks.

ID	Name	Description	Effect	Likelihood	Impact	Risk Mitigation	Likelihood After Mitigation	Impact After Mitigation
R-MFR-1	Supply issues	The supplier of the raw materials is experiencing difficulties and cannot deliver them to manufacturer for UAV production in time	The production process has to be halted until new materials arrive	2	3	Have a warehouse with backup batches of materials	1	2
R-MFR-2	A manufacturing machine is inoperative	A machine used in the production process stops working unexpectedly or is being maintained	Production experiences down time, leading to delays in the design	2	3	Have mechanics on site to quickly repair broken machinery or have alternative machines available	2	2
R-MFR-3	Injury	A worker is injured during the manufacturing process	Workforce is reduced, possibly leading to delays	2	2	Make sure safety measures are in place and up to date. Ensure substitute workers are available.	2	1
R-MFR-4	Damage to the materials/components	Materials get damaged during the production (i.e. worker mistake, machine malfunctioning, etc.)	Materials or assemblies have to be scrapped, causing price increase and delay	2	4	Regular instruction sessions on operating the machines and materials shall be organised for workers. Workers shall also be regularly instructed on how to act if unexpected situations/accidents occur.	1	3
R-MFR-5	Cost increase	The costs involved in manufacturing are drastically higher than the estimated ones	The cost requirements set by stakeholders are not met	2	4	Ensure regular tracking and management of the expenditures. Adhere to the cost budgets set by the team.	1	3
R-MFR-6	Poor quality management	The quality management practices in the company are not up to modern standards/ is performed poorly	The manufactured products may be of low quality or damaged, potentially causing structural failure of the final system	2	4	Hire a new quality management team, reinforce the quality management more strictly and educate the workers about the importance of such management	1	2
R-MFR-7	Manufacturing company goes bankrupt	The company responsible for manufacturing of the system goes out of business	A new manufacturing company has to be found, imposing delays and extra costs	1	5	Hire people responsible for tracking the financial state of the company and preparing a list of stand-in manufacturers	1	3
R-MFR-8	Changing laws	A new law changes the legality of a production method	The production method has to be reconsidered	1	4	Hire a person to help prepare in advance and deal with legal aspects of manufacturing	1	2
R-MFR-9	Inexperienced manufacturer	The workers of the manufacturing company do not have the required competencies or perform the work poorly	The manufactured products are delivered late and/or are faulty or damaged	2	5	Inform the company about the inexperienced workers and replacing the poor performing workers	1	4
R-MFR-10	Environmental regulations	Environmental regulations change, making it illegal to use certain materials or production processes	A new material or production process has to be used	1	3	Choose environmentally friendly materials, hire a person to deal with environmental regulations	1	2

Table 16.4: System risks.

ID	Name	Description	Effect	Likelihood	Impact	Risk Mitigation	New Likelihood	New Impact
R-SYS-1	Battery failure	The UAV experiences power loss as a result of battery malfunction/failure	UAV communication, instrumentation and control systems do not function, leading to crash or limited flight time	2	5	The UAV has redundancy implemented in the power system and ability to quickly land in case of emergency	2	2
R-SYS-2	Structural failure	The structure of the UAV partly breaks	The UAV is inoperable and needs to be repaired or crashes in case of total failure	1	5	During the design process extreme load cases are identified and accounted for	1	4
R-SYS-3	Thermal runaway	The battery used to power the electronics experiences thermal runaway	The UAV battery explodes, UAV catches on fire and crashes	2	5	Make sure high quality batteries are chosen and used within predetermined conditions	1	5
R-SYS-4	Software mallfunction	A software bug stops a (sub)system from functioning	The subsystems stop working or work incorrectly, leading to crash or loss of control	2	4	Proper verification and validation on the software shall be performed and software shall be made fail-safe	1	2
R-SYS-5	Anti-icing system failure	The anti-icing systems of the UAV malfunction	Ice starts to build up on the UAV surfaces, hindering operations	1	3	Implement a redundant de-icing method (e.g anti-ice coating)	1	2
R-SYS-6	Heating system failure	The heating system fails	Components get too cold and no longer function properly	1	4	Have redundancy in the heating system	1	1
R-SYS-7	Cooling system failure	The cooling system fails	Components get too hot and no longer function normally	2	4	Have redundancy in the cooling system	1	3
R-SYS-8	Communication link failure	The UAV communication system fails	The UAV is no longer able to communicate with the ground station	2	4	Have an auto homing feature that bring the UAV back to the ground station if connection is lost	2	3
R-SYS-9	Sensor failure	The sensors for wildlife, wildfire and orography detection or collision-avoidance sensors malfunction	The UAV can no longer make relevant observation and gather data	2	2	Have redundancy in the sensors and use high quality sensors	2	1
R-SYS-10	Control surface failure	The control surfaces malfunction	The UAV is no longer controlable and crashes	1	5	Implement multiple means to control the UAV	1	3
R-SYS-11	Thrust system failure	The thrust system provides too little or no thrust at all	The UAV may start to fall uncontrollably and crash or only be partly controllable	1	4	Implement a parachute to land the inoperative UAV in emergency state	1	2
R-SYS-12	GPS interference	GPS signal experiences interference from internal or external sources	The UAV experiences partial loss of control and/or data collected is inaccurately	3	3	Implement signal amplifiers and software in ground stations/aerovehicle to tacke interference. Accommodate the UAV with possibility to alert ground station about signal losses.	3	2
R-SYS-13	Data loss	UAV experiences local data loss or corruption	No data is available or the data is not readable	2	4	Implement regularly updated cloud-based data storing	2	2
R-SYS-14	Cycle life degradation	The capacity of the battery drastically degrades after extensive use	UAV discharges too quickly/has low energy capacity, resulting in shorter & incomplete missions.	5	3	Avoid extreme operating conditions, follow proper charging techniques, implement Depth of Discharge management, perform semi-annual inspection of batteries	3	2

16.4. RAMS Analysis

A Reliability, Availability, Maintainability, and Safety (RAMS) analysis is a tool which provides a framework to assess the performance and risks of a design to determine how effectively it can complete its desired mission. It considers how reliable the system can operate when it is available, how easy it is to maintain and the system's safety concerns. It is therefore closely related to the design's requirements as these are important drivers behind how the four attributes are constrained.

16.4.1. Reliability

The reliability of the system determines the likelihood of the system to fail. Naturally, this is essential to the successful operation of the system. The remaining three attributes are closely linked to reliability as will be explained below. There is one main reliability requirement:

- **REQ-GEN-8**: The system shall have a reliability of at least 90% for every 500 hrs of service.

However, estimating reliability is complex and would require a full in-depth analysis which was not possible

for the team. Many components of the system are off-the-shelf components whose reliability has already been proven. Moreover, the general design and operations of the UAV system are relatively reliable due to its simple concept (quadcopter-VTOL with fixed wing) compared to more complex design concepts such as tilt rotors, slingshot takeoff, etc.

16.4.2. Availability

The availability of the system entails the degree to which the system is available to perform its mission. The system is operational 24/7, at any given moment a UAV can lift off and fly a mission. Due to each GS consisting of two UAVs, not only is there redundancy in case a UAV fails but there will also always be at least one UAV that has sufficient battery levels to perform an unscheduled response mission. Every UAV has an endurance of 2 hrs, however, this will only be needed in case of a response mission which will likely occur much less frequently relative to a nominal surveillance mission of 40 min (Section 5.4). For a mission of 40 min only about 29% of the battery will be used thus charging time will amount to about 35 min. As this is shorter than the mission time it should never occur that there are no UAVs that can perform a mission as a result of operation unavailability. However, other factors such as adverse weather conditions or system failures could lead to lower availability. Requirements that will drive the availability are the following:

- **REQ-GEN-19**: The surveillance area shall be surveilled twice a day.
- **REQ-PM-CS-2**: The drone shall be controllable in winds up to 50 km/h.
- **REQ-PM-CS-4**: The drone shall be controllable in rainy conditions up to 1 mm per hour.
- **REQ-PM-SM-11**: The drone shall be able to withstand dust of level IP6X (dust tight).
- **REQ-PM-SM-12**: The drone shall be water resistant until IPX4 (sprayed water).

16.4.3. Maintainability

Maintainability describes the ease of performing maintenance on the system in terms of cost, time and complexity such that the system can remain operable. Logistically this will largely depend on the location of the surveillance area. As the system is likely to be used in remote areas maintainability is a point of concern. However, the need to perform maintenance was taken into account during the design process. For example, a major pitfall for electric battery-powered UAVs is the fast degradation of lithium batteries. To alleviate this problem the designed depth of discharge is limited to 70% and as mentioned before the DOD will be as low as 29% during nominal missions. Once more consulting Figure 14.2 one can see that at a DOD of about 30%, the Cycle Life increases by a 7-8 fold relative to a 100% DOD. This will significantly improve the battery's lifetime and thus the required maintenance. Considering the batteries have full capacity for at least 300 full charge cycles[1], this increases the life cycle to $300 \cdot 7.5 = 2250$ cycles. With each UAV performing 6 flights per day, this equates to 375 days of operation. Thus scheduled maintenance/replacement of the batteries will need to occur roughly once a year. Furthermore, the UAV has many off-the-shelf parts which allow for easy replacement during unscheduled maintenance. Parts such as solar panels wi. In general, to keep maintenance to a minimum, it is desirable to have high reliability.

16.4.4. Safety

The safety attribute relates to preventing the system from harming the environment and humans. Several measures are taken to ensure this safety. Fire retardant coating will be applied to CFRP, which is the main structural material. The ARES 6S batteries have a max charging current of 60 A, however a low charging current of 15 A is used to charge the batteries. This significantly reduces the likelihood of overheating the batteries and subsequent leakage or catching fire. Furthermore, a crucial condition for the UAV is that it must not disturb the environment noise-wise, which can also be categorised under safety. The noise produced by the UAV has been extensively analysed in Chapter 11 and was determined to be lower than the maximum allowable level. Below all requirements relating to safety have been listed.

- **REQ-PM-COM-4**: The communication system shall be designed such that data breaches are prevented.
- **REQ-EOL-1**: The drone shall be able to make a safe emergency landing when a critical failure is detected.
- **REQ-EOL-2**: The drone shall be able to deploy its emergency landing systems in case critical failure is

[1] `https://www.t-drones.com/goods-1154-Ares+6S+30Ah.html`, accessed on 15/06/2023

detected.

- **REQ-EOL-3**: The drone shall be able to activate its recovery beacon in case of an emergency landing.
- **REQ-NTC-NOI-4**: The drone shall produce less than 40 dBA of DEN-level noise.

Unfortunately, not all of these requirements are fulfilled. The team was not successful in incorporating an emergency landing system into the design such as a parachute due to weight and size limitations. Another important aspect of determining safety is the safety-critical functions. Below they are listed:

- VTOL motors and propellers must remain functional.
- The Veronte Autopilot 1X must remain functional
- The batteries must remain functional.

If any of these functions fail, the UAV will critically fail, i.e. not be able to fulfil its mission and likely crash. In order to mitigate the effects of these functions failing, the motors produce enough thrust to function with one propeller/motor inactive and the batteries are wired in parallel, thus one failing will not cause the other to fail as well. The amount of power will decrease but should be sufficient to make an emergency landing. Finding a workaround for the Veronte Autopilot remains an issue though, but fortunately, it is a component with high reliability and typically does not fail.

Chapter 17: Financial Analysis

One of the key metrics to assess the success of any engineering project is its financial performance. For that reason, it is extremely important to first identify the market and its needs to create a reasonable technical & non-technical cost overview of all project elements, which would then lead to a profit estimation.

17.1. Market Analysis

The market volume depends on the amount of land area of all operational habitats in the world. From Figure 5.3, it is estimated that approximately 65% of the Earth's land area is within the operational limits. Taking into account only the relevant 1% of the operational area, this is roughly equal to a ground surface area of 1×10^9 km^2.

Based on the proposed system design where one ground station with two UAVs can cover 6 tiles of 30 km^2 each, it adds up to a total coverage of approximately 180 km^2. This means that approximately 5556 hexagonal coverage areas can fit in the 1 million square kilometre area, or 5556 ground stations and 11112 UAVs could be sold if a UAV is sold to cover every square meter (this is an approximation of the total market volume). Since the design objective mainly focuses on African wildlife and the market is highly competitive, a percentage of 10% of the market volume is assumed as the market share. This results in a Q_{UAV} of 1112 and a Q_{GS} of 556. It is also assumed that this market share can be reached in 10 years of production and operation. This allows time for marketing to reach the relevant customers, UAVs to be produced, and the UAV end-of-life to be reached for at least some of the customers (meaning new orders for replacements will start forming a steady stream).

In addition to the wildlife surveillance market discussed above, the UAV is competitive in the wider surveillance UAV market. Market trends within the drone surveillance market[1] show that the incorporation of LiDAR and AI processing on the edge is on the rise. The market analysis specifically mentions the off-shore oil rig and ship market as a developing area, but overall the industry is on the rise. Market analysis[2] also shows that adoption of hybrid VTOL UAVs (such as the one proposed in this report) is on the rise.

The UAV surveillance market was estimated to have a \$142 million market cap in 2021 with a predicted compound annual growth rate (CAGR) of 18.9%[3]. This would put the market at approximately \$198 million in 2023.

The entire UAV market is worth approximately \$15.4 billion with a CAGR of 14%[4]. A large part of this market is consumer drones, agriculture and payload delivery. While the UAV proposed here is not directly compatible with these target uses its reasonably large payload capacity ($>$5 kg) may allow for a modified version (with fuselage or another form of payload attachment) to be developed.

For now, the decision was made to initially focus on the UAV surveillance markets (both wildlife and others). There are numerous reasons for this decision, but the main ones are as follows. First is the large market size, meaning that there is plenty of growth opportunity for the company: a market share of a mere 1% would already provide millions in revenue with large ($>$ 14%) year-on-year growth. Furthermore, the UAV proposed in this report addresses the market opportunities, incorporating AI and advanced sensor technology.

Finally, the blended wing body design of this UAV gives limited flexibility in adopting non-surveillance (or even changeable) payloads. This can undoubtedly be addressed with a secondary line of UAVs that share a lot of the intellectual property developed as part of the surveillance UAV. However, developing this alongside the surveillance UAV would necessitate designing and manufacturing two different designs (likely incorporating different parts and design features). This would ultimately spread the limited resources (be it a budget, engineering time, or parts on hand) thin. Especially as the designs diverge and changes to one design are not automatically incorporated into the other design, this can significantly increase the development time. A successful business

[1] https://www.alliedmarketresearch.com/drone-surveillance-market-A13907, accessed on 16-06-2023

[2] https://www.fortunebusinessinsights.com/industry-reports/drone-surveillance-market-100511, accessed on 16-06-2023

[3] https://www.fortunebusinessinsights.com/industry-reports/drone-surveillance-market-100511, accessed on 16-06-2023

[4] https://www.mordorintelligence.com/industry-reports/uav-market, accessed on 16-06-2023

practice also suggests that startups only focus on a single product[5].

In short, the strategy is to first develop the best surveillance UAV platform possible, fixing the issues in the process and only later expand into other markets with designs that incorporate this proven technology.

Earlier market analysis performed during the baseline stage of the design suggests an average price of UAV and ground station of a little over $250000 based on comparable UAVs from competitors[35]. Based very roughly on the cost analysis (described later), the production cost of a single UAV divided by a single ground station is approximately 4. Dividing this system price based on this ratio, a ground station would be sold for $50000 and a single UAV would be sold for $200000. This would bring the total system cost (that covers six 30 km^2 tiles and uses one ground station as well as two UAVs) to $450000. This is approximately $50000 (10%) cheaper than typical numbers quoted for a preventative system[6]. This means the UAV is very competitive within the wildlife surveillance market, especially considering its fully autonomous and AI-using nature.

To gain a preliminary insight into the number of units produced per year, the two markets are considered. First is wildlife monitoring, where the estimated 1112 UAVs and 556 ground stations produced over 10 years yield an average of 111 UAVs and 56 ground stations produced per year. For other markets, assuming a mere 5% market share five years selling one-GS, two-UAV packages (at $450000 for a package) yields an additional revenue source of approx. $7.76 million at the midpoint of the time interval (5 years from now), or 17 packages (equating approx. 17 ground stations and 34 UAVs). This would put the total number of UAVs produced yearly at 145 and ground stations at 73.

It is worth noting that the revenue source from wildlife monitoring is rather large, approximately $25.2 million (or almost 18% of the entire worldwide UAV surveillance market in 2021). However, wildlife protection and monitoring is attracting increasingly more funding with some estimates putting additional government funding needed at $700 billion per year[7]. Because of this and the system's autonomous capabilities, the authors believe it can play an integral part in achieving the governments' wildlife conservation needs. As such, a rapid expansion of the surveillance market into wildlife surveillance is expected and this large market share is considered reasonable.

To help characterize the strengths and weaknesses of the proposed design compared to competitor products, a SWOT (Strengths, Weaknesses, Opportunities and Threats) analysis can be performed. The results of this SWOT analysis have been shown in Figure 17.1.

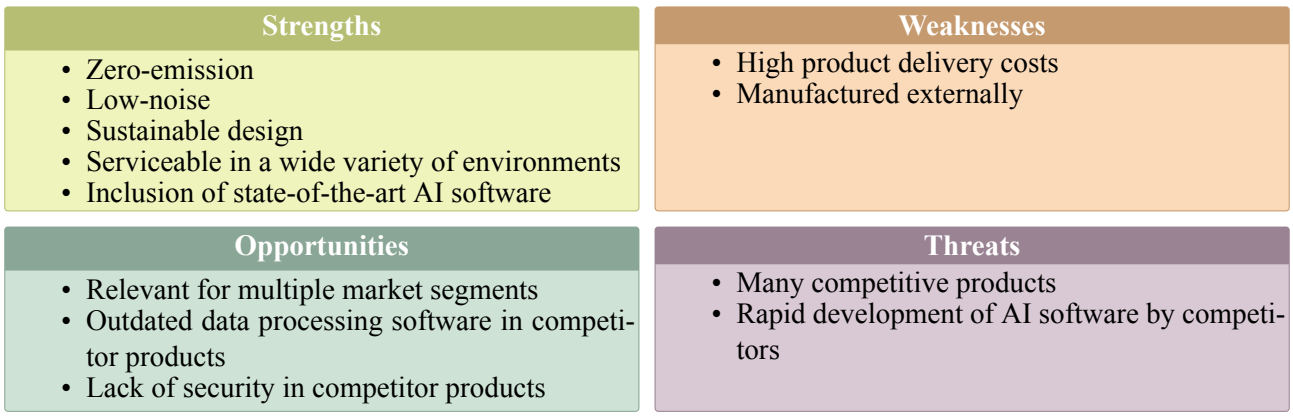

Figure 17.1: SWOT Analysis

17.2. Cost Analysis

The expenses of the UAV and ground station that are imposed upon the company consist of several elements and can thus be divided up based on the product design stages, i.e. development, production and delivery, operational and end-of-life costs.

[5] https://fastercapital.com/content/Build-a-Successful-Startup-by-Focusing-on-One-Product.html, accessed on 16-06-2023

[6] https://wildtech.mongabay.com/2015/11/using-drones-for-anti-poaching-first-know-your-mission/, accessed on 16-06-2023

[7] https://www.weforum.org/agenda/2021/05/biodiversity-deforestation-global-investment-inititive/, accessed on 16-06-2023

17.2.1. Development

To begin with, the development costs can be calculated. The team consists of 10 members, which have an assumed gross wage of $40\,€\,h^{-1}$. Provided the social security contributions, wage tax rate, insurance, etc., the hourly cost for the employer is 30% higher than gross wage[8], resulting in $52\,€\,h^{-1}$ per employee. With 10 weeks of development and 8 hours every working day, this results in 208 000 € of development costs.

Moreover, the software development costs involved during this phase shall also be accounted for. An experienced software engineer hired from Romania (lower cost than Dutch) is expected to program all AI, control and data logging software in a time span of 1.5 years with a monthly wage of 2941 €. This will cost the company $2941 \cdot 18 \cdot 1.3 = 68\,819.4\,€$.

The **total development costs** result in 276 819 €.

17.2.2. Production & Delivery

It is no surprise that a major fraction of project costs is incurred during the production and delivery of the system. To simplify the calculations, the costs are split into the UAV and ground station-related expenses and analysed separately. Note that the cost estimates are considering only major components and the operation, maintenance & infrastructure construction costs are addressed later.

UAV expenses

The UAV costs can be split into payload (instrumentation + GNC & Comms), propulsion system and structural elements. As such, the costs (per component of a single UAV) are:

Table 17.1: Estimated component costs of a single UAV (excl. operation & maintenance)

Expense	Cost [€]	Comments
Veronte Autopilot 1X[9]	6150	-
Antenna Swarmlink MPSL2200[10]	150	-
Battery Ares 6S 30Ah[11]	660.36	2 batteries are used per UAV
Industrial module Jetson Orin NX 16Gb[12]	662.79	-
Camera Trillium HD40-LV[13]	34672	-
Li-Dar sensor Blickfeld Cube 1 Outdoor[14]	4165	-
GPS Antenna AS-ANT2B-HEL-L1L2-SMA-00[15]	127	-
Motor MN701S KV280[16]	404.82	4 VTOL motors are used per UAV
Motor AT4130 Long Shaft KV450[17]	110.65	1 horizontal push propeller per UAV
SSD Samsung Fit Plus 256GB Type-A 400MB/s USB 3.1 Flash Drive[18]	27.91	-
Location beacon tBeacon Onyx[19]	54.19	Used to track down UAV location in case of crash or lost contact
Motherboard reComputer J202[20]	168.19	-
Structure	11000	The structure is made entirely from CFRP (assumption). Cost is preliminary estimation, including external production assumption
Total Cost: 60 228.31 € (per UAV)		

Note that the structural cost estimation is based on two steps. First, the propulsion and payload systems are subtracted from the MTOW of the UAV (results in 5.78 kg) and multiplied by the average CFRP price per kilogram of material ($\sim 190\,\$/kg$). Secondly, the structures are all different (e.g. wing, fuselage, boom tail, etc.), so assuming they are outsourced and delivered in batches on the assembly site, a significant price increase has to be incorporated to account for the fact that they are bought instead of self-manufactured. This factor is assumed to be 10 000 € per UAV. One shall also consider that the structural weight found in step 1 includes *everything* that is not propulsion or payload, e.g. wiring, joints, glue, etc.

[8] https://business.gov.nl/running-your-business/staff/payment-and-wages/overview-of-personnel-costs/, accessed on 17-05-2023

[9] https://www.embention.com/product/veronte-autopilot-1x/, accessed on 14-06-2023

[10] https://www.unmannedsystemstechnology.com/company/mp-antenna/swarmlink-mpsl2200-multipolarized-antenna/, accessed on 14-06-2023

[11] https://www.t-drones.com/goods-1154-Ares+6S+30Ah.html, accessed on 14-06-2023

[12] https://www.arrow.com/en/products/900-13767-0000-000/nvidia, accessed on 14-06-2023

[13] https://www.trilliumeng.com/gimbals/hd40, accessed on 14-06-2023

[14] https://www.mybotshop.de/Blickfeld-Cube-1_5, accessed on 14-06-2023

[15] https://shorturl.at/rAM06, accessed on 14-06-2023

[16] https://store.tmotor.com/goods-473-MN701-S+KV280+-+2PCSSET.html, accessed on 14-06-2023

[17] https://store.tmotor.com/goods-828-AT4130+Long+Shaft.html, accessed on 14-06-2023

[18] https://tweakers.net/pricewatch/1230797/samsung-fit-plus-256gb-zwart/specificaties/, accessed on 15-06-2023

[19] https://tbeacon.org/tbeacon-onyx-en, accessed on 15-06-2023

[20] https://www.antratek.nl/j202-carrier-board-for-jetson-nano-xavier-nx, accessed on 15-06-2023

It must be mentioned the UAV also has to be manufactured, assembled and tested. For that, a number of additional costs arise such as worker salaries, design-specific and general machinery expenses and testing facility costs as well as transportation expenses. However, it is assumed that a collaboration with a manufacturing company takes place, so the general machinery and testing are rented from them. Also, the structural parts of the UAV are presumed to be outsourced, thus removing the need for manufacturing workers, such that only assembly/testing labourers are used. This, however, results in higher structure prices as mentioned in Table 17.1. While the exact number for the aforementioned costs is hard to estimate, the following can be considered:

- Aircraft manufacturers are paid at an average gross of 20 € per hour[21]. As discussed previously, an average of 145 UAVs have to be produced each year. With 234 working days annually, ∼3 UAVs are to be made each week. Assuming it takes 3 days for a single worker to assemble and test a UAV, 1.85 workers are required to achieve such a production rate. As this is infeasible, it is assumed that assembly will be done by 2 full-time workers with the possibility to employ more workers later on if company growth requires it. Given the 234 working days annually, the yearly salary of the single worker becomes 37 440 €, resulting in 97 344 € charge for an employer (earlier mentioned 30% rule). per two workers.
- The costs of renting and maintaining assembly machinery as well as testing facilities are assumed to be not more than 200 000 € a year.
- It is assumed that TU Delft provides the space for storing components and assembling the UAVs at a start-up discount, charging 1000 € per month for ∼150 m^2.

As such, the **yearly UAV production-related costs** amount to

$$145 \cdot 60228.31 + 97344 + 200000 + 12 \cdot 1000 = 9.04\,\text{mil}\,€$$

Ground station expenses

The proper functioning of the ground station requires a number of off-the-shelf components and infrastructural elements. Per ground station, this includes include solar panels, charging pads as well as the data transmission/reception and processing modules. The costs can then be summarized as follows:

Table 17.2: Estimated component costs of a single ground station (excl. operation & maintenance)

Expense	Cost [€]	Comments
Solar Panels Jinko Solar Tiger Neo 565W[22]	280.8	11 panels for central GS, 9 for each other GS. Cost provided is for non-central GS.
Microphone VM1000[23]	2.05	1 microphone at each GS and 280 microphones placed all around 50x50km^2 area
Starlink High Performance Kit[24]	2850	Only used at central GS
Computer ThinkStation P358[25]	979	Used in every ground station
Live Feed Monitor Beetronics 15VG7M[26]	295	Used in every ground station
Weather Station ECOWITT[27]	189	Used in every ground station
Charging Pad[28]	5000	2 charging pads per ground station. Cost is a preliminary estimation.
Antenna AH-1726-16 [29]	1850	2 antennae used per ground station.
970 EVO Plus NVMe™ M.2 SSD 1TB[30]	58.44	Used in every ground station.
Total Cost: 17750.69 / 21162.29€ (per standard/central ground station)		

Similarly to UAVs, an average of at least 73 GS have to be manufactured every year to achieve the proposed market share. Provided the 50x50 km surveilled area contains 13 regular GS and 1 central ground station, it is assumed that 13 regular GS always require one central GS to operate. It is worth noting the only major difference between central and regular GS is the Starlink High-Performance Kit for establishing a connection with the rest of the world.

One shall again consider the following:

[21] https://www.payscale.com/research/US/Industry=Aircraft_Manufacturing/Hourly_Rate

[22] https://jinkosolarcdn.shwebspace.com/uploads/JKM565-585N-72HL4-(V)-F3-EN.pdf, accessed on 14-06-2023

[23] https://vespermems.com/products/vm1000/, accessed on 14-06-2023

[24] https://www.starlink.com/orders/?processorToken=30436070-cf51-46c7-8399-5333c7a116d2, accessed on 14-06-2023

[25] https://shorturl.at/pqMQR, accessed on 14-06-2023

[26] https://www.beetronics.nl/15-inch-monitor-4-3-inbouw, accessed on 14-06-2023

[27] https://www.amazon.de/-/en/stores/ecowitt/page/ADFF4518-F762-4641-B54D-73A8A893F851?ref_=ast_bln, accessed on 14-06-2023

[28] https://youtu.be/dQw4w9WgXcQ, accessed on 14-06-2023

[29] https://youtu.be/dQw4w9WgXcQ, accessed on 16-06-2023

[30] https://www.samsung.com/uk/memory-storage/nvme-ssd/970-evo-plus-nvme-m-2-ssd-1tb-mz-v7s1t0bw/, accessed on 15-06-2023

- It is estimated that $\frac{73}{234} \cdot 5 = 1.6$ GS have to be delivered each working week on average. Contrary to the assembly of the UAVs, the ground station needs to be deployed and installed on-site as it consists of several elements (charging pods, solar panels & data processing modules), making it impossible to assemble it before delivery to the operational site. It is thus assumed that by default, the installation is left for the customers themselves. Nevertheless, the company can offer a GS installation service for a fee by establishing an agreement with qualified local labourers. The main operational area is Africa (e.g. Nigeria), so the local labour rates are very low compared to Europe. With an average salary of 708 €/month or $4.43\,€/h$[31] (value based on Nigeria), the UAV company is willing to double this ($8.96\,€/h$), meaning the costs per installing a single ground station (assuming it takes 6 work days and 2 people) are $\sim 860.2\,€$. In 234 work days (year), the total costs for installing 73 GS become $860.2 \cdot 73 = 62\,794.6\,€$
- The machinery and testing-related expenses are the same as the ones in the UAV cost calculation and thus already encapsulated in the total production costs since the machinery needed for both UAV and GS assembly is assumed to be the same.
- Similarly to UAVs, delivering all the elements that comprise a single GS would require one 40 ft cargo container, costing the aforementioned $1700\,€$. For 73 GS yearly, this totals $146\,900\,€$, including the land transportation and rental of containers.

The **total yearly cost for production & delivery of all GS** equals

$$5 \cdot 21162.29 + 68 \cdot 17750.69 + 62794.6 + 146900 = 1.52\,\text{mil}\,€$$

17.2.3. Operational costs

The operational costs refer to the expenses regarding both the actual operation and maintenance of the aerial system.

Operations

As the UAV is autonomous and battery-powered, the number of financially aided operations is relatively low. All of these operations are not performed on-site but rather at the headquarters of the company in the Netherlands. Firstly, the company provides customer support regarding technical and administrative queries. To ensure the fastest possible response time, a person is hired full-time to provide this service as well as deal with administrative & legal issues. In addition to that, another full-time worker is employed whose responsibilities include, marketing and sales of the aerial system as well as preparing the instructional content for customers (e.g. tutorials). With the number of employees growing each year, the technical staff training is assumed to be performed by the experienced development engineers, who are also responsible for remote diagnostics of the GS, or assembly workers while the matters regarding all other aspects of the business are covered by the administrative staff. Considering a gross wage of $12.47\,€/h$[32], the company experiences yearly costs of $60\,694\,€$ for those two workers.

After the initial development phase of 10 weeks, the company is presumed to provide 2 of the 10 development engineers with a full-time, $40\,€/h$ gross wage position in a company to allow for design iterations and a possibility to address the design issues that are encountered during the production/operation of the aerial system. This results in an annual $194\,688\,€$ costs for the employer (234 working days/year).

Maintenance

The maintenance costs of an aerial system are also associated either with the UAV or the ground station. Starting with the UAV, minor issues affecting the operation of the UAV (minor defects, annual battery replacement, etc.) are to be done by the local specialists. Nevertheless, the company provides a paid service to assist in resolving these issues if the customer requires it. As the costs for such travel are high (round trip tickets, accommodation, health guarantees, food, etc. can be estimated to cost $\sim 2000\,€$ for 3 days trip to e.g. Nigeria), this service would be provided at a steep price. Such maintenance fee would have to cover travel expenses plus the salary, resulting in $\sim$4000 € per repair fee (just for service, repair part shall be bought by the customer unless a manufacturing defect is present). It can be assumed that 10% of UAVs would experience such maintenance a year, resulting in about $24\,000\,€$ in costs. In the case of major technical/operational problems, the company will fly out a specialist

[31] https://www.timedoctor.com/blog/average-salary-in-nigeria/, accessed on 16-06-2023

[32] https://www.payscale.com/research/NL/Job=Customer_Service_Representative_(CSR)/Salary, accessed on 16-06-2023

to the location to solve the issues free of charge. In the case of the ground station, the Starlink module provides its services for a monthly fee of 289 €[33] or 3468 € a year. As 5 central GS are produced each year, this becomes 17 340 €/year. In addition, the UAV cleaning mechanisms in the charging stations (2 per GS) are assumed to take up 13 140 € annually (180 € per GS) for all 73 GS.

Both the UAV and ground station require yearly inspection. Assuming it takes 2 work days and one mechanical engineer to do a full inspection of both and considering an average mechanical engineer salary of 5.62 €/h in Africa (number based on South Africa[34]), the expenses experienced by UAV company yearly are $\sim$ 90 € per UAV+GS. In the hypothetical case of *all* 145 UAVs being used in Africa, this would amount to $\sim$13 350 €/year, assuming no money is spent on the training (in reality, this would have to be done at least in the first year). In addition, major software bug fixing and performance improvements need to be regularly taken care of for UAVs and GS. For that, an external software engineer can be hired. To save on costs, the engineers hired are Romanian, working at a gross wage of 18.84 €/h[35], resulting in the annual IT-related costs of $\sim$ 45 849 €.

So, the **total annual operational costs** amount to $\sim$ 369 061 €.

17.2.4. End-Of-Life costs

The end-of-life costs are the costs introduced once the UAV is no longer operational or used. These include the disassembly and disposal of the aerial system, corresponding logistic costs (e.g.transportation) and labour involved. In general, all of these activities are assumed to be carried out by the customers themselves, thus the company bears no end-of-life costs. It is, however, important to consider that the company might be interested in the retrieval of defunct UAVs for the extraction of materials or components that are still functional. Given the annual depreciation rate for high utility aircraft is around 15%[36], this can be exploited for estimating the decrease in UAV value over 10 years. Over such a period, the UAV value will decrease to 20% of the initial value or 11 884.95 €. It is thus very likely that the UAV company will buy back some of the UAVs. However, the exact number is hard to estimate and will be omitted in the total cost calculation.

Total annual end-of-life expenses for the company are therefore 0 €.

17.3. Return On Investment & Profits

As the economic profit and marketability of the UAV is a top-level priority for investors, it is important to evaluate how profitable the UAV production is. This aspect is generally examined in the form of Return On Investment, also known as ROI. By definition, ROI is defined as the ratio of net profit over the total cost of the investment[37].

$$ROI = \frac{\text{Total Profits} - \text{Total Costs}}{\text{Total Costs}} \tag{17.1}$$

The costs for any engineering design include the development, manufacturing, testing, transport and direct operational costs. As such, the ROI in the case of a wildlife surveillance system can be defined even more accurately:

$$ROI = \frac{P_{UAV}Q_{UAV} + P_{GS}Q_{GS} - (C_{dev} + C_{prod/del} + C_{oper} + C_{EOL})}{(C_{dev} + C_{prod/del} + C_{oper} + C_{EOL})} \tag{17.2}$$

As briefly mentioned in the market analysis, each UAV is sold for 200 000 € while each ground station assumes a market price of 50 000 €. Each year, 145 UAVs are 73 GS are sold. Note that development costs are only present in the first year. Given this, everything mentioned earlier can be summarized in Table 17.3:

[33] https://www.starlink.com/orders/?processorToken=c75e90a4-4e13-4872-bb95-12f7715f5c35, accessed on 19-06-2023

[34] https://za.indeed.com/career/mechanical-engineer/salaries, accessed on 19-06-2023

[35] https://www.levels.fyi/t/software-engineer/locations/romania, accessed on 16-06-2023

[36] https://www.forbes.com/sites/forbesbusinesscouncil/2023/02/02/why-cant-an-aircraft-owner-make-a-profit-ownership-costs/, accessed on 19-06-2023

[37] https://mailchimp.com/marketing-glossary/roi/, accessed on 2023-06-13

Table 17.3: Return On Investment (ROI) of the project

Return On Investment	
P_{UAV}	200 000 €
Q_{UAV} (over 10 yr)	1450
P_{GS}	50 000 €
Q_{GS} (over 10 yr)	730
C_{dev}	276 819 €
$C_{\text{prod/del}}$ (over 10 yr)	105.6 mil €
C_{oper} (over 10 yr)	3.69 mil €
C_{EOL} (over 10 yr)	0
Return On Investment (10 years)	198%
Annualized Return On Investment	11.5%

Note that the annual ROI is *not* found by dividing 10-year ROI by 10 as doing so would ignore the effects of compounding. Instead, the following relation is used[38]:

$$\text{Annualized } ROI = (1 + ROI)^{\frac{1}{n}} - 1 \tag{17.3}$$

[38] https://www.investopedia.com/articles/basics/10/guide-to-calculating-roi.asp, accessed on 20-06-2023

Chapter 18: Conclusions and Recommendations

This report outlines the design process of an unmanned autonomous aerial surveillance system to monitor wildlife and orography, detect environmental threats, and identify the location of litter. The final concept following from the midterm report is studied in detail in this report. Systems and subsystems are designed to meet the requirements set by the stakeholders. While the design has been optimized to the best possible extent within the given time constraints, there are areas that can be further improved on to enhance the UAV's performance.

Understanding the UAV's operations is crucial to verify whether the UAV meets the mission requirements. Different grids and flight paths can be used to surveil a $50\,\text{km}$ by $50\,\text{km}$ area. The selection of a grid system composed of hexagons where each hexagon is subdivided into triangles ensures effective coverage of the area. This means 14 ground stations and 28 UAVs are needed to cover the required area. Each triangle of $30\,\text{km}^2$ requires a flight path length of $51\,\text{km}$ which can be surveilled in 40 minutes with cruise conditions, fastly exceeding the minimum area covered by a single flight and doing so in a mission time much shorter than the 2-hour stakeholder requirement.

The stakeholders require the UAV to operate without any greenhouse emissions. This means that the UAV cannot use fossil fuels for its propulsion system. Batteries are chosen as the best alternative for the mission where two $30\,\text{Ah}$ batteries suffice to meet the mission requirements.

To control and stabilize the UAV during cruise flight a tail sizing analysis was performed based on the longitudinal moment equilibrium and longitudinal moment equilibrium derivatives. To ensure longitudinal static stability and controllability a tail area of $0.40\,\text{m}^2$ is required with a boom length of $2.85\,\text{m}$ measured from the centroid of the front VTOl propeller and the leading edge of the horizontal tail. Dynamic controllability and stability are achieved using the control surfaces which are controlled by the autopilot. The UAV contains three main control surfaces, namely the elevator, ailerons and rudders. The length, chord and area are $1.2\,\text{m}$, $0.09\,\text{m}$, and $0.108\,\text{m}^2$ for the Elevator; $0.5\,\text{m}$, $0.07\,\text{m}$, and $0.035\,\text{m}^2$ for the Aileron; and $0.24\,\text{m}$, $0.14\,\text{m}$, and $0.034\,\text{m}^2$ for the Rudder.

Before the UAV is actually built and tested it is more cost effective to create a flight simulation. The open-source and widely adopted JSBSim flight dynamics model was used to create a non-linear six-degree of freedom simulation that has the ability to simulate the entire flight regime. An aerodynamic analysis of the CATIA mesh using VLM analysis in openVSP provided inputs for the flight simulations. To verify whether the openVSP software gives the correct results it is verified that the results of the analyses converge for an increasing number of iterations. Other than providing a proof-of-concept of the tooling and architecture used for the UAV's brains, the simulation was used to confirm various performance estimations. Firstly, it showed that the maximum achievable speed of the UAV is approximately $145\,\text{km}\,\text{h}^{-1}$. Secondly, it showed that the take-off and transition procedure could be completed in less than a minute. This is important information to verify whether the UAV meets the time constraints of the fast response mission. Lastly, it showed that it was possible to cover a straight-line distance of almost $4\,\text{km}$ in less than 4 minutes after the UAV takes off from the ground.

All these components need to be connected together by a structure which will have to be able to withstand load factors ranging between -2 and 4.5 for speeds up to $29\,\text{m/s}$. A doghouse plot shows the turn climb performance maximum bank angle within the operating aforementioned conditions and can be used to give a more precise maximum operational environment of the UAV if it would be deployed in a different mission in the future.

To not disturb the wildlife and to not notify the poachers of the presence of the UAV it is essential that the UAV shall operate as quietly as possible. The main source of noise is the propellers. The noise source levels were estimated using Hanson's model for propeller noise. A sound pressure level is obtained from the Hanson model which is combined with the sound exposure level and the Day-Evening-Night average level to determine the noise impact of the operation of the UAV. The system was found to have a mission noise level of $37.79\,\text{dB}$ which complies with the stakeholder requirements.

Sustainability considerations play a significant role in the design. Emissions of the UAV should be minimized and a good end-of-life plan shall be in place to minimise the impact on the environment. The emissions of the UAV during flight will be much more significant than the emissions during production. The UAV is therefore

designed in such a way that the operational emissions are reduced at the cost of higher production emissions.

Next to the technical aspects of the design, the risk profile and financial performance of the design need to be addressed. Identifying the risks and developing mitigation strategies for them allows to drastically reduce the extent of negative consequences while a thorough financial cost & profit analysis allows to minimize financial losses and evaluate the success of the project.

Furthermore - upon completing a ten-week design process for this UAV - several positive aspects, as well as shortcomings, have been identified. Due to time constraints and the limited scope of the project, many of the shortcomings will have to be further investigated.

Starting with the UAV itself, the elevator and ailerons are designed based on pitch and roll acceleration, respectively. Due to the limited amount of literature on rudder sizing, the sizing is currently done based on a formula given in [13], stating that the rudder surface area is 0.4 times the vertical stabilizer surface area. However, this can only be considered as preliminary sizing, as a rudder sizing method will have to be found or created in order to perform realistic sizing. Furthermore, the rudder design has to be based on performance requirements like obstacle avoidance and turn performance requirements to optimize the size. In future designs, the location of the cg should be re-examined as the centre of gravity in this design results in a very large horizontal stabilizer. Lastly, the simulation provided a yaw control of only 2 deg/s. This value is very low and should be re-examined in future design phases.

In this report, no sensitivity analysis on the structures or on aerodynamics has been performed. It is recommended that a sensitivity analysis on those subsystems is conducted in a future design process in order to demonstrate the overall feasibility of the design. Furthermore, no sensitivity analysis was conducted on the amount of energy used during flight and on landing in general.

The feasibility of the use of solar panels on the ground station's roof has not been analyzed in this design. This could decrease the environmental footprint of the ground station. Moreover, the ground station has been designed using high-emissions materials. In future design stages, it is important to look at a more environmentally friendly solution.

Based on the current aerodynamic analysis, the wake of the booms over the main wings is not taken into account. Further iterations on the main wings are much needed, as the size could also be reduced. Currently, the wings produce an excessive amount of lift and therefore also an excessive amount of drag. Reducing the wing size, will create a snowball effect and reduce the weight accordingly therefore reducing the weight of the battery.

Many structural considerations were not taken into account due to time constraints. Proper testing like three-point bending tests and compression tests will be needed on testing parts. No vibrational loads are currently taken into account, therefore, extensive analysis and testing will be needed for it. To be able to access the payload for maintenance, a significant-sized hatch is added, which has not been taken into account when structurally calculating the fuselage. This is crucial to calculate, as stress concentrations can add many failure modes and will need additional stiffening in the structure. Added to that, the manufacturability of the stringers will have to be further analyzed. The stringers are currently very thin whilst being curved in two directions. This is extremely difficult to manufacture consistently and has almost no safety margin. Lastly, the structures of the landing gear have only been minimally calculated and should therefore be further investigated.

In this report, the climb has only been analyzed in a limited fashion. It is therefore suggested to decrease the level of fidelity in future climb analyses. Moreover, in this design, it was noted that flying for orography and flying for surveillance reduces the performance of the UAV. It is recommended in future designs to reconsider the use of a permanent orography system integrated into the overall design. Furthermore, the choice to make the design fully autonomous results in a drastically more expensive system. The use of manpower reduces the cost.

Taking into account all the recommendations that have been considered, it is evident that there are still areas for improvement. However, given the time constraint provided, the design has been optimized to the best possible extent.

References

[1] F. Oliviero. *Requirement Analysis and Design principles for A/C stability & control (Part 1)*. Lecture Slides. Mar. 2022.

[2] Job de Vries et al. *Autonomous Quiet Aerial Surveillance System Midterm Report*. Tech. rep. Delft University of Technology, 2023.

[3] Jian Li et al. "UAV Path Planning Model Based on R5DOS Model Improved A-Star Algorithm". In: *Applied Sciences* 12.22 (2022), p. 11338.

[4] Ziwen Jiang et al. "An autonomous landing and charging system for drones". PhD thesis. Massachusetts Institute of Technology, 2019.

[5] S. Garrido-Jurado et al. "Automatic generation and detection of highly reliable fiducial markers under occlusion". In: *Pattern Recognition* 47.6 (2014), pp. 2280–2292. ISSN: 0031-3203. DOI: https://doi.org/10.1016/j.patcog.2014.01.005. URL: https://www.sciencedirect.com/science/article/pii/S0031320314000235.

[6] Katharina Pentenrieder, Peter Meier, Gudrun Klinker, et al. "Analysis of tracking accuracy for single-camera square-marker-based tracking". In: *Proc. Dritter Workshop Virtuelle und Erweiterte Realitt der GIFachgruppe VR/AR, Koblenz, Germany*. Citeseer. 2006.

[7] Arexy Monterroso. "Preliminary sizing, flight test, and performance analysis of small tri-rotor VTOL and fixed-wing UAV". PhD thesis. 2018.

[8] Andrew J. Keane, András Sóbester, and James P. Scanlan. *Small unmanned fixed-wing aircraft design: a practical approach*. John Wiley & Sons, June 2017.

[9] R. Vos, M.F.M. Hoogreef, and B.T.C. Zandbergen. *3 - Wing loading thrust loading 1 [PowerPoint]*. Feb. 2021.

[10] R. VOS and J. A. Melkert. "Aerospace Design and Systems Engineering Elements I: Wing and Propulsion System Design". In: (2021).

[11] Gregory A. Williamson et al. *Summary of Low-Speed Airfoil Data*. Vol. 5. SoarTech Publications, 2021.

[12] R. Colgren M. Sadraey. "A Systems Engineering Approach to the Design of Control Surfaces for UAVs". In: *AIAA Aerospace Sciences Meeting and Exhibit* (Jan. 2007). DOI: 10.2514/6.2007-660.

[13] Md. Samad Sarker et al. "Detail design of empennage of an unmanned aerial vehicle". In: *AIP Conference Proceedings* (Dec. 2017). DOI: 10.1063/1.5018551.

[14] J.D.Anderson. *Aircraft Performance and Design*. Tata McGraw Hill Education. ISBN: 978-0-07-070245-5.

[15] R. C. Hibbeler. *Mechanics of Materials*. Pearson, 2022.

[16] T.H.G Megson. *Aerospace Engineering - Aircraft Structures for Engineering Students*. 4th ed. Butterworth-Heinemann. ISBN: 978-0750667395.

[17] *Toray TC380*. Toray Advanced Composites. July 2019.

[18] Joris Melkert and Calvin Rans. *Buckling (AE2135-I Structural Analysis & Design)*.

[19] Howard D. Curtis. *Fundamentals of Aircraft Structural Analysis*. Richard d Irwin. ISBN: 978-0256192605.

[20] George Lubin and A. Marshall. "Sandwich Construction". In: *Handbook of composites*. Van Nostrand Reinhold, 1982, pp. 557–601.

[21] Jon Berndt. "JSBSim: An open source flight dynamics model in C++". In: *AIAA Modeling and Simulation Technologies Conference and Exhibit*. 2004, p. 4923.

[22] Oihane Cereceda Cantarelo, Luc Rolland, and Siu O'Young. "Validation discussion of an Unmanned Aerial Vehicle (UAV) using JSBSim Flight Dynamics Model compared to MATLAB/Simulink AeroSim Blockset". In: *2016 IEEE International Conference on Systems, Man, and Cybernetics (SMC)*. 2016, pp. 003989–003994. DOI: 10.1109/SMC.2016.7844857.

[23] D.B. Hanson. "Near-Field Frequency - Domain Theory for Propeller Noise". In: *AlAA 8th Aeroacoustics Conference*. 1983.

[24] R.M. Martinez. *Sound Metrics for Aircraft Noise Assessment*. Lecture Slides. May 2023.

[25] T. Motshweni. *Screening-Level Noise Impact Assessment for the Proposed Development of Makwase Crusher Plant*. Tech. rep. SustainDev Services, 2017.

[26] *The Environmental Management (Standards for the Control of Noise and Vibrations Pollution)*. National Environment Management Council, 2014.

[27] F. Langers C.M. Goossen. *Geluidbelasting in het Centraal Veluuws Natuurgebied*. Tech. rep. Alterra Research Instituut voor de Groene Ruimte, 2003.

[28] R.C. Hibbeler. *Engineering Mechanics Statics*. 14th ed. ISBN: 978-1-292-08923-2.

[29] M. den Hoed et al. "Modelling propeller noise emissions at low Reynolds number produced by clean and turbulent inflow". In: *TU Delft AE2223-I* (2022).

[30] A.Cervone and B.T.C. Zandbergen. *Electrical Power Systems for Aerospace Vehicles*. Feb. 2017.

[31] B. Fu K. R. Mallon F. Assadian. "Analysis of On-Board Photovoltaics for a Battery Electric Bus and Their Impact on Battery Lifespan". In: *Energies* (2017).

[32] Matty Janssen et al. "Life Cycle Assessment of Lignin-based Carbon Fibres". In: *14th Conference on sustainable development of energy, water and environment systems (SDEWES)*. Dubrovnik, Oct. 2019.

[33] Jonathon M. Chard et al. "Shades of Green: Life Cycle Assessment of a Urethane Methacrylate/Unsaturated Polyester Resin System for Composite Materials". In: *Sustainability* 11.4 (2019). ISSN: 2071-1050. DOI: 10.3390/su11041001. URL: https://www.mdpi.com/2071-1050/11/4/1001.

[34] Fanran Meng. "Environmental and cost analysis of carbon fibre composites recycling". PhD thesis. University of Nottingham UK, 2017.

[35] Job de Vries et al. *Autonomous Quiet Aerial Surveillance System Baseline Report*. Tech. rep. Delft University of Technology, 2023.

Appendix A: Functional Breakdown Figures

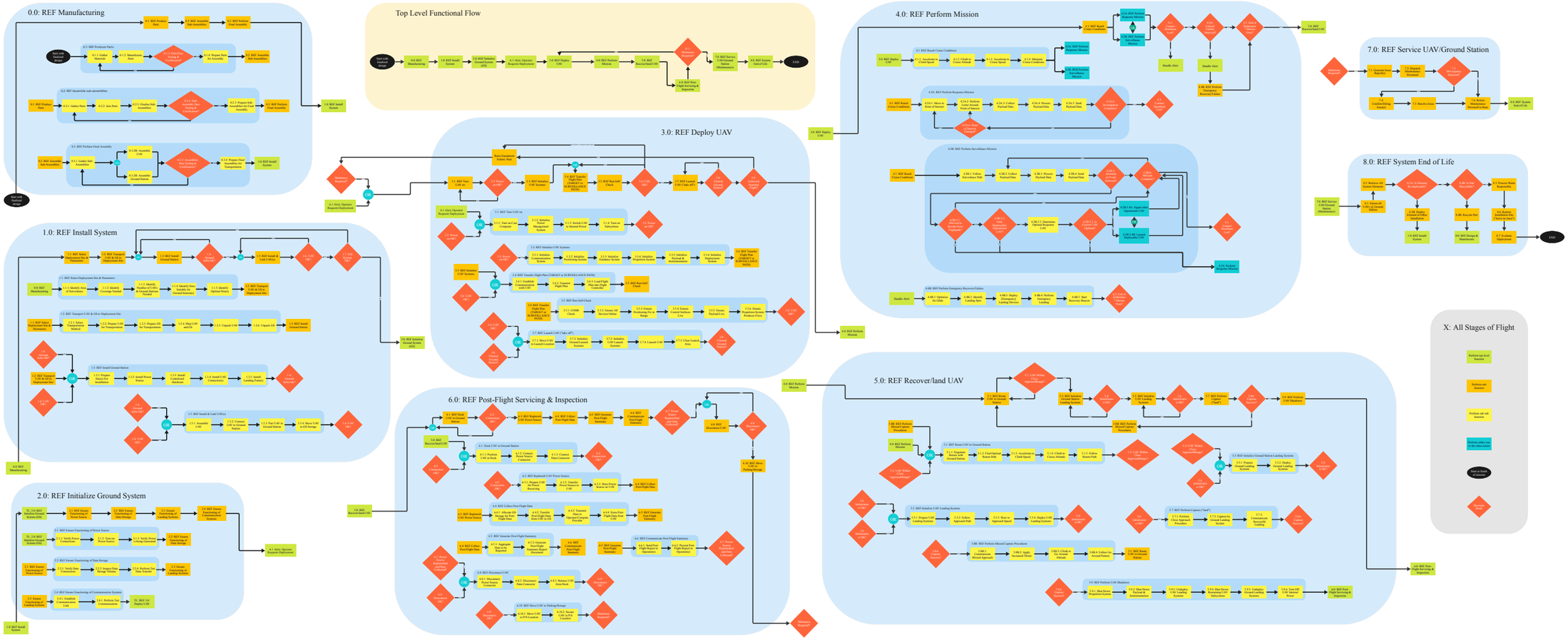

Figure A.1: Functional Flow Diagram.

Figure A.2: Functional Breakdown Structure.